Optical Analysis of $[Ca^{2+}]i$ and Mitochondrial Signaling Pathways: Implications for the Selective Vulnerability of Motoneurons in Amyotrophic Lateral Sclerosis (ALS)

Dissertation
zur Erlangung des Doktorgrades
der Mathematisch-Naturwissenschaftlichen Fakultäten
der Georg-August-Universität Göttingen

vorgelegt von
Manoj Kumar Jaiswal
aus Bharkhar (Kaemur), Indien

Göttingen, 2007

D7
Referent: **Prof. Dr. Reinhold Hustert**
Koreferent: **Prof. Dr. Friedrich-Wilhelm Schürmann**

Tag der mündlichen Prüfung: 23.01.08

Dedicated to my Parents
& All who love and
Care for me

Contents

ABBREVIATIONS……………………………………………………………...VI

1. INTRODUCTION……………………………………………………..1

1.1 Motor System …………………………………………………………………….1

1.1.1 Upper and lower motoneurons ………………………………..……............2

1.1.2 Selective vulnerability of motoneurons in ALS…………………......................2

1.2 Amyotrophic Lateral Sclerosis (ALS)…………………………..……….……....3

1.2.1 Sporadic ALS (sALS)……………….………………...............................….5

1.2.2 Familial ALS (fALS)………….….….………………..............................…5

1.2.3 In-Vitro cell culture model of ALS……………….……...................................6

1.3 **Metabolic Malfunction and Disease Mechanism in ALS……………………...….7**

1.3.1 Oxidative stress………….………………………..…..............................8

1.3.2 Mitochondrial dysfunction………………………………………….……….9

1.3.3 Disrupted calcium homeostasis abnormalities in ALS….….…………….………...11

1.3.4 Glutamate transmission and excitotoxicity……………………………….....13

1.3.5 Abnormal misfolded protein stress………………………………………….…....15

1.3.6 Cytoskeletal disorganisation and neurofilament defects……..……………….…16

1.3.7 Abnormalities in intracellular axonal transport……………………………....17

1.3.8 Toxicity linked to mutation of Cu-Zn superaoxide dismutase1 (SOD1)……....18

1.4 Neuron-Glia Communication …………………………………….……………….…20

1.4.1 Neuron-Glia imaging …………………………………………..……..........21

1.4.2 Glia Ca^{2+} signaling …………………………………………………….…..........22

1.4.3 Glia Ca^{2+} signaling as determinants of disease progression in ALS…..……...24

1.5 Neuroprotective Study of Drugs (Riluzole and Melatonin) in ALS……..…..…..25

1.5.1 Effect of Riluzole in ALS neuroprotection……………………..……...........25

1.5.2 Effect of Melatonin in ALS neuroprotection……………….……..…..……26

1.6 Mitochondrial Dysfunction, Ca^{2+} Homeostasis and ALS: an Integrative outlook….……..27

2. MATERIALS AND METHODS…………………...……….……..…...29

2.1 Experimental Set-up……………………………………………….……..……......29

2.2 Transgenic Mice and PCR Genotyping……….……….……..……….……….........30

2.3 Preparation of Mice and Rat Brain Stem Slices……………………...….……........31

2.4 Identification of Hypoglossal Motoneurons in the Brain Stem Slices……..……33

2.5 WT and $SOD1^{G93A}$ Transfected SH-SY5Y Neuroblastoma Cell Culture...........34

2.6 CCD Camera Imaging…………………………………………………….….…...34

2.7 Monitoring of Mitochondrial Parameters (Membrane Potential)…...................36

2.8 Intracellular Microfluorometric Ca^{2+} Measurement.…………..…………........36

2.9 Simultaneous Measurement of changes in $[Ca^{2+}]_i$ and $[Ca^{2+}]$m……………...…38

2.10 Calbindin-D_{28k} Buffering and Estimation of Decay Time Constant (τ)…..…....39

2.11 Targeted Pressure Injection of Mitochondrial and Ca^{2+}-Sensitive Dye……..…..40

2.12 Confocal Laser Scanning Microscopy (CLSM)……………………………….…41

2.13 Ca^{2+} Imaging using Confocal Laser Scanning Microscope…..……….……..…..42

2.14 2-Photon Imaging of Ca^{2+} and ΔΨm in Motoneurons and Glial Cells……..…..43

2.15 Drugs (Riluzole and Melatonin) Neuroprotection study in ALS…………...….43

2.16 Materials……..………………………………………………………….............44

2.17 Analysis…………………………..…………………………………………..….45

3. RESULTS………………………………………………………………..47

3.1 Role of Mitochondria and Calcium Signaling in Motoneurons…………….…...47

3.1.1 Pharmacological manipulation of mitochondria in motoneurons by the mitochondrial uncoupler FCCP ………….…………………………........48

3.1.2 Pharmacological manipulation of mitochondria in motoneurons by blocking the F_1, F_0-ATP synthase…………………..…………………..……..51

*3.1.3 Impact of plasma membrane depola*risation on mitochondrial function……....53

3.1.4 Impact of plasma membrane depolarisation and inhibition of F_1, F_0-ATP synthase on FCCP evoked responses of the Δ Ψm in brain stem slices of juvenile and adult mice…………………………………………………..54

3.1.5 Measurement of Ca^{2+}-release responses in motoneurons………….…………...57

3.1.6 FCCP causes differential calcium release and Ca^{2+} transients in brain stem slices of juvenile and adult WT and $S0D1^{G93A}$ mice……………...……...58

3.1.7 *Impact of plasma membrane depolarisation on mitochondrial Ca^{2+} uptake and $[Ca^{2+}]i$ release in brain stem slices of juvenile and adult WT and S0D1^{G93A} mice*……………….…..……………………………...…....59

3.1.8 *Pharmacological manipulation of ER in motoneurons by cyclopiazonic acid (CPA) inhibition of SERCA and its impact on differential Ca^{2+} store regulation*……………………………………………………….61

3.1.9 *Interaction between ER and mitochondria in differential Ca^{2+} store regulation and the role of ER as a Ca^{2+} sequestering organelle in juvenile and adult brain stem slices of WT and S0D1^{G93A} mice*……………………….…..63

3.2 Role of Mitochondria in SH-SY5Y Cells in defining Ca^{2+} Metabolism of ALS Vulnerable Motoneurons ……………………………………….….….…66

3.2.1 *Impaired ability of SH-SY5Y Neuroblastoma cells transfected with SOD1^{G93A} to cope with FCCP-induced Ca^{2+} influx*………………………….……..66

3.2.2 *Effect of High K^+-evoked Ca^{2+} transient and its impact on FCCP-induced Ca^{2+} influx in WT and SOD1^{G93A} transfected SH-SY5Y neuroblastoma cells*....67

3.3 Simultaneous Measurement of Cytosolic and Mitochondrial Ca^{2+} Concentrations in WT-SOD1 and SOD1^{G93A} transfected SH-SY5Y Neurobalstoma Cells Culture Model of Motoneuron Disease……………….……..70

3.3.1 *Monitoring cytosolic (Fura-2) and mitochondrial (Rhod-2) Ca^{2+}concentration with a temporal resolution in the millisecond time domain after inhibition of mitochondrial Ca^{2+} sequestration in WT-SOD1 and SOD1^{G93A} transfected SH-SY5Y cells* ……..………………………………………………….……..…71

3.3.2 *Involvement of ER and mitochondria in shaping $[Ca^{2+}]i$ and $[Ca^{2+}]m$ regulation in WT-SOD1 and SOD1^{G93A} transfected SH-SY5Y cells*…………...73

3.4 Study of Calcium Buffering Capacity and its Impact on Motoneurons……...…76

3.4.1 *Calbindin-D_{28k} decreases $[Ca^{2+}]i$ following stimulations in motoneurons*…....76

3.4.2 *Calbindin-D_{28k} decreases the susceptibility of motoneurons to excitability and increases the decay time constant (Ca^{2+} clearance rates (τ)*……………..78

3.5 Validation of Riluzole and Melatonin as a Neuroprotective Drug by Inhibition of Ca^{2+} Signaling in HMNs of WT and SOD1^{G93A} Mice ………...……….….…..80

3.5.1 *Riluzole mediate mild and reversible but delayed blockade of the $[Ca^{2+}]i$ in fura-2/AM loaded HMNs exposed to Na^+-azide in 14-15 weeks old symptomatic SOD1^{G93A} transgenic mice*…………………………..…..…....80

3.5.2 Melatonin fails to block [Ca^{2+}]i signaling through Na^{+}-channels in fura-2/AM loaded HMNs in WT and symptomatic $SOD1^{G93A}$ mice ………….….83

3.6 Dynamic Calcium Signaling between Neuron-Glia and its implications in Physiology and Pathophysiology……………………………………….…....86

3.6.1 Loading of Calcium sensitive dye and identification of glial cells distinct from motoneurons in brain stem slices……………………………..................86

3.6.2 Spontaneous Calcium oscillations in brain stem glial cell network: Endogenous Ca^{2+} excitability……………………………………................89

3.6.3 Intracellular Ca^{2+} waves: glia-to-glia communication in brain stem slice network…………………………………….……….....................91

3.6.4 Glutamate induced [Ca^{2+}]i signaling in motoneuron-glia network In rat brain stem slices: implications for ALS…………..……..……….........91

3.6.5 CN^{-} (chemical hypoxia) -evoked [Ca^{2+}]i signaling in motoneuron-glia network in rat brain stem slices………………………………....................97

3.6.6 FCCP-evoked [Ca^{2+}]i in motoneuron-glia network in rat brain stem slices after hypoxia………………..99

3.6.7 Effect of metabolic inhibitors on ΔΨm of motoneuron-glia network in rat brain stem slices………...102

3.6.8 Glutamate-mediated ΔΨm in motoneuron-glia network of rat brain stem slices………….……………………………………………………....103

3.6.9 Mitochondrial complex IV inhibitor (CN^{-}) induced/s depolarization of mitochondrial membrane in motoneuron-glia network in rat brain stem slices…….………………………………….……………….…104

3.6.10 Impact of mitochondrial uncoupler FCCP depolarization efficacy on ΔΨm in motoneuron-glia network in rat brain stem slices………………….…..…107

3.6.11 Assessment of long term ΔΨm recordings to check slice viability for glutamate, hypoxia and mitochondrial uncoupler induced neurotoxicity in motoneuron-glia network in rat brain stem slices…………………………...109

4. DISCUSSIONS…………………………..…………………………..……111

4.1 Monitoring ΔΨm in HMNs of WT and $mSOD1^{G93A}$ Mice Disrupting Mitochondrial Integrity by Mitochondrial Uncoupler FCCP…..…….………113

4.2 Mitochondrial Status in Vulnerable HMNs of $SOD1^{G93A}$ Mice…….………...114

4.3 The Effect of Mitochondrial Inhibition on [Ca^{2+}]i Release-Uptake Phenomenon and Ca^{2+} Transient in WT and $SOD1^{G93A}$ Mice/Cell Culture Model of ALS………………………………………………………...116

4.4 Mechanism Underlying Mitochondria-ER Ca^{2+} Stores Coupling………..…...118

4.5 Simultaneous Measurements of [Ca^{2+}]i and [Ca^{2+}]m and Ca^{2+} Sequestration Source Specificity and Spatiotemporal Properties of WT and $SOD1^{G93A}$ Transfected SH-SY5Y Cells...120

4.6 Characteristic Low Ca^{2+} Buffering Capacity of MN and its Impact on Selective MN Vulnerability……..……………………………………………121

4.7 Cross-Talk Between Neuron-Glia in ALS Vulnerability and Pathogenesis….123

4.8 Drug Targets in ALS: Design and Implementation of Multi drug Therapies, Where Should We Aim? …………………………………………………..….....124

4.9 Consequence of Disturbed Mitochondrial Mechanism, Selective Vulnerability and its Implications for Pathogenesis - Proposed Mechanism and Interactive Model……………………………………………………………………......126

Conclusions……………………………………………………………………..129

SUMMARY………………………………………………..…………..…………...130

5. BIBLIOGRAPHY……………………………………………………..133

Acknowledgements……………………...……………………………………….……156

Publications………………………………………………………………………....158

Meeting-conference abstracts, talks & Summer School…………..……..………..……..159

Curriculum vitae……………………………………………………….……..........160

Abbreviations

AAV-2	Adeno-associated virus-2
aCSF	Artificial cerebrospinal fluid
CSF	Cerebrospinal fluid
ALS	Amyotrophic lateral sclerosis
AM	Acetoxy methyl
AMPA	α-amino-3-hydroxy-5-methyl-4-isoxazole propionic acid
ATP	Adenosine triphosphate
AUC	Area under the time-concentration curve
BAPTA	1, 2-bis (o-aminophenoxy) ethane-N,N,N',N'-tetraacetic acid
Ca^{2+}	Calcium
$[Ca^{2+}]i$	Intracellular calcium concentration (Cytosolic Ca^{2+})
$[Ca^{2+}]m$	Mitochondrial calcium concentration
CB-D_{28k}	Calbindin-D_{28k}
CCD	Charge-coupled device
CCS	Copper chaperone of SOD1
CLSM	Confocal laser scanning microscope
CN^-	Cyanide
CNQX	6-cyano-7-nitroquinoxaline-2, 3-dione disodium salt
CNS	Central nervous system
COX	Cytochrome *c* oxidase
CPA	Cyclopiazonic acid
D-AP-5	D(-) 2-amino-5-phosphonopentanoic acid

D-MEM	Dulbeccos modified eagles medium
DMSO	Dimethylsulfoxide
DNA	Deoxyribonucleic acid
EAAT	Excitatory amino acid transporter
e.g.	For example
ER	Endoplasmic reticulum
et al	et alteri (and others)
ETS	Electron transport system
FCCP	Carbonyl cyanide 4-trifluromethoxyphenylhydrazone
FCS	Fetal calf serum
FMN	Facial motoneuron
g	Gramm (9.81m/s^2)
GABA	Gamma-aminobutyric acid
GluR	Glutamate receptor
G93A	Glycine to alanine at position 93
GΩ	Giga Ohm
HMN	Hypoglossal motoneuron
InsP3	Inositol-1,4,5-trisphosphate
l	Liter
LSM	Laser scanning microscope
kDa	Kilodalton
kHz	Kilo Hertz
MCU	Mitochondrial calcium uniporter
min	Minute
MNs	Motoneurons

mol	Molar
mosmol	Milliosmol
MPM	Multi photon microscopy
mRNA	Messenger ribonucleic acid
mSOD1	Mutant superoxide dismutase 1
mM	Mili molar
mV	Millivolts
NF	Neurofilament
nm	Nanometer
nM	Nanomolar
NADH	Nicotinamide adenine dinucleotide, reduced form
NMDA	N-methyl D-aspartate
OMN	Oculomotor neuron
ONOO-	Peroxynitrite ion
PBC	Pre-Botzinger complex
PBS	Phosphate buffer saline
PET	Positron emission tomography
pH	Negative logarithm of relative hydrogen ion Concentration
psi	Pounds per square inch
Rhod 123	Rhodamine 123
ROI	Region of interest
ROS	Reactive oxygen species
rpm	Revolution per minute
RPMI	Roswell park memorial institute
RyR	Ryanodine receptor

s	Second
S.D.	Standard deviation
S.E.M.	Standard error mean
SERCA	Sarcoendoplasmic reticulum Ca^{2+}-ATPase
SMN	Spinal motor neurons
SOD1	Superoxide dismutase 1
t	Time
TBS	Trichloroethylene-buffered saline solution
TMN	Trochlear motoneuron
TTX	Tetrodotoxin
UV	Ultraviolet
VDCC	Voltage dependent calcium channel
VS.	Versus
WT	Wild type
ΔΨm	Mitochondrial membrane potential
µm	Micro meter
µ	Micro(10^{-6})
°C	Degree Celsius
λ	Wave length
%	Percent
τ	Decay time constant

1. Introduction

Neurons are highly complex structures consisting of an axon, soma, and a dendritic tree. Protection of the functional and structural integrity of neurons throughout life is a complex task that requires sophisticated transport, damage control and repair machinery. Identifying the mechanisms underlying the aging and degeneration of neurons is an important task in the study of neurodegenerative diseases (diseases that cause the premature loss of neurons). In general, neurodegenerative disease are characterized by the degeneration of specific groups of neurons, e.g. cortical neurons in Alzheimer's disease and dopaminergic neurons of the substantia nigra in Parkinson's disease. The subject of this thesis is amyotrophic lateral sclerosis (ALS), a neurodegenerative disorder of motoneurons (MNs). ALS, dementia and Parkinsonism are characterized by a decrease in nervous system functionality due to loss of neurons through shared or discrete mechanisms. Although the complex etiologies of each of these disorders are not yet fully understood, there is increasing evidence that these three neurodegenerative disorders may share distinct neurodegenerative pathways leading to overlapping clinical features and neuropathological characteristics. A major breakthrough in ALS research came with the identification of mutations in the superoxide dismutase 1 (SOD1) gene in 1993. In the present study, we used a mouse model as well as cell culture model of ALS to unravel the factors that contribute to the pathogenesis of ALS focusing on three potential pathogenic factors: Calcium homeostasis, mitochondrial signaling and oxidative stress pathway in MNs.

1.1 Motor System

Sherrington called the MN the final COMMON PATH because all the neural influences that have to do with movement or posture converge on it. Each MN innervates a group of muscle fibres and together with them forms a functional unit which regulates different body muscles, and is called the Motor Unit. Sherrington wrote on one occasion “To move things is all mankind can do…. whether whispering or feeling a forest” (Grillner & Dickinson, 2002). His words meant that the only output channel of the brain is the motor system. Motor systems that maintain posture and produce coordinated movements are organised in an orderly hierarchy.

1.1.1 Upper and Lower Motoneurons

The term MNs are used for those neurons in the spinal cord and the brainstem that innervate skeletal muscle fibers, also referred to as α-motoneurons. These MNs are organized in the central nervous system into definite motor nuclei along the brainstem and spinal cord (Lower Motoneurons, LMN; Fig. 1.1). Cerebral motor cortex neurons maintain accurate motor behaviour by sending their axons either to the medulla region of the brain stem or to the ventral horn of the spinal cord, called the Upper Motoneurons (UMN; Fig. 1.1). They represent the center for coordination of the motor function for goal-oriented output. In clinical terminology, α-motoneurons are referred to as 'lower motoneurons'. α-Motoneurons are usually grouped into three classes depending on their size, firing properties and the properties of their muscle fibers. Small tonically active α-motoneurons innervate muscle fibers that contract relatively slowly and generate small forces, but are fatigue resistant. Large α-motoneurons innervate muscle fibers that are rapidly fatigued but are fast and produce large forces as required for running or jumping. A third class of α-motoneurons is intermediate in size and innervates muscle fibers with intermediate properties. 'Upper motoneurons' are neurons primarily localized in the motor cortex that control movement by directly or indirectly controlling the activity of α-motoneurons. In addition, γ-motoneurons are a class of small motoneurons that innervate muscle fibers within a muscle spindle.

1.1.2 Selective Vulnerability of Motoneurons in ALS

Amyotrophic lateral sclerosis (ALS) is a multifactorial disease characterized by the selective loss of upper and lower MNs. The salient clinical feature of ALS is the loss of muscle strength due to muscle atrophy leading to difficulties in performing voluntary and involuntary movements including locomotion, breathing, swallowing and speech. Symptoms due to loss of UMN are distinct from those due to loss of LMN. LMN degeneration results in weakness, fatigue, muscle atrophy and loss of reflex reaction and fasciculations; however, small α-motoneurons are relatively unaffected in ALS. UMN damage causes untimely reflex responses, stiffness and slowing of movements. γ-motoneurons that innervate muscle fibers within a muscle spindle are mostly unaffected in ALS.

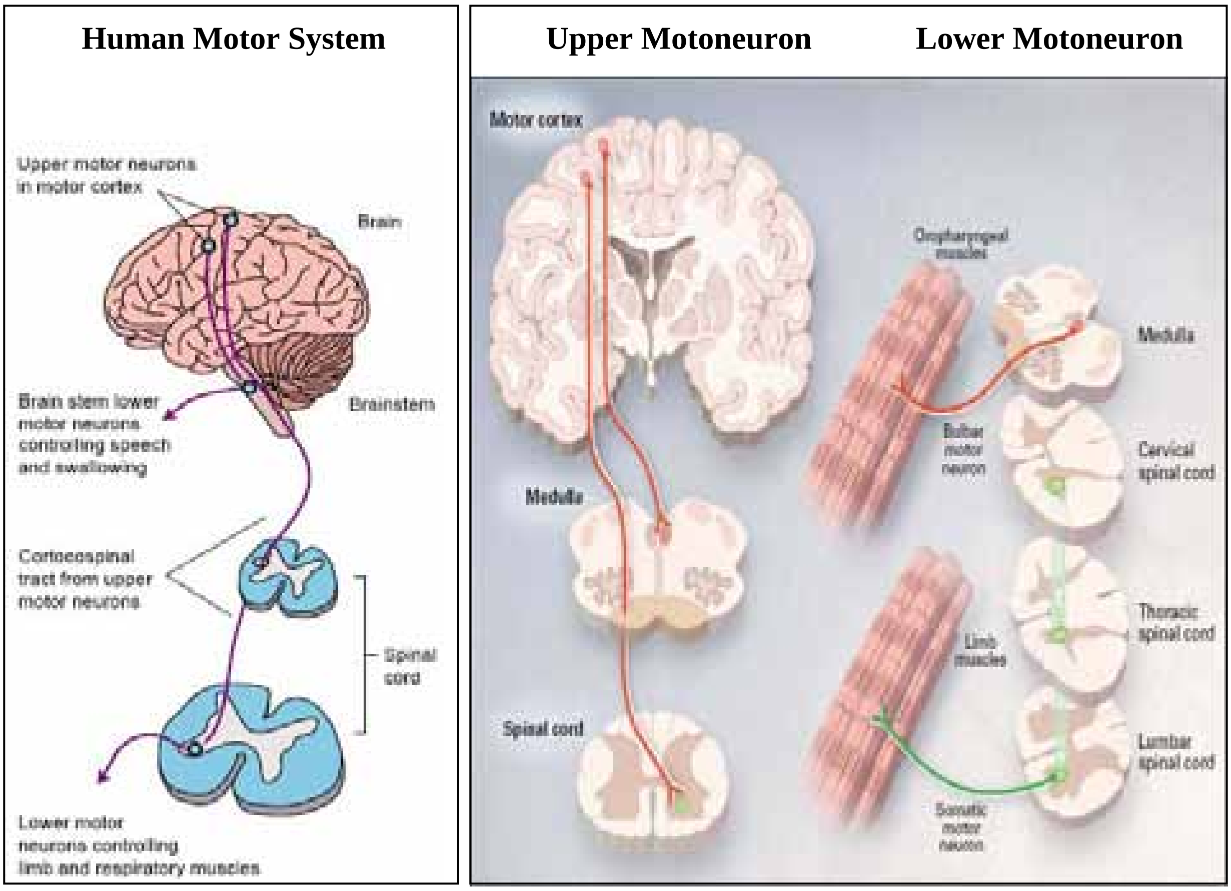

Human Motor System

Upper Motoneuron

Lower Motoneuron

Upper motor neurons in motor cortex
Brain
Brain stem lower motor neurons controlling speech and swallowing
Brainstem
Corticospinal tract from upper motor neurons
Spinal cord
Lower motor neurons controlling limb and respiratory muscles
Motor cortex
Medulla
Spinal cord
Oropharyngeal muscles
Medulla
Bulbar motor neuron
Cervical spinal cord
Limb muscles
Thoracic spinal cord
Lumbar spinal cord
Somatic motor neuron

Fig. 1.1: Lower motor neurons originating in the brain stem control speech and swallowing; lower motor neurons that originate in the spinal cord control limb and respiratory muscles, both be affected in ALS. The motoneurons in the motor cortex, brainstem motoneurons and motoneurons of the ventral horn of spinal cord are seen to degenerate in ALS. (Adapted from Rowland & Schneider, 2001; Goodall & Morrison, 2006).

1.2 Amyotrophic Lateral Sclerosis (ALS)

ALS was first described, in 1873 by the French neurologist Jean Martin Charcot who also coined the term Amyotrophic lateral sclerosis (sclerose lateral amyotrophique). His precise and systematic clinical observations still hold true. The word *amyotrophic* is derived from Greek word “amyotrophique” meaning ‘no nutrition for the muscles’. ALS is a fatal adult-onset neurodegenerative disorder characterised by selective MN loss of upper and lower MNs as well as brainstem and spinal cord, leading to progressive weakness and muscle atrophy with eventual paralysis and death within five years of clinical onset. ALS is also commonly known as motor neuron disease in English speaking countries (term introduced by Gowers) or Lou Gehrig’s disease after the famous U.S.A baseball player Lou Gehrig who fell victim to the disease and died of the disorder in 1936 (Fig. 1.2).

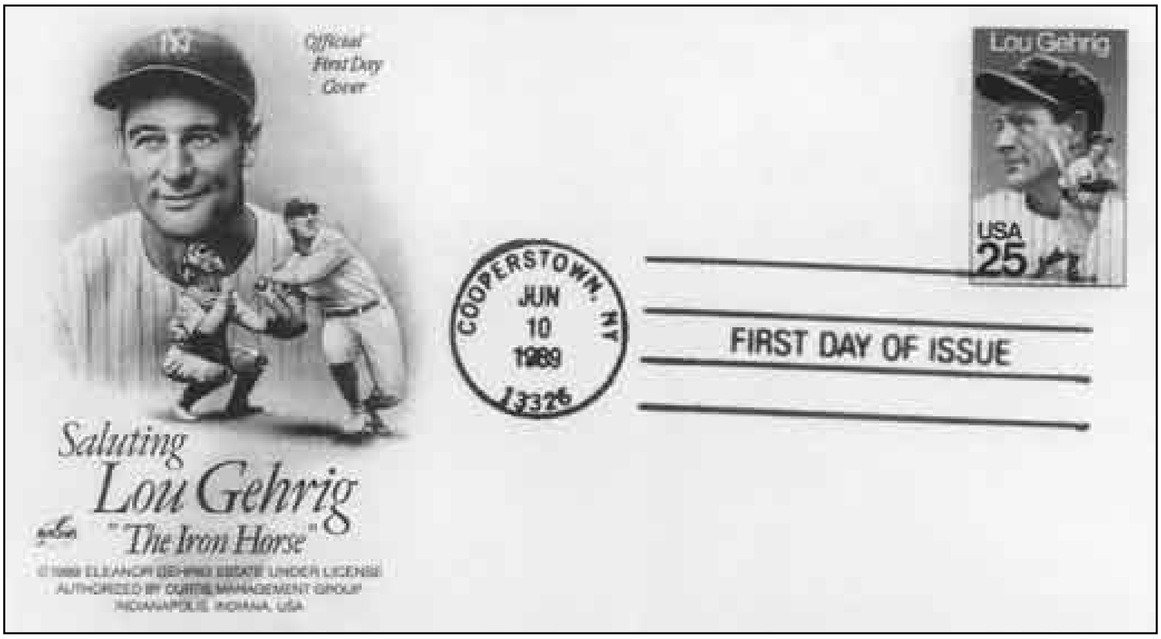

Fig. 1.2: Lou Gehrig, Philatelic Postal Stamps issued on June 10, 1989 by United States Govt. in the honor of Lou Gehrig.

ALS is defined as an adult onset progressive disease that (eventually) involves both lower and upper MNs .The affected age group is 50 to 60 years, though there are rare reports of juvenile onset as well. The prevalence of ALS is 1-2 in 100.000 persons per year. The incidence of ALS in most European countries is between 2 and 3 per 100.000 persons whereas approximately 300-450 people per year are diagnosed with ALS in Germany alone. ALS patients die on an average 3 years after disease onset, although 20% of the patients survive for more than 5 years. Initial symptoms involve fatigue, muscle cramps, and weakness in the muscles of one of the limbs, progressing to paralysis and spreading to other parts of the body. These symptoms are accompanied by fasciculation (muscular twitching) and atrophy (decrease in size) of the muscles involved, and by hypertonia and hyperreflexia due to involvement of upper MNs. In some cases symptoms start with difficulties in swallowing or slurred speech (bulbar ALS; Rowland, 1998).

There are two subsets of ALS. ‘Sporadic’ ALS (sALS) is the most common form of ALS, and the genetic variant, Familial ALS or fALS, represents a minor fraction (~10%) of all ALS cases. There are no apparent differences in the onset and disease progression between both types. Therefore it is plausible that both forms of ALS have common etiology (Brown & Robberecht, 2001). In both forms of ALS, respiratory failure is the common cause of death and survival possibilities are age or gender independent.

1.2.1 Sporadic ALS (sALS)

The pathogenesis of ALS is still poorly understood. In the majority of patients (90%) the disease is sporadic, i.e. without a clear inheritance pattern of an abnormality in the genetic constitution of the patient (Bruijn *et al*., 1998; Rowland & Shneider, 2001). Many pathological mechanisms have been suggested to play a role in the etiology of sporadic ALS, including glutamate excitotoxicity (Rothstein *et al*., 1992; Heath & Shaw, 2002; Guo *et al*., 2003), disruptions in Ca^{2+} metabolism (Llinas *et al*., 1993; Appel *et al*., 1994, 1995), mitochondrial malfunction and deformities (Bowling *et al*., 1993; Kong & Xu, 1998), disorganisation and a typical accumulation of neurofilaments in the cytoplasm in soma as well as in axonal branches (Figlewicz *et al*., 1994), accumulation of oxidative stress mediated damage, accumulation of misfolded and aggregated proteins (proteolytic stress), caspase activation, Fas transduction, excessive excitation of MNs (excitotoxicity), abnormalities in intracellular transport, abnormal activation of cell death pathways, lack of trophic support, virus intoxication, autoimmunity and heavy metal intoxication. MN damage in sporadic ALS is also accompanied by prominent reactive gliosis (damaged neurons are replaced by glial cells). It has been repeatedly proposed that several of these pathogenetic factors may operate together or sequentially and that therapeutic approaches should be designed to target all these different factors.

1.2.2 Familial ALS (fALS)

In a subset of ALS, in particular in familial forms, atypical features such as sensory deficits or dementia occur. Approximately 5-10% of ALS cases are familial and inherited as an autosomal dominant family trait, the remaining 90% cases being diagnosed as sporadic. In general, fALS is clinically and pathologically similar to sALS. The genetic causes underlying fALS are now beginning to be unraveled (Kunst, 2004). Approximately 20% of familial ALS cases are caused by a mutation in the gene encoding Cu,Zn Superoxide Dismutase 1 (SOD1) with a high inter-subject variation of progression. The only animal model available at present for the study of ALS pathogenesis is based on the SOD1 mutation. The point mutation G93A is one of those occurring in fALS. In this mutation, the amino acid glycine is replaced by alanine at position 93 in the SOD1 protein sequence (Rosen *et al*., 1993; Gurney *et al*., 1994; Carri *et al*., 1997; Andersen *et al*., 2003). However, the alanine 4 to valine mutation on exon1 of the SOD1 gene is described as the most commonly detected and one of the most clinically severe mutations reported in ALS cases (Rosen *et al*., 1994). At present more than 60 mutations are reported for SOD1, leading to specific motoneuron degeneration.

1.2.3 In-Vitro Cell Culture Model of Amyotrophic Lateral Sclerosis

To elucidate the underlying molecular events and cellular alterations involved in oxidative stress induced by aberrant copper chemistry of fALS SOD1, we used SH-SY5Y neuroblastoma cells transfected with the G93A mutant form of SOD1 typical for fALS (G93A-SOD1-SH-SY5Y or SH-SY5Y^{SOD1}) and SH-SY5Y cells transfected with wild-type (WT) human SOD1 (SH-SY5Y^{WT}) in a previously established *in-vitro* cell culture model of ALS-a situation resembling that of heterozygous patients (Carri *et al*., 1997, 2003). SH-SY5Y cells expressing SOD1^{G93A} show increased intracellular Reactive Oxygen Species (ROS; Ciriolo *et al*., 2000). This particular mutation was chosen, because it does not affect the activity of SOD1 (Fig. 1.2.3). The advantage of using neuroblastoma cell lines is that they proliferate and can be used for a long time. The disadvantage is that, although it is possible to differentiate the cells to specific neuron types, there is no guarantee that those cells will ever have the same characteristics as differentiated neurons since they originate from tumor cells. These *in-vitro* systems offer an ease of manipulation by the possibility of direct pharmacological administration or simple gene transfections that cannot be achieved in live animals. We studied the consequences and impact of protonophore FCCP and different drug cocktails on mitochondrial vulnerability and Ca^{2+} homeostasis in SOD1 transfected SH-SY5Y neuroblastoma cell line.

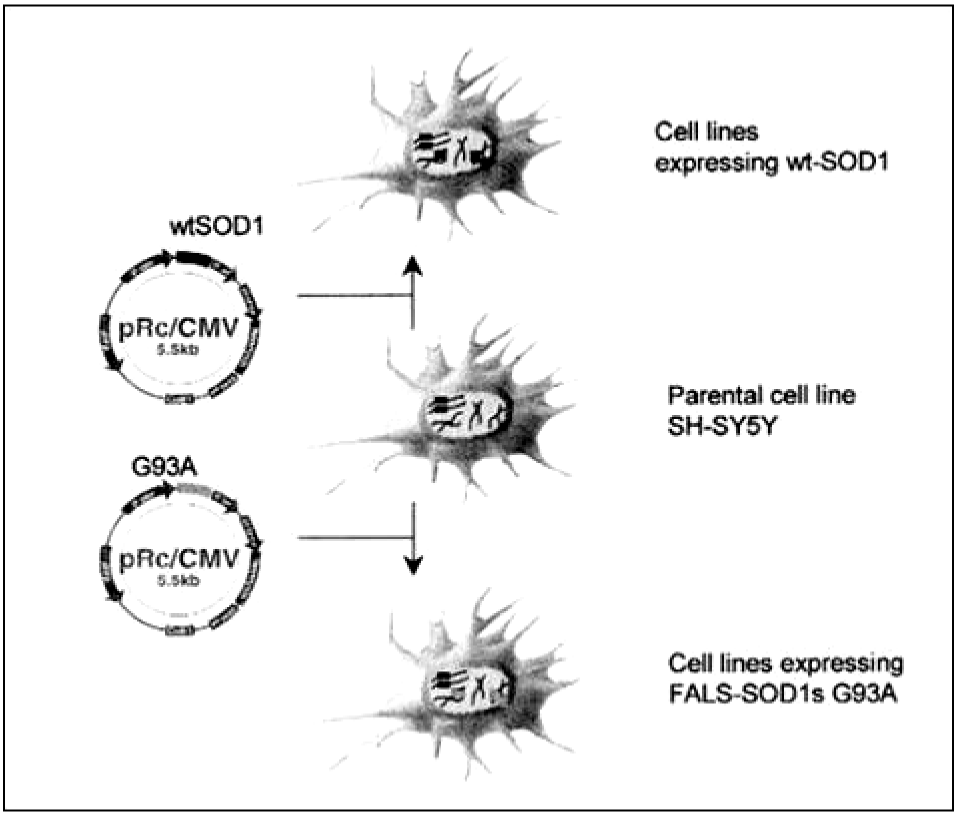

Fig. 1.2.3: In-Vitro cell culture model of ALS. Cartoon illustrating the transfection strategy of SH-SY5Y Cells, serving as an experimental model for SOD1-linked fALS (Modified after Carri *et al.*, 2001).

1.3 Metabolic Malfunction and Disease Mechanism in ALS

Many pathophysiological mechanisms have been suggested to play a role in the etiology of ALS. Corresponding to the clinical feature, ALS is characterized by a progredient loss of cortical, spinal and brain stem MNs. MN damage as a result of oxidative stress and excitotoxicity is a key hypothesis in ALS etiology. The present evidence supports the mitochondrial dysfunction hypothesis acting with oxidative stress to cause neurodegeneration via an apoptotic mechanism. Oxidative stress is also linked with other proposed disease mechanisms such as excitotoxicity leading to increased intracellular calcium, which in turn leads to increased nitric oxide formation. Peroxynitrite, generated by the reaction of superoxide anions and nitric oxide, can subsequently lead to oxidative damage (Rao & Weiss, 2004). Glutamate excitotoxicity is another mechanism implicated in ALS pathogenesis through disruption of intracellular calcium homeostasis and free radical production (Heath and Shaw, 2002). The oxidative stress evident in ALS might also promote increased excitotoxicity, as glutamate transporters are particularly susceptible to disruption by oxidants, and oxidative modifications to the transporters have been reported in ALS and the mSOD1 mouse model (Rao and Weiss, 2004).The etiology is likely to be multifactoral. ALS involves an interplay of several mechanisms from initiation of to spread of MN cell death by mitochondrial dysfunction or/and by enhanced MN excitability by intracellular calcium overload (Simpson *et al*., 2003; von Lewinski & Keller, 2005; Goodall & Morrison, 2006). Below we will discuss the hypotheses that have been most influential in the present and past decade.

1.3.1 Oxidative Stress

Oxidative stress is a state where the concentration of oxidants in the cell is higher than normal. Most oxidants are free radicals which are molecules containing at least one unpaired electron. Free radicals have an inherent 'need' to gain or lose an electron there by damaging almost everything in the cell, including proteins, membranes, and DNA. Because of cellular metabolism most biological free radicals contain oxygen. Other oxygen-containing molecules like hydrogen peroxide (H_2O_2) and peroxynitrite ($ONOO^-$) can easily form oxygen free radicals and are therefore, together with oxygen free radicals, called ROS. ROS are formed as a by-product of normal mitochondrial metabolism and are sometimes even produced specifically for physiological functions.

Oxidative stress is implicated in the pathogenesis of both normal aging and neurodegenerative diseases. Motoneuron damage as a consequence of oxidative stress is supposed to be the key premise in ALS. A number of studies have established the presence of elevated oxidative metabolism in ALS, such as the detection of increased biochemical markers of oxidative injury in post mortem samples from patients. Free radical scavenging proteins like SOD1, mitochondrial manganese SOD (SOD2), catalase, and cytochrome c can neutralize free radicals but this cannot prevent cellular damage by ROS (Beal, 2002; Simpson *et al*., 2003). Increased $^{\cdot}OH$ generation may occur as a consequence of either enhanced peroxidase activity or decreased Cu-binding affinity of mSOD1. mSOD1 transgenic (Tg) mice show elevated levels of protein and lipid oxidation at both pre and post-symptomatic stages (Strong, 2003). Oxidative stress is also associated with other proposed disease mechanisms such as excitotoxicity and axonal transport defects.

1.3.2 Mitochondrial Dysfunction

Morphological and ultrastructural abnormalities of mitochondria observed in both sporadic and familial forms of ALS suggest crucial involvement of mitochondria in ALS (Beal, 2000). There are now several observations which suggest that mitochondria play a crucial role in disturbing energy metabolism by predisposing calcium-mediated excitotxicity leading to ROS generation and initiation of apoptotic pathway, thereby jeopardizing cell function and normal cellular metabolism (Bowling *et al*., 1993; Browne *et al*., 1998; Borthwick *et al*., 1999). Abnormalities in mitochondrial function have been found in fALS and some sALS patients. Initial clues were provided by histological observations of mitochondrial abnormalities such as swelling and vacuolization, as some of the earliest sign of pathology in ALS mouse model and in human ALS (Wong *et al*., 1995; Sasaki & Iwata, 1996; Kong & Xu, 1998; Jaarsma *et al*., 2001; Menzies *et al*., 2002; Fig. 1.3.2). Morphological abnormalities were not only confined to CNS but were also found in skeletal muscles, intramuscular nerves and proximal horns (Hirano *et al*., 1984; Hirano, 1991; Siklos *et al*., 1996).

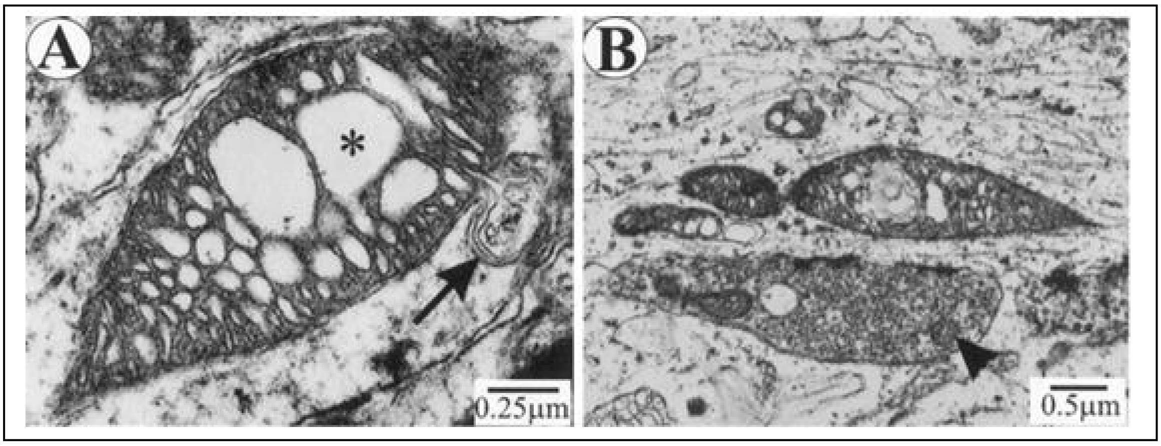

Fig. 1.3.2: Mitochondria in motor neurons of mutant SOD1 transgenic mice. (A) Shows abnormalities like dilated cristae (asterisk) and leaking outer membrane. (B) A swollen dendritic mitochondria with dilated and disorganized cristae (adapted from Kong & Xu, 1998).

Several studies have recently focused on mitochondrial dysfunction, in particular altered activity of the mitochondrial respiratory chain necessary for ATP synthesis and increased production of ROS. Lack of supply of requisite energy can result in the loss of integrity of neuronal cell membranes, leaving them permeable to ions and water that can cause damage. Deficits in the activities of complex I (Wiedemann *et al*., 1998) and complex IV (Vielhaber *et al*., 2000), as a result of mutations in mitochondrial DNA, have been identified in the skeletal muscles and spinal cord of sALS patients (mtDNA; Wiedemann *et al*., 2002). The question of whether alterations in the mitochondrial genome can lead to alterations in cell function has been addressed by transferring mtDNA from ALS subjects to mtDNA-depleted human neuroblastoma cells. This resulted in abnormal electron transport chain functioning, increase in activity of free radical scavenging enzymes, disturbed Ca^{2+} homeostasis and altered mitochondrial ultrastructure, suggesting a pathological role for mtDNA mutations in some forms of ALS (Swerdlow *et al.*, 1998). Other evidences suggest that ROS generated in motoneurons can cross the plasma membrane and cause oxidative disruption of glutamate transporters in neighboring astrocytes by excitotoxic stimulation of AMPA/kainate receptors followed by local excitotoxicity and initiation of a vicious cycle of motoneuron damage (Carriedo *et al.*, 2000; Rao *et al.*, 2003*)*. A striking recent research work provided evidence that mSOD1 might disrupt association of complex IV (cytochrome c) with the inner mitochondrial membrane, and by this interfere with mitochondrial respiration. Cultured MNs expressing mSOD1 and MNs in brain slices where complex IV was inhibited by cyanide also show mitochondrial involvement (Kruman *et al.*, 1999; Bergmann & Keller, 2004; Kirkinezos *et al*., 2005).

Although these results are intriguing, they do not resolve the question of whether mitochondrial abnormalities are causally involved in the disease process or merely a byproduct of neuronal degeneration. However, pathological features like the presence of membrane bound vacuoles in MNs in Tg mice expressing SOD1 mutants G93A or G37R suggest that mitochondrial alterations represent an early event triggering the onset of the disease, rather than simply a byproduct of cell degeneration (Dal Canto & Gurney, 1995; Bendotti *et al*., 2001). Further detailed studies using markers for different mitochondrial compartments demonstrated unequivocally that mitochondrial vacuolization develops from a progressive detachment of the outer membrane from the inner membrane and expansion of the intermembrane space. Once the outer membrane expands to form the mature vacuoles, the inner membrane collapses or disintegrates to become inner membrane remnants inside the vacuoles (Higgins *et al*., 2003; Xu *et al*., 2004). A recent research report demonstrates the localization of a significant fraction of SOD1 in intermitochondrial space thereby causing toxicity. Inhibition of mitochondrial respiratory metabolism is reported in Tg ALS mice models (Liu *et al*., 2004). Independent of the cause of mitochondrial damage, various other studies indicate that chronic mitochondrial inhibition (Chemical Hypoxia) induced by inhibitors like sodium cyanide and azide led to selective motoneuron death, which could be counteracted by free-radical scavengers and AMPA receptor blockers (Kaal *et al.*, 2000). In tune with these observations, ALS-like symptoms can be induced in mice by a targeted deletion that eliminates the ability of vascular endothelial-cell growth factor (VEGF) to respond to tissue hypoxia. Cross-breeding these mice with the mSOD1 severely enhanced MN degeneration, while treatment of SOD1-Tg mice with VEGF delayed progression of symptoms and prolonged survival (Oosthuyse *et al.*, 2001; Lambrechts *et al.*, 2003; Zheng *et al.*, 2004; Azzouz *et al.*, 2004; Wang *et al*., 2007)

1.3.3 Disrupted Calcium Homeostasis Abnormalities in ALS

Several groups have reported that independent of the cellular and molecular events initiating motoneuron degeneration in ALS, disruption of intracellular Ca^{2+} homeostasis plays a key role in disease etiology. Involvement of Ca^{2+} as a risk factor was suggested by the observation that Ca^{2+}-binding proteins such as calbindin (CB)-D_{28k} and parvalbumin (PV) were absent in MN populations lost early in ALS (cortical, spinal and lower cranial nerve motoneurons), whereas MNs damaged late or infrequently in the disease (oculomotor, trochlear and abducens nerves) expressed markedly higher levels of CB-D_{28k} and/or PV (Alexianu *et al.*, 1994). These findings are in good agreement with a quantitative comparison of Ca^{2+} homeostasis in functionally intact, vulnerable versus resistant MNs in brain-slice preparations. This observation identified a low cytosolic Ca^{2+} buffering capacity as an important risk factor for MN degeneration. Data from different groups shows that vulnerable populations of MNs display low endogenous calcium buffering capacity (Elliot & Snider, 1995). The ability of MNs to buffer increases in intracellular Ca^{2+} is restricted due to the low expression level of Ca^{2+}-buffering proteins. This low Ca^{2+}-buffering capacity could be essential under physiological conditions as it allows rapid relaxation times of Ca^{2+} transients in MNs during high frequency rhythmic activity. However, these characteristics make MNs more susceptible to an excessive influx of Ca^{2+} ions by evoking large amplitudes of intracellular free Ca^{2+} concentrations and thus increasing the risk for activation of excitotoxic second messenger cascades and related cellular disturbances (Von Lewinski & Keller, 2005; Fig. 1.3.3). Another argument in favor of this hypothesis is that high concentration of mobile buffers accelerates the dispersion of local Ca^{2+} gradients by a process commonly known as buffering diffusion. According to this concept, under pathophysiological conditions, differential buffering reflects a basic diversity in the spatio-temporal organization of Ca^{2+}signaling rather than a singular difference in one cellular parameter (Zhou & Neher, 1993; Klingauf & Neher, 1997; Lips & Keller, 1999). Likewise, an increase in cytosolic Ca^{2+} buffering capacity could protect vulnerable MNs from degeneration both *in vitro* and *in vivo* (Beers *et al.*, 2001; Van Den Bosch *et al.*, 2002).

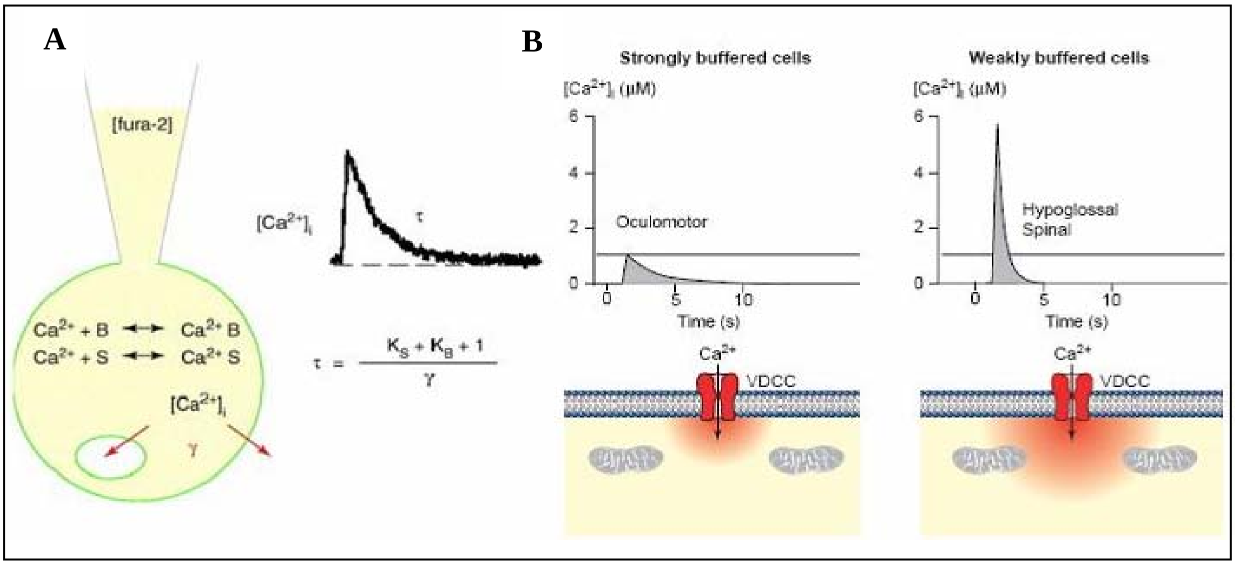

Fig. 1.3.3: Ca^{2+} homeostasis and its correlation with the weakly and strongly buffered motoneurons. (A) The Ca^{2+} buffering capacity (K_S) of a cell, reflecting relative fraction of bound versus free Ca^{2+} in the cell, can be calculated by using the 'added buffer' approach by linear one-compartment model. The recovery time of cytosolic $[Ca^{2+}]_i$ elevations (τ) depends on the amount of endogenous buffer (S; denotes Ca^{2+}-binding proteins), the amount of exogenous buffer (B; i.e. Fura-2) and the transport rate (γ) of Ca^{2+} across cellular membranes. Gradual introduction of exogenous buffer via the patch pipette enables the cytosolic K_S to be determined. K_B indicates the buffer capacity of the exogenous buffer (i.e. Fura-2). (B) Specialized Ca^{2+} homeostasis in weakly and strongly buffered MNs. Low cytosolic Ca^{2+}-buffering capacity has several implications for spatial and temporal Ca^{2+} signaling. The amplitude of Ca^{2+} transients is several times larger in weakly buffered cells (e.g. hypoglossal and spinal MNs) than in strongly buffered cells (e.g. oculomotor neurons), and the recovery time is significantly accelerated (τ). Low cytosolic Ca^{2+} buffering capacity promotes Ca^{2+} accumulation and formation of subcellular domains around influx sites (red), and by this facilitates the interaction with intracellular organelles such as mitochondria (taken from Vanselow & Keller, 2000; Von Lewinski & Keller, 2005).

The observation of high buffering capacity in selectively resistant MNs is consistent with earlier immunocytochemical studies of endogenous calcium buffering proteins and vice-versa. Moreover, *in-vitro* cell culture models have shown that elevated cytosolic buffer concentration reduce ALS related MN damage providing further support in favor of the idea that increased buffer concentrations demonstrate beneficial protection (Roy *et al.*, 1998). Several lines of evidence implicate disturbance of glutamate neurotransmission and subsequent glutamate-triggered Ca^{2+} entry as important steps. Increased extracellular glutamate levels presumably result from reduced glial glutamate uptake, which can be caused by oxidative damage to the Excitatory amino acid transporter 2 (EAAT2) or by aberrant RNA processing. The low Ca^{2+} buffering properties, together with a high AMPA/kainate current density, could explain the particular vulnerability of MNs to increased stimulation by glutamate and concomitant Ca^{2+} influx (Maragakis & Rothstein, 2001). Another factor could be an ALS-related immune reaction targeted at voltage-dependent calcium channels, where disruption of endogenous homeostasis results from impaired voltage dependent calcium influx (Appel *et al*., 1995). Furthermore, synaptic glutamate transport is also thought to be involved in other forms of ALS-related neurodegeneration. In the cell-culture study, partial protection was also obtained by treatment with nifedipine, implicating Ca^{2+} entry through voltage-gated Ca^{2+} channels, in addition to glutamate receptors, in mediating the toxicity of mSOD1 in MNs. Recently, the crucial role of Ca^{2+}-permeable AMPA receptors was further underlined by cross-breeding of Tg SOD1 mice with mice that showed markedly reduced Ca^{2+} permeability of AMPA/kainate receptors, due to GluR2 overexpression (Tateno *et al.*, 2004). Finally impaired mitochondrial calcium loading capacity in mSOD1 mice may produce two consequences. First, it links mitochondrial dysfunction to glutamate excitotoxicity and secondly elevation of cytosolic calcium levels in neurons compromise mitochondrial integrity and function by inducing enhanced production of free radicals from mitochondria (Stout *et al*., 1998).

1.3.4 Glutamate Transmission and Excitotoxicity

Glutamate is known as the dominant primary excitatory neurotransmitter in the CNS acting at both ionotropic and metabotropic receptors. It is synthesized and stored in synaptic nerve components and released in response to depolarization of the neuron. Extracellular glutamate levels are tightly regulated by different classes of transporters on neurons. Glutamate excites the receptors on the post synaptic neuron after release into the synaptic cleft thereby conducting the excitatory signal. Excess synaptic cleft glutamate is actively removed by specialized transporters on the perisynaptic glial cells to terminate the excitatory signal. Excessive glutamate exposure is toxic to neurons as a result of glutamate-triggered Ca^{2+} influx (Choi *et al*., 1988; Goodall & Morrison, 2006; Fig. 1.3.4).

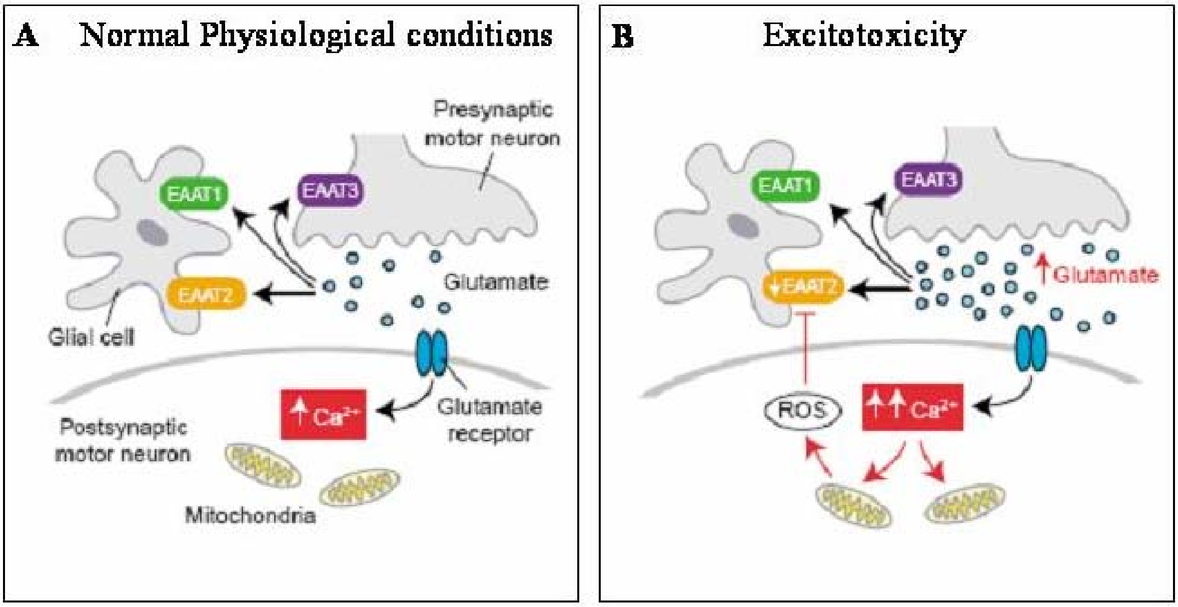

Fig. 1.3.4: Glutamatergic transmission in central nervous system under A, normal physiological and B, excitotoxicity conditions. (A) Glutamate is released from the presynaptic nerve terminal and diffuses into the synaptic cleft. It acts on several glutamate receptors on the postsynaptic neuron. The action of glutamate in the cleft is terminated by its rapid reuptake via glutamate transporter proteins. EAAT1 and EAAT2 are expressed on glial cells; EAAT3 is expressed mainly on presynaptic motor neurons. EAAT2 is responsible for most glutamate reuptake in the human brain. Under normal physiological conditions postsynaptic activation of glutamate receptors results in a small rise in intracellular calcium that can be buffered in the cell. (B) When excess glutamate is present, there is a greater elevation in intracellular calcium postsynaptically. This triggers mitochondrial production of reactive oxygen species (ROS), which then inhibit glial EAAT2 function. This leads to further increases in glutamate concentrations in the synapse and further rises in postsynaptic calcium levels (taken from Goodall & Morrison, 2006).

Sodium-dependent glutamate transporters tightly control glutamate levels in the synapse, particularly EAAT2 expressed in glial cells. Several studies indicated increase glutamate levels in the cerebrospinal fluid (CSF) at least in a subset of ALS patients. Elevation of this glutamate level may be attributed to deficient glutamate transporter capacity (loss of EAAT2 function), as decreased levels of the transporter have been found in some post mortem ALS brains (Shaw *et al*., 1995; Rothstein *et al*., 1995; Heath & Shaw, 2002). Although it is not clear how EAAT2 disruption occurs in ALS. Furthermore, inhibitors of glutamate uptake cause selective motoneuron damage in organotypic slices (Rothstein *et al*., 1995) and in dissociated spinal cord culture models (Carriedo *et al*., 1996), suggesting that loss of glutamate transport could contribute to the motoneuron damage seen in the disease. The most important argument for a role of excitotoxicity in ALS is riluzole, the only drug which proved effective against disease progression in patients and has anti-excitotoxic properties. It was shown that this drug inhibits the release of glutamate due to the inactivation of voltage-dependent Na^+ channels on glutamatergic nerve terminals as well as to activation of a G-protein-dependent signal transduction process. Riluzole can also block some of the postsynaptic effects of glutamate by non-competitive inhibition of NMDA and AMPA receptors (Doble, 1996).

In-vivo evidence for a possible role of AMPA receptor subunits GluR1-4 in ALS comes from the several studies. Studies show that transgenic mice lacking GluR2 (GluR2 subunit is a component in the AMPA receptor complex, which renders them particularly impermeable to calcium) does not suffer from MN disease. This suggests that a low GluR2 level is a modifier of motoneuron degeneration rather than being sufficient to cause ALS (Jia *et al*., 1996). Furthermore, glutamate excitotoxicity in sALS is caused by a selective loss of astrocytic glutamate transporter-1(GLT-1) and is reproduced in mice by knockout of GLT-1, a homologue of EAAT-2 (Rothstein *et al*., 1996). Oral administration of glutamate inhibitors prolonged life of $SOD1^{G93A}$ mice (Gurney *et al*., 1996). Further studies have provided the significance of GluR2 in neuronal survival where phenotypes of transgenic mice in which the extent of RNA edition at the Q/R site leads to generation of a lethal phenotype involving seizure and acute neurodegeneration (Higuchi *et al*., 2000). Recent studies have provided clues that Glu2-N overexpression induces a progressive decline in the functions of spinal cord as well as long-onset degeneration of spinal motoneurons (Kuner *et al*., 2005).

1.3.5 Abnormal Misfolded Protein Stress

Abnormal protein aggregates are an inevitable byproduct of protein synthesis and degradation. Several disorders including most neurodegenerative disorders (Alzheimer's disease, Parkinson's disease, Huntington's disease, several cerebellar ataxias and ALS) are characterized by the presence of insoluble aggregates of proteins that are deposited in intracellular inclusions or extracellular plaques, which are characteristic for the diseases. Unfolded proteins including bunina bodies, ubiquitinated inclusions and neurofilament rich hyaline in ALS (Strong *et al*., 2005), amyloid and tau in Alzheimer’s disease, α-synuclein in Parkinson’s disease and huntingtin in Huntington’s disease are pathological hallmarks. Potentially dangerous misfolded proteins also arise through oxidation, isomerization or glycation and by transcriptional or translational errors. Such proteins engage in non-native interactions and aggregate to form oligomeric complexes that are insoluble and metabolically stable, ultimately harmful to the cell (Wetzel, 1994; Soto, 2003). Cells have quality control machinery that consists of 1) molecular chaperones that assist in protein folding or refolding and 2) the ubiquitin proteasome proteolytic pathway that recognizes and degrades misfolded proteins, to prevent damage from unfolded and aggregated protein, and 3) aggresome-autophagosome pathway that degrades aggregated proteins. The rate of misfolded protein production can increase markedly upon exposure of cells to oxidative or thermal stress, or as a result of mutations, and in these conditions the amount of misfolded protein production may exceed the capacity of the protein quality control machinery, disturbing cell function and inducing cell death (Sherman & Goldberg, 2001).

A variety of data point out that misfolded protein stress, consisting of irregular loosely arranged bundles or spherical inclusions may contribute to the pathogenesis of ALS. Ultrastructurally, these ubiquitinated structures consist of various types of filamentous or amorphous materials consistent with protein aggregation. In SOD1-linked ALS patients inclusions contain mSOD1, but in sALS patients SOD1 usually is not present in ubiquitinated structures (Valentine & Hart, 2003). Ubiquitinated and non-ubiquitinated aggregate of SOD1 is a constant feature prior to the death and disappearance of MNs in Tg mSOD1 mice. However, the presence of ubiquitinated structures in mSOD1 mice and studies in chimeric mice have shown that MNs that do not express mSOD1 may become strongly immunoreactive for ubiquitin (Hoffman *et al.*, 1996). There is ongoing debate whether this aggregate accumulation contributes to the death of MNs or they represent the cell’s protective machinery in ALS pathology. Inhibition of intracellular organelles like mitochondria by SOD1 containing inclusions through accumulation within or on the organelles is also suggested (Bruijn *et al.*, 2004).

1.3.6 Cytoskeletal Disorganisation and Neurofilament Defects

Neurofilaments are intermediate cytoskeletal fibrils composed of the neuron specific heavy (NFH), middle (NFM) and light (NFL) triplet proteins. Neurofilament subunits are synthesized and structured in the cell body and are transported along the axon by slow component of the axonal transport. Phosphorylated neurofilaments often accumulate in the chromatolytic neurons and swollen axons, followed by impaired axonal transport in patients suffering from sporadic or SOD1 mutant fALS, as well as in SOD1-knockout mice. Abnormalities in neurofilaments could be either casual or a by-product of neuronal degeneration (Ince *et al.*, 1998; Julien & Beaulieu, 2000). The direct involvement of neurofilaments in pathogenesis was suggested by the finding that overexpression of the WT NFL subunit in mice causes progressive motor neuropathy without MN loss similar to those seen in patients with ALS (Xu *et al*., 1993). On the other hand knock out of the endogenous WT NFL subunit in G85R mice delays the onset of MN disease (Williamson *et al*., 1998). Peripherin and internexin are two other intermediate-filament proteins that co-localise with neurofilaments and form part of the axonal inclusion bodies in patients with sALS and mice with SOD1 mutations. Overexpression of peripherin or internexin in Tg mice induced selective degeneration of motor axons (Ching *et al*., 1999). Peripherin is encoded by a single gene and has splice variants of 56, 58 and 61 kDa. Peripherin (61 kDa) is toxic to primary motor neuron cultures, even at very low levels, and has been detected in the spinal cord of sALS patients (Robertson *et al*., 2003).

In the past decade, studies on mSOD1^{G93A} mice spinal MNs shown that there is increased population of neurofilaments and mitochondria in the axon hillock and initial segment of these MN. This abnormality continues with aging in Tg mice compared to WT mice (Sasaki & Iwata, 2005). The reason for this remains unclear but two theories have been proposed. First, the accumulated neurofilament protein might provide a buffer for other deleterious processes such as increases in intracellular calcium from excitotoxicity or aberrant protein modification caused by oxidative stress. Second, trapping neurofilament protein in the cell body might reduce the burden on axonal transport (Williamson *et al*., 1998).

1.3.7 Abnormalities in Intracellular Axonal Transport

The transport of molecules and organelles is a fundamental cellular process that is important for the development, function and survival of neurons. The molecular motors for anterograde and retrograde transport are kinesin and dynein-dynactin complex respectively. Several findings indicate that defects in axonal transport might contribute to the demise of MNs in ALS. One of the characteristics of ALS is the reduced activity of axonal transport, described initially in patients with ALS (Sasaki & Iwata, 1996) and more recently in Tg mouse model of ALS (Sasaki *et al*., 2005). The mSOD1 mouse shows axonal transport defects as one of the earliest pathological features, and recent reports suggest this may even occur in embryonic developing neurons (Kieran *et al*., 2005).

It is important to note that abnormalities in anterograde transport do not lead to MN death but cause diseases of the axon and usually affect both sensory and motor neurons. In contrast, several lines of evidence have linked impaired dynein-dynactin dependent (i.e. retrograde) trafficking to ALS. The dynein–dynactin complex is involved in fast retrograde transport. Mutations in the p150 subunit of dynactin have been reported in a family with an unusual LMN disorder that begins with vocal cord paralysis (Puls *et al*., 2003). Mutations in dynein impaired retrograde axonal transport leads to MN disease in two lines of induced mouse mutants (Hafezparast *et al*., 2003). Furthermore, mice overexpressing the p50 subunit of dynactin have reduced axonal transport and develop progressive MN degeneration (LaMonte *et al*., 2002). Interestingly, crossing mouse overexpressing p50 with the mSOD1 mouse results in amelioration of the disease and increased survival (Kieran *et al*., 2005). Finally, aberrant neurofilament aggregation, a common pathological hallmark in ALS MNs, has been linked to abnormal dynein trafficking (Bruijn *et al*., 2004). The question still perplexing scientists is why impairment of dynein trafficking selectively afflicts MNs. A possible explanation is that MNs, more than other cells, depend on retrograde trophic signaling (Holzbaur, 2004; Caviston & Holzbaur, 2006).

1.3.8 Toxicity Linked to Mutation of Cu-Zn Superoxide Dismutase 1 (SOD1)

SOD1 is the cytosolic homodimeric protein consisting of 153 amino acids and a molecular weight of 17 kDa. It is the Cu-Zn binding isofrom of SOD (EC 1.15.1.1) that catalyzes the detoxification of superoxide radical (O_2^-) to convert it to hydrogen peroxide H_2O_2.

$$2O_2^- + 2H^+ \xrightarrow{\text{Cu-Zn SOD1}} O_2 + H_2O_2$$

Enzymatic reaction catalyzed by SOD1 converts the toxic superoxide radical into hydrogen peroxide (detoxified by the enzyme catalase) and molecular oxygen. A reaction mechanism is given below.

$$\text{SOD1-Cu}^{2+} + O_2^{\cdot -} \longrightarrow \text{SOD1-Cu}^{+} + + O_2$$

$$\mathit{SOD1\text{-}Cu}^{+} + \mathrm{O}_2^{\cdot -} \longrightarrow \mathit{SOD1\text{-}Cu}^{2+} + H_2O_2$$

Mutations in the gene for SOD1 reverse this reaction leading to production of toxic hydroxyl radicals. A reaction mechanism is given below.

$$\mathit{SOD1\text{-}Cu}^{2+} + H_2O_2 \longrightarrow \mathit{SOD1\text{-}Cu}^{+} + \mathrm{O}_2^{\cdot -} + 2H^{+}$$
$$\mathit{SOD1\text{-}Cu}^{+} + H_2O_2 \longrightarrow \mathit{SOD1\text{-}Cu}^{2+} + \mathrm{OH}^{\cdot} + OH^{-}$$

SOD1 is predominantly a cytosolic protein but some exceptional localization of SOD1 to the intermembrane space of mitochondria was also reported. There are two other SOD molecules: SOD2 is a manganese SOD located in mitochondria and SOD3 is an extracellular SOD which also binds Cu and Zn. There are at least 3 different inheritance patterns for fALS. The most common inheritance pattern for fALS is called autosomal dominant. It is also important to note that inheriting the gene for fALS in no way guarantees that a person will develop symptoms of ALS. If a child does not inherit the gene mutation for ALS, they cannot pass it onto their children. Several studies confirmed localization of endogenous SOD1 protein as well as exogenously expressed normal and mutant SOD1 protein within mitochondria in the CNS (Higgins *et al*., 2002).

Till now more than 125 mutations in SOD1 have been discovered, most of them are heterozygous missense point mutations (Andersen *et al*., 2003) spanning all five axons of SOD1. These mutations are specific for fALS, and are infrequently found in sALS (~1% of cases). The fALS mutations include variants linked to chromosomes 21q22.1-22.2 (autosomal dominant), 2q33.35 (autosomal recessive), 9q34 (autosomal dominant), and 15q12-21(autosomal recessive) and sex chromosome (X-linked dominant). Among these variants, 21-linked variant has been investigated most intensively because this variant is associated with SOD1. The gene encoding SOD1 was first linked to chromosome 21q22.1 (Siddique *et al*., 1991) in 1991. It contributes to 1% of the total brain protein. Approximately 35% of fALS disease occurrence is due to either Guanine (G) to Adenine (A) or Adenine to Guanine mutation on the sense strand. The most extensively studied animal models are mice with G93A, G85R (Glycine to Arginine at position 85), 37R and transgenic rats carrying G93A or H46R (Histidine to Arginine at position 46) SOD1 mutations.

One hypothesis proposes that disease in mice is not due to loss of function of SOD1 enzyme but rather due to a gain of new toxic functions. Early focus on a ‘loss of activity’ of the SOD1 enzyme was disproved by studies where overexpression of $\text{mSOD1}^{\text{G93A}}$ in mice caused MN disease despite the presence of elevated SOD1 activity (Gurney *et al*., 1994). Moreover, the total elimination of SOD1 did not cause MN disease in mice where SOD1 was either inactivated or knocked out (Reaume *et al*., 1996). Initial studies have focused on copper mediated catalysis as potential source of toxicity. Reactive oxygen radicals also target the mitochondrial DNA and cause damage in the spinal cord of Tg ALS mice (Warita *et al*., 2001). Another hypothesis was that the misfolding of SOD1 induced by mutations would allow the access of abnormal substrates such as peroxynitrite (ONOO-) instead of superoxide to the catalytic side leading to the nitration of tyrosine residues into highly toxic reactive nitronium (NO^{2+}) which can readily react with tyrosine residues of proteins and damage them (Beckman *et al*., 1990).

$$\textit{SOD1-Cu}^{2+} + \text{ONOO}^{-} \longrightarrow \textit{SOD1-Cu}\text{O}\ldots\text{NO}^{2+}$$

$$\textit{SOD1-Cu}\text{O}\ldots\text{NO}^{2+} + \textit{Tyr} \longrightarrow \textit{SOD1-Cu}^{2+} + \textit{OH}^{-} + \text{NO}_2\text{-Tyr}$$

Moreover, mutation of the copper chaperone of SOD1 (CCS) that delivers copper to SOD1 catalytic site had no effect on disease progression in mice expressing mSOD1 Tg mice. Further hypothesis propose that mSOD1 fails to bind zinc properly, allowing the rapid reduction of the SOD1-bound copper which, in its reduced state, catalyses the formation of superoxide anion rather than dismutation (backward catalysis) leading to enhanced release of copper and zinc, triggering copper-zinc mediated toxicity (Estevez *et al*., 1999). However, the involvement of copper bound to the active site of SOD1 in pathogenesis is disproved. Exogenously expressed SOD1 also leads to the abnormal accumulation of mSOD1 in *Caenhorabditis elegans* (Oeda *et al*., 2001).

1.4 Neuron-Glia Communication

Neuron-glia circuits trigger integrative processes in the nervous system. Two-way communication amid neurons and glia is indispensable for axonal conduction, synaptic transmission, and information processing and consequently required for normal functioning of the nervous system during development and all the way through adult life. The signals between neurons and glia include ion fluxes, and specialized signaling molecules released from synaptic and nonsynaptic regions of neurons. In contradiction to the serial flow of information along chains of neurons, glia communicates with other glial cells through intracellular waves of calcium and via intracellular diffusion of chemical messengers (Fields & Stevens-Graham, 2002). Glial calcium signals are triggered by activation of many receptors, expressed in glial membranes, which regulate both Ca^{2+} entry and Ca^{2+} release from the mitochondria and ER.

1.4.1 Neuron-Glia Imaging

The relationship between structure and function is mostly unidentified at the cellular level for most CNS tissues. Powerful techniques such as positron emission tomography (PET) are utilized to monitor brain structure *in vivo*. However, study of fast activity in central nervous system (CNS) micro circuits is not possible using PET due to a low temporal and spatial resolution. Rather, confocal or two-photon microscopy is used *in-vivo* and *in-vitro* for simultaneous imaging of brain cell activity and morphology.

A rapidly increasing number of cellular processes are being monitored with neuron-glia imaging *in-vitro* and *in-vivo* using genetically encoded fluorescent dyes expressed in target cells, e.g. Cameleons, a protein based dye (Ruangkittisakul & Ballanyi, 2007). A number of dyes are quite selective for organelles e.g. Rhodamine 123 (Rhod 123) is used to monitor both mitochondrial structure and membrane potential. Dual dye labeling allows ratiometric measurements for a better signal-to-noise ratio and calibration of concentrations of cellular factors. Neurons and glia in culture can without difficulty be labeled with morphological dyes of the `Alexa fluor` or “BODIPY” families or with Ca^{2+}-sensitive dyes for Ca^{2+} imaging. In contrast to cultures, cells in acute brain slices remain in their natural environment *in situ* and thus often show features close to *in-vivo* situation. However, in mature brain structures in situ loading of neurons by addition of acetoxymethyl (AM) forms of Ca^{2+}-sensitive dye to the superfusate may not be successful due to diffusion or uptake problems. In such cases, pressure injection of the AM dye can provide adequate loading of glia and neurons in both brain slices and *in-vivo* (Yuste *et al.*, 2000).

Ca^{2+}-sensitive dyes are the most potent tools for neuron-glia imaging. For assessment of morphological features e.g. spine formation, it is important that the dye fluoresces brightly even at low concentrations (nM). For that purpose, Fura-2 can be used with most video camera and two-photon imaging systems. Confocal laser scanning microscopy is often not possible with fura-2 as most commercial systems cannot use ultraviolet light, while Calcium-Green or Fluo-4 can be used with most imaging systems. If neuronal networks in AM Ca^{2+} dye loaded systems are studied, such as respiratory brain stem slices, it is important to choose the right intracellular dye concentration because not only the excitability of individual cells, but rather major parts of the network, may be affected by high intracellular Ca^{2+} dye concentrations.

1.4.2 Glial Ca^{2+} Signaling

Glial cells, which account for 60% of all cells in the CNS of rodents and approximately 90% of all neural cells in humans, perform a wide variety of vital functions. A two-way communication between axons and glia is important for maintenance of both glia and axons. On a molecular level, integration within neuronal-glial networks very much relies on a specific signaling system that uses ions as the universal cellular messenger. Although glial cells are non-excitable from the classical physiological point of view, they are able to respond to external stimulation by generation of intracellular Ca^{2+} signals. Indeed Ca^{2+} signaling systems control integration within glial sanctum by providing the glia with the means of long-range signaling by propagating calcium waves resulting from activation of Ca^{2+} fluxes either through plasmalemma or through intracellular membrane. Importantly, free Ca^{2+} ions within the lumen of ER and mitochondria act as the main regulators of both Ca^{2+} release channels and SERCA Ca^{2+} pumps. Ca^{2+} waves serve as a substrate for long-range signaling in glial sanctum; as glial Ca^{2+} waves are able to cross cell-to-cell boundaries and travel a long distance through astroglial networks (Cornell Bell *et al*., 1990; Verkhratsky *et al*., 1998). Mechanisms responsible for the generation of propagating Ca^{2+} waves are intricate and involve diffusion of InsP3 through gap junctions that connect astroglial cells, and, release and extracellular diffusion of transmitters such as glutamate (Bennett *et al*., 2005; Fig. 1.4.2). Calcium signals traveling within astrocytes also create a functional connection between neuronal activity and local circulation.

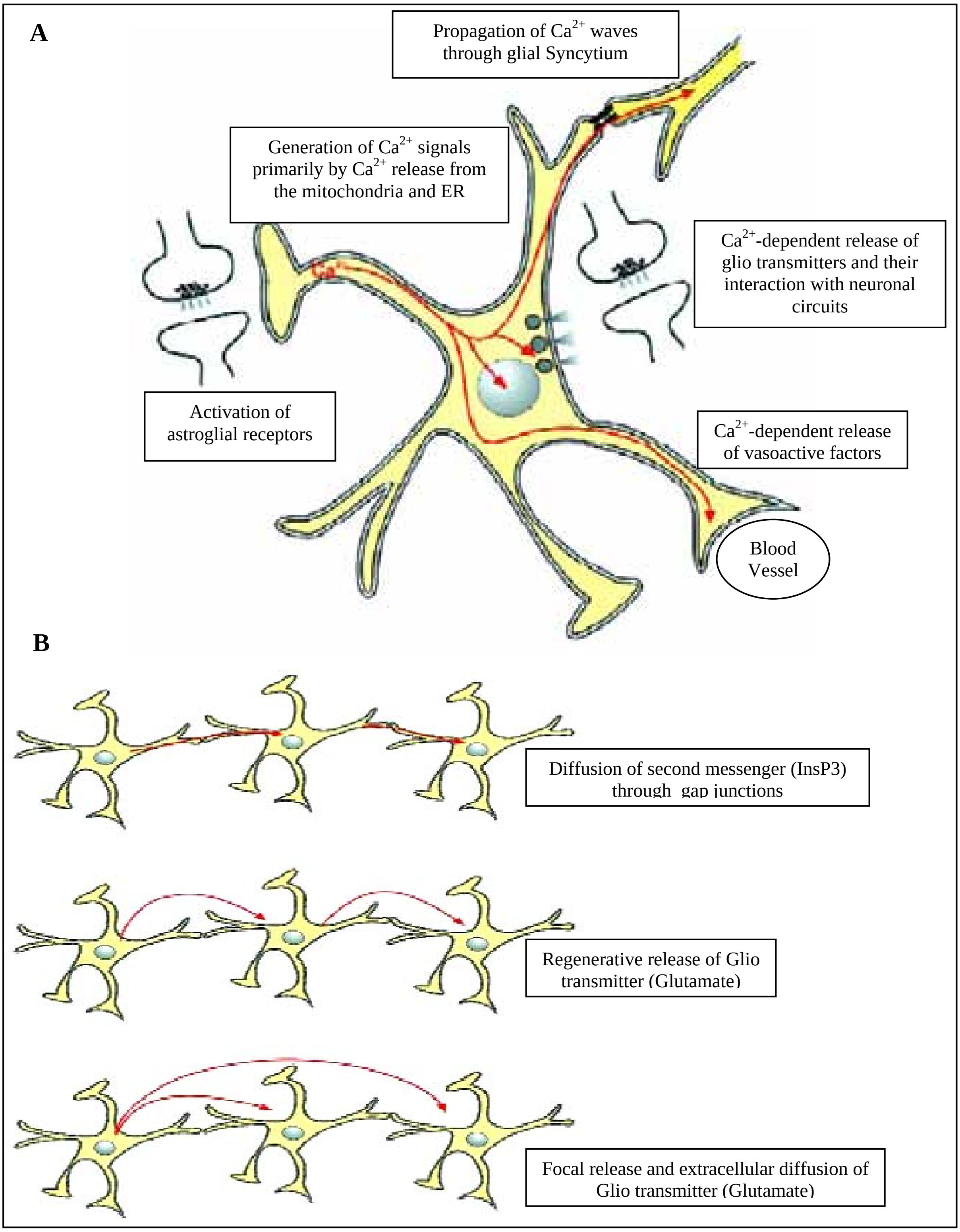
A
Propagation of Ca^{2+} waves through glial Syncytium
Generation of Ca^{2+} signals primarily by Ca^{2+} release from the mitochondria and ER
Ca^{2+}
Ca^{2+}-dependent release of glio transmitters and their interaction with neuronal circuits
Activation of astroglial receptors
Ca^{2+}-dependent release of vasoactive factors
Blood Vessel
B
Diffusion of second messenger (InsP3) through gap junctions
Regenerative release of Glio transmitter (Glutamate)
Focal release and extracellular diffusion of Glio transmitter (Glutamate)

Fig. 1.4.2: Mechanism of Glial calcium signaling. (A) Calcium signaling and integration in glial-neuronal-vascular units. (B) Mechanism of Ca^{2+} wave propagation through glial syncytium (Modified after Verkhratsky, 2006).

In conclusion, glial calcium signaling acts as a molecular mechanism for integration within glial syncytium and between glial and neuronal circuits. Chemical hypoxia results in Ca^{2+}

influx, which in turn triggers a massive release of glutamate followed by activation of ionotrophic receptors that further exacerbates cellular Ca^{2+} overload. Persistent and severe elevation in $[Ca^{2+}]i$ in turn compromises mitochondria, induces oxidative stress and activates numerous proteolytic enzymes. Several features of neuron-glial communication e.g. how glutamate and other chemical messengers are released from glia in response to physiological stimuli remains controversial and hotly debated. We believe that, in glia, information is integrated and transmitted by intracellular Ca^{2+}, but the ubiquitous involvement of Ca^{2+} as a second messenger makes it difficult to distinguish direct effects. In pathological conditions calcium signals regulate glial response to injury, which might have both protective and detrimental effects on the CNS (Verkhratsky, 2006).

1.4.3 Glial Ca^{2+} Signaling as Determinants of Disease Progression in ALS

Microglial cells have been long suspected as central components in neurodegenerative diseases where their role may include secretion of trophic or toxic molecules. Their role during neuronal degeneration during development is well established (Marin-Teva *et al.*, 2004). In ALS, microglial activation has been described in the brain and spinal cord of the patients (Henkel *et al.*, 2004; Turner *et al.*, 2004) and in the spinal cord of different mSOD1 mouse models (Hall *et al.*, 1998; Kriz *et al.*, 2002). The microglial reactivity is initiated before MN loss.

Several groups have tried to treat motor neuron disease by using minocycline, shown to inhibit microglial activation. Minocycline was potent in increasing survival of ALS mice and reduced microglial activation. Since minocycline also exerts an anti-apoptotic property on neurons, it is unclear in which cells the minocycline effect was active (Kriz *et al.*, 2002; Van Den Bosch et al., 2002; Zhu et al., 2002). Additional evidence implicating microglia in pathogenesis of ALS arose from forced activation of the immune system using chronic administration of lipopolysacchride, a well known microglial activator. In addition, mSOD1, which has now been reported to be released by motor neurons, is a potent activator of microglial cells (Urushitani *et al.*, 2006), emphasizing the likely crosstalk between motor neurons, microglial cells, and potentially other nonneuronal cells that may cooperate to drive disease progression.

1.5 Neuroprotective Study of Drugs (Riluzole and Melatonin) in ALS

1.5.1 Effect of Riluzole in ALS Neuroprotection

Riluzole (2-amino-6-(trifluoromethoxy)-benzothiazole) is a compound that has been reported to have neuroprotective effects in multiple *in vitro* and *in vivo* models (Jehle *et al*., 2000; Obinu *et al*., 2002). It is used clinically in the treatment of MN disease (Bensimon *et al*., 1994). It also has anaesthetic properties at high concentrations (Mantz *et al*., 1992), and has also been reported to have anticonvulsant effects (De Sarro *et al*., 2000). Riluzole has been used to treat amyotrophic lateral sclerosis due to its neuroprotective, anticonvulsant, anxiolytic and anaesthetic properties (Wagner & Landis, 1997). It appears to act via both presynaptic and postsynaptic mechanisms to attenuate glutamatergic neurotransmission and act as antiglutamate drug (Wokke, 1996; Bryson *et al*., 1996; Doble, 1996) and block depolarisation-evoked calcium transients in MNs (Hubert *et al*., 1994; Hubert *et al*., 1998). It is noteworthy that more potent and efficacious anti-glutamate agents are not as effective in ALS as riluzole (Eisen *et al*., 1993). While it has not yet been determined whether riluzole acts directly at these ion channels or inhibits their activity indirectly through second-messenger systems, all these actions may contribute to attenuating ion influx mediated, excitotoxic neuronal death.

How riluzole exerts these clinical effects is largely unknown. The mechanisms of action by which riluzole exerts its effects are complex. Multiple studies have shown that riluzole inhibits Na^+ channels (Siniscalchi *et al*., 1997; Shaw & Ince, 1997; Stefani *et al*., 1997; Yokoo *et al*., 1998), inhibits Cl^- channels (Bausch & Roy, 1996), increases glutamate uptake (Azbill *et al*., 2000) and inhibits γ-aminobutyric acid reuptake (Kretschmer *et al*., 1998). Additionally, riluzole was shown to attenuate neurotoxicity in brain preparations and in an animal model (Malgouris *et al*., 1994; Lang-Lazdunski *et al*., 2000). A rise in intracellular free Ca^{2+} concentrations ($[Ca^{2+}]i$) is a pivotal messenger for diverse pathophysiological events in cells (Berridge, 1993; Berridge, 1997); however, abnormal $[Ca^{2+}]i$ increases are cytotoxic (Budd, 1998, Budd *et al*., 2000). The inhibitory effect of riluzole on Ca^{2+} influx *in-vitro* coupled to its *in-vivo* neuroprotective action is unknown. Some of the studies found that riluzole inhibits the fast transient Na^+ current by shifting the steady-state inactivation curve towards more negative potentials. Riluzole has also been reported to activate multiple types of

K^+ channels, including SK, TREK-1,TRAAK channels (Duprat *et al*., 2000; Grunnet *et al*., 2001) and two pore-domain channels (Lesage, 2003).

1.5.2 Effect of Melatonin in ALS Neuroprotection

Melatonin (N-acetyl-5-methoxytryptamine) is a compound derived from tryptophan. It is a potent cellular antioxidant and can efficiently scavenge toxic free radicals and associated reactants (Reiter *et al*., 2000; Jou *et al*., 2004). Recent evidence has suggested that melatonin may directly act at the mitochondrial level to reduce mitochondrial oxidative stress induced damage. For example, the toxicity of azide/CN, which blocks complex IV of the mitochondrial electron transport chain, is reversed by melatonin (Yamamoto & Tang, 1996). Moreover, melatonin increases the activities of the respiratory chain complexes I and IV and thwarts mitochondrial damage induced by ruthenium red, which inhibits the mitochondrial Ca^{2+} uniporter for Ca^{2+} uptake and acts to cause mitochondrial uncoupling and oxidative stress (Martin *et al*., 2000). Furthermore, melatonin stimulates activities of the oxidative phosphorylation enzymes and the production of ATP (Martin *et al*., 2002). Acutely administered melatonin restores hepatic mitochondrial physiology in aging mice, particularly complex I and IV activities, and limits ischemia-and reperfusion-induced mitochondrial injury (Okatani *et al*., 2003).

In addition, recent studies demonstrate that melatonin significantly reduced laser irradiation-induced mitochondrial ROS formation and apoptosis in RBA-1 cells (Jou *et al*., 2002). Melatonin is also neuroprotective in *in-vitro* models of Alzheimer’s disease through its stimulatory effects on complex IV activity (Pappolla *et al*., 1997). Other studies show antiepileptic properties of melatonin, possibly due to regulation of the central GABA benzodiazepine receptor complex and inhibition of the glutamate-mediated response. Collectively these results explain the protective effects of melatonin in neurodegenerative diseases and other disorders which involve mitochondrial dysfunction. In the context of these studies, in March 2001, three ALS patients with an estimated onset of disease 2-4 years earlier, were included in a pilot study in Goettingen, set up to explore potential effects and side effects of chronic high dose melatonin. Given that mitochondria are a major cellular ROS source, are frequent targets of ROS damage, and play a crucial role in executing malfunction in ALS disease, the precise cellular mechanisms of action of melatonin at the mitochondrial level requires further investigation. The capability of these drugs to limit cellular damage in different experimental conditions, however, has raised some open questions. Indeed, the mechanism of action of these drugs is not fully clear yet.

1.6 Mitochondrial Dysfunction, Ca^{2+} Homeostasis and ALS: An Integrative Outlook

Combining the lessons from multiple animal models as well as cell culture model used to determine pathogenic mechanisms in ALS, the central insight is that selective vulnerability of MNs likely arises from a combination of several mechanisms; two of them, mitochondrial dysfunction and Ca^{2+} homeostasis (Duchen, 2002), are prominent. Documenting the involvement and importance of mitochondrial dysfunction and Ca^{2+} homeostasis we hypothesize that MN possess large number of voltage and ligand gated Ca^{2+} channels that, when activated, cause rapid Ca^{2+} influx, which, in part because of relatively weak cytosolic Ca^{2+} buffering, results in mitochondrial Ca^{2+} overload and strong ROS generation. Alternatively, the extrusion mechanisms, characterized by the plasma membrane calcium ATPase, Na^+/Ca^{2+} exchanger and accumulation by intracellular organelles contribute to the removal of calcium ions. Furthermore, their selective loss goes a long way explaining the oxidative damage, mitochondrial abnormalities and apoptotic contributions observed in ALS MNs. Chronic mitochondrial membrane depolarisation due to Ca^{2+} entry can cause the release of pro-apoptotic proteins and activate enzymes involved in apoptotic pathways (Pivovarova *et al*., 2004; Rosenstock *et al*., 2004).

Apparently, in the last few years, attention was drawn to the role of mitochondria as an efficient regulator of cytosolic calcium signals (Rizzuto *et al*., 1993; Gunter *et al*., 2004). Further, studies with mitochondria targeted calcium probes indicate a rapid, dramatic increase in free intramitochondrial calcium. This uptake by mitochondria has an immense effect on the metabolic state of the cell as it can up regulate the activity of the enzymes in oxidative metabolism ((Rizzuto *et al*., 1994, 2003; Rutter *et al*., 1996). malformation in mitochondrial structure and massive vacuoles derived from degenerating mitochondria found in post mortem human ALS samples (Sasaki & Iwata, 1996; Kong & Xu, 1998) further strengthen the proposition. Although the exact molecular mechanism is still not known, we hypothesize that vulnerability to ALS is a consequence of specific physiological features, particularly highly specialized Ca^{2+} homeostasis , continuous activity-dependent Ca^{2+} cycling and the predominant role of mitochondria in buffering Ca^{2+} transients. Mechanism illustrated in Fig. 1.6.

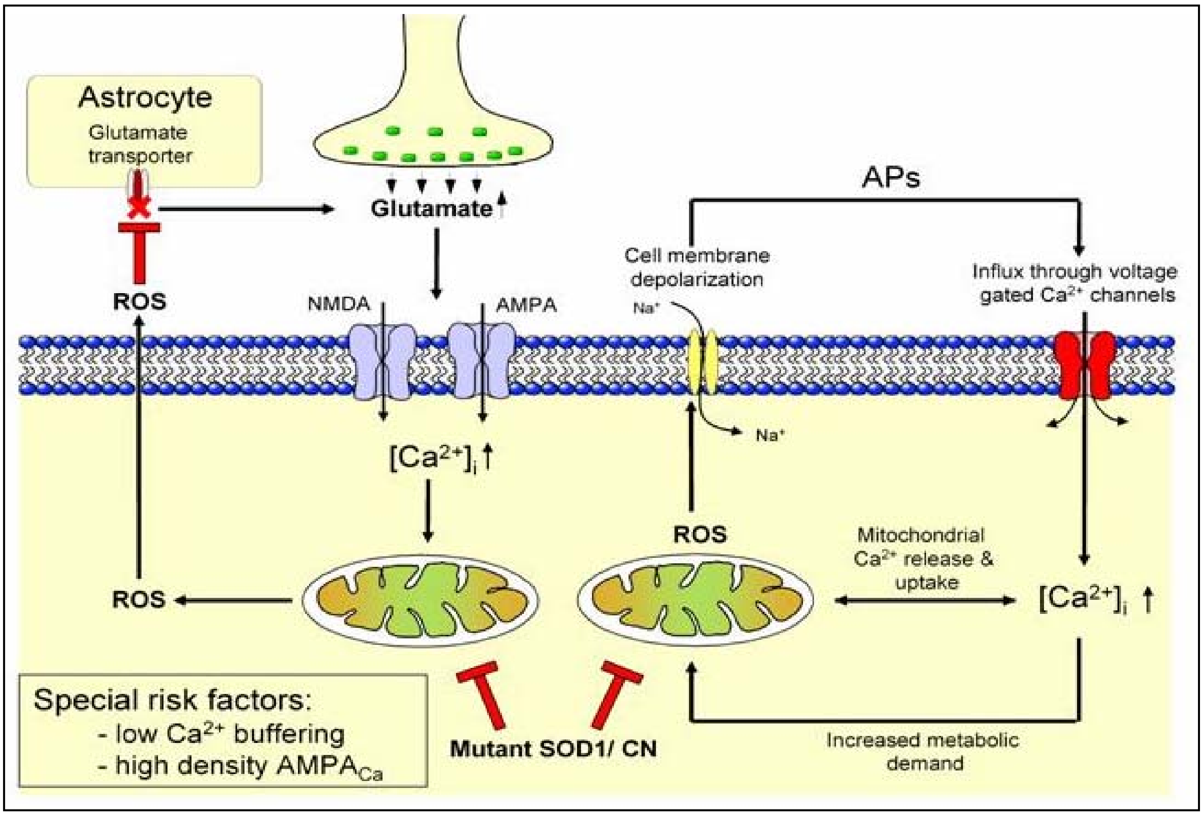
Astrocyte
Glutamate transporter
Glutamate
ROS
NMDA
AMPA
APs
Cell membrane depolarization
Na⁺
Influx through voltage gated Ca²⁺ channels
[Ca²⁺]ᵢ ↑
ROS
Mitochondrial Ca²⁺ release & uptake
ROS
[Ca²⁺]ᵢ ↑
Special risk factors:
- low Ca²⁺ buffering
- high density AMPA_Ca
Mutant SOD1/ CN
Increased metabolic demand

Fig. 1.6: Mitochondrial disturbance is predicted to be the key trigger to ALS etiology. The rampant production of reactive oxygen species (ROS) by disturbed mitochondrial metabolism can be readily cytotoxic as ROS can destroy the membrane integrity by averting the specificity of membrane channels or triggering the opening of particular leak channels as well as by destroying the lipid components of the membrane. It is also hypothesised that ROS produced in motoneurons can escape to the extracellular environment and can damage the glutamate transporters on astrocytes (Modified after Von Lewinski & Keller, 2005).

2. Materials and Methods

2.1 Experimental Set-up

All the imaging experiments were performed using the set-up installed in the physiology institute as well as at European Neuroscience Institute (old building) in Goettingen, Germany. All confoacl and 2-photon experiments were performed in collaboration with Prof. Klaus Ballanyi laboratory at Alberta Neuroscience Center and Heritage medical research center, Edmonton in Canada.

In Goettingen, most of the experiments performed with a set-up consisting of an upright microscope (Axioscope, Zeiss, Göttingen Germany), a monochromator (Till photonics, Graefelfing, Germany), a Charge-coupled device (CCD) camera for fluorescence signal detection (Till photonics, Graefelfing, Germany), and an instruments for patch clamp recording (Heka, Germany). The recording chamber (volume, 1.0 ml) for brain slices and cell culture was fixed on the microscope table and it allowed X-Y axis manipulations under the microscope. Besides, the microscope stage was placed on sliding table (Spindler & Hoyer, Goettingen, Germany) allowing further flexibility in visualisation by enabling movement in X-Y direction. Brain slices and cell lines loaded with dyes were excited at different wavelengths by a monochromator through an optic fibre cable focussed to suitable diachroic mirrors; beam splitter and band pass filters. The whole imaging set-up was fixed on a table equipped with an air suspension and enclosed by a faraday cage with the aim of protecting the set up from vibration and electric noise. Continuous perfusion of recording chamber was allowed with aCSF via Tygon® tube connection. Superfusate was administered at a flow rate of 6-7 ml/min via a peristaltic pump (Watson-Marlow**,** Mühlenweg, Germany). Optical measurements were done using 20X water immersion objective (Achroplan, Zeiss) for visualisation and 63X water immersion objective (Achroplan, Zeiss) for signal recordings. All light microscopy and light green staining was performed at Department of Neurology, University of Goettingen, Germany. 40X oil immersion objective (Achroplan, Zeiss) were used for this purpose.

In Canada, most of the experiments were performed using either a confocal microscope and software (20X XLUMPlanF1, numerical aperture, 0.95, objective; Olympus FV300; Carsen group, Markham, Ontario, Canada) or a FV300 connected with a Titanium:Saphir laser (10W Mira/Verdi; Coherent, Santa Clara, CA) for 2-photon imaging (Nikolenko *et al*., 2003).

2.2 Transgenic Mice and PCR Genotyping

TgN (SOD1-G93A) 1Gur (Fast Line) mice were obtained from The Jackson Laboratory (Bar Harbour, Maine, USA). The transgenic (Tg) strain can be considered a model for human amyotrophic lateral sclerosis (hALS). The mice carry a variation of the human SOD1 gene, where at position 93 the amino-acid glycine is replaced by alanine (Gurney *et al*., 1994). These mice develop paralysis in the limbs and die at 4-5 months of age, which is due to the continuously expanding loss of MNs from the brainstem and spinal cord. After the onset of symptoms life expectancy varies from 4 to 6 weeks. Animal experiment procedures were approved and carried out in accordance with the guidelines of the ethics committee of the Medical Faculty of the University of Göttingen and ethics committee of the University of Alberta, Edmonton.

The Tg male mice were bred with female B6SJL F1-hybrids obtained from the Jackson Laboratory (Bar Harbour, Maine, USA) and from Charles River (Germany).Tg mice were identified using polymerase chain reaction. Within the first few days after birth (1-5 days), a piece of the mouse tail was dissected and 300µl diagnostic buffer (20mMTris HCl at pH: 8.4, 50mM KCl, 0.45% NP40, 0.45% Tween 20) and 5µl Proteinase K (20mg/ml) were added. After stirring, the process of digestion was supported by incubation for 2 hours at 55°C and denaturalising for 10 min at 95°C. The homogenate was then put on ice for 10 min and centrifuged at 1000xg for 1min. For amplification DNA (1µl) from the digestion process, Aqua dest (47.5µl), Taq PCR Master mix kit (50µl, Qiagen, Hilden, Germany) and special primers (0.4 µl for each primer, ARK Scientific) were used to identify two genes: first the human SOD1 gene on exon 4 consisting of 236bp (primer1:oIMR114:5’-CGC GAC TAA CAA TCA AAG TGA-3’ and primer 2:oIMR113: 5’-CAT CAG CCC TAA TCC ATC TGA -3’) and secondly the endogenous murine Il2 gene consisting of 324bp (primer 3:oIMR042: 5’-CTA GGC CAC AGA ATT GAA AGA TCT-3’ and primer 4:oIMR043:5’-GTA GGT GGA AAT TCT AGC ATC ATC -3’). The Il2 gene is used as a control for DNA amplification. The transgene carriers will amplify both genes; the wild-type samples will amplify only Il2-gene.

The amplification runs 35 cycles including 4min at 94°C for initial denaturation, 1min at 92°C, 1min at 60°C and 1min at 72°C. Finally the temperature is held at 72°C for 5min and then cools down to 10°C. 10µl PCR-product and 5µl 6X loading buffer (MBI Fermantas, Vilnus, Lithuania) were run on a 2% agarose gel (80ml tray with 7µl ethidium bromide dye) along with a 100bp DNA ladder (MBI Fermantas, Vilnus, Lithuania) to estimate the size of the products.

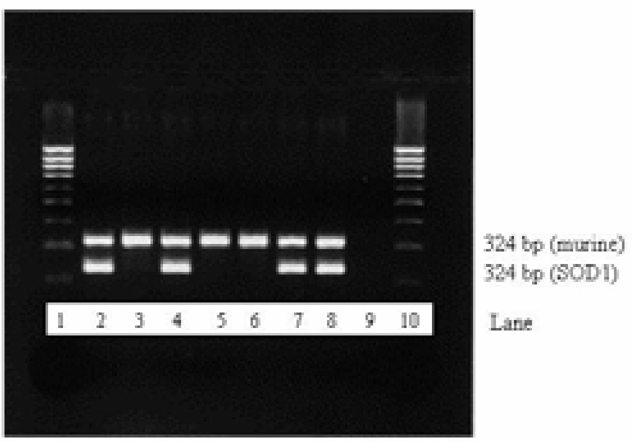

Fig. 2.2: PCR gel. Lanes 1 and 10, molecular mass marker (bp size: 80, 100, 200, 300, 400, 500, 600, 700, 800, 900, 1031); lanes 2, 4, 7, 8: transgenic mice; lanes 3, 5, 6: normal mice; lane 9, control (primers without DNA, adapted from Hoyaux *et al.*, 2000).

2.3 Preparation of Mice & Rat Brain Stem Slices

All the animal experiments (physiological and optical recordings) described here were performed on transverse acute brainstem slices prepared from postnatal days 0(P0) to 4(P4) NMR1, adult (8-9 and 14-15 weeks) WT and mSOD1^{G93A} mice and Wistar (WS) rats between postnatal days P0 and P4. Animals were anesthetized with diethyl ether vapor until the paw withdrawal reflex disappeared and then decapitated; brains were carefully dissected and quickly transferred to cold (4°C) aCSF containing the following (in mM):118 NaCl, 3 KCl, 1.5 $CaCl_2$, 1 $MgCl_2$, 25 $NaHCO_3$, 1 NaH_2PO_4, and 30 D-glucose (pH adjusted to 7.4, Osmolarity was 325 mosmol l^{-1}) and was bubbled with carbogen (95% O_2, 5% CO_2). After removal of the telencephalon by scalpel, cerebellum and brain stem were separated by an axial cut. The brainstem was glued with the rostral side of the brainstem directed upwards with the ventral side facing the blade (Fig. 2.3). Serial transverse sections of the brain stem with a thickness of ~200µm were made using a vibratome (Leica VT 1000s vibroslicer, Leica instruments GmbH, Nussloch, Germany) and were maintained at optimal conditions.

Mechanical and age specific disturbances during the slice preparation were minimized by continuous low temp and oxygen supply during slice preparation.

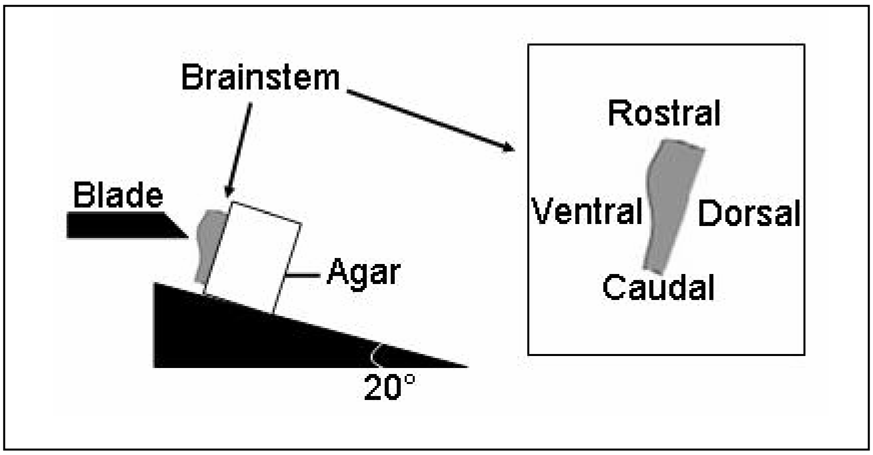

Fig. 2.3: Position of the isolated mouse brainstem during slicing. Orientations of brain stem are highlighted in the box.

Sectioning was begun when the 4th ventricle had crossed its largest diameter, and was stopped at the appearance of landmarks identifying closing of 4th ventricle (Fig. 2.3.1). Up to 3-4 slices containing HMNs were obtained per preparation. All the experiments were conducted at 25-27^{0}C. In slice chamber, all slices were fixed with U-shaped platinum wire, on which nylon strings were glued.

In Canada, Wistar rats were anesthetized with 2-3% isoflurane until the paw withdrawal reflex disappeared. They were then decerebrated and the neuraxis isolated at 18-20°C in saline containing the following (in mM): 120 NaCl, 3 KCl, 1 $CaCl_2$, 2 $MgSO_4$, 26 $NaHCO_3$, 1.25 NaH_2PO_4, and 20 D-glucose (pH adjusted to 7.4 by gassing with 95% O_2, 5%CO_2). After removal of the cerebellum and transverse sectioning at the pontomedullary junction and just rostral to the C_1 cervical segment, the brainstem was glued rostral side down to a metal plate. Serial transverse sections were made with a vibratome (Leica VT1000S; Leica Microsystems, Richmond Hill, Ontario, Canada) in caudal-to-rostral direction starting near the pyramidal decussation (Schwarzacher *et al.*, 2002). Sectioning was stopped based on the appearance of landmarks identified by on-line histology (Ruangkittisakul *et al.*, 2006). Slice thickness of 200 and 400µm non rhythmic and one PBC containing slice with rostrocaudal thickness of 600 or 700µm was cut and fixed (caudal surface up) with insect pins on the silicone layer covering the bottom of the recording chamber (volume, 1.5 ml). Superfusate was administered at a flow rate of 5 ml/min via a peristaltic pump (Watson-Marlow Alitea-AB;

Sin-Can, Calgary, Alberta, Canada). Superfusate temperature in the recording chamber was kept at 25-27°C (TC-324B; Harvard Apparatus, Saint-Laurent, Quebec, Canada).

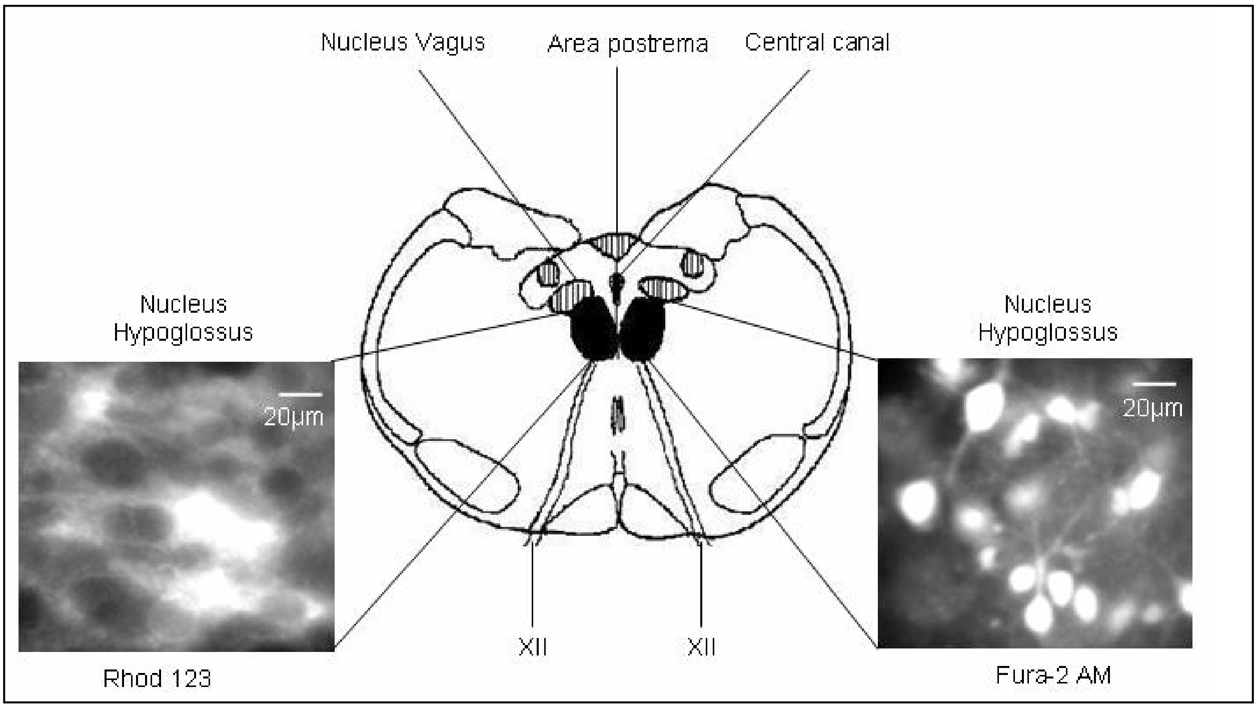

Fig. 2.3.1: Slice preparation and graphical illustration of the HMNs staining of slices with different dye. Illustrations of an adult mouse brain stem slice containing the nucleus (Ncl.) hypoglossus. On the left, a CCD camera image (4x4 binning) showing hypoglossal motoneurons (HMNs) loaded with Rhod 123 (excitation at 485 nm).On the right, a CCD camera image (4x4 binning) showing hypoglossal motoneurons (HMNs) loaded with Fura-2 AM (excitation at 360 nm).

2.4 Identification of Hypoglossal Motoneurons in the Brain Stem Slices

Hypoglossal motoneurons (HMNs) in slices were visually identified based on their localization in the hypoglossal nucleus paramedian ventral of the 4th ventricle or the central channel (Fig. 2.4) as well as their location close to other prominent brain areas with the help of ‘The Mouse Brain in stereotaxic coordinates’ atlas by Keith B. J. Franklin & George Paxinos (Academic press), while cutting the brainstem transversely. Nucleus hypoglossus (XII) and dorsal vagus nucleus (X) are located close to the fourth ventricle / central canal. HMNs were further distinguished from neighbouring neurons by their large size (somatic diameter usually >15µm) and their distinguished rounded outline. During physiological patch clamp experiments HMNs were identified by their ability to fire action potentials in drug-free (TTX) solution and the occurrence of spontaneous synaptic activity and extensive dendritic arborisation (Bergmann & Keller, 2004).

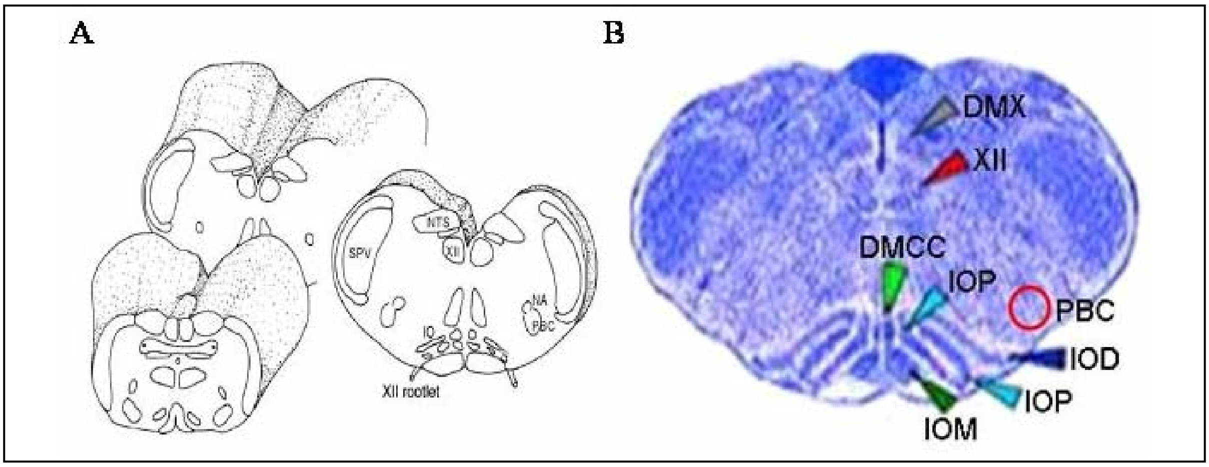

Fig. 2.4: Schematic and thionine stained brainstem tissue. (A) Schematic drawing of the medulla oblongata, from which slices were taken containing the hypoglossal nucleus (XII), ambiguous nucleus (NA), pre-Bötzinger complex (PBC), solitary tract nucleus (NTS), the spinal part of the trigeminal nucleus (SPV) and the inferior olive (IO; modified after Ramirez *et al.*, 1997). (B) Location of different marker nuclei under study in the fixed, thionin-stained brainstem tissue from P2 Wistar rat. Dorsal vagal motonucleus(DMX); hypoglossal motonucleus (XII, oval circle); Dorsomedial cell column(DMCC) of inferior olive (IO); principal inferior olive(IOP) ; medial inferior olive(IOM) ; dorsal inferior olive (IOD); Pre-Bötzinger complex (PBC; Adapted from Ramirez *et al.*, 1997; Ruangkittisakul *et al.*, 2006).

2.5 WT and SOD1^{G93A} Transfected SH-SY5Y Neuroblastoma Cell Culture

An *in-vitro* model to study the cellular alterations associated with mutations of SOD1 was constructed by transfection of the human neuroblastoma cell line SH-SY5Y with G93A-SOD1 (previously described by Carri *et al.*, 1997). Transfected human neuroblastoma cell lines constitutively expressing either WT human SOD1 or the G93A mutant form of this enzyme associated with fALS was made available by Prof. Roland Nau group (Work done in collaboration with Prof. Dr. Roland Nau, Department of Neurology, Georg-August University, Goettingen, Germany). They were routinely maintained in Dulbecco´s MEM-F12 (Gibco, Invitrogen, Karlsruhe, Germany) containing 15% fetal calf serum (FCS), 100U/ml penicillin and 100µg/ml streptomycin (Invitrogen, Karlsruhe, Germany) at 37°C in a humidified atmosphere with 5% CO_2. Cell lines were kept in selection by addition of 200 µg/ml geneticin (G418 sulphate, Gibco, Invitrogen, Karlsruhe, Germany); geneticin was removed two days before performing the experiments.

2.6 CCD Camera Imaging

For fluorescence measurements and monitoring of dynamic changes in $[Ca^{2+}]i$ and mitochondrial parameters of HMNs in the slice/cell culture, a modified version of the CCD camera system (TILL Photonics, Planegg, Germany) was employed in experiments as described previously (Ladewig & Keller, 2000; Bergmann & Keller 2004). Briefly, a computer-controlled monochromator based on a galvanometric scanner (Polychrome II, TILL Photonics, Gräfelfing, Germany) was connected to an upright microscope (Axioskope, Fa. Zeiss, Göttingen, Germany) via quartz fiber optics and a minimum number of optical components for maximum fluorescence excitation (objective Achroplan W 63x, 0.9W) was employed. The emitted light was directed to a dichroic mirror with mid reflection depending on the fluorescent dye used (Fura: 425 nm, Rhod 123: 510 nm; Zeiss, Germany).

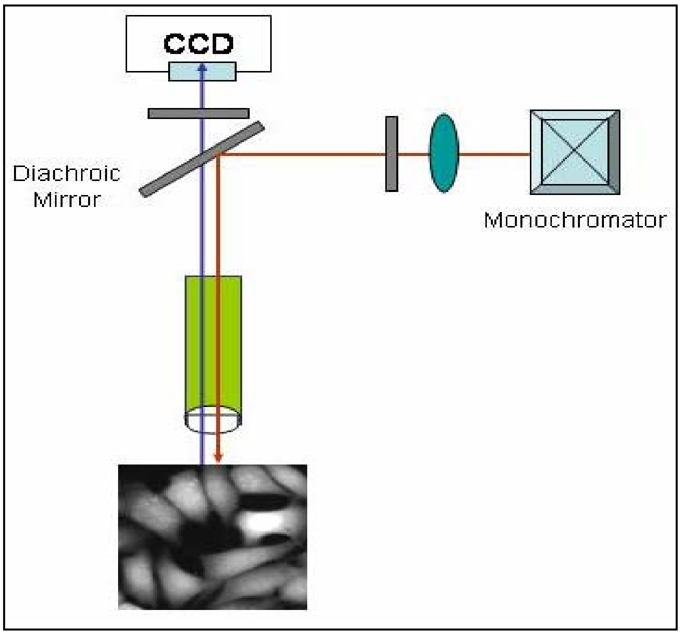

Fig. 2.6: Schematic representation of the CCD-imaging setup used for calcium imaging in the brain stem slice / cell line preparation. Note also the view of brains stem motoneurons under microscope.

A 12 bit peltier-cooled (-15°C) slow scan CCD camera with A/D converter (PCO, Germany) was employed to monitor fluorescence changes in defined “regions of interest” (ROIs) using a PC running TILL Vision Software V3.3 and V4.0 (TILL Photonics, Martinsried, Germany); binning of which was set to 4x4 (120x160 pixel) allowing sampling rates up to 15 Hz at reasonable spatial resolution , exposure time was 30-80 ms, sampling rate varied between 3 and 13 Hz. Data analysis and calculations of intracellular Ca^{2+} concentrations, mitochondrial membrane potentials ($\Delta\psi_m$) and fluorescence signals was performed off-line using IGOR (Wavemetrics, Lake Oswego, OR, U.S.A.), Origin-7 software (Origin Lab, Northampton, MA, USA) and ImageJ software. Fig. 2.6 shows the schematic assembly of the CCD-imaging setup used for calcium imaging experiments in the Slice preparation as well as cell culture experiments.

2.7 Monitoring of Mitochondrial Parameters (Membrane potential)

Mitochondrial membrane potential ($\Delta\psi_m$) was monitored using rhodamine 123 (Rhod 123), a cationic non-ratiometric dye which is used as an indicator of intactness of mitochondrial membrane potential (Mostafapour *et al.*, 1997). Briefly, brainstem slices were incubated in aCSF containing 5µg/ml Rhod 123 at room temperature for 20 min. Because of its positive charge, Rhod 123 accumulates in negatively charged mitochondrial matrix where its fluorescence is quenched. Slices were thoroughly rinsed in aCSF and placed in the perfusion chamber for fluorescence analysis. Upon depolarization of $\Delta\psi_m$, Rhod 123 is released from mitochondria and fluorescence increases. Rhod 123 was excited at 475nm and a dichroic mirror with mid-reflection at 510 nm was used for collection of signal (Fig. 2.7). Changes in Rhod123 fluorescence are reported in relative values, F/F_0, where F_0 is the baseline fluorescence before stimulus or drug application and F is the fluorescence after stimulus or drug application. Slices were washed with indicator-free medium at RT for >30 min prior to onset of imaging. Staining of HMNs with Rhod 123 dye and absorption and fluorescence emission spectra of Rhod 123 dye is illustrated in Fig. 2.7.

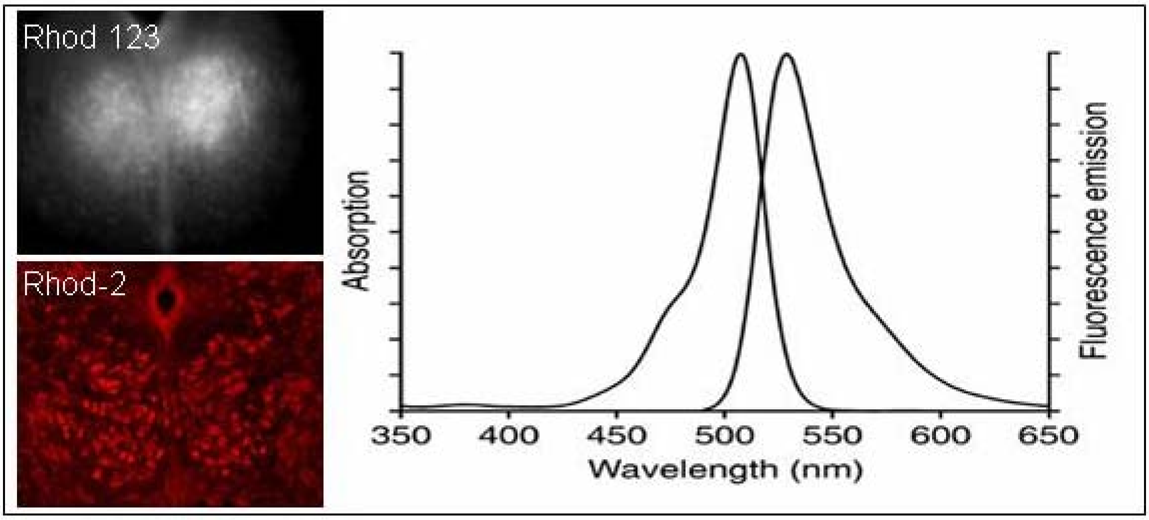

Fig. 2.7: Rhodamine 123 (up)/Rhod-2 (down) stained mice brain stem slice showing high density of mitochondria in hypoglossal motoneurons (Left; staining done by Dr. Freidrike Von Lewinski) and absorption and fluorescence emission spectra of non ratiometric dye rhodamine 123, in methanol (Right). Fluorescence excitation wavelength is 475 nm and emission wavelength is 510 nm (taken from Molecular Probes homepage).

2.8 Intracellular Microfluorometric Ca^{2+} Measurement

Changes in cytosolic Ca^{2+} ($[Ca^{2+}]_i$) were monitored using fura-2 (K_d ~ 0.2 µM). The fluorescent dye was introduced into cells either by addition of their potassium salts to the patch pipette solution (100-500 μM), or by loading the slice with their membrane-permeable AM-ester forms (5 μM, 40 min, at 32°C) called bolus loading. In this report injection and bath loading (incubation) was utilized for slice loading. All slices were washed with indicator free medium at RT for 30 min prior to onset of imaging. If not indicated otherwise, experiments were carried out at RT. Fura-2 and related Ca^{2+} indicators are classical ratiometric dyes. Several papers describe their application in a wide variety of cells due to shift in their excitation spectrum upon binding of Ca^{2+} (Fig. 2.8).

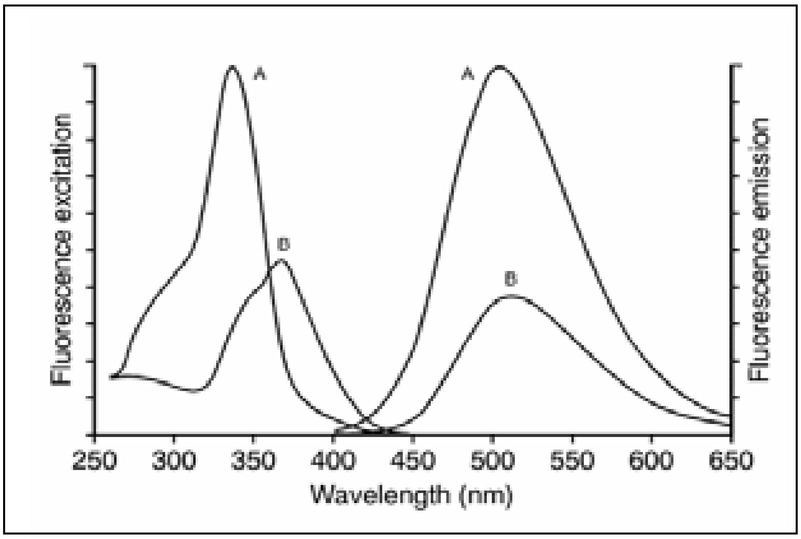

Fig. 2.8: Fluorescence excitation (detected at 510 nm) and emission (excited at 340 nm) spectra of Ca^{2+}-saturated (A) and Ca^{2+}-free (B) fura-2 in pH 7.2 buffer (taken from Molecular Probes homepage).

During increase of $[Ca^{2+}]i$, the fluorescence activity of Fura decreases when excited at ~385 ± 5 nm, whereas the fluorescence activity increases when excited at ~340 nm (Fig. 2.8). Ratioing considerably reduces the effects of uneven dye loading, leakage of dye, photobleaching and problems associated with measuring Ca^{2+} in cells of unequal thickness. Furthermore, measurements of Fura-2 fluorescence can usually be made over a period of an hour without significant loss of fluorescence resulting from either leakage or bleaching. In addition, Fura-2 is bright enough to permit measurements at intracellular concentrations of dye unlikely to cause significant Ca^{2+} buffering or damping of Ca^{2+} transients. At ~360 nm, fura displays its isosbestic point, where the emission is not dependent on Ca^{2+}. In the experiments described here, we excited Fura at 360 and 390 nm; these changes have been done as the objectives used did not transmit light at wavelengths around 340 nm. Excitation at 360 nm is furthermore beneficial, because it allows precise estimation of the dye concentration in the cell (Neher, 1995).

Changes in the cytosolic calcium ($[Ca^{2+}]_i$) were measured in SH-SY5Y cells expressing either WT-SOD1 or G93A-SOD1 gene attached to glass cover slips after 2–5 days in culture. Cell layers were incubated with RPMI-1640 + 10% FCS (Gibco, Invitrogen, Karlsruhe, Germany) containing 10µM Fura-2 AM at 37°C for 30 min. The RPMI-1640 medium used contains 0.846 mM Ca^{2+} (supplier's data). Cells were rinsed with RPMI-1640 and further incubated for 20 min at 37°C to allow complete deesterification. Changes in $[Ca^{2+}]_i$ were measured using a CCD camera system and a computer-controlled monochromator described above.

Excitation of Fura-2 was alternately done at 360 nm and 390 nm, emitted light was directed to a dichroic mirror with mid-reflection at 425 nm and in some experiments filtered by a band pass filter (505-530 nm). Since in AM loaded slices and cell culture the background fluorescence is not clearly determinable, fluorescent changes in defined ROIs are given in relative values F/F0, where F0 is the fluorescence before stimulus or drug application. We assume calculated Ca^{2+} concentrations (F/F0) as an approximation of the real concentration. Therefore, for AM ester-loaded MNs in slices and culture cells, changes in $[Ca^{2+}]$i are given in Fig. as changes in Fura-2 ratio units (360/390 nm). However, fluorescence intensities of Fura-2 were possible to converted into Ca^{2+} concentrations according to Grynkiewicz *et al* (Grynkiewicz *et al.*, 1985), assuming $K_d = 224$ for HMNs (Lips & Keller, 1999; Ladewig & Keller, 2000). R_{min} and R_{max} were determined by exposing the cells to 15 µM ionomycin in the presence of aCSF either containing 0 mM Ca^{2+} and 10 mM EGTA or 10 mM Ca^{2+}. The resulting ratio trace to calculate Ca^{2+} values was calculated according to the equation (Grynkiewicz *et al.*, 1985) given below.

$$[Ca^{2+}]_i = Kd\,(\mathrm{Rmax} / R_{min})\,(R-R_{min}) \;/\; (R_{max}-R)$$

Where $[Ca^{2+}]_i$ is the intracellular calcium concentration; *Kd* is the dissociation constant of the calcium indicator dye Fura-2, R_{max} is the maximum fluorescence ratio and R_{min} is the minimum fluorescence ratio. A change of 0.1 in Fura-2 ratio corresponds to a change in $[Ca^{2+}]_i$ of ~100 nM (Von Lewinski & Keller, 2005).

2.9 Simultaneous Measurement of Changes in $[Ca^{2+}]_i$ and $[Ca^{2+}]$m

Simultaneous fluorometric measurements of cytosolic $[Ca^{2+}]_i$ and mitochondrial calcium $[Ca^{2+}]$m were measured utilizing calcium-sensitive fluorescent dyes (5µM Fura-2 AM for

$[Ca^{2+}]_i$ and 10µM Rhod-2 AM for $[Ca^{2+}]$m). For dye loading SH-SY5Y cells expressing either WT-SOD1 or G93A-SOD1 gene attached to glass cover slips after 2–5 days in culture were first loaded with 5µM Fura-2 AM at 37°C for 30 min as described above. Subsequently, cells were washed with RPMI for 20 min and further incubated with 10 µM Rhod-2 AM for 20 min at 37°C, 5% $C0_2$, and 95% 0_2). The coverslips were rinsed with RPMI and further incubated for 20 min at 37°C to allow complete deesterification. The cells were imaged as describe above. Dyes were excited at 390 and 550 nm, respectively, with a Polychrome II monochromator (TILL Photonics, Martinsried, Germany). Emitted light was separated by 565 nm dichroic mirrors and filtered with a 510 nm long-pass emission filter. Imaging of $[Ca^{2+}]$i and $[Ca^{2+}]_m$ in the same cell was achieved by stimulating once at 390 nm, followed by 550 nm, and by repeating this alternate excitation and averaging the relevant signals (Fig. 2.9). An interval of 5 ms between each stimulus was required to allow re-establishment of baseline calcium levels; for long duration stable recordings and data acquisition. Changes in $[Ca^{2+}]$i and $[Ca^{2+}]_m$ were measured using a CCD camera system and a computer-controlled monochromator described above.

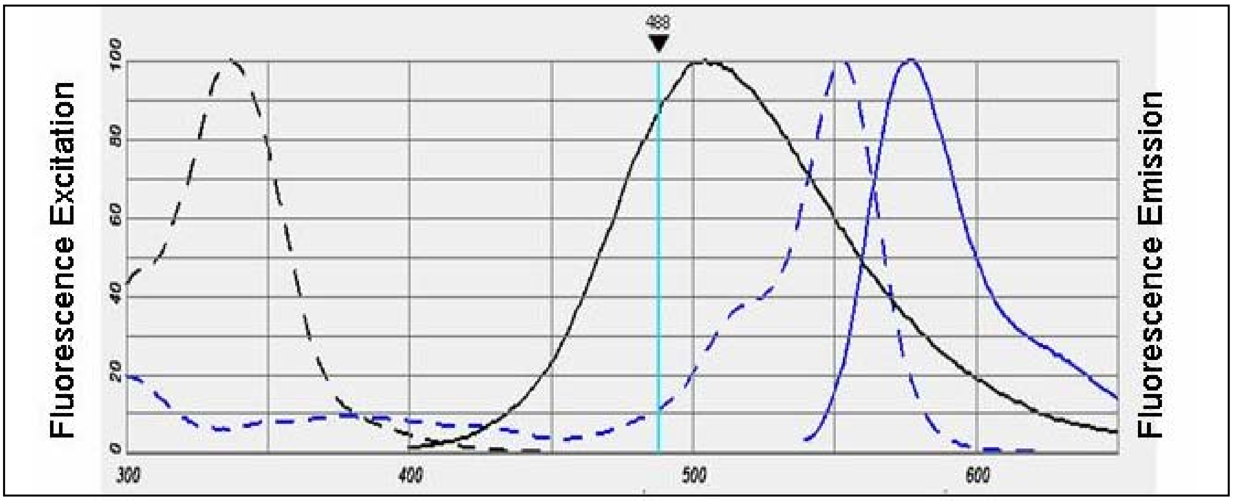

Fig. 2.9: Spectral view of simultaneous measurements of $[Ca^{2+}]$i and $[Ca^{2+}]_m$ generated by molecular probes spectral view program. Fluorescence excitation was done at 390 and 550nm respectively and emission at 510 nm, separated by 565 nm diachroic mirror (Fig. generated by the Molecular Probes spectral view program).

2.10 Calbindin-D_{28k} Buffering and Estimation of Decay Time Constant (Ca^{2+} clearance rates, τ)

CB-D_{28k} and or Parvalbumin (PV) appear to influence selective vulnerability of MNs in ALS. Ca^{2+} involvement as a risk factor was proved by the observation that Ca^{2+}-binding proteins such as CB-D_{28k} and PV were absent in MN populations lost early in ALS (HMNs/SMNs), whereas MNs damaged late or infrequently in the disease (oculomotor, trochlear and abducens nerves) expressed markedly higher levels of CB-D_{28k} and or PV (Alexianu *et al.*, 1994).

In order to check whether CB-D_{28k} protects cells from degeneration via buffering of $[Ca^{2+}]i$, we developed a culture of primary neuronal cells from E18 mouse cortex that express different levels (low and high) of CB-D_{28k} (work done in collaboration with Dr. Sebastian Kugler, Department of Neurology, University of Goettingen). Non- transfected as well as Primary cell culture transfected with different levels of CB-D_{28k} via adeno- associated virus (AAV-2) was used in Ca^{2+} imaging studies following depolarization induced stimulus (60mM K^+). Using a stimulus of 60mM K^+, which caused a fast transient increase in $[Ca^{2+}]i$ followed by a sustained plateau increase, the F/F0 value of transient (peak value) and sustained increase in CB-D_{28k} transfected and non-transfected cell lines was compared.

Analyzing Ca^{2+} dynamics according to the one-compartment model neglects nonlinearities in Ca^{2+} clearance mechanisms (Blumenfeld *et al*., 1992). However, for estimation of $[Ca^{2+}]i$ clearance rates, decay kinetics of Ca^{2+} transient recoveries after depolarization evoked Ca^{2+} transients before and after 60mM K^+ application in CB-D_{28k} transfected and non-transfected cells were fitted with a single exponential decay curve to determine the decay time constant (τ), approximating that the Ca^{2+} extrusion after a response is linear. The quantitative model of somatic calcium homeostasis predicts that under such experimental conditions decay times of calcium transients are a linear function of Fura-2 buffering capacity. Plots from transients with similar amplitudes were pooled (N= 4) for CB-D_{28k} transfected and non-transfected cells after 60mM K^+ induced stimulus and the resulting polynomial fits -one for each condition- were then plotted as a function of the transient amplitude. Finally, the decay time constant (τ) was calculated as

$$\tau = A/I$$

Where A denotes the area under the time-concentration curve and I denotes the amplitude of the fluorescence intensity.

2.11 Targeted Pressure Injection Loading of Mitochondrial and Ca^{2+}-Sensitive Dye in Brain Stem Slice Preparation

A versatile approach for targeted staining of slices was utilized based on targeted pressure injection of dye into the tissue of interest. This can be used for a large spectrum of indicator dyes. Mitochondrial dye Rhod 23 (1mg/ml-5µl) and the membrane-permeable Ca^{2+}-sensitive dye Fluo-4 AM (0.5mM in superfusate) was backfilled into a broken patch pipette (outer diameter, 5-10µm) and pressure (0.7-1.0 psi) injected for 10-15 min into the HMNs from the caudal surface. With in 10-20 min after injection, labeling revealed basic neuronal morphology and stained areas were 300-400µm in diameter. Fluorescence signals were measured using either a confocal or two-photon system. $\Delta\Psi m$ and Ca^{2+} fluorescence signals were imaged at tissue depth of upto 60µm for confocal and 90µm for two-photon microscopy.

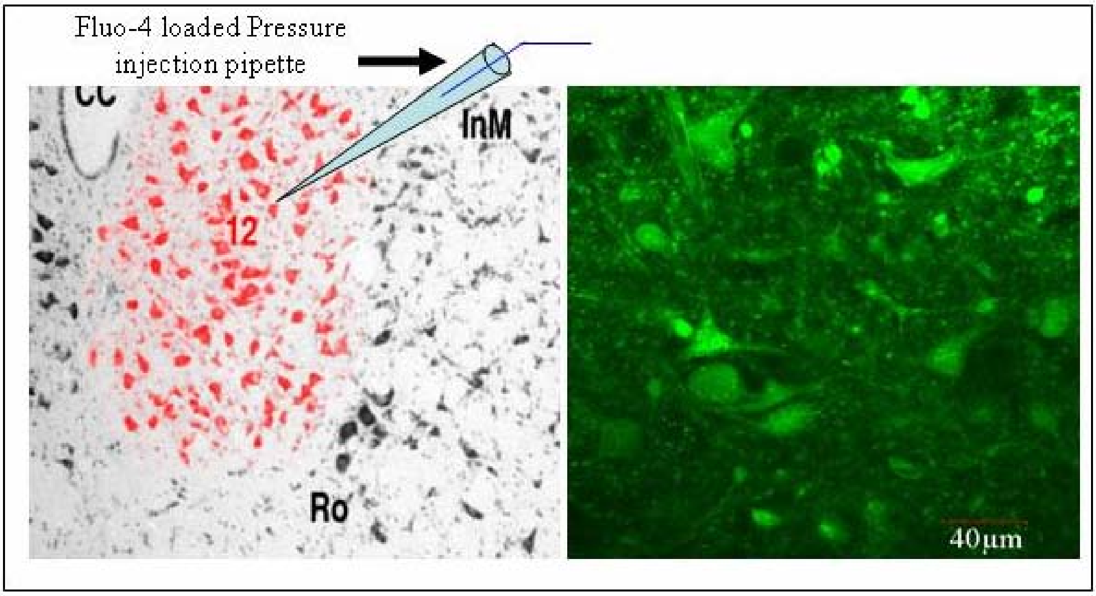

Fig. 2.11: Identification of Hypoglossal nucleus (Left) and pressure injection loading of Fluo-4 dye in mice brain stem slice (Right) showing robust staining of motoneuron and glial cells (Left, modified after Paxinos *et al.*, 1999, Academic Press). Scale bar 40µm.

2.12 Confocal Laser Scanning Microscopy (CLSM)

In order to produce a two-dimensional picture, the specimen was scanned point wise by a laser beam. The resulting picture contains information of a plane through the specimen orthogonal to the optical axis. By moving the objective in z-direction it is possible to make a stack of two-dimensional pictures of the specimen along the z-direction. In a confocal laser scanning microscope (CLSM) a fluorescent specimen is excited with laser light and the emitted fluorescence is then detected confocally. The goal of this optical arrangement is to detect the fluorescence light emitted by the specimen in the focal plane and to prevent the detection of out-of-focus light. A confocal laser scan system (Olympus, FV300) was used for localization studies of Ca^{2+} and $\Delta\Psi m$ in respiratory MN and glial cells of brain stem slices. In these experiments, acute slices were loaded with 5µM Rhod 123 for 15 min followed by 20 min wash for $\Delta\Psi m$ measurement in MN and glial cells of brain stem slices. For Ca^{2+} imaging slices are loaded with Fluo-4/AM for 30 min followed by a 30 min wash. Slices were placed into a custom built recording chamber mounted on the microscope table and perfused with aCSF. Rhod 123 and Fluo-4 were excited at 475 nm line of argon laser and fluorescence was collected using 510LP and 530SP filter. Data acquisition and analysis was done using the LSM software FluoView. Schematic representation of the optical path of a confocal laser-scanning microscope is shown in Fig. 2.12.

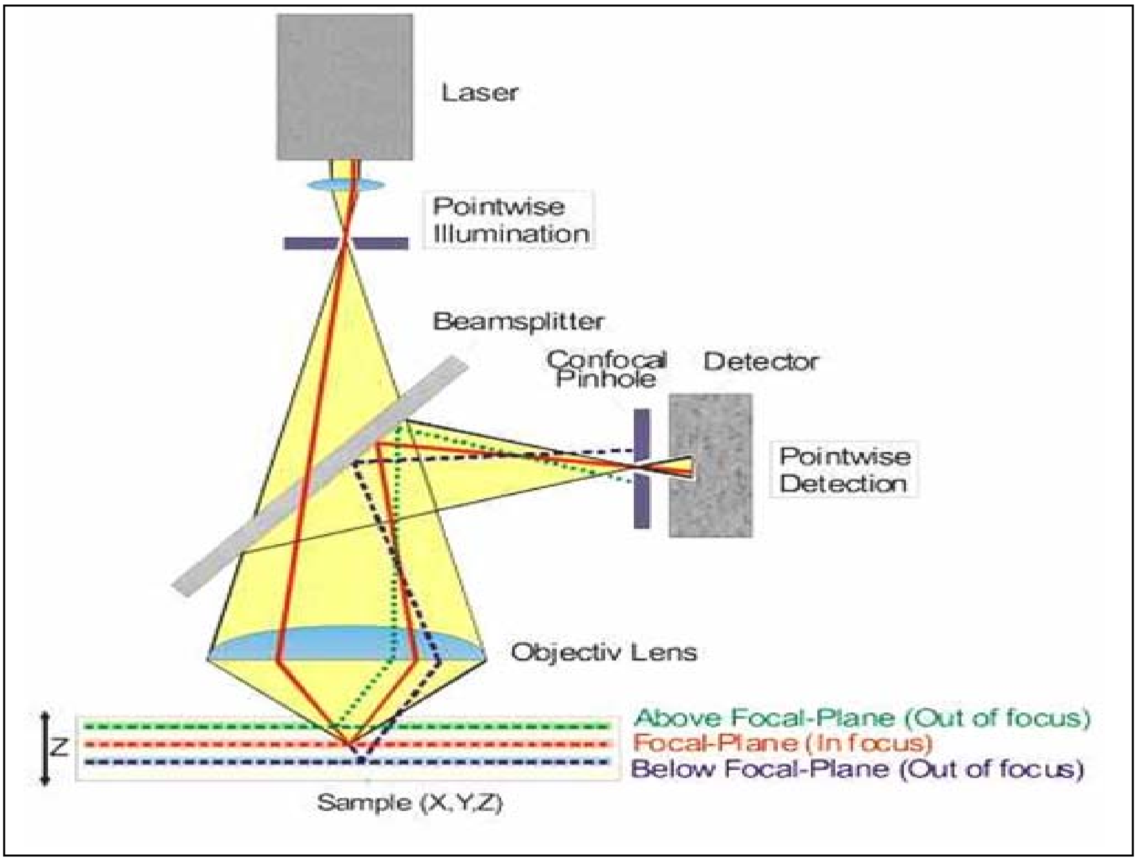
Laser
Pointwise Illumination
Beamsplitter
Confocal Pinhole
Detector
Pointwise Detection
Objectiv Lens
Z
Above Focal-Plane (Out of focus)
Focal-Plane (In focus)
Below Focal-Plane (Out of focus)
Sample (X,Y,Z)

Fig. 2.12: Schematic representation of the optical path of a confocal laser-scanning microscope

2.13 Calcium Imaging using Confocal Laser Scanning Microscope

High spatial resolution is a great advantage of calcium imaging with the CLSM. However, most of the commonly used fluorescent calcium dyes, e.g. Fura-2, are UV excitable and are not readily utilized with the majority of confocal microscopes. Moreover, the sequential line-by-line-scanning of the object makes the system slow. Usually one line of the object is scanned in about 2 ms and the whole object in about 0.5 to 1 s depending on the size of the selected scanning area. Thus, the signals received from two different points of the specimen are actually shifted in time. Higher temporal resolution can be achieved by skipping points or lines, or by decreasing the scanning area. However, this faster time resolution has to be paid for by loss of 2D-resolution. Nevertheless, CLSM perfectly fits to calcium imaging characterized by slow second-rate dynamics. In our study Ca^{2+} imaging of rhythmic and non rhythmic slices was done in a single XY-image plane. The stained region was monitored using (typically 8-10 cells) a 3x digital zoom with full frame acquisition (512x512 pixels) sufficient to detect 100% peak Ca^{2+} rises after drug modulation.

2.14 Two-Photon Imaging of Ca^{2+} and Mitochondrial Membrane Potential in Motoneuron and Glial Cells of Brain Stem Slices

In experiments performed at the Center for Neuroscience, Dept. of Physiology and Pediatrics, University of Alberta, Canada (Lab. Head Prof. Klaus Ballanyi), Ca^{2+} imaging and $\Delta\Psi m$ in respiratory MN and glial cells of brain stem slices was monitored using 2-photon microscopy. This approach allowed for a higher spatial resolution of cellular structures in the slice as compared to CCD camera imaging. Also advantageous was the fact that 2-photon microscopy restricts the excitation volume to the focus level (<1µm), so that no background fluorescence occurs.

In the experimental set-up used, the laser beam was provided by a titanium-saphir-laser system (Mira/Verdi; Coherent, Santa Clara, CA, USA), directed into a Bio-Rad MRC-600 scanning box with laboratory-built detection systems mounted on an Olympus FV500 upright microscope equipped with water immersion objectives (20x NA 0.95, Carsen Group, Markham, Ontario, Canada). The fluorescence emitted was filtered by a BG39 filter set (Chroma, Rockingham, VT, U.S.A.) and detected by a photomultiplier tube (Hamamatsu, Bridgewater, NJ, U.S.A.). In time series, dynamic changes were evaluated in defined ROIs using Olympus FluoView software.

2.15 Drug (Riluzole & Melatonin) Neuroprotection Study in ALS

To investigate the impact of riluzole and melatonin on vulnerable HMNs in mice, and cellular ALS model of WT-SOD1 as well as $SOD1^{G93A}$ transfected SH-SY5Y cells imaging experiments were performed on slices and on 2-3 days culture cells in medium where mitochondrial function was disturbed by either bath application of 2 mM sodium azide, which inhibits complex IV of the electron transport chain or by modulation and exposure of different drug cocktails which directly or indirectly disturb mitochondrial metabolism. Application of azide seemed to be useful, because i) both in sporadic and in familial forms of ALS, a frequent decrease in activity of complex IV of the mitochondrial electron transport chain has been observed (Menzies *et al.*, 2002; Wiedemann *et al.*, 2002) and ii) its action has been described as quick and reversible (Nowicky & Duchen, 1998; Müller *et al.*, 2002). Melatonin protection studies were also done in the same pattern like riluzole.

2.16 Materials

Caffeine	Sigma-Aldrich
Cyclopiazonic acid (CPA)	Sigma-Aldrich
D-MEM	Gibco, Scotland, UK
DMSO	Sigma-Aldrich
Ethanol	Merck, Darmstadt, De
FCCP (Carbonyl cyanide 4-triflurомethoxyphenylhydrazone)	Sigma-Aldrich
Fetus calf serum	Gibco, Scotland, UK
Fluo-4/AM	TEF Labs, Austin, TX
Fura-2/AM	Molecular Probes
Geneticin F-480	Gibco, Scotland, UK
Glutamate	ICN Biochemicals
Melatonin	Sigma-Aldrich
Oligomycin	Sigma-Aldrich
Paraffin (Paraplast)	Kendall, Mansfield, USA
PBS or TBS	Biochrom, Berlin, De
Penicillin	Sigma-Aldrich
Pluronic acid	Sigma-Aldrich

Riluzole	Sigma-Aldrich
Rhod-123	Molecular Probes
Rhod-2	Molecular Probes
RPMI 1640 (with Glutamate)	Gibco, Scotland, UK
Sodium chloride	Roche, Mannheim, De
Sodium cyanide	Sigma-Aldrich
Sodium Azide	Sigma-Aldrich
Streptomycin	Sigma-Aldrich

Medium and Buffer

RPMI-Medium	**D-MEM-Medium**
89% RPMI	42% D-MEM
10% FCS	42% HAM F-12
1% P/S	15% FCS
	1% P/S

Stock solutions of chemicals were prepared as follows: FCCP was dissolved in ethanol, CPA in DMSO, and sodium cyanide, azide was dissolved in distilled water. The corresponding drug was then included in the bath solution and bubbled with 95% O2, 5% CO2, at room temperature, before and during the experiments. Fluo-4/AM dye used for injection and loading as well as Fura-2 AM and Rhod-2 used for loading was dissolved in DMSO + 20% pluronic acid (Pluronic F-127) to a concentration of 1mM. Rhodamine-123 was dissolved in ethanol (10mg/ml). Riluzole and melatonin were dissolved in ethanol (10 mg/ml and 10mM, respectively). Oligomycin was dissolved in DMSO (5 mg/ml). Caffeine and glutamate were dissolved in distilled water.

2.17 Analysis

Each brain stem slice was used for a single experiment, indicating one cell per slice in patch clamp experiments, and more than one cell in Fura-2/AM, Fluo-4/AM, Rhod-2 and Rhod 123 imaging experiments for injection and incubation (Bath Loading). For Ca^{2+} buffering capacity studies in MNs many cells were imaged from singe glass cover slips after 2–5 days in culture. All results are expressed as mean ± standard deviation of the mean except Ca^{2+} buffering and MNs-glia experiment where results are expressed as mean ± standard error of mean, and represent a minimum of 4±1 imaging experiments for 4±1 separate slices. If not indicated otherwise, values in the text are given as mean ± standard deviation (S.D.); error bars in Fig. represent S.D. too. The significance after pharmacological intervention was calculated using Student's *t* test and one-way anova. For noise elimination five point smoothing was perform on simultaneous $[Ca^{2+}]_i$ and $[Ca^{2+}]$m fluorescent measurement.

Further analysis was performed off-line using IGOR software (Wavemetrics, Lake Oswego, OR, USA). The area under the time-concentration curve (AUC) was calculated with the baseline 0 by the equation: $In[Ca]it = {}_{\mathbf{t1}}\int^{\mathbf{t2}} [Ca]i.dt$ with the help of Origin software, version 7.5.

$$\boxed{In[Ca^{2+}]it = {}_{\mathbf{t1}}\int^{\mathbf{t2}} [Ca^{2+}]i.dt}$$

Where, In = Fluorescence intensity under the time-concentration curve,

[Ca]i = Cytosolic calcium,

t = Time

3. Results

PART A

3.1 Role of Mitochondria and Calcium Signaling in motoneurons

Over the past decade, there has been an increased understanding of local interactions between Ca^{2+} and its target signaling pathways. In particular, an impaired interaction between calcium signaling and mitochondrial processes has been identified as one cellular factor contributing to neurodegenerative mechanisms like those found in motoneuron diseases. Hence, understanding the functions of Ca^{2+} signaling and mitochondria mediated toxicity is crucial and of great importance. In addition, previous studies also indicate the importance of calcium and mitochondria for physiological processes in motoneurons (Bergmann & Keller, 2004, Von Lewinski & Keller, 2005), including control of electrical excitability. An attractive way to investigate motoneuron (MN) function under physiological and pathophysiological conditions is to perform whole cell patch clamp recordings and simultaneously monitor cytosolic signal pathways by fluorescence microscopy (Ladewig & Keller, 2000). Unfortunately, the application of the patch clamp technique to isolated brain stem slice preparations from adult mice is exceptionally difficult and therefore it is important to also employ alternative technical approaches. Accordingly, we monitored the function of individual motoneurons by using optical techniques including CCD imaging, confocal laser microscopy (CLM) and multiphoton measurements (MPM). More specifically, we focused our analysis on two types of animals, wild type and transgenic mice ($SOD1^{G93A}$), which are accepted as mouse models of human motoneuron diseases (see Introduction, Rosen *et al*., 1993; Gurney *et al*., 1994). Moreover, the WT and $SOD1^{G93A}$ animals were further sub divided on the basis of age, either as juvenile (8 to 9 weeks) or adult (14 to 15 weeks). While all animals investigated showed a normal motor behaviour in the juvenile state, adult $SOD1^{G93A}$, but not WT animals displayed clear signs of degenerative motor impairment. Accordingly, juvenile and adult $SOD1^{G93A}$ animals were noted as pre-symptomatic and symptomatic, respectively.

An attractive way to monitor the interaction between mitochondria and calcium signaling pathways is to measure the mitochondrial electorchemical potential $\Delta\Psi m$ (Mostafapour *et al*., 1997). In particular, Rhod 123 has been established as a valuable fluorescent indicator of ΔΨm both in cell culture and slice preparations (see Methods, Schuchmann *et al*., 2000; Koväcs *et al*., 2005). Rhod 123 is a positively charged membrane-permeant fluorescent dye that crosses the plasma membrane of cells and accumulates in mitochondria in response to the standing electrochemical potential gradient. When mitochondria depolarizes, the dye redistributes to the cytoplasm where it is dequenched. This is observed as a reliable increase in the fluorescence signal that can be monitored by microscopic analysis.

3.1.1 Pharmacological manipulation of mitochondria in motoneurons by the mitochondrial uncoupler FCCP

To measure ΔΨm in brain stem slices, MNs were loaded with 5µg/ml Rhod 123 and the corresponding fluorescence changes were monitored in hypoglossal motoneurons (HMNs) of WT and SOD1^{G93A} mice using videomicroscopic fluoroscopy. Photomicrographs of confocal laser scanning and CCD camera images of Rhod 123 loaded slices of rat (P1) and mice (WT and SOD1^{G93A}) are shown in Fig. 3.1.1a. Fig. 3.1.1a, (A) displays acute rat brain stem slice (P1; 400 µm thick) seen in transmitted light under 4x and 20x magnification (B). The dashed line surrounds the hypoglossal nucleus paramedian, ventral of the central channel. Fig. 3.1.1a (C) shows acute rat brain stem slice seen under 4x and (D) 20x in Rhod 123 fluorescence light with 3x zoom magnification. The white arrows point to HMNs whereas red arrows point to glial cells. As shown in Fig. 3.1.1a, (E) and (F) shows CCD camera image of Rhod 123 stained mouse brain stem slice of pre-symptomatic (8-9 week juvenile mice) in WT and SOD1^{G93A}, respectively whereas Fig. 3.1.1a (G) and (H) shows CCD camera image of Rhod 123 stained adult mouse brain stem slice of 14-15 week adult mice in WT and SOD1^{G93A}, respectively. Slice thickness from (E)-(H) is 200 µm.

To investigate the functional interplay between mitochondria and cytosolic calcium signaling, specific and rapidly acting pharmacological tools can be utilized. In this context, FCCP is widely used as a mitochondrial “uncoupler” that depolarizes the electrochemical potential by creating an ionic pore across the inner mitochondrial membrane (Billups *et al*., 2002; Duchen *et al*., 2003; Vergun *et al*., 2003). More specifically, FCCP is a lipophilic weak acid and therefore readily passes through surrounding cellular membranes. Besides disrupting ΔΨm, it has been shown to abolish mitochondria-mediated calcium regulation and to cause the release of stored [Ca^{2+}]$_i$ from mitochondria (Kanno *et al.*, 2002; Feeney *et al.*, 2003; Wyatt & Buckler, 2004; Jaiswal *et al*., 2005).

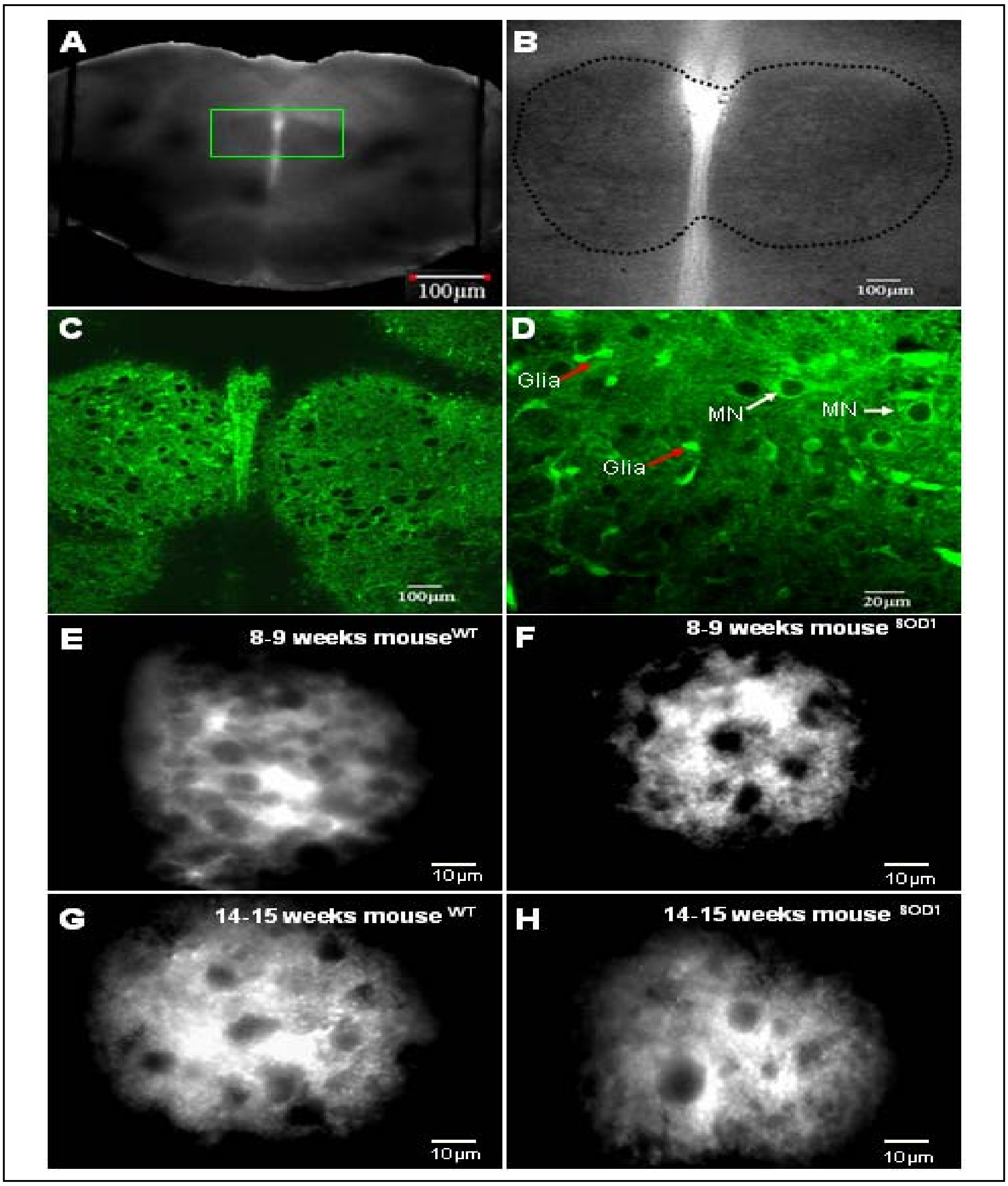
A
100µm
B
100µm
C
100µm
D
Glia
MN
MN
Glia
20µm
E
8-9 weeks mouse WT
10µm
F
8-9 weeks mouse SOD1
10µm
G
14-15 weeks mouse WT
10µm
H
14-15 weeks mouse SOD1
10µm

Fig. 3.1.1a: Confocal laser scanning and CCD camera photomicrographs of Rhod 123 loaded brain stem slices of neonatal rat (P1) and mouse (WT and SOD1^{G93A}) in 8-9 weeks (juvenile) and 14-15 weeks (adult) mice. (A) Acute rat brain stem slice (P1; 400 µm thick) seen in transmitted light under 4x and (B) 20x magnification. The dashed line surrounds the hypoglossal nucleus paramedian, ventral of the central channel. (C) Acute rat brain stem slice seen under 4x and (D) 20x in fluorescence light with 3x zoom magnification. The white arrows point to HMNs whereas red arrows point to glial cells. (E) CCD camera image of Rhod 123 stained WT mouse brain stem slice of 8-9 week juvenile mice. (F) Rhod 123 stained SOD1^{G93A} mouse brain stem slice in pre-symptomatic stage (8-9 week juvenile mice). (G) CCD camera image of Rhod 123 stained WT adult mouse brain stem slice of 14-15 week adult mice. (F) Rhod 123 stained SOD1^{G93A} adult mice brain stem slice at symptomatic stage (14-15 week adult mice) of motor dysfunction. Slice thickness of brain stem slice from (A) to (D) is 400 µm and in (E) to (H) is 200 µm.

Fig. 3.1.1b displays Rhod 123 fluorescence signal after application of 2 μM FCCP to brain stem slice preparations from different genotypes and age groups. In juvenile animals, hypoglossal motoneurons display a normalized fluorescence of 0.4546 ± 0.0391 (F/F0) for WT and 0.4274 ± 0.0573 (F/F0) for SOD1^{G93A} mice, respectively (Fig. 3.1.1b A and B). Essentially, there are no significant differences in juvenile WT and SOD1^{G93A} littermates. However, fluorescence responses in adult WT animals were almost ~3 fold higher compared to SOD1^{G93A} littermates (0.3357 ± 0.0352 for WT and 0.1106 ± 0.0406 for SOD1^{G93A}, ~3.0353 fold larger, **P<0.001, Fig. 3.1.1b C and D). Fig. 3.1.1b (E) Represents the bar diagram of average mean FCCP induced mitochondrial depolarization in HMNs of WT (n= 15, and 19) and SOD1^{G93A} (n= 13, and 17) mice in 8-9 weeks juvenile and 14-15 weeks adult animals. Data shown represents at least 3 separate experiment (N=3) for each condition, separately in WT and SOD1^{G93A} mice, respectively. These observations already indicate that mitochondria are significantly disturbed in symptomatic SOD1^{G93A} mice.

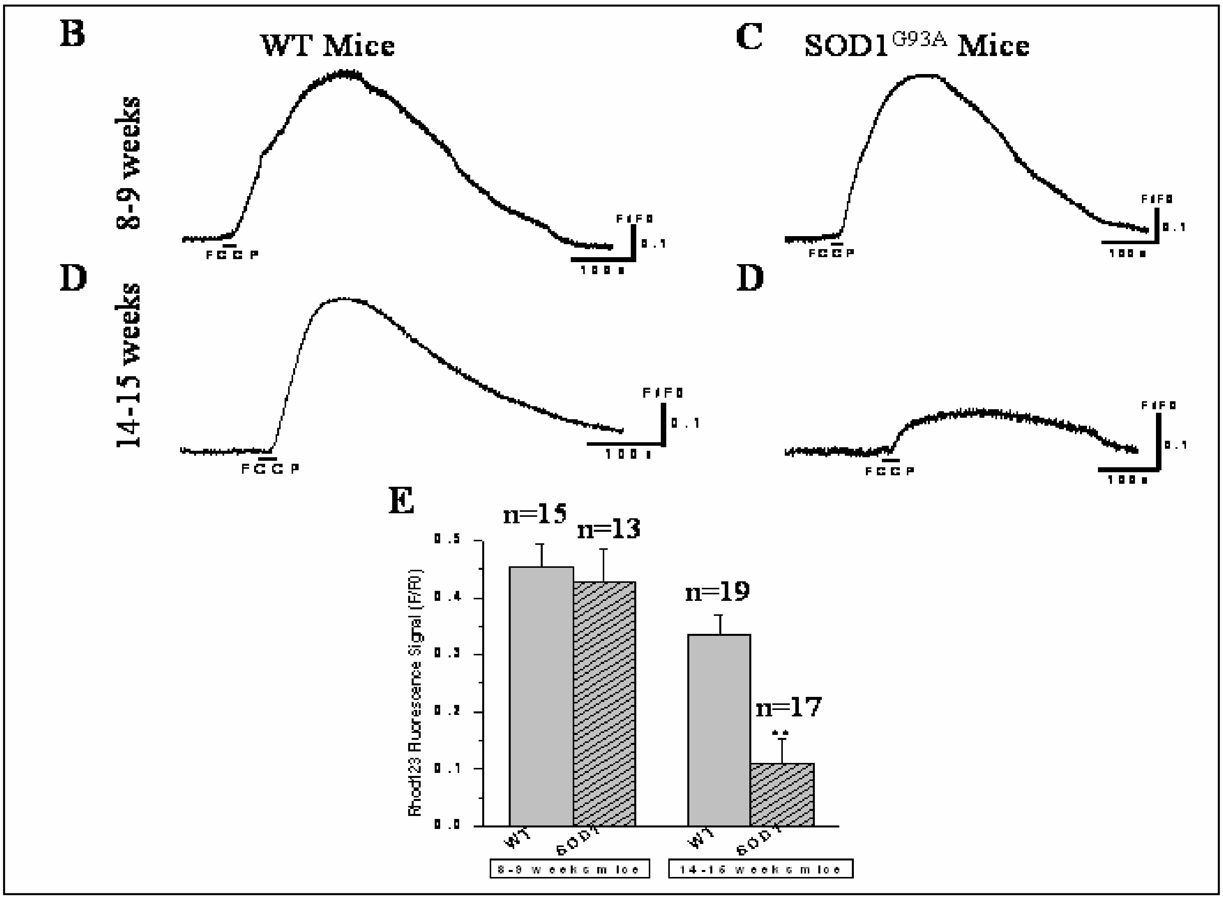

Fig. 3.1.1b: FCCP induced mitochondrial depolarization in HMNs of WT and SOD1^{G93A} mice brain stem slices at 8-9 weeks juvenile and 14-15 weeks adult animals. Cells were loaded with Rhod 123 (5μg/ml) and superfused with artificial cerebrospinal fluid (aCSF). 2μM FCCP was added to the superfusate for 20 seconds (indicated by the black bar), which quickly released the dye quenched by mitochondria thereby depolarization of (A) HMNs of 8-9 weeks juvenile WT and corresponding (B) pre-symptomatic SOD1^{G93A} mice, (C) HMNs of 14-15 weeks adult WT and corresponding littermate of

(D) symptomatic SOD1^{G93A} mice. Data shown represents a single cell from the brain stem slice imaged. Rhod 123 fluorescence signals are represented as normalized (F/F0) values. (E) Bar diagram of FCCP induced mitochondrial depolarization in HMNs of WT (n= 15 and 19) and SOD1^{G93A} (n= 13 and 17) mice in 8-9 weeks juvenile and 14-15 weeks adult animals, respectively. Data shown represents at least 3 separate experiments (N=3) for each condition. Note that in adult symptomatic SOD1^{G93A} mice HMNs mitochondrial disruption by FCCP and thereby Rhod 23 depolarisation signals are quite weak compared to adult WT mice. Rhod 123 depolarization signals in juvenile WT and SOD1^{G93A} littermates are comparable. Data are expressed as means ± S.D.; N= Number of experiments; n=Number of cells. $^{**}P<0.001$.

3.1.2 Pharmacological manipulation of mitochondria in motoneurons by blocking the F_1, F_0-ATP synthase

The ATP synthases (F_1, F_0-ATPases) are multisubunit complexes in the thylakoid membranes of chloroplasts and the inner membranes of mitochondria. ATP synthase is massive protein complexes which resemble a ball on a stick consisting of two main structural domains. The globular catalytic domain known as F_1 and a proton-translocating membrane-embedded domain F_0 are linked by central and peripheral stalks (subunits b, d and F_6) and OSCP (oligomycin sensitivity conferral protein; Gledhill & Walker, 2005, 2006). The F_0 consists six proteins of two different kinds (three α subunits and three β subunits). The F_1 consists of one protein: the γ subunit, which is long and extends throughout the α and β subunits. Both the α and β subunits bind nucleotides, but only the β subunits participate in the ADP phosphorylation reaction. As protons cross the membrane through the base of ATP synthase, the central stem (the subunit) rotates inside the α and β subunits. This movement of the α and β subunits causes their activation and thus the production of ATP (Dimroth *et al*., 2006).

$$ADP^{3+} + HPO_4^{2-} + H^+ \Leftrightarrow ATP^{4-} + H_2O$$

It is proposed that oligomycin inhibits F_1, F_0-ATPase activity by causing a conformational change in the F_0 portion of the complex that is transmitted to F_1, resulting in an impaired binding of the substrate in the catalytic sites (Inhibits ATP synthase by preventing it to pump protons, thus preventing it to generate ATP from ADP and Pi by using the energy of the proton gradient). These observations of apparent conformational interactions between F_0 and F_1 on the mitochondrial membrane are relevant to the mechanism of the coupling device that links the energy store to ATP formation in oxidative phosphorylation (Stock *et al*., 1999).

To measure the impact of oligomycin (5µg/ml) on ΔΨm responses, the brain stem slices were loaded with Rhod 123 and the corresponding fluorescence changes were monitored in juvenile and adult animals. Similar but very weak effects to those observed with the electron transport inhibitors (CN^-; Bergmann & Keller, 2004) were seen with oligomycin. As shown in Fig. 3.1.2, in juvenile animals, oligomycin's impact on the normalized peak of Rhod 123 fluorescence on ΔΨm was 0.0475 ± 0.0156 and 0.0506 ± 0.0168 for WT and corresponding $SOD1^{G93A}$ littermates, respectively (N=2, n=12, Fig. 3.1.2A and B). Furthermore, in adult animals normalized Rhod 123 fluorescence signals after oligomycin application were 0.0669 ± 0.0271 and 0.0526 ± 0.0270 for WT and $SOD1^{G93A}$ littermates, respectively (N=3, n=18, $^*P<0.05$; Fig. 3.1.2C, D and E).

Basically, there is no significant difference either between juvenile or adult WT and $SOD1^{G93A}$ littermates. These results indicate that in contrast to FCCP, blockade of the mitochondrial F_1, F_0-ATP synthase by oligomycin has only a minor contribution to the responses of ΔΨm both in juvenile as well as adult animals without discrimination of genotypes and age groups. It was also noted that occurrence of the reverse in a F_1, F_0-ATP synthase futile cycle or restoration of ΔΨm (Budd & Nicholls, 1996a, b) was very rare and more likely to occur in 14-15 weeks adult $SOD1^{G93A}$ mice since a slightly higher Rhod 123 fluorescence in adults was observed compared to juvenile $SOD1^{G93A}$ mice (Fig. 3.1.2E). This could be due to several factors including aging, vulnerable MNs and the slow activity of the mitochondrial Na^+/Ca^{2+} exchanger.

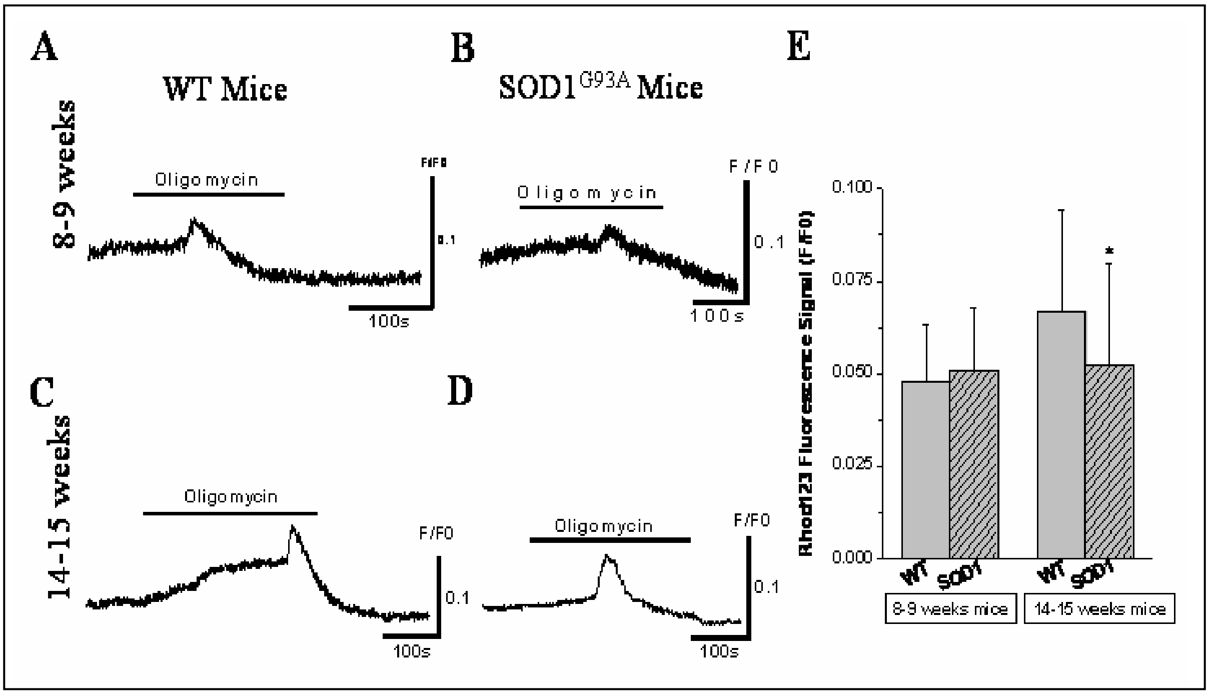

Fig. 3.1.2: Measurement of ΔΨm in brain stem slices incubated with oligomycin to inhibit F_1, F_0-ATP synthase and thereby deplete Ca^{2+} content. Application of 5µg/ml oligomycin causes measurable Rhod

123 fluorescence changes (ΔΨm) not only in HMNs of 8-9 weeks juvenile WT (A, N=2, n=12,) and corresponding SOD1^{G93A} (B, N=2, n=12) animals, but also in 14-15 weeks adult WT (C, N=3, n=18) and corresponding symptomatic SOD1^{G93A} (D, N=3, n=18) animals. Data shown represents a single cell from the slice imaged. Rhod 123 fluorescence signals are represented as F/F0. Comparison of the peak amplitude of changes in Rhod 123 fluorescence signals (ΔΨm) in WT and corresponding SOD1^{G93A} mice at pre-symptomatic and symptomatic stage of motor dysfunction is presented in E. Data shown represents at least 2 separate experiments (N=2) for 8-9 weeks juvenile mice and 3 separate experiments (N=3) for 14-15 weeks adult mice for each genotype. Data are expressed as means ± S.D.; N= Number of experiments; n=Number of cells. **P*<0.05.

3.1.3 Impact of plasma membrane depolarisation on mitochondrial function

To determine the comparative efficiency of mitochondria upon depolarisation and its influence on FCCP evoked ΔΨm responses, juvenile and adult animal’s hypoglossal MNs of brain stem slices were challenged by 2µM FCCP for 4 min after a 30mM K^+ depolarization stimulus (30s).

30mM K^+ stimulation for 30s evokes a prominent depolarization induced mitochondrial signal. Fig. 3.1.3 shows Rhod 123 fluorescence amplitude peaks upon 2µM FCCP evoked ΔΨm responses after 30mM K^+ depolarization of the brain stem slice preparations from different genotypes and age groups. In juvenile animals, the normalized mean peak fluorescence of HMNs was 0.4123 ± 0.1104 and 0.3343 ± 0.0323 for WT (N=3, n=17, Fig. 3.1.3A and E) and corresponding SOD1^{G93A} littermates, respectively (N=3, n=18, Fig. 3.1.3B and E; **P*<0.05). Small differences in normalized mean peak Rhod 123 fluorescence (**P*<0.05) indicates that the impact of plasma membrane depolarization on mitochondrial function is negligible in juvenile WT and SOD1^{G93A} littermates. However, in adult WT animals, responses were almost ~2.62 fold higher compared to SOD1^{G93A} littermates (0.3288 ± 0.0928 for WT and 0.1251 ± 0.0421 for SOD1^{G93A}, ~2.62 fold higher in WT, **P<0.001, Students’s t test, N=3, n=24, Fig. 3.1.3C, D and E). Following previous trends there is a very small difference in ΔΨm responses in 8-9 weeks juvenile WT and SOD1^{G93A} mice. However, exposure to FCCP after depolarizing stimulus (30mM K^+) showed significant differences in ΔΨm responses of adult WT and symptomatic SOD1^{G93A} littermates (~2.62 fold higher in WT, ***P*<0.001, Student’s t test) at late stage of motor dysfunction. These observations further indicate that mitochondria are significantly disturbed in symptomatic SOD1^{G93A} mice.

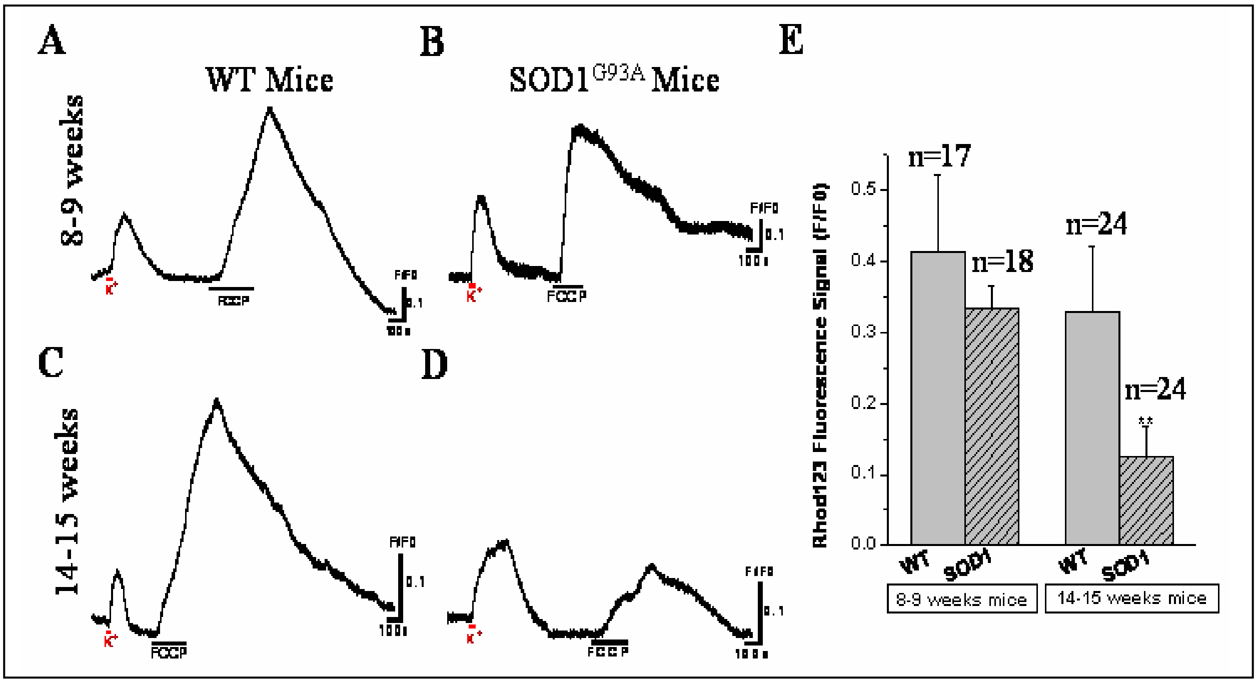

Fig. 3.1.3: K^+ induced plasma membrane depolarisation and its impact on FCCP evoked responses of mitochondrial depolarization in HMNs of WT and corresponding SOD1^{G93A} mice in 8-9 weeks juvenile and 14-15 weeks adult animals. Cells were loaded with Rhod 123 (5µg/ml) and superfused with aCSF. 2µM FCCP was added to the superfusate (indicated by the black bar), after the depolarization of HMNs by 30mM K^+ which quickly released the dye quenched by mitochondria (A) HMNs of juvenile WT and corresponding littermates of (B) pre-symptomatic SOD1^{G93A} mice or (C) HMNs of adult WT and corresponding littermates of (D) symptomatic SOD1^{G93A} mice. Data shown represents a single cell from the brain stem slice imaged. Rhod 123 fluorescence signals are represented as F/F0. (E) A bar diagram of FCCP induced mitochondrial depolarization after the depolarization of cells plasma membrane by 30mM K^+ in HMNs of WT (n= 17 and 24) and corresponding SOD1^{G93A} mice (n= 18 and 24) in juvenile and adult animals. Data shown represents at least 3 independent experiments (N=3) for each genotype. Data are expressed as means ± S.D.; N= Number of experiments; n=Number of cells; $^{**}P<0.001$.

3.1.4 Impact of plasma membrane depolarisation and inhibition of F_1, F_0-ATP synthase on FCCP evoked responses of the $\Delta\Psi m$ in brain stem slices of juvenile and adult mice

In addition to releasing various proapoptotic and toxic substances into the cytosol, mitochondrial membrane permeabilization has the potential to compromise oxidative phosphorylation. Under normal circumstances, cytochrome c is responsible for carrying electrons between the b-c_1 complex and the cytochrome oxidase complex of the electron transport chain. Cytochrome c oxidase accepts electrons from cytochrome c and reduces oxygen to water. This process also generates the proton gradient across the inner mitochondrial membrane ($\Delta\Psi m$) which powers the F_1, F_0-ATPase. Therefore, loss of cytochrome c leads to a buildup of redox equivalents in the electron transport chain, with generation of ROS, and eventual dissipation of the inner membrane potential (ΔΨm), which in turn interferes with the ability of the mitochondria to generate ATP.

Impairment of ΔΨm with FCCP, blocks oxidative phosphorylation and in this state, glycolysis provides the primary means of ATP synthesis. The mitochondrial $F_{1,}$ F_0-ATP synthase may reverse in a futile cycle that attempts to restore ΔΨm when depolarized with FCCP, further depleting the ATP produced via glycolysis (Budd and Nicholls, 1996a, b). Oligomycin (5µg/ml), a specific blocker of mitochondrial F_1, F_0-ATP synthase, was added together with FCCP to prevent any accelerated consumption of cellular ATP by the reverse mode of operation of the ATP synthase (Budd & Nicholls, 1996; Babcock *et al.*, 1997; David *et al.*, 1998). In the following experiments (Fig. 3.1.4) after plasma membrane depolarization (30mM K^+), mitochondrial membrane was permeabilized in the presence of FCCP and oligomycin. In juvenile animals, hypoglossal motoneurons display a normalized Rhod 123 fluorescence of 0.7493 ± 0.0927 (F/F0) in WT (N=2, n=10, Fig. 3.1.4A; Table 1) and 0.5501 ± 0.1903 (F/F0) in SOD1^{G93A} (N=2, n=12, Fig. 3.1.4B; Table 1, *$P<0.05$) mice, respectively. The impact of oligomycin on peak amplitude of Rhod 123 fluorescence was nominal in juvenile mice and there is no significant difference between WT and SOD1^{G93A} mice (0.0256 ± 0.0096 in WT and 0.0234 ± 0.0085 in SOD1^{G93A}; Table 1). However, responses of FCCP together with oligomycin in adult WT (N=3, n=21, Fig. 3.1.4C and E; Table 1) animals were almost ~2.29 fold higher compared to SOD1^{G93A} (N=3, n=17, Fig 3.1.4D and E; Table 1) littermates (0.3252 ± 0.0600 in WT and 0.1416 ± 0.0316 in SOD1^{G93A}, ~2.29 fold higher in WT, **$P<0.001$). Comparative details of normalized Rhod 123 fluorescence signals in juvenile and adult animals are summarised in Table 1.

Rhod 123 Fluorescence Unit (F/F0)		**8-9 weeks mice**		**14-15 weeks mice**	
		WT	SOD1^{G93A}	WT	SOD1^{G93A*}
Peak Amplitude	Oligomycin	0.0256 ± 0.0096	0.0234 ± 0.0085	0.0333 ± 0.0130	0.0312 ± 0.0149
	FCCP+ Oligomycin	0.7493 ± 0.0927	0.5501 ± 0.1903	0.3252 ± 0.0600	0.1416 ± 0.0316*

Table 1: Impact of plasma membrane depolarisation and inhibition of F_1, F_0-ATP synthase on FCCP evoked responses of the Rhod 123 fluorescence signals (ΔΨm) in juvenile (8-9 weeks) and adult (14-15 weeks) WT and SOD1^{G93A} mice brain stem slices are summarised as normalized peak amplitudes (F/F0). *Significantly different from WT.

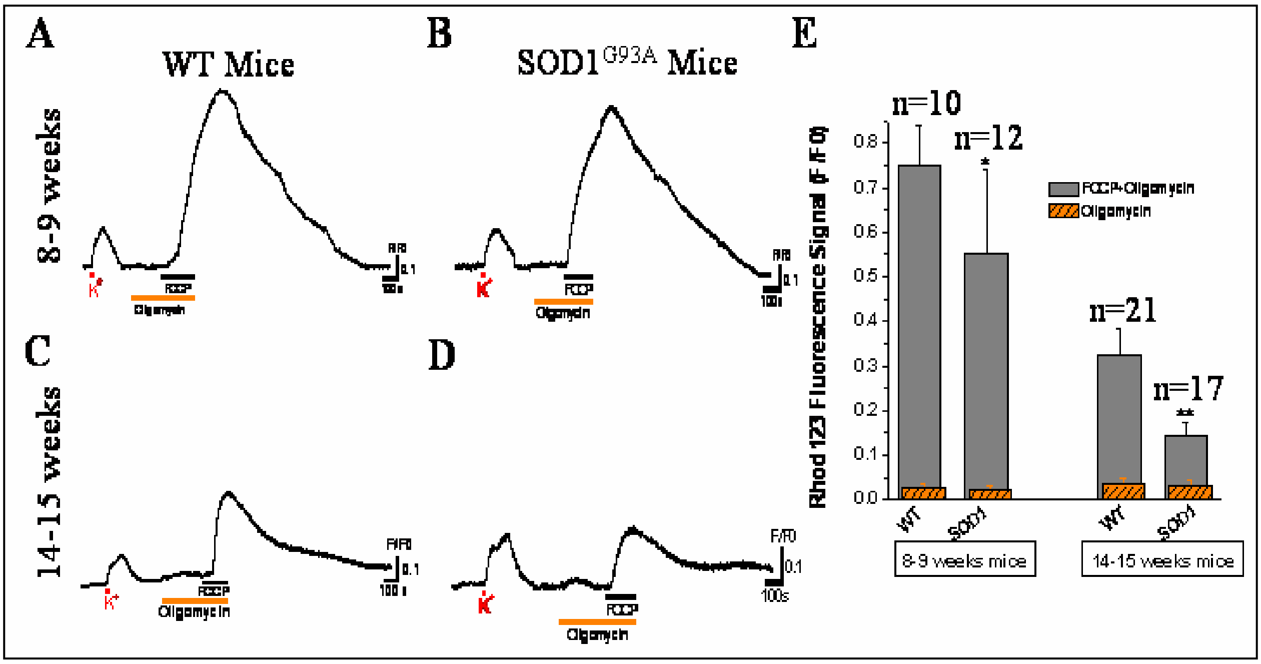

Fig. 3.1.4: Impact of plasma membrane depolarisation and inhibition of F_1, F_0-ATP synthase on FCCP evoked responses of the ΔΨm in brain stem slices of juvenile (8-9 weeks) and adult (14-15 weeks) mice. Rhod 123 fluorescence signals after stimulation-evoked ΔΨm before and after application of oligomycin and FCCP in juvenile WT (A) and SOD1^{G93A} (B) mice were shown. The stimulation-evoked responses are sown in adult WT (C) and corresponding symptomatic SOD1^{G93A} (D) mice. The horizontal red bars, orange bars and black bars indicate duration of K^+ induced plasma membrane depolarisation, stimulation with oligomycin and FCCP, respectively. (E) A graphical representation of the effect of oligomycin and oligomycin together with FCCP on ΔΨm in 8-9 weeks (N=2) and 14-15 weeks (N=3) WT (n=10 and 21) and corresponding SOD1^{G93A} (n=12 and 17) mice. Note that ΔΨm is not significantly affected by oligomycin alone either in 8-9 weeks WT and corresponding SOD1^{G93A} or in 14-15 weeks WT and corresponding symptomatic SOD1^{G93A} mice. FCCP shows a great elevation in Rhod 123 fluorescence signal which was significantly diminished in symptomatic SOD1^{G93A} mice (**$P<0.001$) compared to WT littermates (~2.26 fold higher). Small differences in Rhod 123 fluorescence signals of 8-9 weeks mice of WT and pre-symptomatic SOD1^{G93A} mice littermates (*$P<0.05$) were also noted. Data are expressed as means ± S.D.; N= Number of experiments, n=Number of cells.

Consistent with previous observations (Babcock *et al.*, 1997; Ladewig *et al.*, 2003; Bergmann & Keller 2004; Jaiswal *et al.*, 2006), FCCP induced an increase in peak Rhod 123 fluorescence signals of variable size and duration in brain stem slice preparations from different mice genotypes and age groups apparently reflecting a collapse of mitochondria to a greater extent. This effect is clearly attributable to FCCP, because oligomycin alone did not affect resting normalized Rhod 123 fluorescence signal peak (ΔΨm) within the first 5-7 minutes of application (Fig. 3.1.3 and Fig. 3.1.4). Further experiments suggest that in adult animals, FCCP together with oligomycin fails to generate a similar high Rhod 123 peak fluorescence signal (ΔΨm) in SOD1^{G93A} mice compared to WT littermates. This further strengthens the hypothesis that mitochondria in SOD1^{G93A} mice are selectively vulnerable during late stage of motor dysfunction.

3.1.5 Measurement of Ca^{2+}-release responses in motoneurons

The aim of this study was to test the role of mitochondria as a Ca^{2+} buffer in juvenile and adult mice brain stem slice preparations of WT and SOD1^{G93A} animals under physiological conditions. Accordingly, Fura-2 AM loading protocol was established, which allows measurement of intracellular Ca^{2+} in MNs in brain stem slices without disturbing intracellular structures which generally occurs during patch-clamp recordings. This is advantageous since besides protecting against “wash-out” and rupturing of intracellular structures, the AM loading protocol allows also to the specific stereotaxic and anatomical plane of the brain stem slices that protect it from mechanical aberration and substantially preserve a large fraction of hypoglossal nerve and neuronal network. Cell permeabilization and fluorescence measurements were conducted as previously described in materials and methods section. Changes in Ca^{2+} concentrations in MNs were reported as ratiometric (360/390 nm) normalized F/F$_0$.

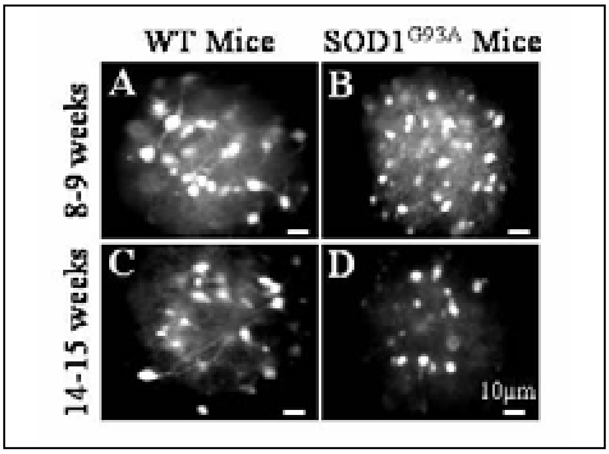

Fig. 3.1.5: CCD camera photomicrographs of Fura-2 AM loaded brain stem slices (200 µm thick) in juvenile (8-9 weeks; A and B) and adult (14-15 weeks; C and D) WT (A and C) and SOD1^{G93A} mice (B and D). Scale bar 10 µm.

Given previous studies which report FCCP not only to inhibit uptake of Ca^{2+} into mitochondria but also to cause a release of pooled Ca^{2+} (Bergmann & Keller, 2004; Herrington *et al.*, 1996), FCCP was used in this study as a pharmacological tool to investigate the functional interplay between mitochondria and cytosolic calcium signaling in MNs. To analyze the possible contribution of the mitochondria as a Ca^{2+} storing organelle and its role in motor dysfunction, brain stem slices were stained with Fura-2/AM dye (Fig. 3.1.5) and $[Ca^{2+}]_i$ was monitored by the ratiometric Ca^{2+}-independent/dependent fluorescence ratio of Fura-2/AM (360/390 nm).

3.1.6 FCCP causes differential calcium release and Ca^{2+} transients in brain stem slices of juvenile and adult WT and S0D1^{G93A} mice

Blocking the mitochondrial calcium uptake by application of 2µM FCCP for ~5 min produced contrasting effects on the $[Ca^{2+}]$i transient and decay time constant (τ) of ALS vulnerable or resistant MNs (Balakrishnan & Keller, unpublished data). It was found that in HMNs and FMNs presence of FCCP significantly delayed the τ. Here, experiments were performed on brain stem slices of juvenile and adult WT and SOD1^{G93A} mice. There is no significant difference in 2µM FCCP evoked increase in $[Ca^{2+}]$i between juvenile WT and SOD1^{G93A} mice brain stem slices, where the normalized peak fluorescence amplitude (F/F0) after 2µM FCCP exposure was 0.1391 ± 0.0598 and 0.1244 ± 0.0535 for WT and SOD1^{G93A} (N=3, n=14; Fig. 3.1.6A and B) littermates, respectively. The kinetics of Ca^{2+} recovery in MNs from WT and SOD1^{G93A} genotypes is also similar in juvenile mice. However, in adult mice brain stem slices, FCCP evoked increase in $[Ca^{2+}]$i was 0.1166 ± 0.0424 and 0.0533 ± 0.0316 for WT (N=3, n=24; Fig. 3.1.6C) and symptomatic SOD1^{G93A} mice (N=3, n=21; Fig. 3.1.6D) littermates, respectively. Average Mean peak fluorescence intensity is summarised in Fig. 3.1.6E.

AS Shown in Fig. 3.1.6, there is no significant difference between WT and SOD1^{G93A} mice (0.1391 ± 0.0598 in WT and 0.1244 ± 0.0535 in SOD1^{G93A}, Fig. 3.1.6A and B). Furthermore, as evident from Fig. 3.1.6, FCCP evoked mitochondrial Ca^{2+} release responses (normalised) in WT adults mice is greater in amplitude and substantially more prominent than corresponding SOD1^{G93A} mice littermates (~2.18 times greater in WT, $^{**}P<0.001$, Student’s t test). These data indicate that the processes responsible for the release of $[Ca^{2+}]$i are qualitatively different (Fig. 3.1.6C and D) in adult WT and SOD1^{G93A} mice. The main difference in the mitochondrial function of adult WT and SOD1^{G93A} mice is their capability in MNs to accumulate extremely rapidly a large amount of Ca^{2+} in WT compared to delayed accumulation of much smaller amounts in SOD1^{G93A}. This supports the model that mitochondrial Ca^{2+} homeostasis is significantly altered in SOD1^{G93A} mice at the symptomatic stage of motor dysfunction.

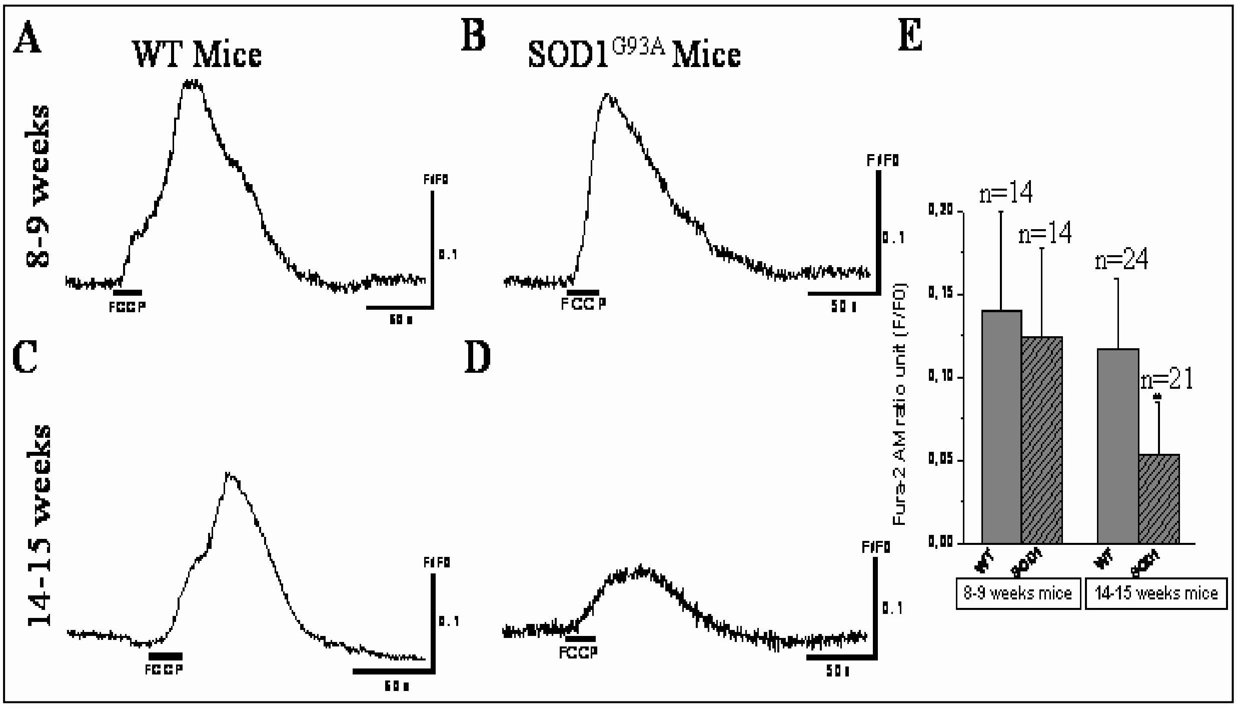

Fig. 3.1.6: Monitoring the impact of FCCP on differential [Ca^{2+}]i release in juvenile (8-9 weeks) and adult (14-15 weeks) WT and $SOD1^{G93A}$ mice. MNs were loaded with fura-2 AM (10µM) and superfused with aCSF. 2µM FCCP was added to the superfusate for 20 seconds (indicated by the black bar), which quickly facilitates cytosolic Ca^{2+} release in (A) HMNs of juvenile WT and (B) $SOD1^{G93A}$ mice or in (C) HMNs of adult WT and (D) $SOD1^{G93A}$ mice. Data shown represents a single cell from the slice imaged. (E), A Bar diagram of FCCP induced cytosolic Ca^{2+} release in HMNs of WT (n= 14 for juvenile and 24 for adult) and corresponding $SOD1^{G93A}$ (n= 14 for juvenile and 21 for adult) mice in juvenile and adult brain stem slices. Fura-2 AM fluorescence signal ratio units are represented as F/F0. Data shown represents at least 3 independent experiments (N=3) for each genotype. Data are expressed as means ± S.D.; N= Number of experiments; n=Number of cells. $^{**}P<0.001$.

3.1.7 Impact of plasma membrane depolarisation on mitochondrial Ca^{2+} uptake and [Ca^{2+}]i release in brain stem slices of juvenile and adult WT and $S0D1^{G93A}$ mice

The following pathways are responsible for the removal of Ca^{2+} ions from the cytosol: (i) accumulation by mitochondria, (ii) sequestration in the intracellular calcium-stores of the ER, and (iii) Ca^{2+} extrusion into the extracellular space by plasmalemmal Ca^{2+} pumps and/or Ca^{2+} exchangers (Pivovarova *et al.*, 1999). Participation of all three of the mentioned pathways in formation of the Ca^{2+} signal could be directly confirmed in this study by utilizing different protocols in juvenile and adult WT and $SOD1^{G93A}$ animals. To analyze the comparative efficiency of mitochondria as a Ca^{2+} sequestering organelle, FCCP was applied to evacuate mitochondria after the cells were exposed to an evoked Ca^{2+} load through a depolarizing stimulus (30mM K^+). When MNs were exposed to 30mM K^+ for 20s, the [Ca^{2+}]i rises rapidly and subsequently returns to basal level. While [Ca^{2+}]i concentrations returned to baseline, mitochondria and ER retain large pools of Ca^{2+}, presumably for later extrusion from the cell.

To determine, if accumulation of Ca^{2+} by mitochondria has any apparent influence on the lifetime of a [Ca^{2+}]i transient and to test if large Ca^{2+} pool exists, FCCP was added to the superfusate after 30mM K^+ induced depolarization. In the case of juvenile mice brain stem slices, application of 2µM FCCP within 5 min of depolarisation induced stimulus (30mM K^+) resulted in calcium release measured as Fura-2 fluorescence ratio of 0.1478 ± 0.0426 and 0.1312 ± 0.0468 (F/F0, N=3, n=19) for WT and $SOD1^{G93A}$ littermates, respectively (Fig. 3.1.7A, B and E). Following previous trends, although, there is a slight increase in fluorescence signal after cell membrane depolarisation (Fig. 3.1.7A and B) compared to fluorescence signal before depolarization (Fig. 3.1.6A and B) there is no significant difference in FCCP evoked Ca^{2+} release responses (normalised, F/F0) after depolarisation induced stimulus between juvenile WT and $SOD1^{G93A}$ mice. Similar application of 2µM FCCP in adult brain stem slices, resulted in calcium release measured as Fura-2 fluorescence ratio of 0.1416 ± 0.0458 and 0.0619 ± 0.0269 (F/F0, N=3, n=11) for WT and adult $SOD1^{G93A}$ animals respectively (Fig. 3.1.7C, D and E), implying that there is a significant difference in the Ca^{2+} accumulation activity of mitochondria between MNs of WT and $SOD1^{G93A}$ mice at late stage of motor dysfunction.

Fig. 3.1.7E shows the comparative analysis of average calcium release caused by FCCP after depolarization of MNs in juvenile and adult WT and $SOD1^{G93A}$ mice studied. It has already been shown that application of FCCP by itself, without predepolarization, induces only small elevations of [Ca^{2+}]i in MNs. But, if FCCP is applied immediately after termination of depolarization, during the decay of the induced transient, FCCP cause release of large amounts of Ca^{2+}, demonstrating the effectiveness of immediate uptake of Ca^{2+} into the cell through plasmalemmal channels (Balakrishnan & Keller, unpublished data). In this study FCCP was applied with a longer interval after termination of depolarization. It was observed that when Ca^{2+} returns to the basal level, it produced only a very small increase in [Ca^{2+}]i responses, although the Ca^{2+} store was ~2.28 folds bigger in adult WT compared to $SOD1^{G93A}$ symptomatic mice. This data can be explained by two plausible reasons: (i) progressive leak of ions from mitochondria back into the cytosol, and or (ii) Ca^{2+} homeostasis is significantly disturbed in vulnerable $SOD1^{G93A}$ MNs and mitochondria have lower capacity to store depolarization induced released Ca^{2+}. Thus, we conclude that mitochondria in WT MNs are capable of retaining Ca^{2+} for a longer time compared to vulnerable $SOD1^{G93A}$ MNs.

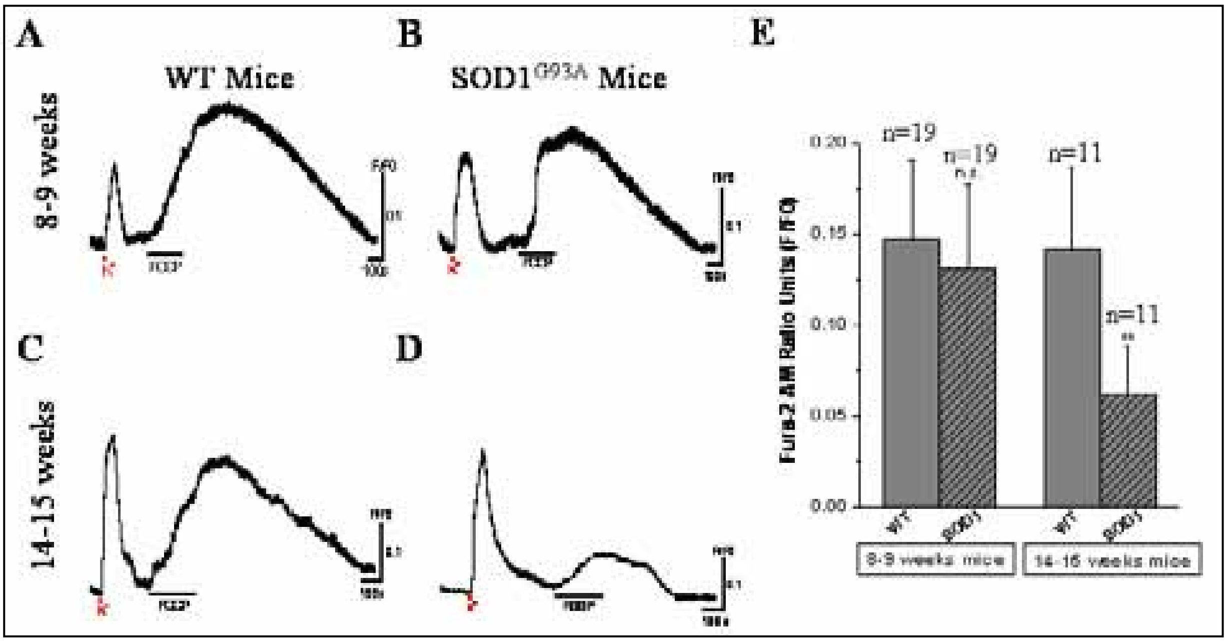

Fig. 3.1.7: Mitochondrial Ca^{2+} uptake (evoked by 30mM K^+) and its impact on $[Ca^{2+}]i$ release in juvenile and adult MNs of WT and $SOD1^{G93A}$ mice studied using 10µM fura-2 AM stained slices. 2µM FCCP was applied through superfusate (indicated by the black bars); shortly after the depolarization induced transient by 30mM K^+. (A) In the HMNs of juvenile WT mice the peak amplitude of Ca^{2+} release was 0.1478 ± 0.0426 (F/F0, N=3, n=19). (B) In the HMNs of juvenile $SOD1^{G93A}$ mice the peak amplitude of Ca^{2+} release was 0.1312 ± 0.0468 (F/F0, N=3, n=19). (C) & (D) In the HMNs of adult mice the peak amplitude of Ca^{2+} release was 0.1416 ± 0.0458 and 0.0619 ± 0.0269 (F/F0, n=11), for WT and $SOD1^{G93A}$ mice, respectively. Data shown represents a single cell from the slice imaged. Fura-2 AM ratiometric fluorescence signals are represented as F/F0. (E) A bar diagram of FCCP induced mitochondrial calcium transient after the depolarization of cells by 30mM K^+ in HMNs of juvenile and adult WT (n= 19 and 11) and $SOD1^{G93A}$ mice (n= 19 and 11). Data shown represents at least 3 independent experiments (N=3) for each genotype. Data is expressed as means ± S.D.; N= Number of experiments; n=Number of cells. $^{**}P<0.001$.

3.1.8 Pharmacological manipulation of ER in motoneurons by cyclopiazonic acid (CPA) inhibition of SERCA and its impact on differential Ca^{2+} store regulation

Endoplasmic reticulum (ER) is an organelle found in all eukaryotic cells. It is an interconnected network of tubules, vesicles and cisternae responsible for several specialized functions including sequestration of calcium. ER functions as an effective Ca^{2+} storing organelle. Active transport of $[Ca^{2+}]i$ into intracellular stores by sarco-endoplasmic reticulum Ca^{2+}-ATPase (SERCA) is important in regulating Ca^{2+} signaling (Cavagna *et al.*, 2000). Moreover, inhibition of Ca^{2+} uptake by ER has been shown to disrupt Ca^{2+} homeostasis (Trump & Berezesky, 1995).

To test whether ER serves either of these roles in MNs of juvenile and adult WT and SOD1^{G93A} mice, we measured endoplasmic reticulum calcium release in the presence of cyclopiazonic acid (CPA), a specific inhibitor of the family of SERCA pumps (Simpson & Russel, 1997). Application of 50µM CPA evoked a rise in [Ca^{2+}]i transient (Fig. 3.1.8), which is indicative of Ca^{2+} leak from the intracellular Ca^{2+} stores. 50µM CPA caused a gradual release of Ca^{2+} from ER stores at basal condition, recorded in both WT and SOD1^{G93A} mice brain stem slices for juvenile and adult animals. 50µM CPA evoked Ca^{2+} release responses (F/F0) in juvenile mice (N=3, n=12) was 0.0857 ± 0.0382 and 0.0667 ± 0.0135 in WT and SOD1^{G93A} littermates, respectively (Fig. 3.1.8A and B). In 14-15 weeks adult mice (N=3, n=12), release of Ca^{2+} (fluorescence, F/F0) caused by CPA was 0.0817 ± 0.0332 and 0.0542 ± 0.0202, in WT and SOD1^{G93A} littermates, respectively (Fig. 3.1.8C, D and E). In these experiments CPA application resulted in more or less identical Ca^{2+} release responses, although in adult SOD1^{G93A} brain stem slices these values are smaller. The comparison of average ER calcium release of HMNs studied in juvenile and adult animals of different genotypes is presented in Fig. 3.1.8E.

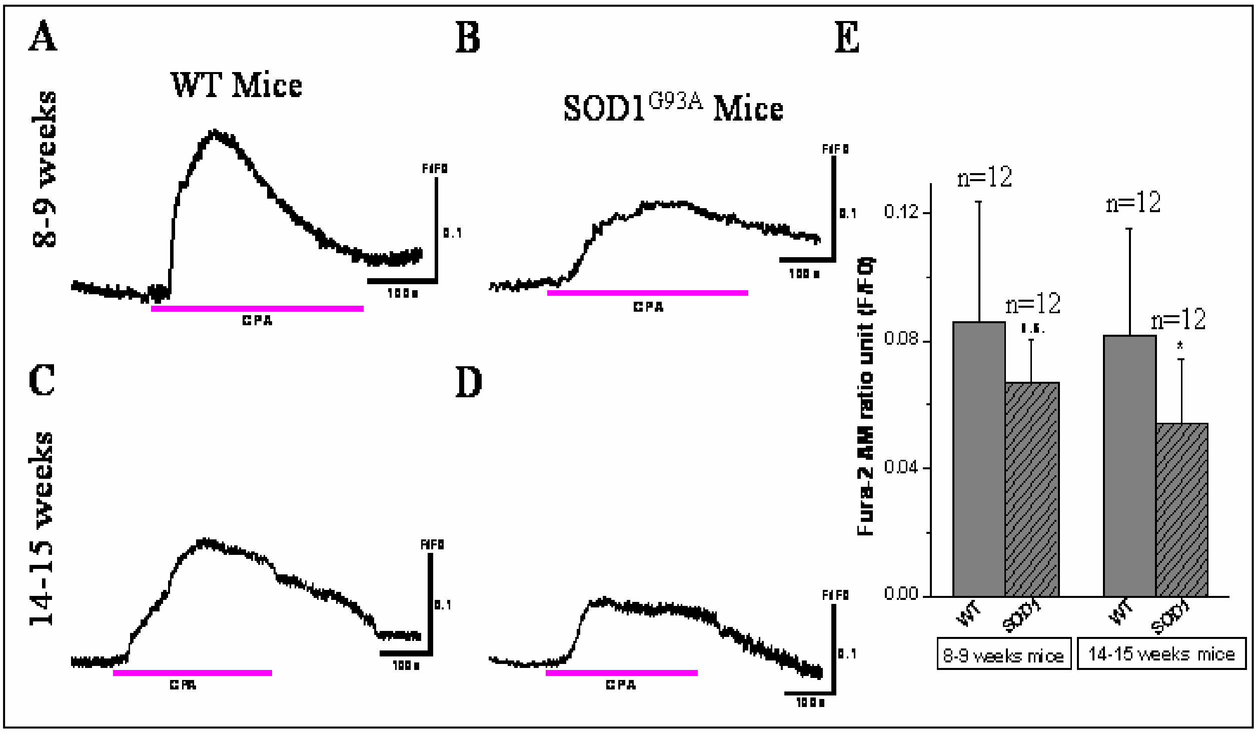

Fig. 3.1.8: Differential Ca^{2+} store regulation of ER in juvenile and adult WT and SOD1^{G93A} mice brain stem slices. Slices were incubated with cyclopiazonic acid (CPA) to inhibit ER Ca^{2+}-ATPase and thereby deplete Ca^{2+} content. Application of 50µM CPA causes measurable Ca^{2+} release from the HMNs of juvenile (8-9 weeks) (A), wild type (B), SOD1^{G93A} mice and adult (14-15 weeks) (C), wild type (D), SOD1^{G93A} mice. (A) - (D), Data shown represents a single cell from the slice imaged. Fura-2 AM fluorescence signals are represented as F/F0. Comparison of the amplitude of ER calcium release in these MNs as a result of SERCA pump inhibition has been presented in E. E, Data shown

represents at least 3 independent experiments (N=3, n=12) for each genotype. Data is expressed as means ± S.D.; N=Number of experiments; n=Number of cells. *$P<0.05$.

3.1.9 Interaction between ER and mitochondria in differential Ca^{2+} store regulation and the role of ER as a Ca^{2+} sequestering organelle in juvenile and adult brain stem slices of WT and S0D1^{G93A} mice

Until recently, despite the known role of ER in cellular stress and control of cellular Ca^{2+} homeostasis (Paschen, 2000), its role in neuronal cell injury had not been intensively studied. Evidences are gathering on the reciprocal functional interplay between ER and mitochondria in response of MNs to various toxic agents in ALS, Alzheimer's and Parkinson's disease (Paschen & Frandsen, 2001; Paschen & Mengesdorf, 2005). Previously, it was shown in *C. elegans* that high intracellular Ca^{2+} levels and release of ER-based Ca^{2+} stores are essential steps in the necrotic death mechanism of neurons. Furthermore, Ca^{2+} release from ER contributes to neuronal cell death because Ca^{2+} release blocker dantrolene can protect neurons against bioenergetic failure and cellular damage (Wei & Perry, 1996). If that is true, restoration of ER function or attenuation of secondary dysfunction induced by ER could present a highly promising new avenue for pharmacological intervention to minimize neuronal cell injury in pathological states of the ALS brain and other neurodegenerative disorders.

Comparative analysis of Ca^{2+} storing ability of mitochondria and ER in juvenile and adult WT and SOD1^{G93A} mice brain stem slices was done by using specific drugs that interfere with the integrity of these organelles. FCCP and CPA were used to release sequestered calcium from mitochondria and ER, respectively. There was a significant quantitative difference between ER and mitochondrial Ca^{2+} load in the case of healthy and ALS vulnerable HMNs at late stage of motor dysfunction with the Ca^{2+} release response being high in the mitochondria of WT mice.

As shown in Fig. 3.1.9, in juvenile mice the peak amplitude of mitochondrial Ca^{2+} release after application of FCCP together with CPA was 0.1738 ± 0.04659 and 0.1792 ± 0.0654, in WT and SOD1^{G93A} littermates, respectively (N=3, n=13; Fig. 3.1.9A and B). The impact of CPA on peak amplitude of Ca^{2+} release was nominal compared to FCCP indicating the smaller role of ER compared to mitochondria as a Ca^{2+} storing organelle; as exemplified by juvenile WT and corresponding SOD1^{G93A} animals (0.0342 ± 0.0087 for WT and 0.0335 ±

0.0111 for SOD1^{G93A}; N=3, n=13; Fig. 3.1.9A and B). In adult mice, the peak amplitude of $[Ca^{2+}]$i after CPA application were 0.0497 ± 0.0245 and 0.0311 ± 0.0087 for WT and SOD1^{G93A} littermates, respectively (**P*<0.05, significantly different from WT) whereas FCCP together with CPA response was 0.2095 ± 0.0695 and 0.0967 ± 0.0284 for WT and SOD1^{G93A} littermates, respectively (N=3, n=13; ***P*<0.001, Fig. 3.1.9C, D and E).

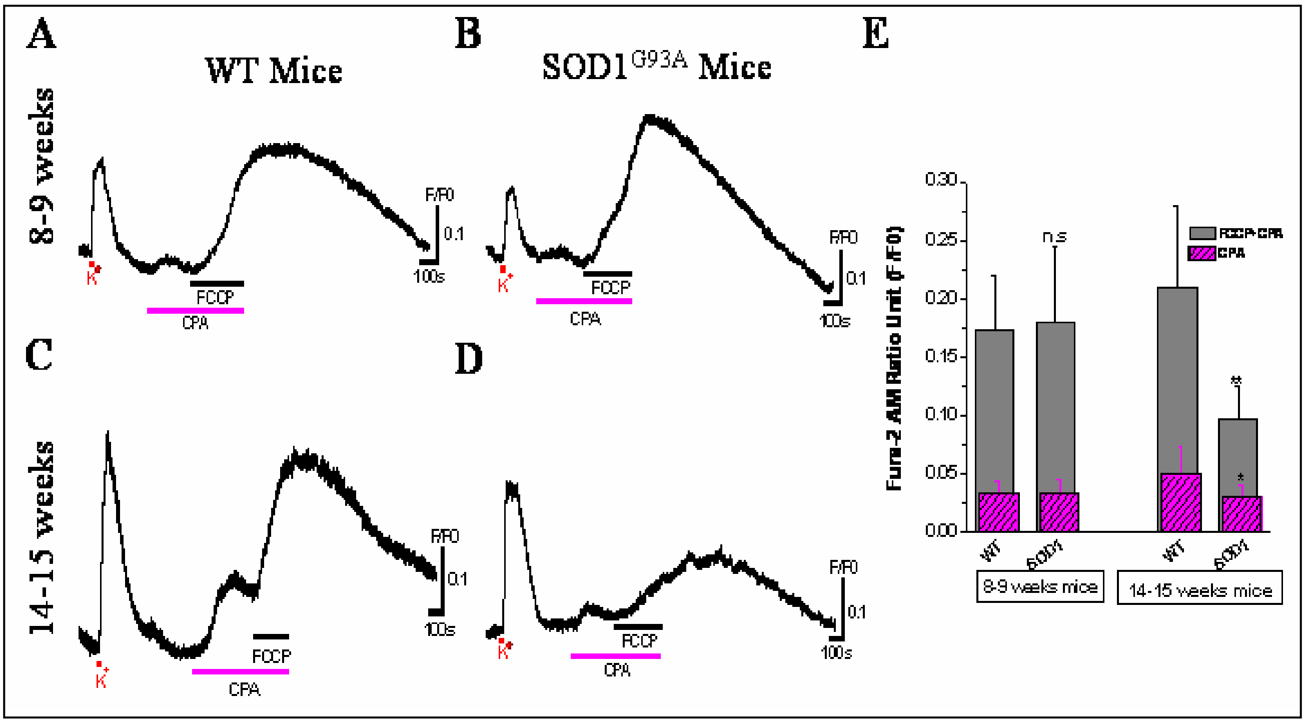

Fig. 3.1.9: Comparative analysis of the differential Ca^{2+} storing ability and store regulation of ER and mitochondria in juvenile and adult WT and SOD1^{G93A} mice brain stem slices. HMNs under study were stimulated using FCCP and CPA that interfere with the integrity of mitochondria and ER and also were used to release quenched calcium from mitochondria and ER, respectively. Quantitative differences between the ER and mitochondrial Ca^{2+} loads were evident in juvenile (A) WT and (B) SOD1^{G93A} as well as adult (C) WT and (D) SOD1^{G93A} mice. The horizontal red, magenta and black bars indicate duration of K^+ induced depolarisation, stimulation by CPA and FCCP together with CPA, respectively. (A)- (D) Data shown represents a single cell from the slice imaged. Fura-2 AM fluorescence signals are represented as F/F0. (E) A graphical representation of the comparison of ER and mitochondrial Ca^{2+} release from 8-9 weeks and 14-15 weeks (N=3) mice HMNs after application of CPA and CPA together with FCCP in WT and SOD1^{G93A} mice (n=13). Note that Ca^{2+} release and mitochondrial load is higher than the ER load. Data shown represents at least 3 independent experiments (N=3, n=13) for each genotype. Data are expressed as means ± S.D.; N=Number of experiments; n=Number of cells. ** *P*<0.001, **P*<0.05.

These data again reveal that ER merely serves as an effective Ca^{2+} storing organelle and contributes nominally in spatiotemporal reshaping and cross talk between mitochondria-ER in juvenile and adult WT and SOD1^{G93A} mice. Interestingly, CPA has a weak effect on Ca^{2+} release responses in symptomatic SOD1^{G93A} mice brain stem slices, indicating that SOD1^{G93A} mutations might also result in defects in Ca^{2+} handling by ER, which may perturb synaptic function while contributing to neurodegeneration. These data suggest that ER does not play a significant role in regulating $[Ca^{2+}]_i$ in the basal state or after imposed Ca^{2+} loads in HMNs of juvenile mice brain stem slices either in WT or $SOD1^{G93A}$ mice. However, in adult mice during ALS progression, the ER does have some contribution in dysfunction of Ca^{2+} loads, suggesting that Ca^{2+} dysregulation due to $SOD1^{G93A}$ mutation is a late onset event and anticipates ALS progression. Application of 2µM FCCP after emptying ER stores with CPA (50µM), resulted in a separate release event, evident from the $[Ca^{2+}]_i$ increase. This release was higher than the general Ca^{2+} release caused by FCCP without emptying ER in juvenile WT and $SOD1^{G93A}$ mice but not in adult symptomatic $SOD1^{G93A}$ mice, which suggests the plausible uptake of the released Ca^{2+} from ER by mitochondria in juvenile WT and $SOD1^{G93A}$ mice. This could indicate a close coupling between these two organelles in healthy MN. Results also indicate that with ALS progression, close coupling between ER and mitochondria is impaired. Comparative details of the normalized Fura-2 ratio of Ca^{2+} release responses (F/F0) in juvenile and adult animals are summarised in Table 2.

Fura-2 AM Ratio Unit (F/F0)		**8-9 weeks mice**		**14-15 weeks mice**	
		WT	$SOD1^{G93A}$	WT	$SOD1^{G93A*}$
Ca^{2+} Peak Amplitude	CPA	0.0342 ± 0.0087	0.0335 ± 0.0111	0.0497 ± 0.0245	0.0311 ± 0.0087
	FCCP + CPA	0.1738 ± 0.0466	0.1792 ± 0.0654	0.2095 ± 0.0695	$0.0967 \pm 0.0284^{*}$

Table 2: Differential peak amplitudes of Ca^{2+} release from ER and mitochondria in juvenile (8-9 weeks) and adult (14-15 weeks) WT and $SOD1^{G93A}$ mice brain stem slices. ***** Significantly different from WT littermates.

PART B

IMPACT OF MITOCHONDRIAL CALCIUM SIGNALING IN SH-SY5Y NEUROBLASTOMA CELL LINE TRANSFECTED WITH WT-SOD1 OR SOD1^{G93A} TRANSGENE

3.2 Role of Mitochondria in SH-SY5Y Cells in defining Ca^{2+} Metabolism of ALS Vulnerable Motoneurons

Mitochondrial damage induced by mSOD1 has been proposed to be a cause in selective degeneration of MNs in ALS. In this regard, it must be recalled that, among the mechanisms involved in the pathogenesis of both sALS and fALS, failure of Ca^{2+} homeostasis and mitochondrial impairment seem to play a crucial role. In order to investigate the role of impaired Ca^{2+} handling mechanism and oxidative stress induced by ROS in fALS, human SH-SY5Y neuroblastoma cells were used to express either WT-SOD1 or SOD1^{G93A} to mimic the situation in heterozygous patients. The effect of continuous expression of WT-SOD1 and/or mSOD1^{G93A} on mitochondrial morphology and Ca^{2+} signaling in SH-SY5Y neuroblastoma cells were compared. Further, the consequences and impact of protonophore FCCP along with other organelle (Mitochondria and ER) specific drugs on mitochondrial vulnerability and Ca^{2+} homeostasis in WT-SOD1 and SOD1^{G93A} transfected SH-SY5Y neuroblastoma cells were studied.

3.2.1 Impaired ability of SH-SY5Y neuroblastoma cells transfected with SOD1^{G93A} to cope with FCCP-induced Ca^{2+} influx

Mitochondria work as a local calcium buffer, thus shaping spatiotemporal aspects of cytosolic calcium signals. The calcium uptake into the mitochondria is undertaken by the mitochondrial calcium uniporter (MCU) located in the inner mitochondrial membrane (Kirichok *et al*., 2004). The accumulation of Ca^{2+} by mitochondria might have a perceptible influence on the existence of a $[Ca^{2+}]i$ transient. This effect was studied by following the dynamics of Ca^{2+} signal under deleterious mitochondrial conditions in SH-SY5Y neuroblastoma cells transfected with WT-SOD1 and/or mSOD1^{G93A}. A comparative analysis of the Ca^{2+} influx in WT and SOD1^{G93A} transfected SH-SY5Y neuroblastoma cells was done in the presence of 2µM FCCP. For these experiments the MNs were loaded with 5µM Fura-2 AM through the incubation method and $[Ca^{2+}]i$ transients were triggered once Fura-2 concentration was equilibrated after washing. Interestingly it was found that in SOD1^{G93A} transfected SH-SY5Y cells Ca^{2+} influx (peak fluorescence) was diminished as compared to WT-SOD1 transfected SH-SY5Y cells where Ca^{2+} influx was much more prominent, peaked within 2-3 min followed by baseline recovery in ~2 min. SOD1^{G93A} transfected SH-SY5Y cells take almost 5-6 min for baseline recovery. However, SH-SY5Y cells transfected with SOD1^{G93A} suffer from a reduced mitochondrial Ca^{2+} concentration after depletion of mitochondrial Ca^{2+} stores with FCCP (Fig. 3.2.1). After exposure to FCCP, the capacity of mSOD1^{G93A} transfected cells to transport $[Ca^{2+}]$i to the extracellular space or to intracellular storage sites was much lower than the capacity of neuroblastoma cells transfected with WT-SOD1 gene. This can account for the increased vulnerabitivity of SH-SY5Y cells expressing mSOD1^{G93A} to mitochondria of MNs.

SH-SY5Y cells transfected with WT-SOD1 and/or SOD1^{G93A} gene were treated with 2µM FCCP (3-4 min) and the $[Ca^{2+}]$i were measured in both cases (Fig. 3.2.1). Fig. 3.2.1B and C show $[Ca^{2+}]$i as cytoplasmic calcium–versus-time curves in 6 representative cells during FCCP challenge. FCCP (2µM) induces a fast transient elevation in $[Ca^{2+}]$i and a fast recovery to baseline in WT-SOD1 transfected SH-SY5Y cells (Fig. 3.2.1B, F/F0 = 0.1766 ± 0.0362; N= 3, n=17) compared to SOD1^{G93A} transfected SH-SY5Y cells, where FCCP induced transient elevation in $[Ca^{2+}]$i fluorescence intensity was lower in magnitude followed by delayed recovery to baseline (Fig. 3.2.1C, F/F0 = 0.0948 ± 0.0223; N= 5, n=23). The FCCP-induced calcium influx peak fluorescence intensity in SOD1^{G93A} transfected cells is diminished by ~ 48 % as compared to the calcium influx peak fluorescence intensity in WT-SOD1 transfected SH-SY5Y cells (Fig. 3.2.1D; $^{**}p < 0.001$).

3.2.2 Effect of high K^+-evoked Ca^{2+} transient and its impact on FCCP-induced Ca^{2+} influx in WT and SOD1^{G93A} transfected SH-SY5Y neuroblastoma cells

To analyze the comparative efficiency of mitochondria as a Ca^{2+} sequestering organelle, 2µM FCCP was applied to evacuate mitochondrial Ca^{2+} after the WT-SOD1 and SOD1^{G93A} transfected SH-SY5Y cells had been exposed to an evoked Ca^{2+} load through a depolarizing stimulus of 30mM K^+ for 30s. Experiments were conducted to check whether mitochondrial Ca^{2+} uptake can affect the FCCP induced Ca^{2+} response of WT-SOD1 and SOD1^{G93A} transfected SH-SY5Y cells, and if yes , how and by how much?

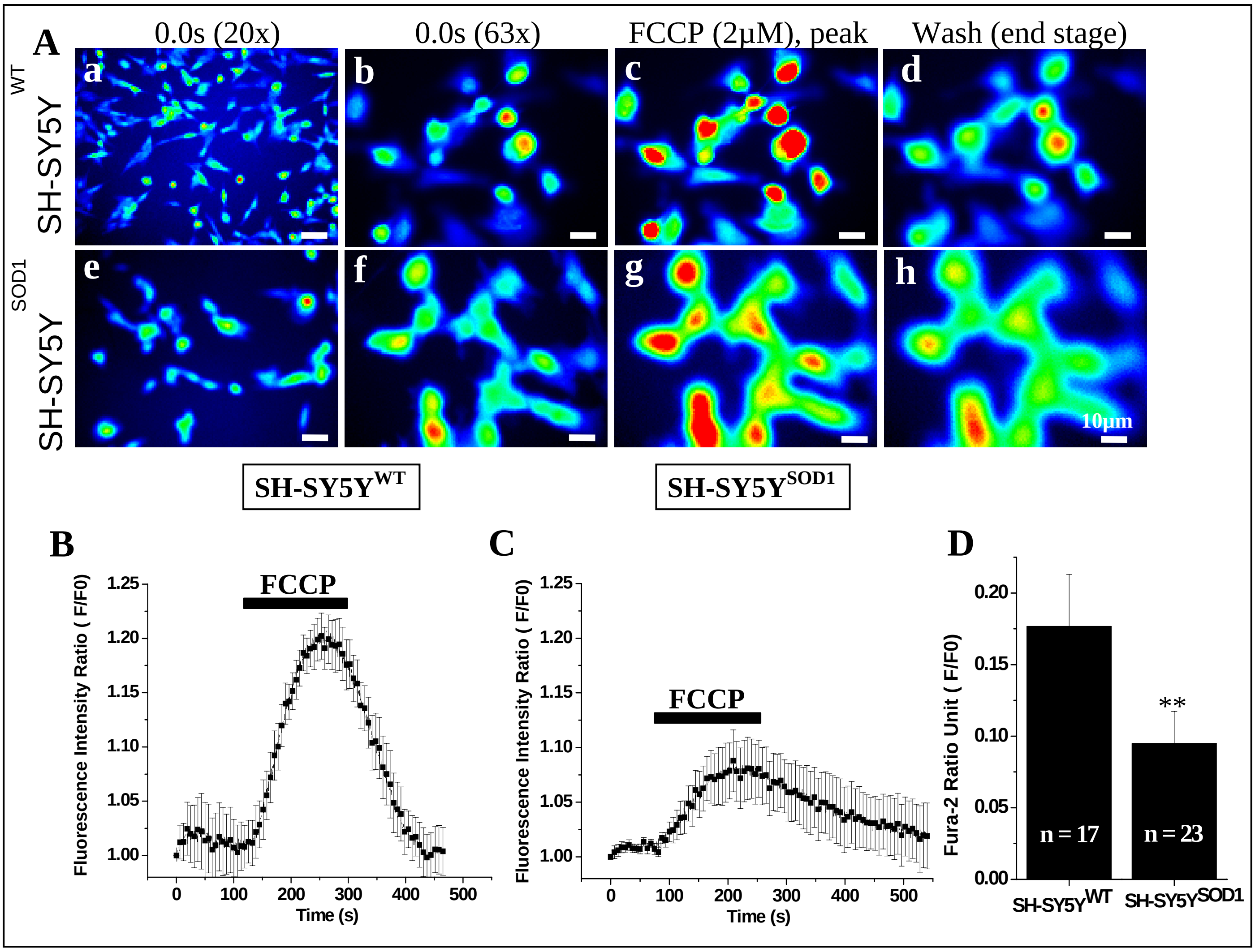

Fig. 3.2.1: Carbonyl cyanide 4-trifluromethoxyphenylhydrazone (FCCP) induced mitochondrial depolarization in SH-SY5Y neuroblastoma cells transfected with SOD1^{G93A} exhibits reduced peak fluorescence amplitude. (A) CCD imaging photomicrograph series showing [Ca^{2+}]i in 7-8 cells before drug application (0.0s), after peak 2µM FCCP challenge added to the superfusate (3 min) and after FCCP wash in WT (a-d) and SOD1^{G93A} (e-h) transfected SH-SY5Y neuroblastoma cells. (B) Illustrate [Ca^{2+}]i fluorescence intensity in 6 SH-SY5Y neuroblastoma cells in an imaging field transfected with WT-SOD1 after FCCP application. FCCP (2µM) induces a fast, transient elevation in [Ca^{2+}]i and a fast recovery to baseline. (C) In SOD1^{G93A} transfected SH-SY5Y neuroblastoma cells, FCCP induced transient elevation in [Ca^{2+}]i fluorescence intensity is lower in magnitude followed by a plateau for 1 min and then delayed recovery to baseline. (D) A bar diagram to illustrate the reduction of the sustained Ca^{2+} response in SOD1^{G93A} transfected SH-SY5Y neuroblastoma cells (F/F0 = 0.0948 ± 0.0223; N= 5, n=23) compared to WT-SOD1 transfected SH-SY5Y cells (F/F0 = 0.1766 ± 0.0362; N= 3, n=17). Value represents means ± S.D., $^{**}p < 0.001$, Scale bar = 10µm.

To determine this, firstly the SH-SY5Y cells transfected with WT-SOD1 and/or SOD1^{G93A} gene were stained with Fura-2AM (Fig. 3.2.2A), and exposed to 30mM K^{+} for 30s, followed by challenge with 2µM FCCP for 3 min. As shown in Fig. 3.2.2B and C, the peak amplitude of 2µM FCCP evoked Ca^{2+} influx after 30mM K^{+} depolarization was 0.2440 ± 0.0696 (N=3, n=20) and 0.1497 ± 0.0362 (N=5, n=20) for the WT-SOD1 and SOD1^{G93A} transfected SH-

SY5Y cells respectively. It was observed that the 30mM K^+ depolarization induced stimulus not only interfered with the post-depolarization recovery of $[Ca^{2+}]i$ after 2μM FCCP challenge but also increased the peak amplitude of 2μM FCCP evoked Ca^{2+} influx by ~ 40% and ~68 % in WT and $SOD1^{G93A}$ transfected SH-SY5Y cells respectively (Fig. 3.2.1D and Fig. 3.2.2D).

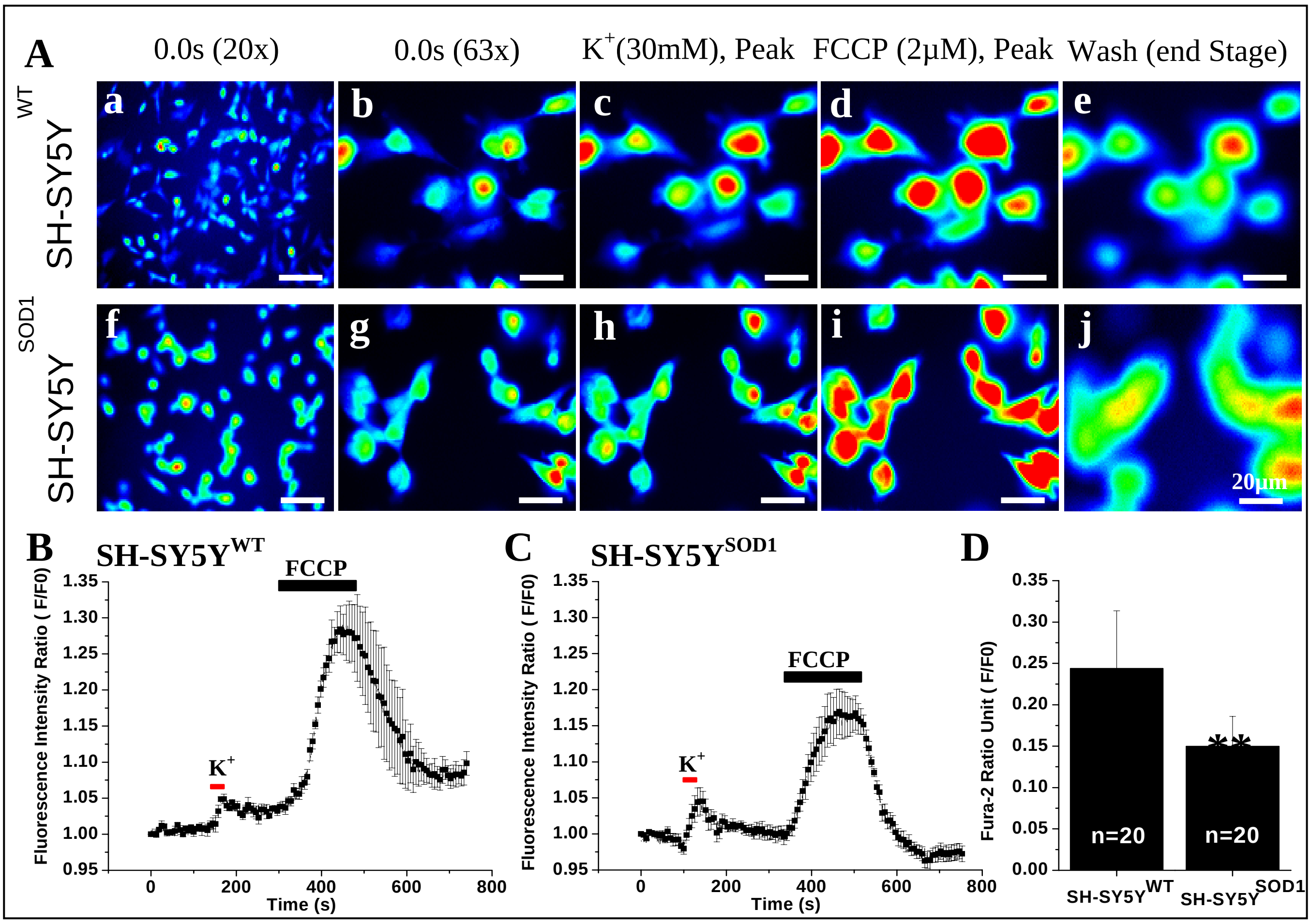

Fig. 3.2.2: Effect of high K^+ (30mM) - evoked Ca^{2+} transient and its impact on FCCP induced Ca^{2+} influx in WT-SOD1 and $SOD1^{G93A}$ transfected SH-SY5Y neuroblastoma cells. (A) CCD imaging photomicrograph series showing $[Ca^{2+}]i$ in 7 cells before drug application (0.0s), after peak 30mM K^+ (30s) depolarization, 2μM FCCP (3 min) challenge added to the superfusate for 3min and after FCCP wash in WT (a-e) and $SOD1^{G93A}$ (f-j) transfected SH-SY5Y neuroblastoma cells. (B) Effect of perturbing mitochondrial Ca^{2+} uptake on the calcium transient (evoked by 30mM K^+ depolarising stimulus for 30s, indicated by red horizontal bar) by 2μM FCCP-evoked Ca^{2+} efflux (indicated by black horizontal bar). FCCP (2μM) induces a fast, transient elevation in $[Ca^{2+}]i$ and a fast recovery to baseline after depolarisation induced stimulus (30mM K^+, 30s) in 7 SH-SY5Y cells, in an imaging field transfected with WT-SOD1 gene. Magnitude of fluorescence intensity did not completely recover to baseline probably due to saturation of the dye. (C) In $SOD1^{G93A}$ transfected SH-SY5Y cells, FCCP induced $[Ca^{2+}]i$ transient elevation after 30mM K^+ depolarisation induced stimulus is minutely delayed (5-10s) and there is reduction in the magnitude of fluorescence intensity followed by complete recovery to baseline. (D) A bar diagram to illustrate the reduction of the sustained Ca^{2+} response in $SOD1^{G93A}$ transfected SH-SY5Y neuroblastoma cells (F/F0 = 0.1497 ± 0.0362; N=5, n=20; **P<0.001) compared to WT-SOD1 transfected SH-SY5Y cells (F/F0 = 0.2440 ± 0.0696; N=3, n=20). Value represents means ± S.D., $^{**}p < 0.001$, Scale bar = 20μm.

Thus it is evident that in the absence of mitochondrial Ca^{2+} uptake, the $[Ca^{2+}]$i signal is more strongly reflected in the cytoplasm of these cells; exemplifying that mitochondria can actively sequester Ca^{2+} during an on-going Ca^{2+} influx as a result of the opening of voltage gated calcium channels. A significant difference in the Ca^{2+} accumulation activity of mitochondria in $SOD1^{G93A}$ transfected SH-SY5Y cells was observed in comparison to WT-SOD1 transfected SH-SY5Y cells which is presumably due to $SOD1^{G93A}$ mediated toxicity. The capacity of mitochondria to restore its Ca^{2+} buffering capacity of cell organelles is heavily compromised in $SOD1^{G93A}$ transfected SH-SY5Y cells. Disturbances of Ca^{2+} trapping in intracellular storage sites and Ca^{2+} extrusion from the cells (Herrington *et al*., 1996) might account for the observed reduced oscillations of $[Ca^{2+}]$i concentrations in $SOD1^{G93A}$ transfected SH-SY5Y cells (Fig. 3.2.2D; $**P<0.001$). Fig. 3.2.2D shows the comparative analysis of average calcium release caused by 2µM FCCP from WT-SOD1 and SOD^{G93A} transfected cells.

3.3 Simultaneous Measurement of Cytosolic and Mitochondrial Ca^{2+} concentrations in WT-SOD1 and $SOD1^{G93A}$ transfected SH-SY5Y Neurobalstoma Cells Culture model of Motoneuron Disease

Mitochondrial Ca^{2+} uptake responds dynamically and sensitively to changes in cytosolic Ca^{2+} levels and plays a crucial role in sequestering the large Ca^{2+} loads induced by FCCP evoked Ca^{2+} influx (Herrington *et al*., 1996). Excessive Ca^{2+} influx into mitochondria may result in mitochondrial dysfunction. Prominent and sustained mitochondrial depolarisation follows intense ion channels receptor stimulation, and closely parallels the incidence of neuronal death (Schinder *et al*., 1996). Substantial Ca^{2+} can be accumulated in mitochondria as a result of overloading the matrix with Ca^{2+}; this disrupts the structural and functional integrity of the organelle. Hence mitochondria may be critical intracellular targets of injury after intense Ca^{2+} channel stimulation and in this way, may act as a plausible link between massive Ca^{2+} influx and mitochondria mediated neurotoxicity in $SOD1^{G93A}$ transfected SH-SY5Y cells. However, the precise relationship between Ca^{2+} influx, cytosolic Ca^{2+} increase and mitochondrial Ca^{2+} uptake remains obscure. The aim of this study was to simultaneously measure the cytosolic and mitochondrial Ca^{2+} concentration changes in WT-SOD1 and $SOD1^{G93A}$ transfected SH-SY5Y cells, reliably and separately at the same time point. The cells were visualised, imaged and the fluorescence signals of mitochondrial Ca^{2+} uptake, in shaping the spatial and temporal properties of $[Ca^{2+}]$i signaling in SH-SY5Y cells transfected with WT-SOD1 and/or $SOD1^{G93A}$

genes were evaluated. For kinetic data analysis only Fura-2 signals and Rhod-2 signals from pre-defined regions of cells were used.

3.3.1 Monitoring cytosolic (Fura-2) and mitochondrial (Rhod-2) Ca^{2+}concentration with a temporal resolution in the millisecond time domain after inhibition of mitochondrial Ca^{2+} sequestration in WT-SOD1 and $SOD1^{G93A}$ transfected SH-SY5Y cells

Accumulation of calcium by mitochondria was inhibited by three separate methods. Firstly by drugs (Rotenone, a complex I blocker; FCCP, a protonophore and oligomycin, a F_OF_1-ATPase blocker preventing maintenance of proton gradient) which disrupt $\Delta\Psi_m$ due to the fact that mitochondrial calcium accumulation is driven by $\Delta\Psi_m$ (Duchen, 2000; Nicholls & Budd, 2000; Billups & Forsythe, 2002). Secondly, by Tetraphenylphosphonium (TPP^+), which blocks mitochondrial efflux without affecting ATP production and mitochondrial calcium uptake (Tang & Zucker, 1997) and thirdly, by RU360 or ruthenium red, a specific inhibitor of the mitochondrial calcium uniporter (Matlib *et al.*, 1998) which prevented the stimulus-induced rise in $[Ca^{2+}]_m$. In order to address the contribution of cytosolic (Fura-2 dye) and mitochondrial (Rhod-2 dye) Ca^{2+} signals in WT-SOD1 and $SOD1^{G93A}$ transfected SH-SY5Y cells, mitochondrial uncoupler FCCP was used in an attempt to prevent the $[Ca^{2+}]_m$ increase while measuring $[Ca^{2+}]$i. As shown previously in Fig. 3.2.1, Ca^{2+} release in $SOD1^{G93A}$ transfected cells is smaller in amplitude and exhibits slower kinetics in comparison to WT-SOD1 transfected SH-SY5Y cells. To confirm that there is a separate Ca^{2+} uptake and release event from the cytosol and mitochondria, transfected cells were treated with 2µM FCCP and $[Ca^{2+}]$i as well as $[Ca^{2+}]_m$ were measured simultaneously in WT-SOD1 and $SOD1^{G93A}$ transfected cells (Fig. 3.3.1).

WT-SOD1 transfected SH-SY5Y cells loaded with Fura-2 AM and Rhod-2 AM showed that FCCP evokes a substantial increase in $[Ca^{2+}]$i (F/F0 = 0.1569 ± 0.0235; Fig. 3.3.1A, means ± S.D. data; N=5; n=17, Fura-2 fluorescence signals) while draining $[Ca^{2+}]$m (F/F0 = -0.1069 ± 0.0181, Fig. 3.3.1A, mean data; N=5; n=17; Rhod-2 fluorescence signals). This data suggests that the FCCP evoked increase in $[Ca^{2+}]$i signals in Fig. 3.2.1(F/F0 = 0.1766 ± 0.0362; N= 3, n=17) was mainly due to $[Ca^{2+}]$i and that there is very little impact of $[Ca^{2+}]$m on it. In $SOD1^{G93A}$ transfected SH-SY5Y cells, FCCP evoked $[Ca^{2+}]$i is smaller and exhibits slower kinetics (F/F0 = 0.1034 ± 0.0248; Fig. 3.3.1B and C, mean data; N=3; n=15; Fura-2 signal) compared to WT-SOD1 transfected SH-SY5Y cells while draining [Ca^{2+}]m (F/F0 = -0.0489 ± 0.0041, Fig. 3.3.1B and C, means ± S.D. data; N=3; n=21; Rhod-2 fluorescence signals).

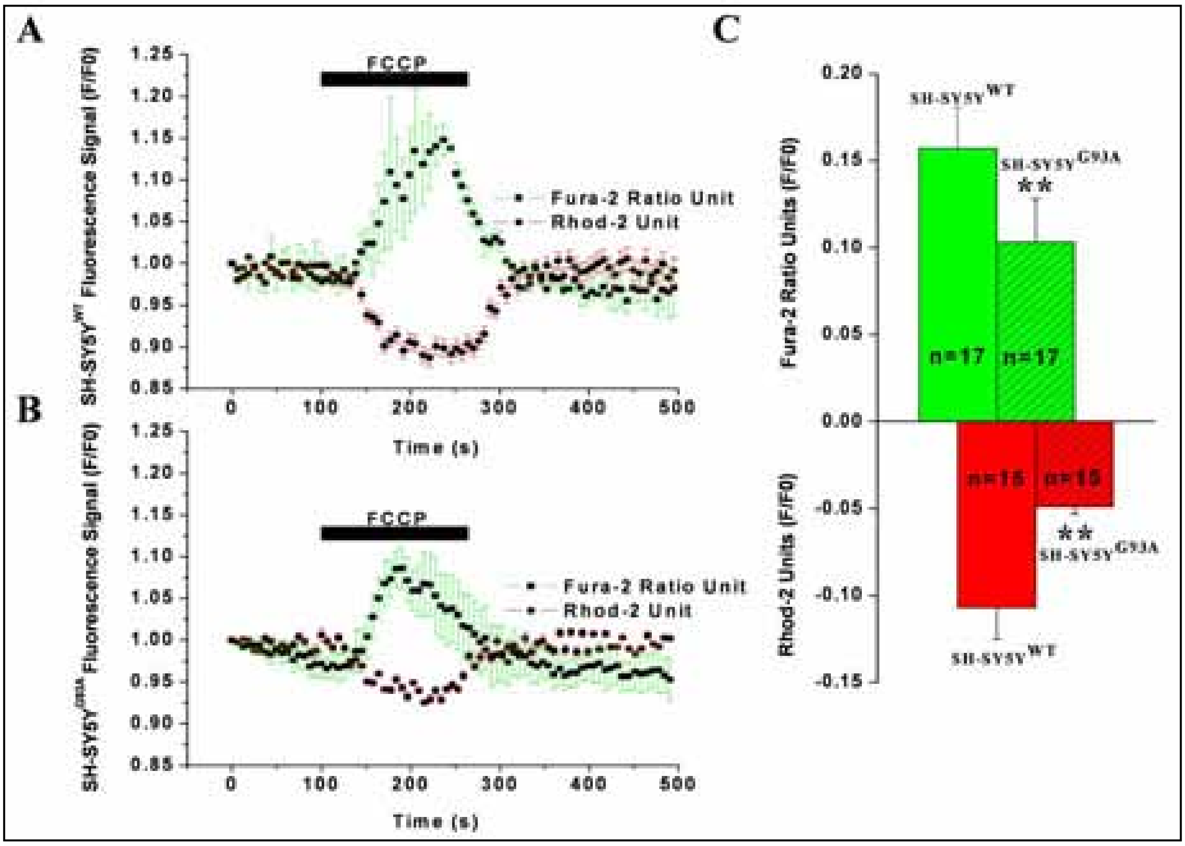

Fig. 3.3.1: FCCP-evoked [Ca^{2+}]$_m$ signals were smaller in amplitude and exhibited slower kinetics in SOD1^{G93A} transfected SH-SY5Y cells compare to WT transfected cells and it is altered from [Ca^{2+}]i efflux. (A) Kinetic profile of the FCCP-evoked Ca^{2+} release in the WT transfected SH-SY5Y neuroblastoma cells, simultaneously from the cytosolic (Error bar green, ■ black square trace) and mitochondrial (Error bar red, ●black circle trace) compartment (Trace represents average mean of 5-6 cells in focus stimulated with 2µM FCCP). (B) Corresponding Kinetic profile of the FCCP-evoked Ca^{2+} release in the SOD1^{G93A} transfected SH-SY5Y neuroblastoma cells, simultaneously from the cytosolic (Error bar green, ■ black square trace) and mitochondrial (Error bar red, ●black circle trace) compartment (Trace represents average mean of 5-6 cells in focus stimulated with 2µM FCCP). (C) Cytosolic (Green bar) and mitochondrial (Red bar) fluorescence signals (F/F0) from WT (Hollow red and green bar, n= 17) and SOD1^{G93A} (Red and green bar with sparse pattern, n=15) transfected SH-SY5Y neuroblastoma cells. Value represents means ± S.D., $^{**}p < 0.001$.

The lower and slower kinetics of [Ca^{2+}]m in SOD1^{G93A} transfected SH-SY5Y cells suggests that these cells have lower affinity for mitochondrial Ca^{2+} upload. These changes are likely to represent severely disturbed and vulnerable mitochondria in SOD1^{G93A} transfected SH-SY5Y cells compare to WT transfected cells (Fig. 3.3.1C; $^{**}p < 0.001$). The study revealed for the first time the simultaneous determination of [Ca^{2+}]i and [Ca^{2+}]m concentrations in WT and SOD1^{G93A} transfected SH-SY5Y cell culture model of motoneuron disease. This data is in good agreement with other findings where SH-SY5Y cells expressing SOD1^{G93A} show damaged and stressed mitochondria including increased ROS (Ciriolo *et al*., 2000; Aquilano *et al*., 2006).

3.3.2 Involvement of ER and mitochondria in shaping $[Ca^{2+}]i$ and $[Ca^{2+}]m$ regulation in WT- SOD1 and $SOD1^{G93A}$ transfected SH-SY5Y cells

For the investigation of ER-dependent Ca^{2+} release, caffeine has been established as a specific activator of Ca^{2+} influx from ryanodine receptor (RyR)-dependent Ca^{2+} stores (Svichar *et al*., 1997). To investigate the relative impact of ER and mitochondria in $[Ca^{2+}]i$ as well as $[Ca^{2+}]m$ regulation together with its consequence on MN degeneration in $SOD1^{G93A}$ transfected SH-SY5Y cells, we tested pharmacological agents that not only selectively block Ca^{2+} uptake into ER/mitochondrial compartments but also trigger Ca^{2+} release from intracellular storage sites. Caffeine, as shown in Fig. 3.3.2, led to relatively slow and weak increase of $[Ca^{2+}]i$ and $[Ca^{2+}]_m$ fluorescence signals, which is very similar for WT (N=3, n=14) and $SOD1^{G93A}$ (N=3, n=14) transfected SH-SY5Y cells. WT transfected SH-SY5Y cells showed that 5mM Caffeine evoked a small and slow increase in $[Ca^{2+}]i$ (F/F0 = 0.0471 ± 0.0190, Fig. 3.3.2A and C, mean data, 5 point smoothing; Fura-2 fluorescence signals) and $[Ca^{2+}]_m$ (F/F0 = -0.0392 ± 0.0183, Fig. 3.3.2A and C, mean data, 5 point smoothing; Rhod-2 fluorescence signals), which occurred with slightly higher kinetics than the $SOD1^{G93A}$ transfected SH-SY5Y cells. In $SOD1^{G93A}$ transfected SH-SY5Y cells peak amplitude increase in $[Ca^{2+}]i$ signals was 0.0353 ± 0.0120 (F/F0, Fig. 3.3.2B and C, mean data, 5 point smoothing) whereas $[Ca^{2+}]_m$ signals was -0.0146 ± 0.0044 (F/F0, Fig. 3.3.2B and C, mean data; 5 point smoothing) after 5mM caffeine application. This data suggests that the caffeine-evoked ER-dependent Ca^{2+} release has either minor contribution in mitochondrial mediated toxicity in $SOD1^{G93A}$ transfected SH-SY5Y cells as reported in other cell types and animal models or occurs upstream of the mitochondria (Pinton *et al*., 2000; Ferrari *et al*., 2002; Pinton *et al*., 2002). It was also noted that the peak amplitude transient of decrease in $[Ca^{2+}]_m$ (Rhod-2 fluorescence signals) after caffeine application was a little bit slower than the rate of increase in $[Ca^{2+}]i$ (Fura-2 fluorescence signals; Fig. 3.3.2A, B and C). It is also interesting to note that the rate of increase in Fura-2 and Rhod-2 fluorescence signals following caffeine application was a little bit slower compared to FCCP evoked signals and did not achieve the baseline with in a few min. We assume that this could be due to the slow activity of the mitochondrial Na^{+}/Ca^{2+} exchanger, the major pathway for mitochondrial Ca^{2+} efflux, as has previously been reported in other findings (leoty *et al*., 2001).

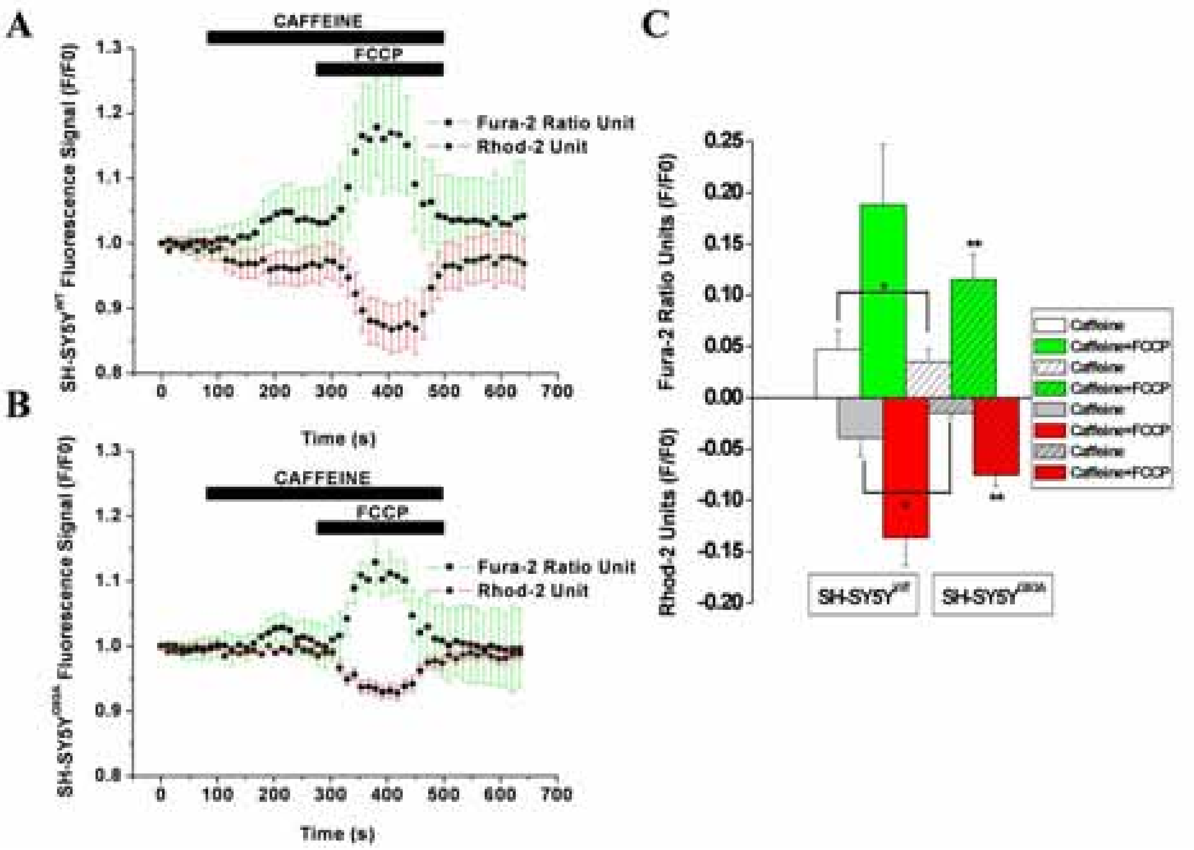

Fig. 3.3.2: Caffeine stimulates mitochondrial Ca^{2+} uptake with slower kinetics and weak transient than the FCCP-evoked $[Ca^{2+}]i$ and $[Ca^{2+}]m$ signal in SH-SY5Y neuroblastoma cells which is prominent in WT transfected SH-SY5Y cells compare to $SOD1^{G93A}$ transfected cells. (A) Kinetic profile of the caffeine and FCCP-evoked $[Ca^{2+}]i$ and $[Ca^{2+}]m$ release in the WT transfected SH-SY5Y neuroblastoma cells, simultaneously from the cytosolic (Error bar green, ■ black square trace) and mitochondrial (Error bar red, ●black circle trace) compartment(representative trace of 5-6 cells in focus stimulated with 5mM caffeine and 2μM FCCP together with 5mM caffeine, normalized data, 5 point smoothed to remove noise). (B) Corresponding kinetic profile of the caffeine and FCCP-evoked $[Ca^{2+}]i$ and $[Ca^{2+}]m$ release in the $SOD1^{G93A}$ transfected SH-SY5Y cells, simultaneously from the cytosolic (Error bar green, ■ black square trace) and mitochondrial (Error bar red, ●black circle trace) compartment (representative trace of 5-6 cells in focus stimulated with 5mM caffeine and 2μM FCCP together with caffeine, normalized data, 5 point smoothed to remove noise). (C) A bar diagram of caffeine and FCCP induced Ca^{2+} release in the WT and $SOD1^{G93A}$ transfected SH-SY5Y neuroblastoma cells. Hollow bar represents cytosolic (White color bar, up) and mitochondrial ((light gray bar, down) fluorescence signals (F/F0) after caffeine stimulation whereas FCCP together with caffeine-evoked Ca^{2+} efflux was represented simultaneously as Cytosolic (Green bar, up) and mitochondrial (Red bar, down) fluorescence signals (F/F0) in WT transfected SH-SY5Y cells. In $SOD1^{G93A}$ transfected cells caffeine induced cytosolic and mitochondrial Ca^{2+} efflux is represented by hollow bar with sparse pattern (up) and light gray with sparse pattern (down) respectively whereas FCCP together with caffeine-evoked Ca^{2+} efflux is represented simultaneously as cytosolic (Green bar with sparse pattern, up) and mitochondrial (Red bar with sparse pattern, down) fluorescence signals (F/F0). N=3, n=14; Value represents means ± S.D., *$p < 0.01$, **$p < 0.001$.

Following stimulation with 5mM caffeine, treatment of cells with 2μM FCCP in presence of 5mM caffeine depolarize the mitochondria and caused a decrease in Rhod-2 fluorescence signals with a corresponding increase in Fura-2 fluorescence signals (Fig. 3.3.2) simultaneously. As shown in Fig. 3.3.2, 5mM Caffeine together with 2µM FCCP led to a rapid and high amplitude increase of $[Ca^{2+}]i$ and $[Ca^{2+}]_m$ which shows very distinct and differential fluorescence response for WT transfected (N=3, N=14) SH-SY5Y cells compared to $SOD1^{G93A}$ (N=3, N=14) transfected SH-SY5Y cells. WT transfected SH-SY5Y cells showed that caffeine together with FCCP, evoked a massive and comparatively fast increase in Fura-2 fluorescence signals (F/F0 = 0.1883 ± 0.0584, Fig. 3.3.2A and C, mean data, 5 point smoothing) and Rhod-2 fluorescence signals (F/F0 = -0.1362 ± 0.0277, Fig. 3.3.2A and C, mean data, 5 point smoothing).

This data suggests that the dye accumulates in mitochondria and the mitochondrial uptake and release event is prominently operated by Ca^{2+} efflux and little by the store operated Ca^{2+} uptake and release phenomenon by mitochondria but not by the ER. In comparison to WT transfected SH-SY5Y cells where the transient of peak amplitude is large, $SOD1^{G93A}$ transfected SH-SY5Y cells shows small increase in peak transient of Fura-2 fluorescence signals (F/F0 = 0.1154 ± 0.0246, Fig. 3.3.2B and C, mean data, 5 point smoothing) and Rhod-2 fluorescence signals (F/F0 = -0.0753 ± 0.0102, Fig. 3.3.2B and C, mean data, 5 point smoothing) after 2µM FCCP application together with 5mM caffeine.

PART C

CALBINDIN-D_{28K} INDUCED CALCIUM BUFFERING AND ESTIMATION OF DECAY TIME CONSTANT (τ) IN MOTONEURONS

3.4 Study of Calcium Buffering Capacity and its Impact on Motoneurons

Differential calcium buffering capacity of ALS vulnerable (Lips & Keller, 1998; Palecek *et al*., 999) and resistant MNs (Vanselow & Keller, 2000) and its significance in ALS etiology has been shown. Ca^{2+} involvement as a risk factor was indicated by the observation that Ca^{2+}-binding proteins such as CB-D_{28k} and PV were absent in MN populations (HMNs/SMNs) lost early in ALS while facial and trigeminal MNs continue to survive (Alexianu *et al.*, 1994; McMahon *et al*., 1998). In order to check whether CB-D_{28k} protect cells from dysfunction and degeneration through buffering of $[Ca^{2+}]i$, calcium buffer concentration of non transfected and CB-D_{28k} transfected cell culture system were studied. In collaboration with Dr. Sebastian Kugler, Department of Neurology, University of Goettingen, we developed a culture of primary neuronal cells at days E18 from cortex of mouse that expresses different levels of (low and high) CB-D_{28k}. Calcium signals were measured by depolarizing the cells with a stimulus of 60mM K^+, which causes a fast transient increase in $[Ca^{2+}]i$. Calculations of AUC and amplitude for bar graphs were done as depicted in materials and methods.

3.4.1 Calbindin-D_{28k} decreases $[Ca^{2+}]i$ following stimulations in motoneurons

Initially, three independent pools of stably transfected primary neuronal cells were generated. These pools were generated from cortex of E_{18} mouse transfected with different levels of CB-D_{28k}. CB-D_{28k} transfected (Low, and High) and non transfected cells attached with coverslips were used for Ca^{2+} imaging studies (atleast 3 experiment for each conditions). CB-D_{28k} (High) transfected cells exhibited low amplitude Ca^{2+} responses following stimulation with high 60mM K^+, compared to low CB-D_{28k} transfected and non-transfected cells.

Under the experimental conditions described in the 'materials and methods' section, there were striking differences in the kinetics of the Ca^{2+} signal in non-transfected (Fig. 3.4.1A, Ba) and CB-D_{28k} transfected (Low and High) cells (Fig. 3.4.1Ab-c and Bb-c). 60mM K^+ depolarization induced stimulus (30s) produced a rapid transient increase in $[Ca^{2+}]i$ and the peak Ca^{2+} release amplitude was 0.4772 ± 0.0177 (F/F0) in non-transfected cells (N=3; n=18; Fig. 3.4.1Ba and C) which reached to peak within 10s. Sustained Ca^{2+} fluorescence

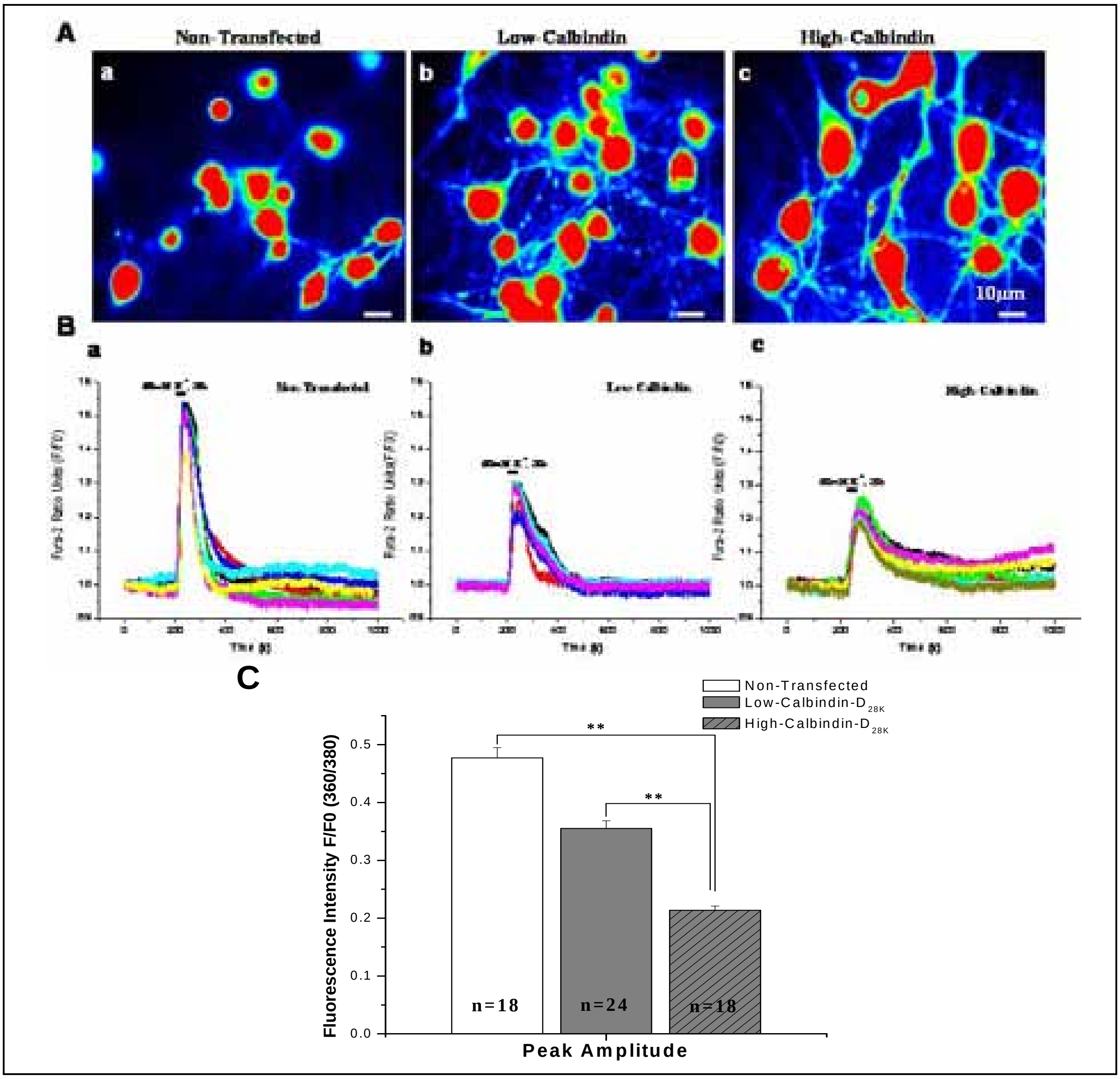

Fig. 3.4.1: The kinetics of calcium transients in Calbindin-D_{28k} transfected culture of primary neuronal cell is slower than the non-transfected cells after 60mM K^+ depolarization induced stimulus. (A) A CCD camera image (4x4 binning) showing primary neuronal cell loaded with fura-2 AM (excitation at 360 nm). Panel (A) a, represents non-transfected culture primary neuronal cells. Panel (A) b and Panel (A) c represents Low and high Calbindin-D_{28k} transfected cells, respectively. (B) $[Ca^{2+}]i$ transients of 7-8 non-transfected cells in an imaging field. In non-transfected cells, which lack Calbindin-D_{28k}, 60mM K^+ induces a fast, transient elevation in $[Ca^{2+}]i$ and relatively fast recovery. Panel (B) a, b and c, illustrates non transfected, low and high Calbindin-D_{28k} transfected cells, respectively in which 60mM K^+ induced $[Ca^{2+}]i$ transients is significantly diminished (~2 times) in the peak amplitude of the sustained Ca^{2+} increase while showing similar fast increase in low and high Calbindin-D_{28k} transfected cells, but a slight increase in time for baseline recovery. (C) A bar diagram of changes in the peak amplitude were calculated as F/F0. N=3, Number of experiments for each conditions; n= 18, 24, and 16 respectively for each condition, Number of cells. $^{**}P<0.001$ compared with non-transfected and low and high Calbindin-D_{28k} transfected cells. Data are expressed as means ± S.E.M. Scale bar 10 µm.

signal increase lasted for 2 min and the peak Ca^{2+} signal declined relatively rapidly (~ 25s) during the recovery to baseline. The low and high CB-D_{28k} transfected cells exhibited similar transient increases in $[Ca^{2+}]i$ in response to high 60mM K^+ and the peak amplitude reached a maxima with in ~15-20s (Fig. 3.4.1Bb-c and C). Although low and high CB-D_{28k} transfected cells exhibited a similar transient increase, in low CB-D_{28k} transfected cells Ca^{2+} release peak amplitude was 0.3550 ± 0.0132 (F/F0; N=3; n=24; Fig. 3.4.1Bb) whereas in high CB-D_{28k} transfected cells Ca^{2+} release peak amplitude was 0.2134 ± 0.0076 (F/F0; N=3; n=16; Fig. 3.4.1Bc). Both low and high CB-D_{28k} transfected cells exhibited a significant (~2times) reduction in the peak amplitude of the sustained $[Ca^{2+}]i$ elevations compared to non transfected cells (Fig. 3.4.1B and C; $^{**}p<0.001$). Decay to baseline in low and high transfected CB-D_{28k} cells was also relatively slower and the baseline recovery time is ~60s, compared to non transfected cells where recovery time is ~30s-35s. Representative responses and traces are shown in Fig. 3.4.1A, B and C.

3.4.2 Calbindin-D_{28k} decreases the susceptibility of motoneurons to excitability and increases the decay time constant (Ca^{2+} clearance rates (τ))

CB-D_{28k} acts as a modulator of depolarisation induced calcium transients. CB-D_{28k} acts by affecting calcium influx in response to high depolarising concentration of K^+ and there by buffering calcium which regulate intracellular responses to physiological stimuli and in addition can protect MNs against calcium mediated neurotoxicity. Changes in amplitude (I) and decay time constant (τ) of non-transfected and CB-D_{28k} transfected cells were closely monitored in fura-2 AM loaded cells. The peak amplitudes of the Ca^{2+} transients reduced as fura-2 bind with CB-D_{28k} and thereby buffer the Ca^{2+} in transfected cells. Under the experimental conditions described in materials and methods, for estimation of $[Ca^{2+}]i$ clearance rates, decay kinetics of Ca^{2+} transients recoveries after 60mM K^+ depolarization evoked Ca^{2+} transients before and after CB-D_{28k} transfection was fit with a single exponential decay curve to determine the decay time constant (τ). In CB-D_{28k} transfected cells (Low and High) decay was relatively slower and did not exhibit the rapid drop from the peak amplitude as seen in non-transfected cells (Fig. 3.4.2A). Changes in amplitude (I) for non-transfected and transfected cells (low and high) are summarized in Fig. 3.4.2B. Both low and high CB-D_{28k} transfected cells exhibited a significant elevation in decay time constant while showing little differences in area under the time- concentration curve (AUC). AUC was 40.0609 ± 3.4060, 38.1086 ± 2.3368 and 47.2297 ± 5.6491 for non-transfected and CB-D_{28k} transfected (Low and High) cells (Fig. 3.4.2C; N=4, n=16) respectively. Decay time constant (τ) in non-transfected cells was 78.8181 ± 5.4602 as compared to 106.5425 ± 6.5024 and 212.5466 ± 23.8114 for low and high CB-D_{28k} transfected cells (Fig. 3.4.2D; N=4, n=16), respectively. We conclude that the transfection of Calbindin slows the time-to achieve peak amplitude in low Ca^{2+} concentrations, but simultaneously alters the kinetics of decay.

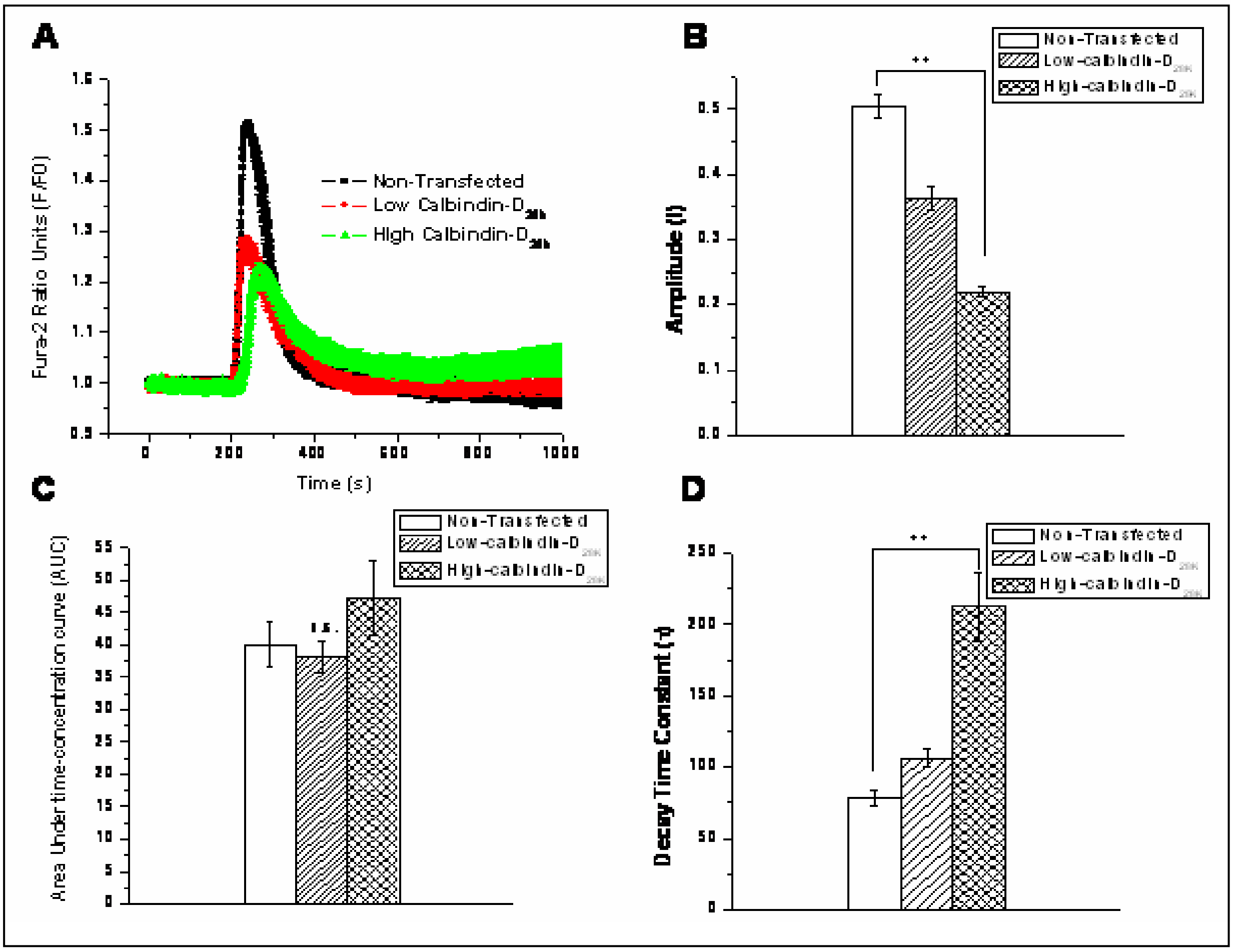

Fig. 3.4.2: The decay time constant (τ) of calcium transients is diminished in Calbindin-D_{28k} transfected cells. (A) Plots from transients with similar amplitudes were pooled (N= 4, n=16) for Calbindin-D_{28k} transfected (Low and High) and non-transfected cells after 60mM K^+ induced stimulus and the resulting amplitude trace - average standard error mean of 6 cells for each condition were plotted as a function of the time. (B) The bar diagram of the changes in peak amplitude are calculated as F/F0. (C) Area under the time-concentration curve (AUC) was calculated with the baseline 0. AUC was 40.0609 ± 3.4060, 38.1086 ± 2.3368 and 47.2297 ± 5.6491, respectively for non-transfected and Low & High CB-D_{28k} transfected cells (N=4; n=16). (D) Both low and high CB-D_{28k} transfected cells exhibited a significant decline in decay time constant compared to non-transfected cells (~ 2 times; N=4; n=16). Data are expressed as means ± S.E.M. N= Number of experiments for each conditions; n= Number of cells. $^{**}P<0.001$.

PART D

INHIBITION OF CALCIUM SIGNALING BY RILUZOLE AND MELATONIN ALONG WITH ITS IMPACT ON NEUROPROTECTION

3.5 Validation of Riluzole and Melatonin as a Neuroprotective Drug by Inhibition of Ca^{2+} Signaling in HMNs of WT and $SOD1^{G93A}$ Mice

The neuroprotective drug riluzole is a sodium channel blocker and an anti-excitotoxic drug having multiple effects on cellular signaling. Melatonin is recognized to be a potent cellular antioxidant and can efficiently scavenge toxic free radicals, ROS and associated reactants (Jou *et al.*, 2004). Present study employed a conventional imaging technique to determine how riluzole and melatonin rescue mitochondria mediated oxidative stress and dysfunction in ALS, by inhibition of Ca^{2+} signaling. It has been shown that $[Ca^{2+}]$i in HMNs increases in response to the stimulation with a mitochondrial electron transport complex IV inhibitor (Sodium azide/Cyanide) using Fura-2/AM as a Ca^{2+}-sensitive dye (Bergmann & Keller, 2004). In light of evidence that azide/cyanide blocked the mitochondrial electron transport chain in HMNs of ALS, riluzole's and melatonin's antioxidative neuroprotection mediated by blockage of sodium current followed by decrease in cytosolic calcium was verified. The effect of the neuroprotective drug Riluzole and Melatonin on the $[Ca^{2+}]_i$ concentration was measured, and the mechanism underlying riluzole and melatonin-modulated Ca^{2+} influx and Ca^{2+} release was evaluated. Data demonstrate that riluzole but not melatonin moderately inhibits Ca^{2+} signaling via multiple mechanisms of ion channel modulation. This drug targeted stabilization of mitochondria-related signal cascades might represent a useful strategy for clinical neuroprotection in ALS.

3.5.1 Riluzole mediate mild and reversible but delayed blockade of the $[Ca^{2+}]$i in Fura-2/AM loaded HMNs exposed to Na^+-azide in 14-15 weeks old symptomatic $SOD1^{G93A}$ transgenic mice

Riluzole (5µM) inhibits spontaneous Ca^{2+} signaling in neuroendocrine cells by activation of K^+ channels and inhibition of Na^+ channels (Beltran-Parrazal & Charles, 2003) whereas in contrast 50-500µmol/l Riluzole caused a mild and sustained plateau increase in $[Ca^{2+}]_i$ in a concentration dependent manner with an EC50=150µmol/l in MG63 human osteosarcoma and IMR 32 neuroblastoma cells (Chen *et al.*, 2001; Wang *et al.*, 2001). Previously it was shown that Riluzole upto 10µM neither affect the cell survival in DA neurons in primary culture nor the growth of SH-SY5Y cells. However, concentrations greater than 50µM have remarkable effect on cell survival (Storch *et al.*, 2000), therefore, here 100µM riluzole challenge with superfusate is used and the protective effects of riluzole in HMNs of 14-15 weeks old WT and corresponding symptomatic SOD1^{G93A} mice brain stem slices *in-vitro* were analyzed. We found that riluzole have nominal effect on cell survival and it slowly and reversibly inhibited Ca^{2+} oscillations in selectively impaired HMNs of symptomatic SOD1^{G93A} mice at higher concentrations (>50µM), whereas at lower concentrations there is no effect (data not shown).

In our experiments the effect of riluzole (100µM)-mediated inhibition of Na^{+}-azide (2mM) induced $[Ca^{2+}]$i release were determined with Fura-2 signals. As illustrated in Fig. 3.5.1A-D, 2mM Na^{+}-azide caused a rise in $[Ca^{2+}]$i transient by complex IV inhibition which goes to peak amplitude of 0.0866 ± 0.0238 and 0.0827 ± 0.0196 (F/F0; N=3, n=14), respectively in HMNs of WT and corresponding symptomatic SOD1^{G93A} mice. This peak Ca^{2+} transient comes to baseline over 1-2 min after wash. In the presence of 100µM riluzole, second application of 2mM Na^{+}-azide caused a rise in $[Ca^{2+}]$i transient which was 0.06535 ± 0.0168 and 0.04971 ± 0.0151 (F/F0; N=3, n=14), respectively in HMNs of WT and symptomatic SOD1^{G93A} mice. The overall inhibition of rise in $[Ca^{2+}]$i in presence of riluzole after second Na^{+}-azide application, in WT and SOD1^{G93A} mice might be due to partial inhibition of complex IV and not due to riluzole. We believe that 1-2 min wash after first Na^{+}-azide application is not sufficient enough to overcome disturbed metabolic state of slice and therefore it might contribute partially to overall inhibition in $[Ca^{2+}]$i increase when applying Na^{+}-azide second time together with riluzole. However, it is interesting to note that the inhibition of peak amplitude of $[Ca^{2+}]$i in symptomatic SOD1^{G93A} mice (F/F0= 0.04971 ± 0.0151) is prominent compared to WT mice (F/F0=0.06535 ± 0.0168; n=14; $P<0.05$, student's two sample t-test) after second application of Na^{+}-azide together with riluzole. The inhibition of peak amplitude of $[Ca^{2+}]$i increase in symptomatic SOD1^{G93A} mice might be attributed either to a mild blockade of Na^{+}-current by riluzole or direct reduction in the entry of Ca^{2+} through voltage-dependent Ca^{2+}-channels after first Na^{+}-azide application. To discern between these two possibilities, the effect of riluzole on WT and corresponding symptomatic SOD1^{G93A} mice was examined under the condition where riluzole is applied through the superfusate in the continuous presence of Na^{+}-azide (Fig. 3.5.1C). Continuous presence of Na^{+}-azide together with riluzole did not alter the peak of [Ca^{2+}]i transient in WT mice and had no significant effect on the Na^{+}-current induced blockade of [Ca^{2+}]i transient. However, in symptomatic SOD1^{G93A} mice, the presence of Riluzole diminished Na^{+}-azide induced [Ca^{2+}]i increase slightly and delayed the baseline recovery by upto 30-60s. These results indicate that riluzole moderately inhibits [Ca^{2+}]$_i$ signaling by moderate blockade of extracellular Na^{+} influx via Na^{+}-channels and intracellular Ca^{2+} release from the mitochondria via an as yet unidentified mechanism(s). Riluzole's inhibition of excitability and Ca^{2+} signaling may be involved in its multiple effects on cellular function in the nervous system.

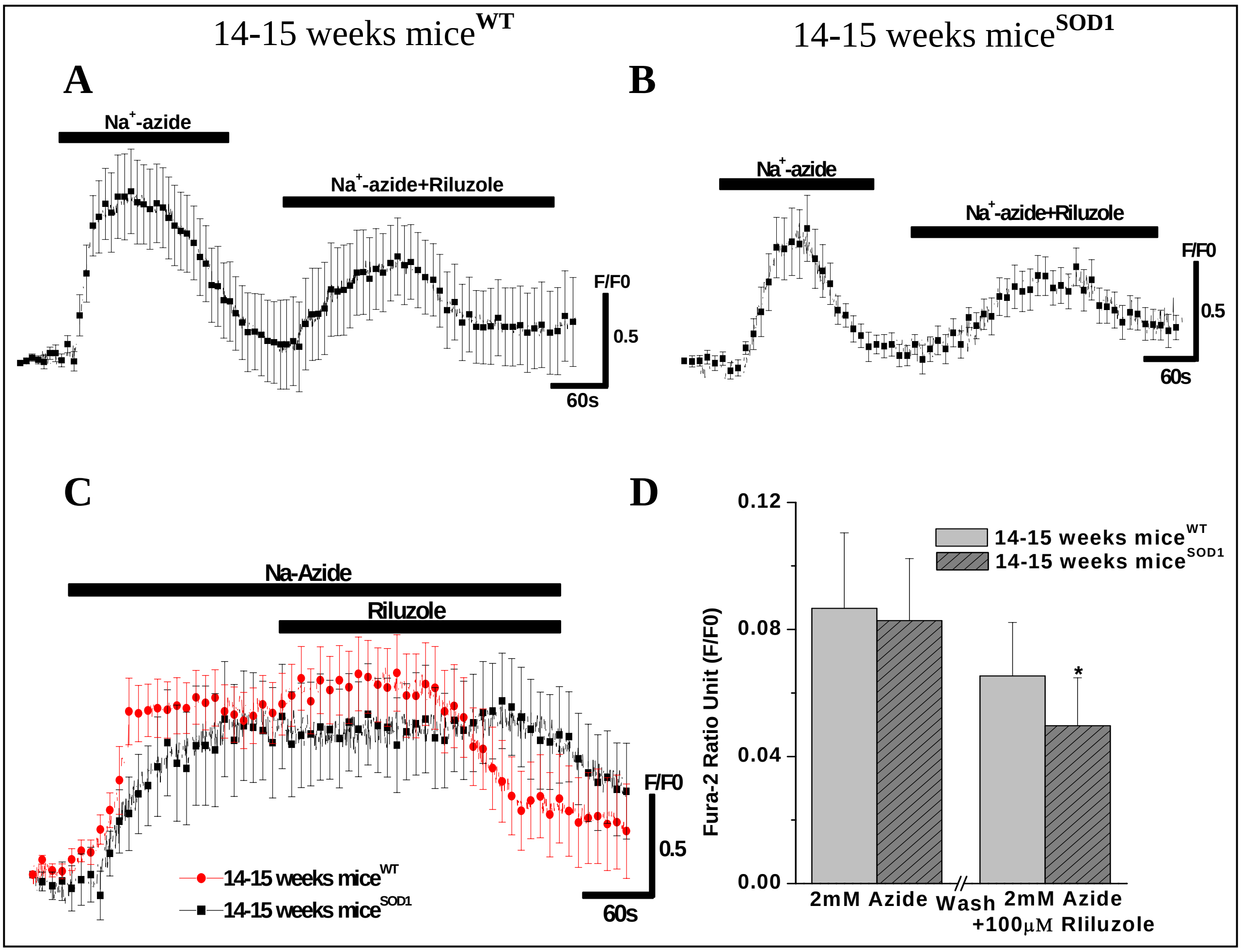

Fig. 3.5.1: Riluzole induce inhibition of the [Ca^{2+}]i in fura-2 AM loaded HMNs exposed to 2mM Na^{+}-azide in WT and symptomatic SOD1^{G93A} mice. (A) 2mM Na^{+}-azide was added in superfusate alone and together with 100µM riluzole and the fluorescence signal was recorded in 14 week old WT mice brain stem slices. (B) 2mM Na^{+}-azide was added to superfusate alone and together with 100µM riluzole and the fluorescence signal was recorded in 14 week old symptomatic SOD1^{G93A} brain stem slices. (C) 100µM riluzole was added to superfusate in the continuous presence of 2mM Na^{+}-azide and the fluorescence signal was recorded in WT and symptomatic SOD1^{G93A} mice brain stem slices. (D) A bar diagram of effect of Na^{+}-azide on [Ca^{2+}]i before wash and effect of 100µM riluzole on Na^{+}-azide induced blockade of [Ca^{2+}]i after wash was measured in WT (Light gray) and symptomatic SOD1^{G93A} (Gray sparse) mice brain stem slices. Data are expressed as mean from 4-5 cells in an imaging field for (A), (B) and (C) from three independent experiments performed from three independent WT and corresponding SOD1^{G93A} mice littermates. The changes in peak amplitude are calculated as F/F0

(360 / 390). **P*<0.05 compared with WT and SOD1^{G93A} mice. Data are expressed as means ± S.D.; N=3, Number of experiments for each genotype; n= 14, Number of cells.

3.5.2 Melatonin fails to block [Ca^{2+}]i signaling through Na^{+}-channels in Fura-2/AM loaded HMNs in WT and corresponding symptomatic SOD1^{G93A} mice

Previously, it was shown that antioxidant melatonin increases the activity of complex I and IV of electron transport chain, thereby improving mitochondrial respiration, energy metabolism and increasing ATP synthesis under normal conditions as well as during stress (Leon *et al.*, 2005). These effects reflect the ability of melatonin to reduce harmful dysfunction in mitochondria mediated injury. In addition, few reports of a treatment and direct action of melatonin as a candidate compound for neuroprotection in ALS (Jacob *et al.*, 2002) have opened a new prospective for us to validate and understand the action of melatonin on the Na^{+}-azide induced [Ca^{2+}]$_i$ signaling in WT and corresponding symptomatic SOD1^{G93A} mice.

In the present work illustrated in Fig. 3.5.2 showed that melatonin (100µM) does not alter either the free [Ca^{2+}]$_i$ or inhibit effect of azide on complex IV, in WT and corresponding SOD1^{G93A} mice at symptomatic stage of motor dysfunction. The results in Fig. 3.5.2 show that the blockade of complex IV by 3mM Na^{+}-azide caused a rise in [Ca^{2+}]i transient peak amplitude in concentration dependent manner (For comparison see Fig. 3.5.1A-E) and was 0.1351 ± 0.0307 and 0.1299 ± 0.0339 (F/F0; N=3, n=14) respectively, in brain stem slices of WT (Fig. 3.5.1A and E) and corresponding symptomatic SOD1^{G93A} mice (Fig. 3.5.1B and E). In the presence of 100µM melatonin, second application of 3mM Na^{+}-azide caused a rise in peak [Ca^{2+}]i transient which was 0.0797 ± 0.0201 and 0.0753 ± 0.0239 (F/F0; N=3, n=14; Fig. 3.5.1 A, B and E), respectively in WT and symptomatic SOD1^{G93A} mice.

As describe earlier, the overall inhibition of elevation of [Ca^{2+}]i in presence of melatonin after second application of azide in WT and SOD1^{G93A} might be due to potential inhibition of complex IV itself by Na^{+}-azide and not due to the effect of melatonin. There are nominal differences in inhibition of rise of [Ca^{2+}]i peak amplitude in SOD1^{G93A} mice (F/F0 = 0.04971 ± 0.0151, Fig. 3.5.2 E) compared to WT mice (F/F0 = 0.06535 ± 0.0168; n=14; Fig. 3.5.2 E, *P*<0.05, students two sample t-test) of the same littermate after second application of Na^{+}-azide together with melatonin. To check whether continuous presence of Na^{+}-azide together with melatonin has any impact on neuroprotection, effect of 3mM melatonin on the WT and

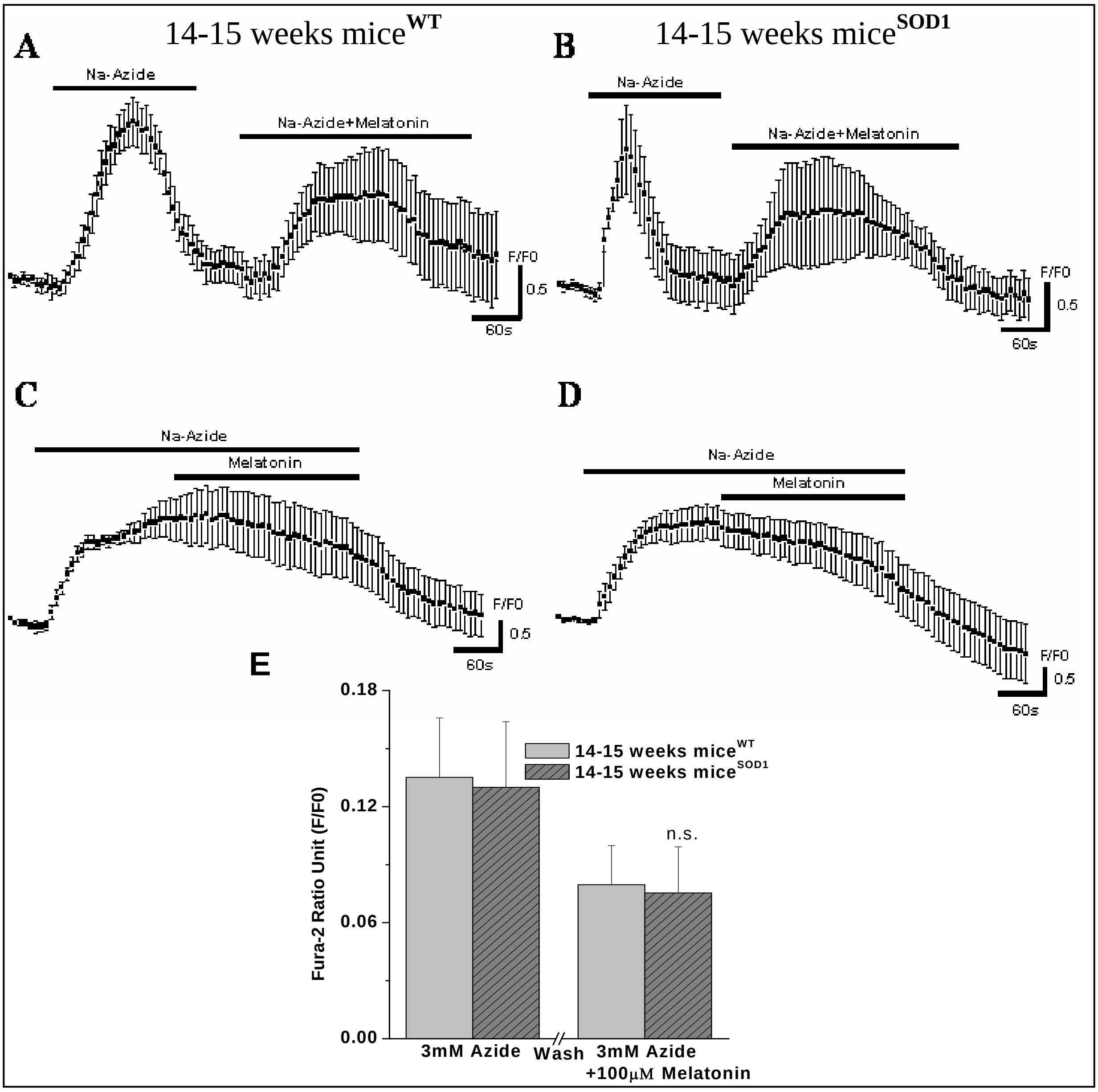

Fig. 3.5.2: Effect of 100µM Melatonin on inhibition of the $[Ca^{2+}]i$ in fura-2 loaded HMNs cells exposed to 3mM Na^+-azide in WT and symptomatic $SOD1^{G93A}$ mice littermates. (A) 3mM Na^+-azide was added in superfusate alone and together with 100µM melatonin and the fluorescence signal was recorded in WT brain stem slices. (B) 3mM Na^+-azide was added alone and together with 100µM melatonin in superfusate and the fluorescence signal was recorded in symptomatic $SOD1^{G93A}$ mice brain stem slices. (C) 100µM melatonin was added in the superfusate in the continuous presence of 3mM Na^+-azide and the fluorescence signal was recorded in WT mice brain stem slices. (D) 100µM melatonin was added in the continuous presence of 3mM Na^+-azide and the fluorescence signal was recorded in symptomatic $SOD1^{G93A}$ mice brain stem slices. (E) A bar diagram of effect of Na^+-azide on $[Ca^{2+}]i$ before wash and effect of 100µM melatonin on Na^+-azide induced blockade of $[Ca^{2+}]i$ after wash was measured in WT (Light gray) and $SOD1^{G93A}$ (Gray sparse) mice brain stem slices. Data are expressed as mean from 4-5 cells in an imaging field for (A), (B), (C) and (D) from three independent experiments performed in different genotypes. The changes in peak amplitude are calculated as F/F0 (360/390). **P*<0.05 compared with WT and $SOD1^{G93A}$ mice before and after the wash. There is no significant difference between WT and $SOD1^{G93A}$ mice before and after 100µM melatonin application after wash. Data are expressed as means ± S.D.; N=3, Number of experiments for each genotypes; n= 14, Number of cells.

symptomatic SOD1^{G93A} mice brain stem slices was examined under the condition where melatonin is applied in the continuous presence of Na^{+}-azide (Fig. 3.5.2 C, D and E). Continuous presence of Na^{+}-azide together with melatonin did not alter the peak [Ca^{2+}]i transient in WT and SOD1^{G93A} mice and had no significant effect on Na^{+}-current induced blockade of [Ca^{2+}]i transient. These results indicate that the melatonin-mitochondria neuroprotective action in ALS might be governed by Complex I inhibition or by as yet unknown mechanism(s).

These two observations may be relevant to understanding the selective vulnerability of motoneurons to the excitotoxic insult that may contribute to the etiopathology of ALS. In brief, depolarization-evoked calcium transients of MNs are slightly blocked by riluzole, thus providing a mechanistic basis for the activity of this drug in the treatment of ALS.

PART E

CALCIUM AND ΔΨm DYANAMICS OF MNs-GLIA NETWORK IN RAT BRAIN STEM SLICES THAT ARE PARTICULARLY VULNERABLE IN ALS-RELATED MOTONEURON DISEASE

3.6 Dynamic Calcium Signaling between Neuron-Glia and its implications in Physiology and Pathophysiology

Calcium homeostasis is vital for development and survival of almost all types of cells including MN and glia of the CNS. For decades, astrocytes, oligodendrocytes and microglia-the major glial cell types in the CNS have been considered to be non-excitable support cells of the brain, which merely acting as a 'brain glue'(Volterra & Meldolesi, 2005). However, recent recognition that they are endowed with a rather sophisticated group of Ca^{2+}-permeable receptors and channels, as well as SOCS and pumps, all of which determine Ca^{2+} homeostasis has changed this view radically and enabled us to develop an understanding of the function of glia in physiology and pathophysiology. In addition, glial cells sense functional activity in neighboring neurons and respond to external stimuli such as neurotransmitters, hormones, ETS blockers or even mechanical stress by means of generating complex changes in the Ca^{2+} signals that can modulate synaptic interactions. Ca^{2+} overloads resulting from dysregulation of channels and pumps controlled by interplay of different mechanisms including plasmalemmal and intracellular Ca^{2+} channels, Ca^{2+} transporters and Ca^{2+} buffers can be deleterious to glia, like with neurons. Ca^{2+} signaling is also an important medium for neuron-glia interaction and an instrument by which glia integrate and propagates signals in the CNS, in spite of the fact that glial cells are not equipped with proper channels to generate action potentials (Cornell-bell *et al*., 1990). Today, glial cells are seen as local communication elements of the brain that can generate a variety of regulatory signals and conduit structures from neuronal to vascular networks that are otherwise disconnected from each other. We studied Ca^{2+} homeostasis in glial cells and its cross-talk with MNs, their specific and essential roles in normal physiological processes and the consequences of its alteration in cell demise in neurological disorders including ALS that involve not only loss of MNs but also glial cell specific malfunction.

3.6.1 Loading of Calcium sensitive dye and identification of glial cells distinct from motoneurons in brain stem slices

We used freshly prepared 400µm and rhythmic 700µm-thick brain stem slices from neonatal rat (P0-P4) containing HMNs and glial cells. The slices were loaded by incubating them (see materials and methods section) as well as by utilizing a versatile approach of targeted staining based on pressure injection of the dye (Ca^{2+}-sensitive dye Fluo-4 and $\Delta\Psi m$ dye Rhod 123) into the tissue of interest and this can be also used for a large spectrum of other indicator dyes. In brief, membrane-permeable Ca^{2+}-sensitive dye Fluo-4 AM (0.5mM in superfusate) and $\Delta\Psi m$ dye Rhod 123 was backfilled into a broken patch pipette (outer diameter, 5-10µm) and pressure (0.7-1.0 psi) injected for 15 min into the hypoglossal region (XII) of the slice from the caudal surface. Within 15-20 min after injection, labeling revealed basic neuronal morphology and on the basis of morphological appearance, most brightly labeled cells were glial cells in accordance with the recent observation using the same pressure injection technique of Ca^{2+} indicator dye (Stosiek *et al.*, 2003; Hirase *et al.*, 2004) whereas MNs have a typical feature containing soma and dendrites. Stained areas (Hypoglossal, XII) were 300-400µm in diameter (Fig. 3.6.1a). Fluorescence signals were measured using either a confocal or a 2-photon system at tissue depth range from 30-60µm for confocal and 40-80µm for 2-photon microscopy (Fig. 3.6.1b). Most intensive labeling occurs between 30-50µm below the slice surface. The diminished fluorescence intensity on the slice surface is probably due to the diluting effect of the washout procedure in the superficial tissue. Though the labeling was dense- soma, dendrites, glia and numerous allied processes, including vessel-containing end feet of single astrocytes could be clearly revealed (Fig. 3.6.1b).

In our initial experiments, for comparison of efficiency of dye loading procedures, we found that in bath loading procedure of Ca^{2+}- sensitive Fluo-4 dye or mitochondrial Rhod-2 dye, neurons did not load properly and appeared as black holes (red arrow, Fig. 3.6.1b) with circular punctate staining, whereas in pressure injection procedure Ca^{2+}- sensitive Fluo-4 dye, Rhod-2 dye as well as mitochondrial membrane potential Rhod 123 dye stained both glia and MNs quite efficiently with distinct features and bright robust fluorescence. Rhod 123 dye staining is equally good with bath loading procedure as well. The loading quality is same for 400µm non rhythmic as well as 700µm rhythmic (Data not shown) thick brain stem slices.

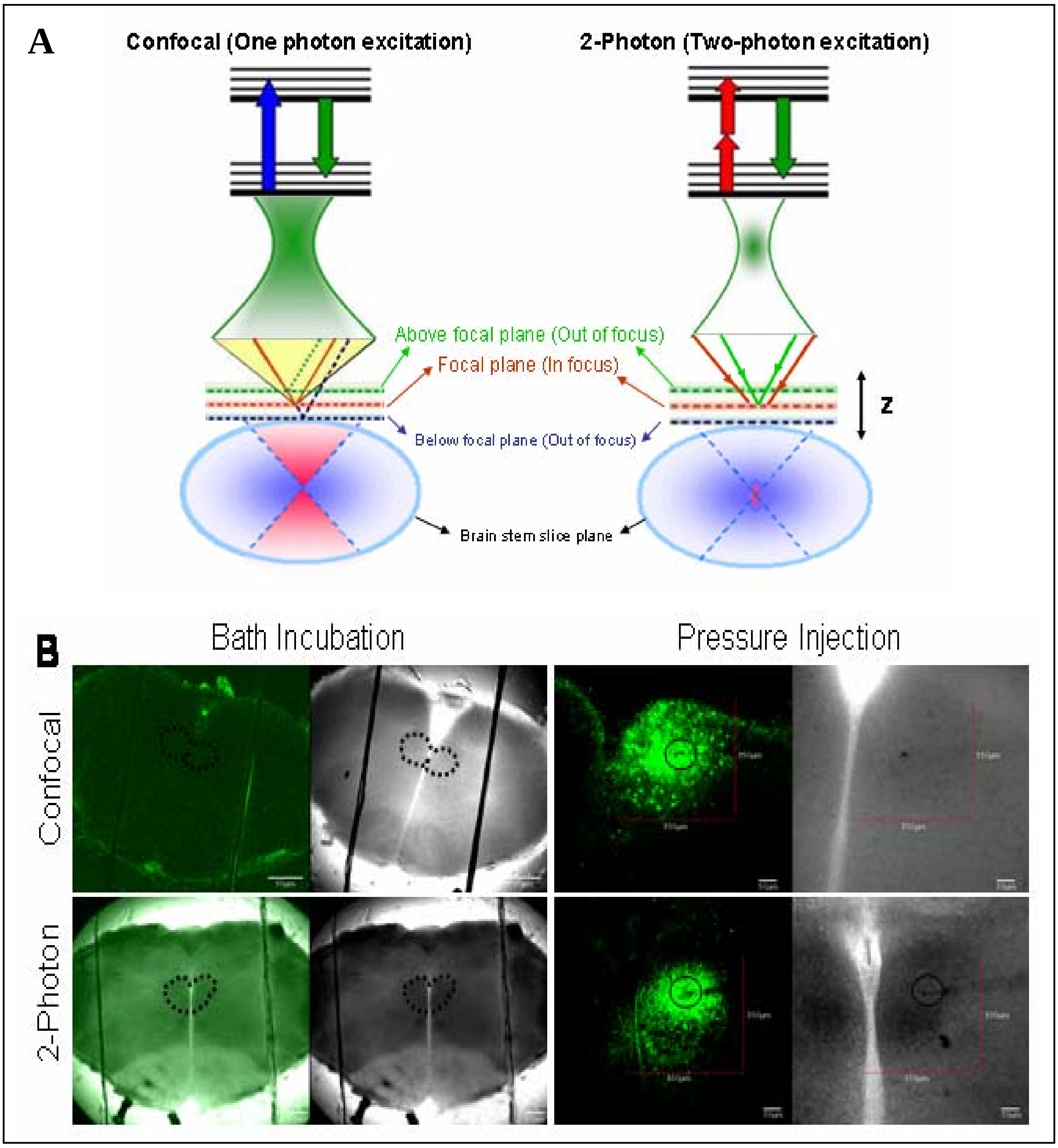
A
Confocal (One photon excitation)
2-Photon (Two-photon excitation)
Above focal plane (Out of focus)
Focal plane (In focus)
Below focal plane (Out of focus)
Z
Brain stem slice plane
B
Bath Incubation
Pressure Injection
Confocal
2-Photon

Fig. 3.6.1a: Schematic drawing, staining procedure and methodology for staining of the slices. (A) Schematic drawing of the confocal (one-photon excitation) imaging compared to 2-photon in scattered tissue. Due to the longer wavelength, less excitation light is scattered when using 2-photon excitation imaging. Ballistic and diffusing fluorescence photons can be used in the case of 2-photon microscopy, but only ballistic photons can be used in the case of confocal microscopy. In a confocal microscope, the detector must be at the same distance as the light source from the illuminated portion of the sample to effectively block the out-of-focus light. The position of the detector in a 2-photon system is variable. (B) Photomicrographs of the Fluo-4 stained slices by bath incubation (left) and targeted pressure injection (right) before wash in 400µm brain stem slices from P1 rat at low magnification (4X objective) using confocal (Up) and 2-photon (Down) microscope. On the left side, the region of interest marked with black dotted lines in slices surrounding the hypoglossal nucleus paramedian, ventral of the central channel. On the right side, slice photomicrographs illustrating the diameter of the stained area varies between 300-400µm in confocal (Up) and 2-photon (Down) microscopy.

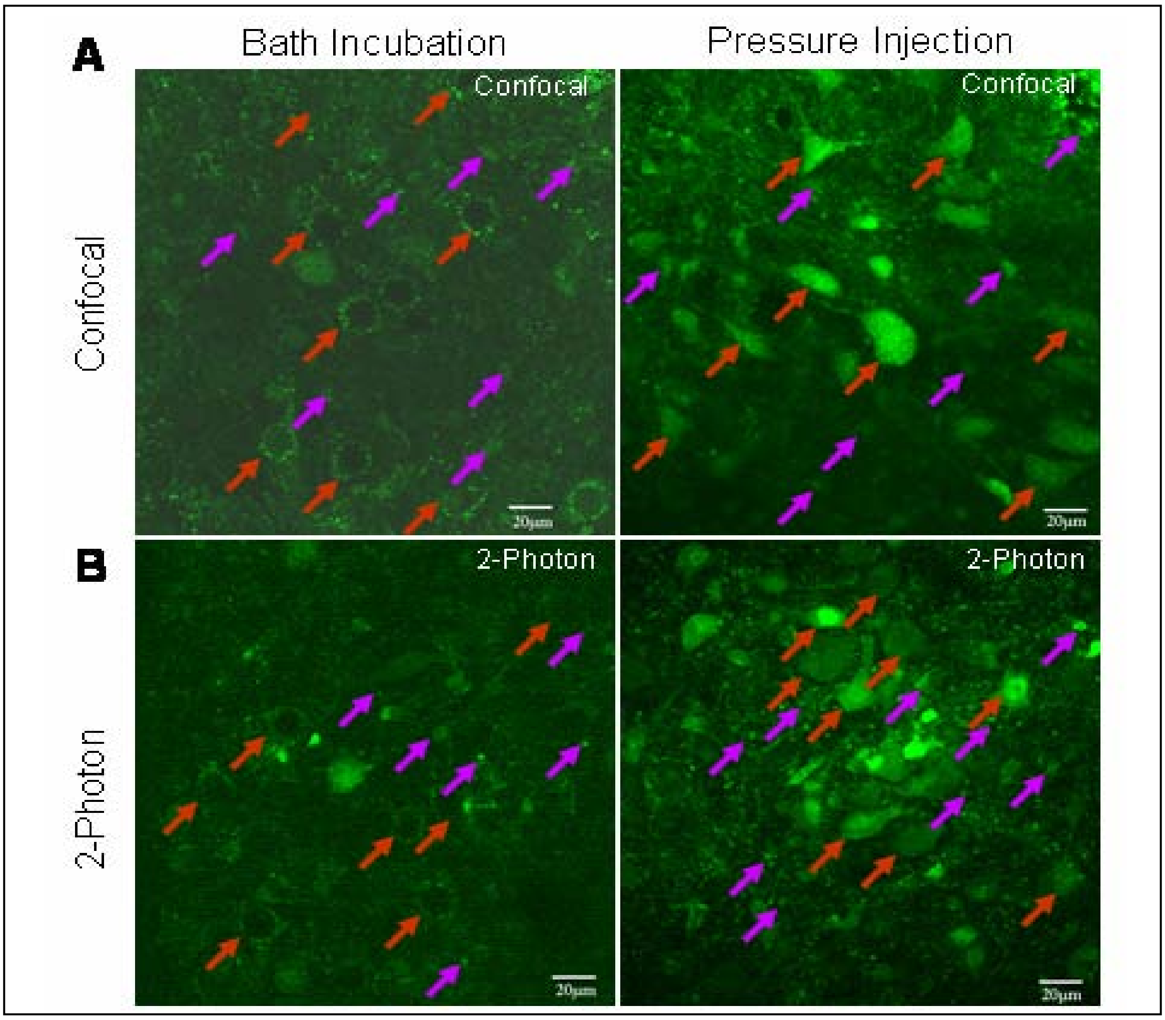

Fig. 3.6.1b: Confocal laser scanning and 2-photon microscope photomicrographs of Fluo-4 loaded slices by bath incubation and pressure injection in neonatal rat (P1) at higher magnification (20X objective) with 3x zoom. (A) Rat brainstem slice (P1; 400µm thick) seen in fluorescent light stained by bath incubation (left) and pressure injection (right) with 3x zoom magnification using confocal microscope. (B) Rat brain stem slice (P1; 400µm thick) seen in fluorescent light by bath incubation (left) and pressure injection (right) with 3x zoom magnification using 2-photon microscope. Red arrows point to HMNs, whereas pink arrows point to glial cells. Scale bar =20µm.

3.6.2 Spontaneous Calcium oscillations in brain stem glial cell network: endogenous Ca^{2+} excitability

Glial cells exhibit an endogenous excitability manifested as spontaneous intracellular Ca^{2+} oscillations that occur in the absence of neuronal activity. Indeed, some recent evidences support the idea that these spontaneous oscillations may serve towards proper development and maturation of the neuronal network and as an autonomous source of glutamate for generation and modulation of neuronal activity (Parri *et al.*, 2001). Previously, these spontaneous Ca^{2+} oscillations have been observed *in-situ* in astrocytes from different brain areas, such as thalamus (Aguado *et al.*, 2002; Parri *et al.*, 2001), hippocampus (Nett *et al.*, 2002), cerebellum(Aguado *et al*., 2002; Grosche *et al*., 1999), cortex (Hirase *et al*., 2004) and neocortex (Peters *et al*., 2003). However, the functional connotation of these spontaneous Ca^{2+} oscillations in brain stem slice preparation of hypoglossal region remains to be fully explored. In our experiments (N=12 slices), cells in hypoglossal region with glial appearance were selected for short term monitoring (200s). A representative experiment was shown in Fig. 3.6.2 where 12 glial cells have variety of spontaneous oscillation activity profile. Most of the glial cells show $[Ca^{2+}]$i spikes (≥ 20% increase in ΔF/F between 0-200s; glial cells:1,2,4,5,6,8,9; Fig. 3.6.2) which last for ~15-20s and remaining plateau (glial cells:3,7,10,11,12; Fig. 3.6.2) which last for ~25-30s.

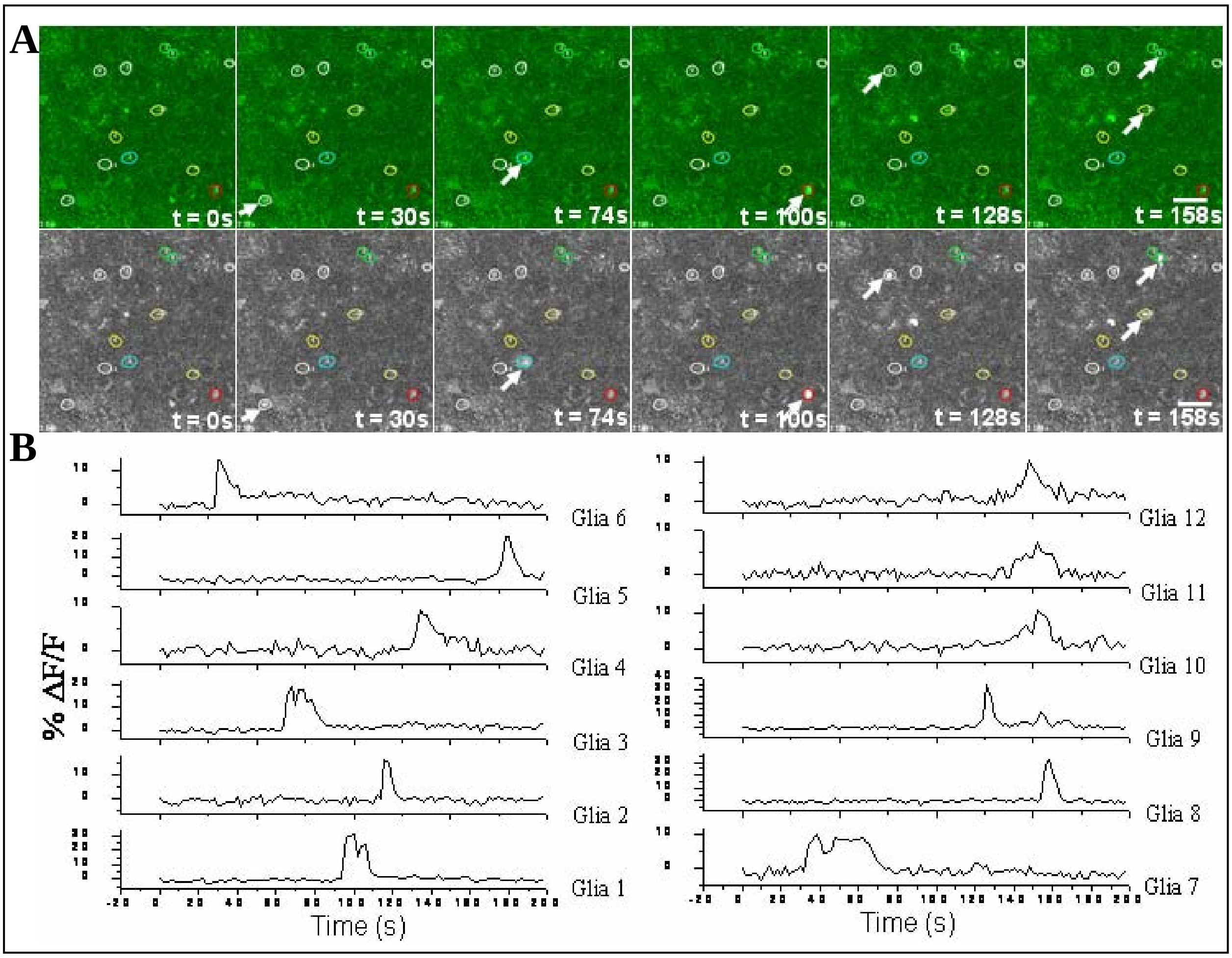

Fig. 3.6.2: Representative spontaneous Ca^{2+} oscillations in glial cell network. (A) Spontaneous intracellular Ca^{2+} waves in Fluo-4 loaded rat hypoglossal region in glial cells. Glial cells were bulk loaded with Ca^{2+}- indicator dye Fluo-4 to monitor the light induced Ca^{2+}- elevations. Images in the pseudocolor mode (Up: green; down: gray scale) represent fluorescence intensity of spontaneous Fluo-4 emission taken during light stimulation of cells at different time scale indicated (0, 30, 74, 100, 128, 158s). Zero time corresponds to the time of light stimulation. Spontaneous activity is indicated with white arrows at different time scale. (B) Spontaneous Ca^{2+} oscillation activity profile in the hypoglossal rat brain stem glial cell network. Glial cells:1,2,4,5,6,8, and 9 shows spike like activity whereas glial cells:3,7,10,11 and 12 shows plateau like Ca^{2+} waves. Scale bar = 40µm.

3.6.3 Intracellular Ca^{2+} waves: glia-to-glia communication in brain stem slice network

Previously, studies in cultured astrocytes confirmed that elevations in Ca^{2+} levels originated in one astrocyte can propagate non-decrementally to neighboring astrocytes, forming Ca^{2+} waves that can extend for several hundred micrometers (Cornell-bell *et al*., 1990; Charles *et al*., 1991). Studies in corpus callosum glial cells showed that Ca^{2+} waves depend on Ca^{2+} release from internal calcium stores (Schipke *et al*., 2002). Therefore, Ca^{2+} elevations that form Ca^{2+} waves may serve as a form of long-range intercellular communication between astrocytes. Though, Ca^{2+} waves have been evidently demonstrated and carefully characterized in cell culture preparations (Charles *et al*., 1991; Araque *et al*., 1998), in organotypic brain slices (Harris-White *et al*., 1998), and in cortical astrocytic networks (Hirase *et al*., 2004), their existence in intact preparations such as acute brain stem slices has barely been studied and is still controversial. Glial cell Ca^{2+} waves have also been observed in hippocampal and cortical slices (Aguado *et al*., 2002) where they have been associated with the “cortical spreading depression”, a phenomenon evoked in ischemia and brain trauma. Recently, Sul *et al*., showed in hippocampal slices that Ca^{2+} elevations in single astrocytes may spread to some , but not all, neighboring cells, and that the number of responding astrocytes may be regulated by the exogenous application of drugs suggesting the existence of plastic functional circuits between astrocytes.

To identify whether and how glia-to-glia communication in the brain stem slice network occurs, and whether it is executed by extracellular or by intracellular molecules, we stimulated 400µm thick brain stem slices chemically by bath application of glutamate (1mM, 10s; Fig. 3.6.3). We show here that glia are interconnected by gap junctions and can form large syncytium propagating Ca^{2+} waves within glial syncytium after 1mM glutamate induced $[Ca^{2+}]i$. This propagating Ca^{2+} signal travel like a wave with a distance over 100µm as also shown earlier in organotypic cultures (Dani *et al*., 1992).

3.6.4 Glutamate induced $[Ca^{2+}]i$ signaling in motoneuron-glia network in rat brain stem slices: implications for ALS

Astrocytes, microglia, and oligodendrocytes express a wide variety of glutamate receptors and transporters that mediate many of the deleterious effects of glutamate. Glutamate is not only the prime excitatory neurotransmitter in the CNS, but is also a powerful neurotoxin that can slay nerve cells in at least two ways: by excitotoxicity and by receptor-independent mechanisms.

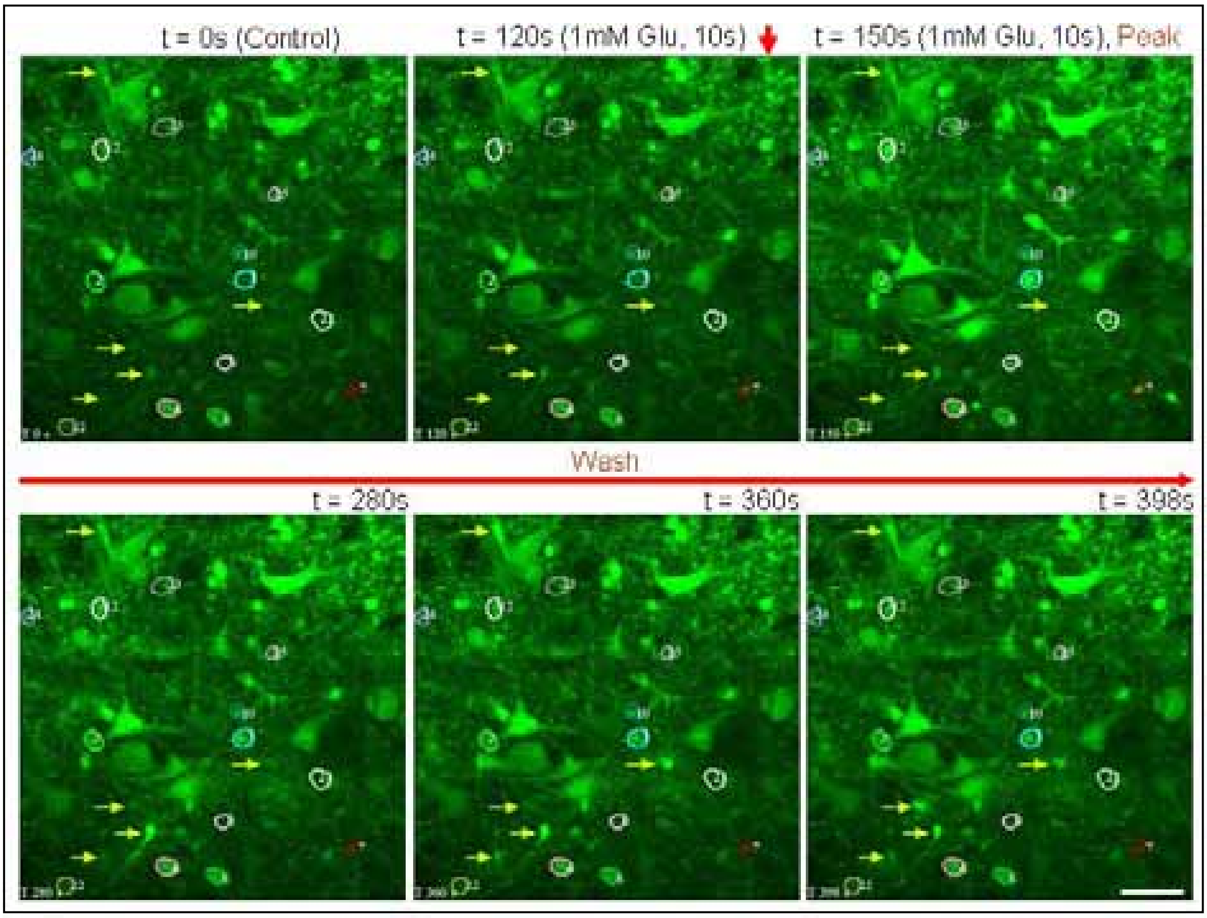

Fig. 3.6.3: Propagation of Ca^{2+} waves in a rat brain stem slice network. A series of fluorescence images just before (0s, control) and at different time intervals (as indicated) after glutamate stimulation (1mM, 10s) illustrates the Ca^{2+} signals within slice glia-to-glia network. The position of the glutamate stimulation marked by red arrow and spread of Ca^{2+} waves in the network during washing were marked by yellow arrows. Flow of the bath indicated with red horizontal arrow. Scale bar = 40µm.

Excessive glutamate signaling can lead to excitotoxicity, a phenomenon whereby over activation of GluRs initiate cell demise, occurs in virtually all neurons that express GluRs (Olney, 1969; Olney & Sharpe, 1969; Matute *et al.*, 2006). Although astrocytes express functional GluRs, they are generally resistant to excitotoxic insults and vulnerability varies from region to region. Prolonged exposure of glial cells (cultured hypothalamic astrocytes) to glutamate does not affect their viability (Prieto & Alonso, 1999). In contrast, similar insults have been reported to alter neurite formation in some studies, while in others it has been reported to kill neocortical astrocytes (David *et al*, 1996). There is evidence that sustained activation of ionotropic GluRs can also kill astrocytes and microglia.

It appears that all macroglial cells differentially express the three major GluTs present in the CNS. These transporters maintain basal levels of extracellular glutamate in the range of 1–2 µM and thus, prevent over-activation of GluRs under physiological conditions. Compelling evidences suggest that disturbed glutamate uptake by glial cells is directly involved in the pathogenesis of ALS. In fact, there is evidence that in brain stem astrocytes of patients with sALS, aberrant splicing of EAAT2 suppresses protein expression. In fALS with mutations in the mitochondrial Cu/Zn SOD1 gene, ROS are formed in MNs following mitochondrial Ca^{2+} overload. ROS inhibit astroglial EAAT2 activity, which leads to extracellular accumulation of glutamate. Glutamate excitotoxicity has also been implicated in acute injury to the CNS and in chronic neurodegenerative disorders (Choi, 1988; Lipton & Rosenberg, 1994). During the past few years, it has been shown that glutamate can also be toxic to glial cells, including astrocytes (Haas & Erdo, 1991) and oligodendrocytes (McDonald *et al*., 1998; Matute *et al*., 1997; Matute *et al*., 2006). Moreover, glutamate can also damage nerve cells by mechanisms that do not involve receptor activation, but rather glutamate uptake (Oka *et al.*, 1993). An emerging hypothesis is that the disease is not one of MNs in isolation, but interactions between MNs and surrounding glial cells might be integral to the pathogenesis (Appel & Simpson, 2001).

In the present study, we have explored the two different staining procedures (Incubation and Injection) and microscopy methods (Confocal and 2-photon) to evaluate whether massive stimulation of glutamate receptors induces Ca^{2+} dysregulation and excessive mitochondrial depolarization in the MNs-Glia network of rat brain stem slice preparation. In our experiments, in bath staining procedure, application of glutamate (1mM) for 10s resulted in a weak rise of $[Ca^{2+}]i$ peak fluorescence intensity and transients for glia is 81.74 ± 4.76 (% ΔF/F; N=3, n=30) whereas for MNs it is 22.84 ± 3.31 (% ΔF/F; N=3, n=14; $p<0.001$ compare to glia). In pressure injection procedure, rise in $[Ca^{2+}]i$ peak fluorescence intensity for glia and MNs is 144.36 ± 5.07 (% ΔF/F; N=3, n=54) and 98.89 ± 13.23 (% ΔF/F; N=3, n=25; $p<0.001$ compare to glia) respectively (Fig. 3.6.4a). In incubation procedure, both in glia and MNs $[Ca^{2+}]i$ returns to baseline after ~3 min wash. However, in injection procedure, $[Ca^{2+}]i$ levels returned to a value within 10% of the initial baseline.

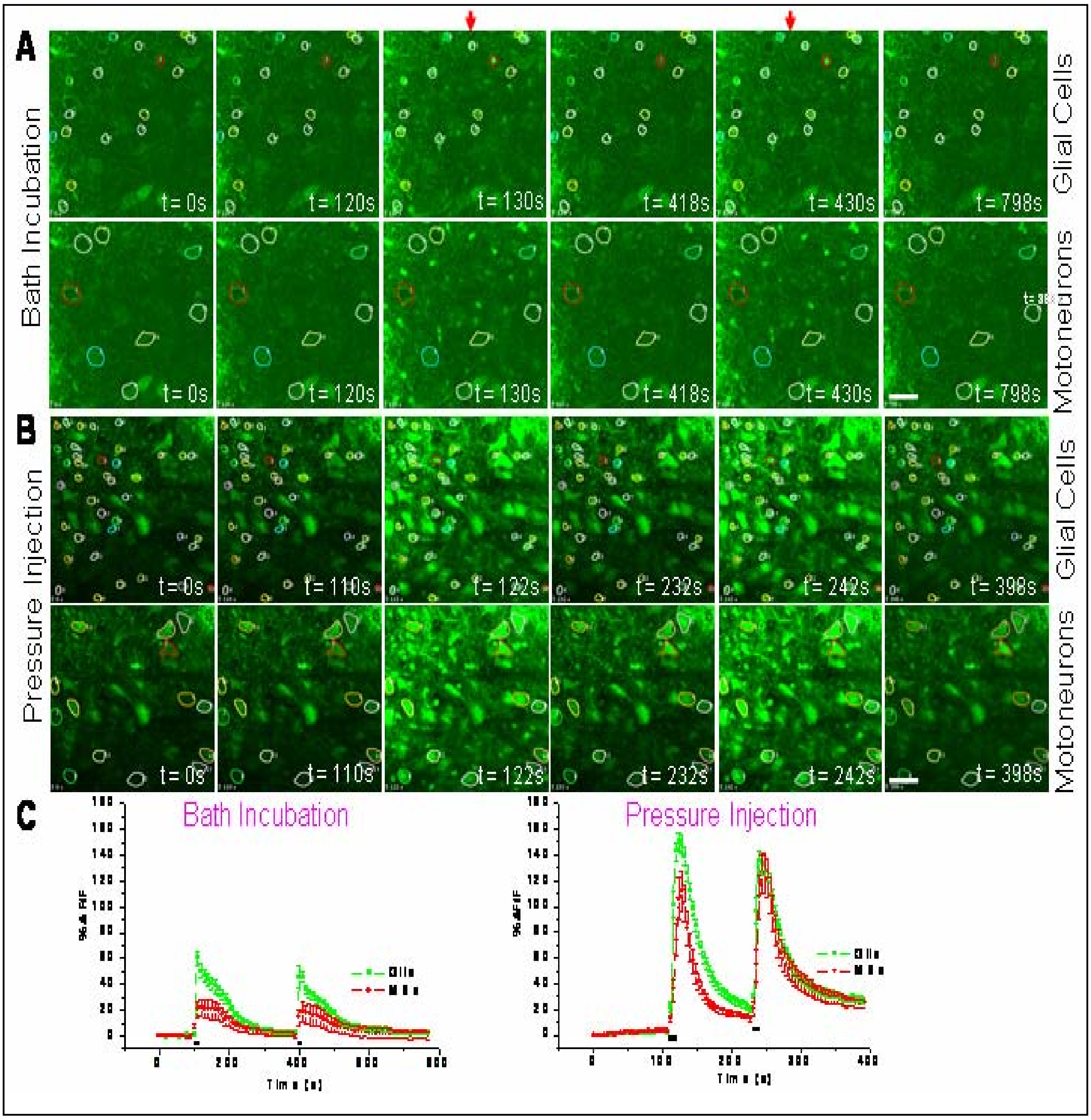
A
Bath Incubation
Glial Cells
Motoneurons
t= 0s
t= 120s
t= 130s
t= 418s
t= 430s
t= 798s
B
Pressure Injection
Glial Cells
Motoneurons
t= 0s
t= 110s
t= 122s
t= 232s
t= 242s
t= 398s
C
Bath Incubation
Pressure Injection
%ΔF/F
Time (s)
Glia
MNs
0
20
40
60
80
100
120
140
160
180
200
300
400
600
800

Fig. 3.6.4a: Glutamate induced variations in [Ca^{2+}]i fluorescence of MNs-glia network in rat brain stem slices loaded with Ca^{2+} indicator dye Fluo-4 applying bath staining and pressure injection procedure. (A) A series of digital fluorescence photomicrographs just before (t=0s, control) glutamate induced initial response (t=120s, 418s, 1mM glutamate for 10s) and at defined time intervals (as indicated) after glutamate induced peak fluorescence intensity (130s, 418s) in glia (up) and MNs(down) of rat brain stem slice network stained with bath loading procedure. The positions of the glutamate induced peak fluorescence intensity were marked with red arrows. (B) A series of digital fluorescence photomicrographs just before (t=0s, control), glutamate induced initial response (t=110s, 232s, 1mM glutamate for 10s) and at defined time intervals (as indicated) after glutamate induced peak fluorescence intensity (122s, 242s) in glia (up) and MNs(down) of rat brain stem slice network stained with pressure injection procedure. The positions of the glutamate induced peak fluorescence intensity were marked with red arrow. (C) Traces (Left, incubation: 13 glial cells, 7 MNs; Right, injection: 26 glial cells, 7 MNs) showing average mean fluorescence intensity normalized to base-line values, as a function of time in glial cells (green) and MNs (red) network in rat brain stem slices for a single representative experiment. Position of glutamate (1mM, 10s, 2 times) applications were indicated with solid black bars between the traces and the horizontal axis. Scale bar = 40µm.

On the basis of the above experiments, following conclusions are drawn: pressure injection staining technique is better compared to bath staining procedure for Fluo-4 Ca^{2+} indicator dye to load glia and MNs efficiently. The glutamate induced fluorescence intensity for MNs in injection procedure is ~6.32 times greater as compared to bath incubation procedure ($p<0.001$). So in the next set of experiment, we utilized the pressure injection technique as a standard protocol. Importantly, in pressure injection technique background signals are significantly reduced as compare to bath loading procedure where the dye is distributed not only to MNs and glia, but throughout the whole slice. Moreover, the baseline recovery after glutamate application for bath loading staining procedure is slightly delayed compared to pressure injection procedure.

In the next set of experiments, two different microscopy methods (Confocal and 2-photon) was evaluated for the suitability of the methods and to determine the efficiency of confocal and 2-photon microscopy for glutamate evoked Ca^{2+} elevation. Application of glutamate (1mM) for 10s evoked an immediate response which is quite similar in transient and peak fluorescence intensity for confocal and 2-photon microscopy. Confocal imaging of glutamate (1mM,10s) induced rise in peak fluorescence intensity of $[Ca^{2+}]i$ for glia is 105.78 ± 6.44 (% $\Delta F/F$; N=3, n=33) whereas 47.08 ± 5.44 (% $\Delta F/F$; N=3, n=15) for MNs. Imaging through 2-photon microscopy resulted in a very similar transient of glutamate induced $[Ca^{2+}]i$ peak fluorescence intensity which is 100.47 ± 3.29 (% $\Delta F/F$; N=4, n=48) for glia ($p>0.05$, not significant difference compare to confocal). However, glutamate induced peak fluorescence intensity of $[Ca^{2+}]i$ for MNs is surprisingly high compared to confocal microscopy and is 80.56 ± 6.26 (% $\Delta F/F$; N=4, n=35; Fig. 3.6.4b; ~1.7 times, $p<0.005$ significant compare to confocal).

Several experiments were done to test the efficiency of the methods (4±1 slice for each experiment separately from 4±1 rat) and it was found that both confocal and 2-photon imaging gave efficient and suitable recordings. Though, in 2-photon imaging glutamate induced Ca^{2+} responses in MNs is slightly higher than confocal imaging. A comparative glutamate induced peak mean Fluo-4 fluorescent intensity is given in Fig. 3.6.4c.

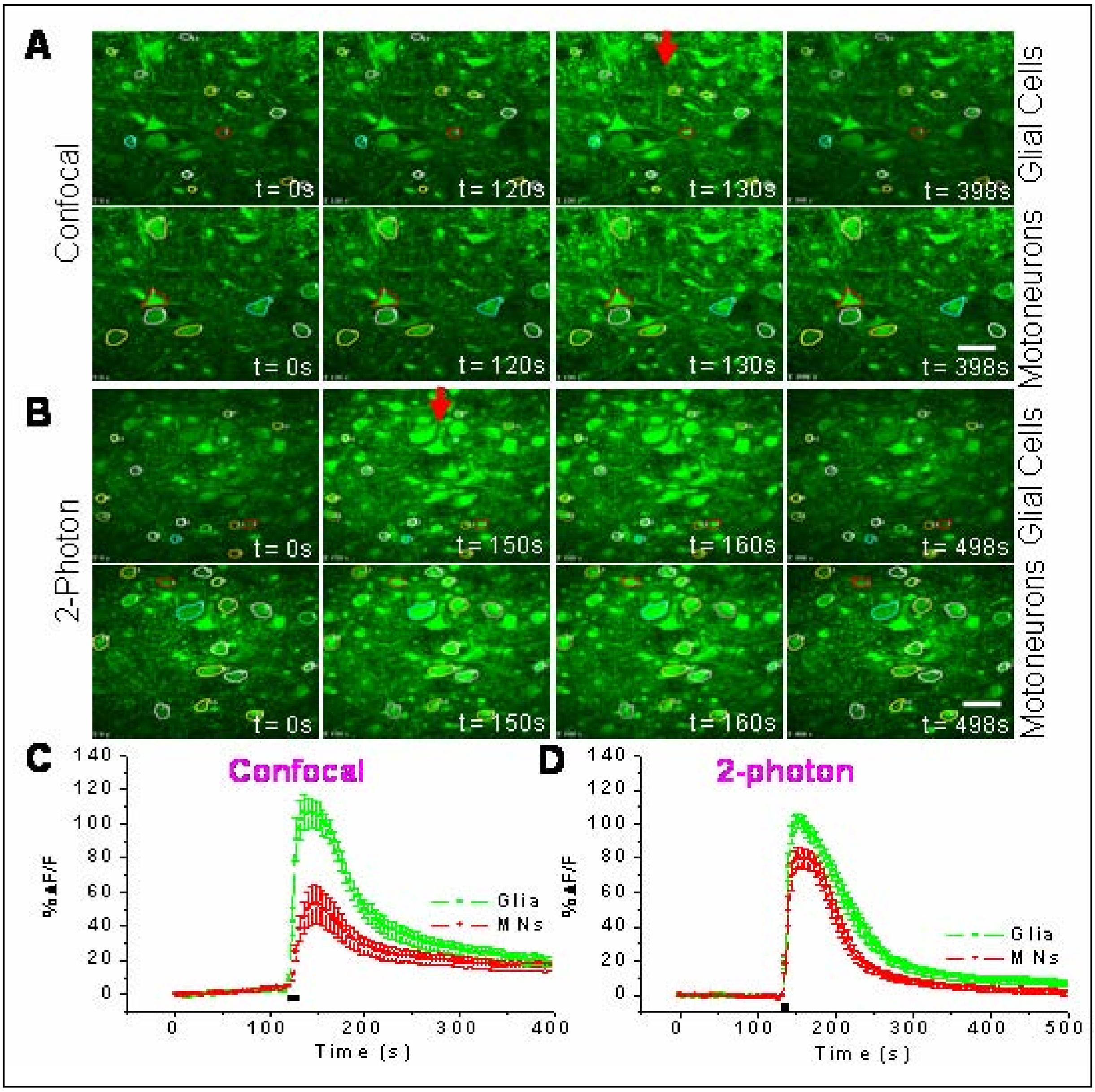

Fig. 3.6.4b: Kinetics of Glutamate induced modulations of [Ca^{2+}]i fluorescence changes in MNs-glia networks in rat brain stem slices loaded with Ca^{2+} indicator dye fluo-4 measuring with confocal and 2-photon microscopy. (A) A series of digital fluorescence micrographs just before drug application (t=0s, control), Glutamate induced initial response (t=120s, 1mM Glutamate for 10s) and at defined time intervals (as indicated) after Glutamate induced peak fluorescence intensity (130s) in glia (up panel) and MNs (down panel) of rat brain stem slice network digitized with confocal microscope. The positions of the peak Glutamate induced fluorescence intensity were marked by red arrows. (B) A series of digital fluorescence micrographs just before drug application (t=0s, control), Glutamate (1mM Glu for 10s) induced peak fluorescence intensity (150s) at defined time intervals (as indicated) and ~10s after peak fluorescence intensity of Glutamate application (160s) in glia (up panel) and MNs (down panel) of rat brain stem slice network digitized with 2-photon microscope. The position of the peak Glutamate induced fluorescence intensity was marked by red arrows. (C) Traces (confocal: 11 glial cells, 6 MNs) showing average mean fluorescence intensity normalized to base-line values as a function of time in glia (green) and MN (red) network in rat brain stem slice for a single representative experiment. (D) Traces (2-photon: 12 glial cells, 12 MNs) showing average mean fluorescence intensity normalized to base-line values as a function of time in glia (green) and MN (red) network in rat brain stem slice for a single representative experiment. Glutamate (1mM, 10s) applications were indicated with solid black bars between the traces and the horizontal axis. Scale bar = 40µm.

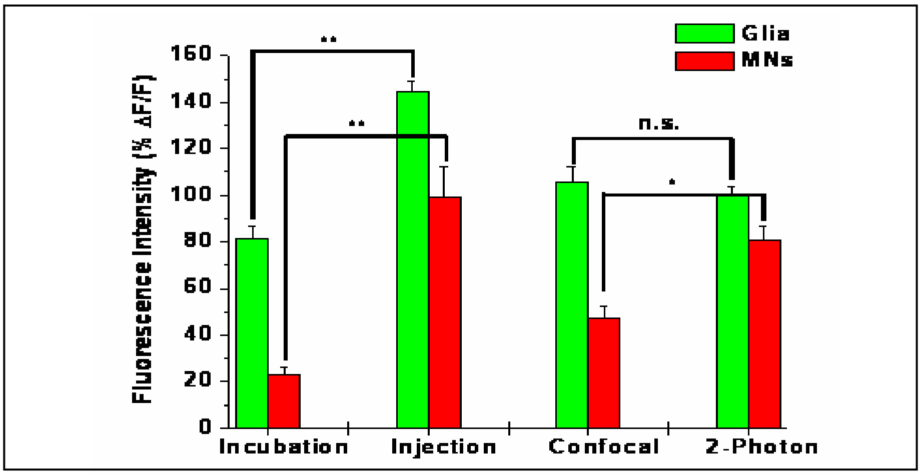

Fig. 3.6.4c: The bar diagram of the glutamate evoked (1mM, 10s) changes in peak mean fluorescence intensity using two different staining procedures (Incubation and Injection) and microscopy methods (Confocal and 2-photon). Graph showing glutamate evoked peak $[Ca^{2+}]i$ fluorescence changes (% ΔF/F) with bath incubation (N=3) procedure for glia (n=30) and MNs (n=14) were 81.74 ± 4.76 and 22.84 ± 3.31 respectively, whereas with targeted pressure injection (N=3) procedure responses for glia (n=54) and MNs (n=25) were 144.36 ± 5.07 ($^{**}p< 0.001$ compared to bath incubation) and 98.89 ± 13.23 ($^{**}p< 0.001$ compare to bath incubation) respectively. Further, glutamate evoked peak Ca^{2+} fluorescence changes (% ΔF/F) with confocal (N=3) microscopy for glia (n=33) and MNs (n=15) are 105.78 ± 6.44 and 47.08 ± 5.44 respectively, whereas glutamate evoked peak Ca^{2+} fluorescence changes (% ΔF/F) with 2-photon microscopy (n=4) were 100.47 ± 3.29 ($p> 0.05$ not significant compared to confocal) and 80.56 ± 6.26 ($^{**}p< 0.001$ significant difference compared to confocal) respectively for glia (n=48) and MNs (n=35). Note that in bath incubation staining procedure fluorescence signals were significantly reduced in glia ($^{**}P< 0.001$) and MNs ($^{**}P< 0.001$) compared to targeted pressure injection staining procedure. There are very small differences in Fluo-4 fluorescence signals in glia measured with confocal and 2-photon microscopy. However, MNs peak fluorescence intensity measured with confocal microscopy is slightly less (~1.7 times) compared to 2-photon microscopy ($^{*}P< 0.005$). Data are expressed as means ± S.E.M., N= Number of experiments; n=Number of cells.

3.6.5 CN^- (chemical hypoxia) -evoked $[Ca^{2+}]i$ signaling in motoneuron-glia network in rat brain stem slices

Inhibitors of the mitochondrial respiratory chain (CN^-, Azide) cause rapid glutamate release from MNs as well as glia. There are several probable reasons for this release. Notably, reduced oxygen supply triggers fast depolarisation of MNs, which greatly reduces their ability to maintain transmembrane ion gradients followed by Na^+ and Ca^{2+} influx into the cells. Substantial Ca^{2+} influx initiates glutamate release from neuronal terminals, thus further amplifying the vicious circle by inducing glutamate excitotoxicity. Another probable reason is substantial ATP depletion inducing failure of the Na^+-pump which in turn causes plasma membrane depolarisation and thus rapid transient excytosis. Earlier, it was shown that hypoxic insults to cultured astrocytes changes the state of Ca^{2+} stores, and in particular, the buffering capacity of mitochondria, so that responses to external inputs are profoundly altered (Smith *et al*., 2003).

To test the impact of hypoxia on MNs-glia network, here the brain stem slices were challenge with 5mM CN^- (60s) after glutamate application (10s pulse). After washout of short 10s pulse of glutamate, a typical Ca^{2+} response to CN^- (5mM) in MNs and glia is seen in brain stem slice preparation kept in Ca^{2+} containing medium (Fig. 3.6.5).

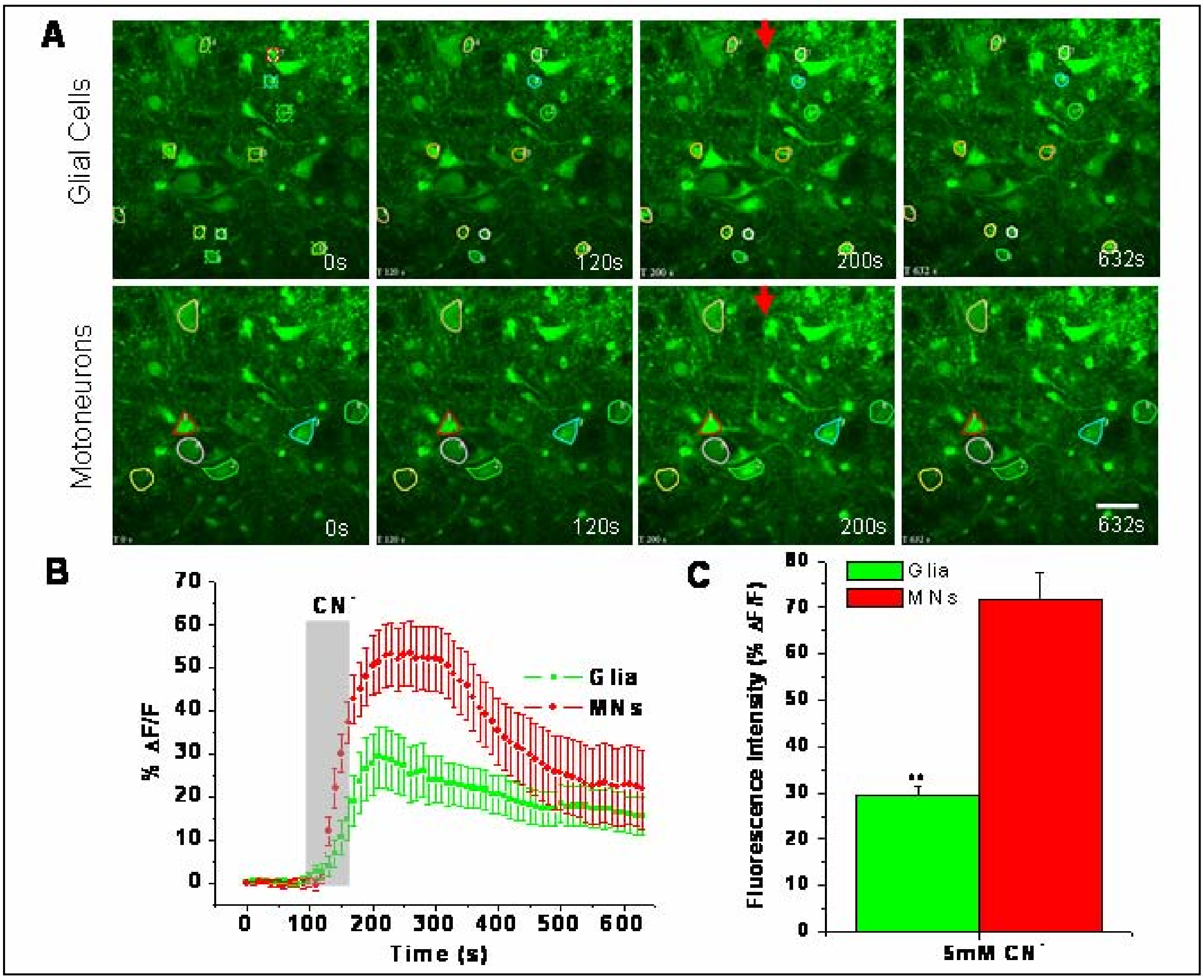

Fig. 3.6.5: Kinetics of hypoxia induced Ca^{2+} fluorescence changes of MNs-glia network in rat brain stem slices loaded with Ca^{2+} indicator dye Fluo-4 after glutamate induced Ca^{2+} release and uptake. (A) A series of digital fluorescence micrographs just before (t=0s, control), hypoxia (5mMCN^- for 65s) induced initial response (t=120s) and at defined time intervals (as indicated) after 5mMCN^- induced peak fluorescence intensity (200s) in glial cells (upper panel) and MNs (Down panel) of rat brain stem slice network digitized with confocal microscope. The position of the peak CN^- induced fluorescence intensity was marked with red arrow. (B) Representative recordings of hypoxia induced (5mM CN^-) mean $[Ca^{2+}]$i fluorescence traces from glia (Green, n=11 glial cells) and MNs (Red, n=7 MNs) showing average mean fluorescence intensity normalized to base-line values, as a function of time in glia (green) and MNs (red) network in rat brain stem slices for a single experiment after glutamate induced Ca^{2+} release and uptake. CN^- (5mM, 65s) application was indicated with solid gray bar between the traces and the horizontal axis. (C) A bar graph of the hypoxia (5mM CN^- for 60± 5s) induced changes in mean peak fluorescence (% ΔF/F) for glia (% ΔF/F = 29.30 ± 1.93; N=6, n=65, green) and MNs (%

ΔF/F = 71.51 ± 6.02; N=6, n=42, red; $p<0.001$ compared to glia) of rat brain stem slices after glutamate induced Ca^{2+} release and uptake. Note that glutamate evoked responses did not alter significantly the CN^- evoked $[Ca^{2+}]i$ fluorescent transient in MNs. However, response is quite diminished in glia cells compared to MNs (**$P<0.001$). Data shows that glutamate has major impact on glial cells excitotoxicity but MNs are only mildly affected. Data are expressed as means ± S.E.M., N= Number of experiments; n=Number of cells. Scale bar = 40µm.

Application of CN^- (5mM) evoked an immediate, transient Ca^{2+} peak in glial cells (Fig. 3.6.5B). Quantification of the response showed peak mean Ca^{2+} level increase of 29.30 ± 1.93 (% ΔF/F; N=6, n=65) above baseline (Fig. 3.6.5C). In contrast, a similar but immediate and high increase in $[Ca^{2+}]i$ was found in MNs (Fig. 3.6.5C) showing a peak mean fluorescence value of 71.51 ± 6.02 (% ΔF/F; N=6, n=42; $p<0.001$ compared to glia) above initial baseline (Fig. 3.6.5C). In the presence of CN^-, glia and MNs both get rid off most of the $[Ca^{2+}]i$ load and after the 5 min wash the Fluo-4 fluorescence was only 17 % and 23 % above initial baseline (Fig. 3.6.5B) for glia and MNs respectively. However, the typical CN^- (5mM) response is not altered rather relatively high after glutamate evoked $[Ca^{2+}]i$ in MNs which shows that MNs mitochondria indeed stores Ca^{2+} released from glia after glutamate application and is not vulnerable to glutamate induced neurotoxicity at least for acute exposures. Glial cells have relatively weaker response and the baseline recovery is delayed by 30-40s. This suggests that glial cells might be partially vulnerable to glutamate induced Ca^{2+} neurotoxicity. In some experiments, Ca^{2+} oscillations were observed in some glial cells during the experiment (results not shown). Here, experiments shows that mitochondria and ER in MNs buffer the rising level of $[Ca^{2+}]i$ evoked by glutamate and acute hypoxia that liberate $[Ca^{2+}]i$ from an intracellular pool. The degree of Ca^{2+} liberation from intracellular store was modest in MNs but was not prominent in most of the glial cells.

3.6.6 FCCP-evoked $[Ca^{2+}]i$ in motoneuron-glia network in rat brain stem slices after hypoxia

Mitochondria have a large capacity for calcium uptake through the potential-driven Ca^{2+} uniporter (Nicholls DG & Akerman KEO, 1982). They might be neuroprotective by removing calcium from the cytoplasm. However, calcium uptake into the mitochondria might have injurious effects or mitochondrial calcium cycling may contribute to bioenergetic failure (Patel *et al.*, 1996). Studies on cultured MNs and motor nerve terminals showed a large increase in the amplitude of Ca^{2+} transients as a result of mitochondrial metabolic inhibition (Carriedo *et al.*, 2000; David & Barrett, 2000). Therefore, it is likely that FCCP by itself or the lack of mitochondrial Ca^{2+} buffering as a consequence of FCCP action, might influence voltage-activated Ca^{2+} influx in a way similar to that described for chromaffin cells (Hernandez-Guijo *et al.*, 2001).

To explore the mechanism and investigate this issue, using Confocal and 2-photon microscopy, we show that application of acute (3 min) FCCP (4µM) challenge after hypoxia (5mM CN^-) evoked an immediate elevation of Ca^{2+} response which is quite robust, irreversible (Before hypoxia, it is reversible as shown by Bergman & Keller and several others) and reproducible (transient and peak fluorescence intensity). Transient of Fluo-4 fluorescence form constant plateau shaped traces in MNs; whereas, in glia it was not down regulated after wash in rat brain stem slice network. Confocal imaging (Fig. 3.6.6C, left) of FCCP (4µM, 3 min) induced rise in peak plateau shape average mean fluorescence intensity of $[Ca^{2+}]i$ is 60.89 ± 7.41 for glia (% ΔF/F; N=4, n=44; not down regulated) and 50.58 ± 6.05 for the MNs (% ΔF/F; N=4, n=27; p>0.05 not significantly different from glia). Imaging through 2-photon (Fig. 3.6.6C, right) microscopy produced the very similar transient of FCCP (4µM, 3 min) induced $[Ca^{2+}]i$ average mean peak fluorescence intensity which is 66.69 ± 4.22 (% ΔF/F; N=3, n=39) for glia and 48.09 ± 4.05 (% ΔF/F; N=3, n=28) for MNs (p>0.05 not significantly different from glia). In MNs the FCCP-evoked Ca^{2+} response was plateau shaped and the $[Ca^{2+}]i$ remained at 99 % above the initial baseline after the application of FCCP (4µM, 3 min) even after extended washing until 30 min (Fig. 3.6.6C). There is no significant difference between confocal and 2-photon average mean fluorescence intensity of $[Ca^{2+}]i$ for glia and MNs (p>0.05 not significantly different).

Here, attempt to discriminate the causes of excitotoxic cell death by blocking mitochondrial function were describe. To test this issue, we dissipated the ΔΨm and eliminated calcium uptake into mitochondria using the mitochondrial uncoupler FCCP. Although glutamate-stimulated increase in $[Ca^{2+}]i$ (intracellular free calcium concentration) and CN^- evoked hypoxic influence were significantly potentiated by these drugs, transient inhibition of mitochondrial function during FCCP stimulation prevented hypoxia-induced cell death in MNs but failed to do so in glial cells as it is not down regulated even after washing and remains up regulated even after 30 min of extended washing.

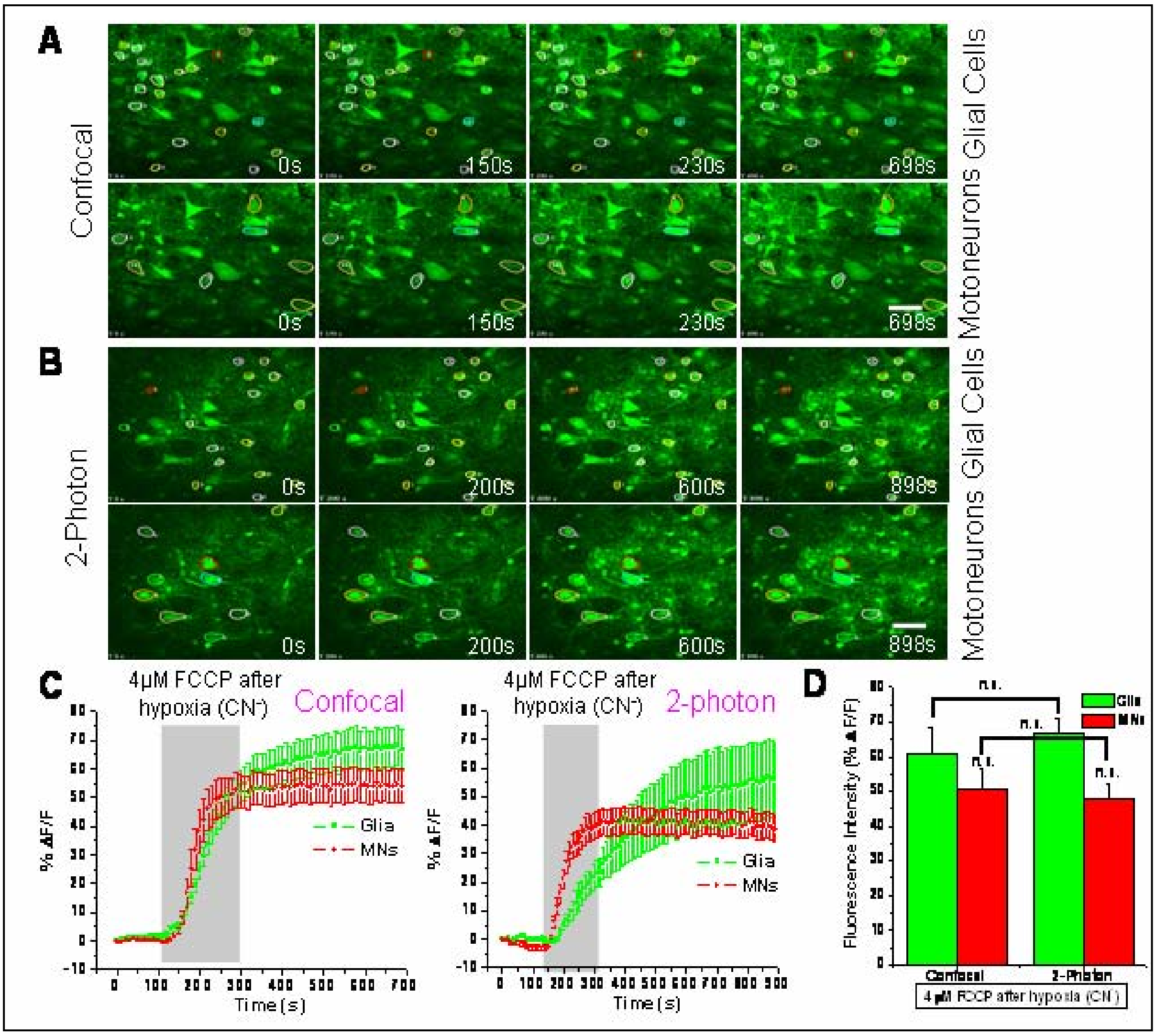

Fig. 3.6.6: FCCP (4μM) -evoked [Ca^{2+}]i fluorescence intensity in MNs-glia network in rat brain stem slices after hypoxia (5mM CN^-) using confocal and 2-photon microscopy. (A) A series of digital fluorescence micrographs just before (t=0s, slice after 15 min wash treated acutely with CN^-), FCCP-evoked initial fluorescence response (t=150s, 4μM FCCP for 3 min) and at defined time intervals (as indicated) after FCCP induced peak fluorescence intensity (230s) in glia (up) and MNs (down) of rat brain stem slice network imaged with confocal microscopy. (B) A series of digital fluorescence micrographs just before (t=0s, slice after 15 min wash treated acutely with CN^-), FCCP-evoked initial fluorescence response (t=200s, 4μM FCCP for 3 min) and at defined time intervals (as indicated) after FCCP induced peak fluorescence intensity (600s) in glia (up) and MNs (down) of rat brain stem slice network imaged with 2-photon microscopy. (C) Left traces (confocal: 14 glial cells, 8 MNs) and right traces (2-photon: 7 glial cells, 8 MNs) show average mean fluorescence intensity normalized to baseline values as a function of time in glia (green) and MNs (red) network in rat brain stem slices for a single representative experiment. 4μM FCCP (3 min) applications were indicated with the solid gray bars between the traces and the horizontal axis. (D) A bar diagram of the FCCP (4μM, 3 min) - evoked changes in average mean peak [Ca^{2+}]i fluorescence intensity (% ΔF/F) using confocal (N=4) and 2-photon (N=3) microscopy. FCCP-evoked average mean peak Ca^{2+} fluorescence changes (% ΔF/F) with confocal (N=4) microscopy for glia (n=44) is 60.89 ± 7.41 and 50.58 ± 6.05 for MNs (n=27) whereas FCCP-evoked average mean peak Ca^{2+} fluorescence changes (% ΔF/F) with 2-photon microscopy (n=3) is 66.69 ± 4.22 and 48.09 ± 4.05 respectively for glia (n=39) and MNs (n=28). Note that for both confocal and 2-photon, average peak fluorescence signals and transients show similar trends and are not significantly different for glia as well as MNs (*P*>0.05, not significantly different). Data are expressed as means ± S.E.M., N= Number of experiments; n=Number of cells. Scale bar = 40μm.

These results indicate that mitochondrial calcium uptake is necessary for expression of excitotoxicity in MNs but its implication is doubtful in glial cells. Many reports demonstrate a correlation between activation of calcium-dependent cytoplasmic enzymes and glutamate toxicity (Favaron *et al*., 1988; Dykens *et al*., 1987), but here a condition in which glutamate-stimulated increase in $[Ca^{2+}]i$ is extremely high with mild toxicity in glia and little or no apparent toxicity in MNs were shown. Therefore, we ought to believe that glial cells are vulnerable to glutamate induced toxicity. However, MNs are generally resistant to glutamate induced toxicity by compromising glutamate-stimulated increases in $[Ca^{2+}]i$ with their internal mitochondrial and ER stores, at least in our preparation and conditions described here.

3.6.7 Effect of metabolic inhibitors on ΔΨm of motoneuron-glia network in rat brain stem slices

Permeant cationic fluorescent probes are widely employed to monitor ΔΨm. The application of such potential-dependent probes in conjunction with fluorescence microscopy and fluorescence spectroscopy allows the monitoring of ΔΨm in individual living cells as well as in large population of cells. Substantial ΔΨm loss may be a common feature in injurious processes, because it favors the opening of the mitochondrial permeability transition pore and the release of proapoptotic factors (Zoratti & Szabo´, 1995). Recurrent mitochondrial Ca^{2+} ion load during pathophysiology, resulting from dysregulation of Ca^{2+} might act on ΔΨm, proton motive force swelling and necrotic cell death (Ward *et al*., 2000; Krieger & Duchen, 2002). Because of the use of spatially averaged measures of ΔΨm and mitochondrial Ca^{2+} ion concentration ($[Ca^{2+}]m$), the contribution of glia-MNs network to the signal and its subcellular localization in pathological condition remained unidentified. To further explore the interplay between glia-MNs network, by using confocal and 2-photon laser-scanning microscopy, we investigated and elucidated the impact of glutamate induced depolarization, hypoxia induced metabolic inhibition and mitochondrial uncoupler FCCP induced changes in ΔΨm. The mitochondrial compartment was identified by monitoring ΔΨm in the glia and MNs of rat brain stem slice network, stained with bath loading and targeted pressure injection using the mitochondria-specific dye Rhod 123. Bath staining procedure with Rhod 123 staining is illustrated in Fig. 3.1.2A-D. Pressure injection staining procedure and methodology for staining of slices is illustrated in Fig. 3.6.7.

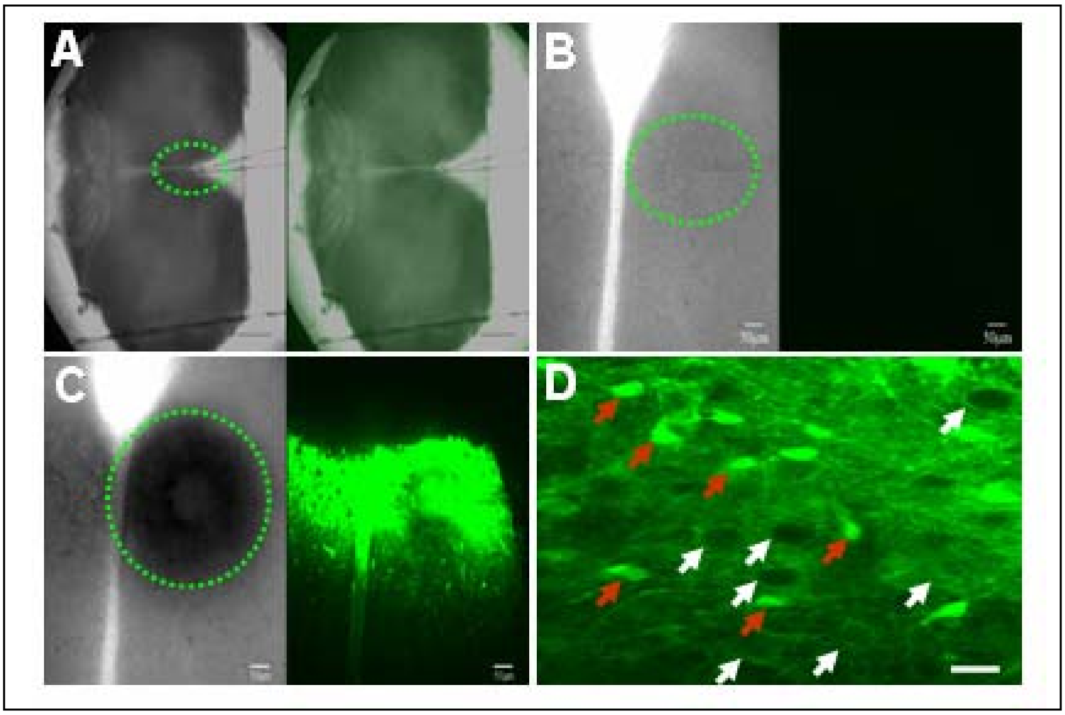

Fig. 3.6.7: Rhod 123 dye staining procedure and methodology for staining of slices through targeted pressure injection using confocal microscope. (A) Photomicrograph of a typical 400µm thick brain stem slice. (B) A photomicrograph of the typical 400µm thick brain stem slice before dye injection at low magnification (4X objective). Area in the black circle indicate tip of the pipette in hypoglossal region. (C) A photomicrograph of the typical 400µm thick brain stem slice after targeted pressure injection of the Rhod 123 dye at low magnification (4X objective). (D) A photomicrograph of the typical 400µm thick brain stem slice just after Rhod 123 dye staining at high magnification (20X objective) using confocal microscope. Red circle denote HMNs, whereas white circle denote glial cells. Scale Bar for Fig.D = 20µm.

3.6.8 Glutamate-mediated ΔΨm in motoneuron-glia network of rat brain stem slices

Activation of Ca^{2+} entry via voltage-gated channels need cell depolarization. Alternatively, cell depolarization can occur by activating ligand-gated ion channels. Mitochondrial Ca^{2+} can also be released into the intracellular compartment, for example, by dissipating the mitochondrial transmembrane potential as shown for glial precursor cells (Kirischuk *et al.*, 1995). A glutamate-mediated depolarization has indeed been reported to activate Ca^{2+} channels in glia and glial precursor cells (Porter & McCarthy, 1995). In all oligodendrocytes, glia and astrocytes studied so far, activation of $GABA_A$ receptors leads to a depolarization of the ΔΨ, in contrast to mature neurons where GABA hyperpolarizes the membrane (Blankenfeld *et al.*, 1992). So far we are unaware of a physiological stimulus in glia leading to release of Ca^{2+} from the mitochondrial pool, but it is possible that this might occur under pathological conditions such as Ca^{2+} dysregulation and during hypoxia. The aim of this study was to elucidate the effect of glutamate mediated changes on the ΔΨm of the glial cells and MNs network in rat brain stem slices.

The ΔΨm was measured after treatment with glutamate. Rhod 123 released during depolarization was quantified by measuring Rhod 123 fluorescence signals (% ΔF\F) in a defined region of interest in glia and MNs. The fluorescence of Rhod 123 released was normalized to baseline obtained after superfusion with aCSF medium (F), which represents the amount of Rhod 123 accumulated in the cytosol over the nucleus. In glia and MNs, the ΔΨm increases in response to glutamate challenge using both bath staining and pressure injection procedure. Although, application of glutamate (1mM) for 60s evoked a moderate Rhod 123 release, the difference of glutamate-released Rhod 123 between MNs and glia is not significant (*P*>0.05, the population means are not significantly different) which was 19.22 ± 1.74 (% ΔF/F; N=3, n=23) and 18.47 ± 0.70 (% ΔF/F; N=3, n=26), respectively for glia and MNs in bath incubation procedure. In pressure injection procedure, glutamate-released Rhod 123 was 12.23 ± 0.98 (% ΔF/F; N=3, n=25; P>0.05) and 12.63 ± 0.97 (% ΔF/F; N=3, n=24; P>0.05), respectively for MNs and glia (Fig. 3.6.8). The Rhod 123 fluorescence signals are slightly bigger in case of bath incubation procedure (*P*<0.05 compare to pressure injection) which might be due to unusual distribution of dye throughout the slice and due to background signals. In both staining procedure, Rhod 123 fluorescence signals in MNs return to baseline after ~2 min washing. However, glutamate evoked Rhod 123 fluorescence signals in glia after washing goes below baseline (5-7% negative of the initial baseline) in both bath staining and pressure injection procedure. The data demonstrates that glutamate might alter ΔΨm slightly in glia, although there is no significant impact on MN membrane property in rat brain stem slice network (Fig. 3.6.8A and B).

3.6.9 Mitochondrial complex IV inhibitor (CN^-) induced/s depolarization of mitochondrial membrane in motoneuron-glia network in rat brain stem slices

Acute chemical hypoxia (CN^-) mediates various cell processes, such as cell excitability and membrane depolarization through the regulation of ion channel activity. CN^- insults to the brain result in prominent changes of MNs-glia properties including cell morphology, metabolic activity and proliferation (Hori *et al.*, 1994). The initial signals that result in these long-term changes are not yet well understood and barely explored in MNs-glia network in detail. *In-vitro* and *in-vivo* hypoxia models have revealed that brief exposures of astrocytes to hypoxic or hypoglycemic conditions trigger [Ca^{2+}]i elevations which arise from both activation of voltage-gated Ca^{2+} channels and Ca^{2+} release from internal pools (Duffy & MacVicar, 1996). Previously, measurement of ΔΨm using Rhod 123 fluorescent dye in mice rat brain slices were performed and it was shown that acute CN^- exposure causes a rapid, robust and reversible ΔΨm depolarization (Bergman & Keller, 2004). Given the central role of ΔΨm in the physiological and pathological functioning of MNs as well as glial cells, we have investigated how acute hypoxia regulates such signaling, and compared the results with those evoked by glutamate and FCCP.

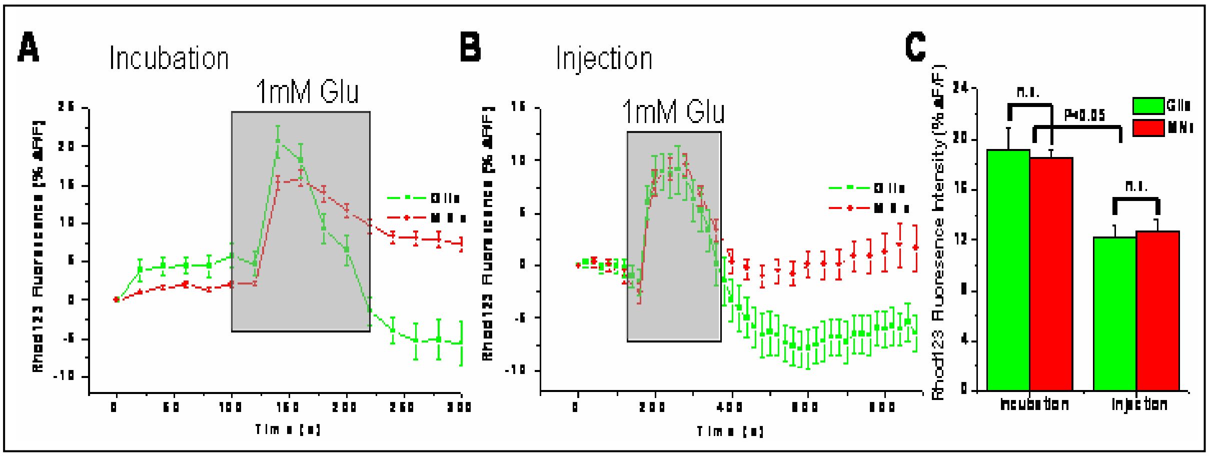

Fig. 3.6.8: Glutamate evoked ΔΨm signals of MNs-glia network in rat brain stem slices with bath staining and pressure injection procedures. (A) Traces (Left, bath incubation: 11 glial cells, 8 MNs) showing average mean Rhod 123 fluorescence signals normalized to base-line values, as a function of time in glial cells (green) and MNs (red) network in rat brain stem slice for a single representative experiment after 1mM glutamate application for 2 min. (B) Traces (Right, pressure injection: 12 glial cells, 10 MNs) showing average mean Rhod 123 fluorescence signals normalized to base-line values, as a function of time in glial cells (green) and MNs (red) network in rat brain stem slice for a single representative experiment after 1mM glutamate application for 2 min. Positions of glutamate (1mM, 120s) applications are indicated with the solid gray bars between the traces and the horizontal axis. (C) A bar diagram of the glutamate evoked (1mM, 120s) changes in peak mean fluorescence intensity of Rhod 123 fluorescence signals normalized to base-line using two different staining procedures (Incubation and Injection) and confocal microscopy. Graph showing glutamate evoked peak Rhod 123 fluorescence signals changes (% ΔF/F) with bath incubation (N=3) procedure for glia (n=23) and MNs (n=26) were 19.22 ± 1.74 and 18.47 ± 0.70 ($p > 0.05$ compared to glia, not significantly different) whereas with targeted pressure injection (N=3) procedure responses for glia (n=25) and MNs (n=24) were 12.23 ± 0.98 ($^*p < 0.05$ compared to bath incubation) and 12.63 ± 0.97 ($p > 0.05$ compared to glia, not significantly different; $^*p < 0.05$ compared to bath incubation), respectively. Note that in bath incubation staining procedure glutamate mediated fluorescence signals were slightly higher for glia ($^*P < 0.05$) and MNs ($^*P < 0.05$) compared to targeted pressure injection staining procedure. There are very small differences in Rhod 123 fluorescence signals between glia and MNs measured with either incubation or injection procedure applying confocal microscopy. Data are expressed as means ± S.E.M., N= Number of experiments; n=Number of cells.

Here, we measured changes in ΔΨm after glutamate wash in the presence of 5mM CN^- (60s) of glial cells and MNs network in rat brain stem slices using confocal and 2-photon microscopy. Hypoxia (5mM CN$^-$) produced robust, reversible and reproducible larger ΔΨm depolarization in MNs (% ΔF/F= 34.42 ± 1.48; N=6, n=69; Fig. 3.6.9C) as well as glial cells (% ΔF/F= 27.69 ± 1.89; N=6, n=64; Fig. 3.6.9C; *$P<0.01$ compared to MNs, significant difference) measured with confocal microscopy. 2-photon microscopy fashioned similar results where ΔΨm depolarization in MNs (% ΔF/F; N=7, n=49; Fig. 3.6.9C) and glial cells (% ΔF/F; N=7, n=55; Fig. 3.6.9C) were 38.26 ± 3.56 and 29.56 ± 2.59 (* $P<0.05$ compared to MNs, significant difference) respectively. In the presence of CN$^-$, both glia and MNs depolarize and there is an increase in Rhod 123 fluorescence signals. However, after ~5 min of CN$^-$ washing in glia, Rhod 123 signals went below baseline (7-12 % negative of initial baseline) whereas MNs nicely recovered to baseline. We also found that CN$^-$ responses in MNs are faster by 25-35s in comparison to glial cells, indicating large number of channels and receptors accompanying MNs. This also suggests that it might be possible that hypoxia induced signals from MNs pass to glia and may contribute in glial signaling.

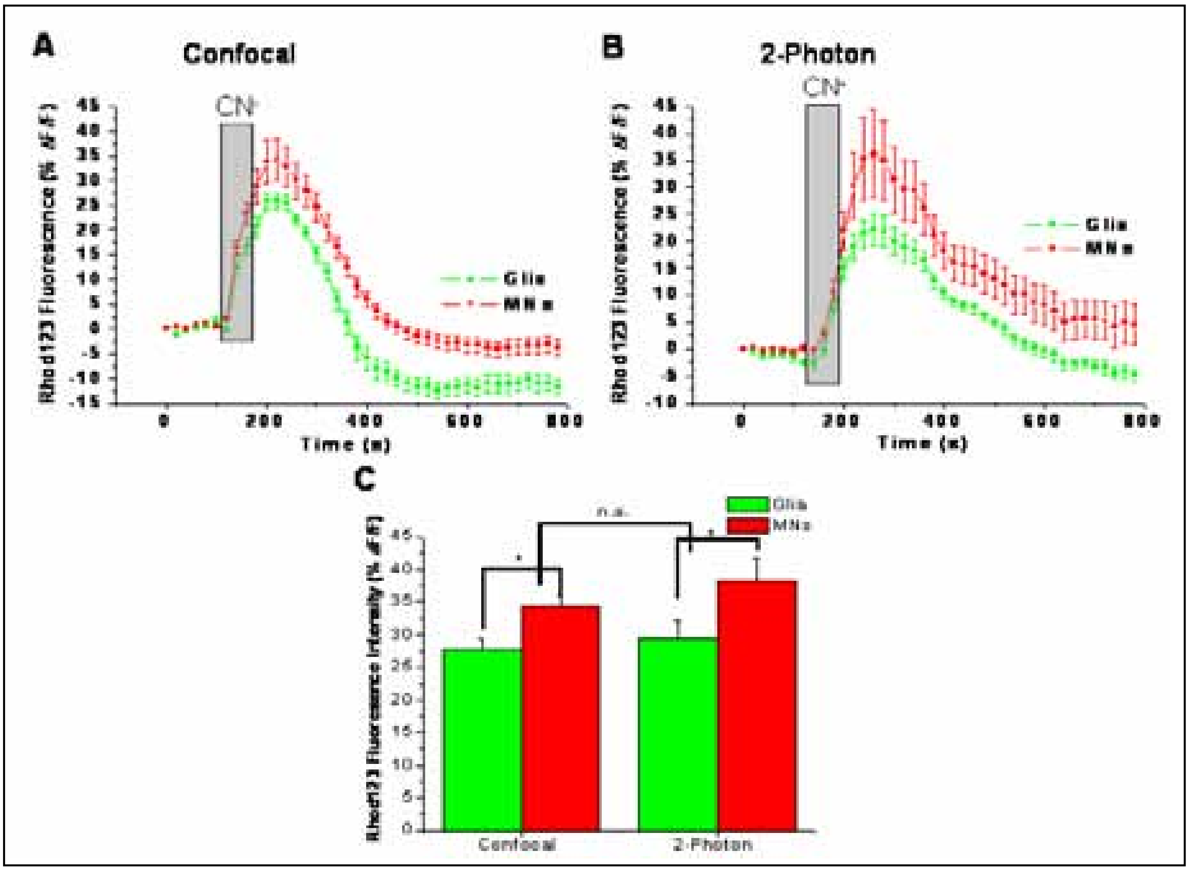

Fig 3.6.9: Mitochondrial membrane potential measured by chemical hypoxia (5mM CN$^-$) evoked Rhod 123 fluorescent signals released in MNs and glial cells of rat brain stem slices using confocal and 2-photon microscopy. (A) Traces (confocal microscopy: 9 glial cells, 9 MNs) showing average mean Rhod 123 fluorescence signals normalized to base-line values, as a function of time in glial cells (green) and MNs (red) network in rat brain stem slices for a single representative experiment after 5mM CN$^-$ application for 60s. (B) Traces (2-photon microscopy: 5 glial cells, 5 MNs) showing average mean Rhod

123 fluorescence signals normalized to base-line values, as a function of time in glial cells (green) and MNs (red) network in rat brain stem slices for a single representative experiment after 5mM CN^- application for 60s. Positions of CN- (5mM, 60s) applications were indicated with the solid gray bars between the traces and the horizontal axis. (C) A bar diagram of the CN^- evoked (5mM, 60s) changes in peak mean fluorescence intensity of Rhod 123 fluorescence signals normalized to base-line using confocal and 2-photon microscopy. Graph showing CN^- evoked peak Rhod 123 fluorescence signal changes (% ΔF/F) measured with confocal microscopy (N=6) for glia (n=64) and MNs (n=69) were 27.69 ± 1.89 and 34.42 ± 1.48 (**P*<0.01 compared to glia, significantly different) respectively, whereas measurement with 2-photon microscopy (N=7), Rhod 123 fluorescence signal responses in glia (n=55) and MNs (n=49) were 29.56 ± 2.59 and 38.26 ± 3.56 (**P*<0.05 compare to glia, significantly different) respectively. Note that in both confocal and 2-photon measurements there are moderate but significant differences between glia and MNs Rhod 123 fluorescence signals evoked by CN^-. Data are expressed as means ± S.E.M., N= Number of experiments; n=Number of cells.

3.6.10 Impact of mitochondrial uncoupler FCCP depolarization efficacy on ΔΨm in motoneuron-glia network in rat brain stem slices

To discriminate between the causes of hypoxia and excitotoxic cell death by blocking mitochondrial function, we dissipate the ΔΨm and eliminate the calcium uptake into mitochondria by using mitochondrial uncoupler FCCP in MNs-glia of rat brain stem slices. The ΔΨm was measured 15 min after treatment with CN^- wash. We subsequently induced complete depolarization with the uncoupler FCCP. A large amount of FCCP releasable Rh123 dye indicates a high mitochondrial potential and vice-versa. The depolarization observed with FCCP stimulation was slightly different both in intensity of fluorescence signals as well as spatial and temporal profile of traces compared to observe with 5mM CN^- (Fig. 3.6.10A-C).

To test this issue under control conditions, 4µM FCCP (60s)-mediated depolarization resulted in a large Rhod 123 fluorescence increase above initial baseline of 68.89 ± 3.20 (% ΔF/F; N=5, n=70; Fig. 3.6.10C) in MNs and 54.98 ± 3.38 (% ΔF/F; N=5, n=82; Fig. 3.6.10C) in glia (***P*<0.001 compared to MNs, significant difference) of brain stem slice network measured with confocal microscopy. Measurement with 2-photon microscopy fashioned more or less similar results where ΔΨm depolarization in MNs (% ΔF/F; N=4, n=16; Fig. 3.6.10C) and glial cells (% ΔF/F; N=4, n=27; Fig. 3.6.10C) were 67.82 ± 6.99 and 55.97 ± 4.18 respectively. The fluorescence signals obtained with FCCP is significantly higher than that observed with 5mM CN^- (***P*<0.001 compared to CN^-, significant difference for both glia and MNs) and glutamate (***P*<0.001 compared to glutamate, significant difference for both glia and MNs). These results indicate that unlike FCCP, glutamate treatment alone does not cause significant mitochondrial membrane depolarization, though 5mM CN^- does cause moderate depolarization. We further show that inhibition of mitochondrial function by glutamate and CN⁻ is reversible atleast for acute exposures, but inhibition by 4µM FCCP leads to profound ΔΨm depolarization and takes >10 min recovery time to recover from the effect of uncoupler (Fig. 3.6.10A and B). These results indicate that mitochondrial calcium uptake is necessary for expression of excitotoxicity. Finally, comparative studies in glial cells and MNs for the relationship of ΔΨm revealed that MNs are more prone to mitochondrial depolarisation after mitochondrial metabolic inhibition in comparison to glial cells.

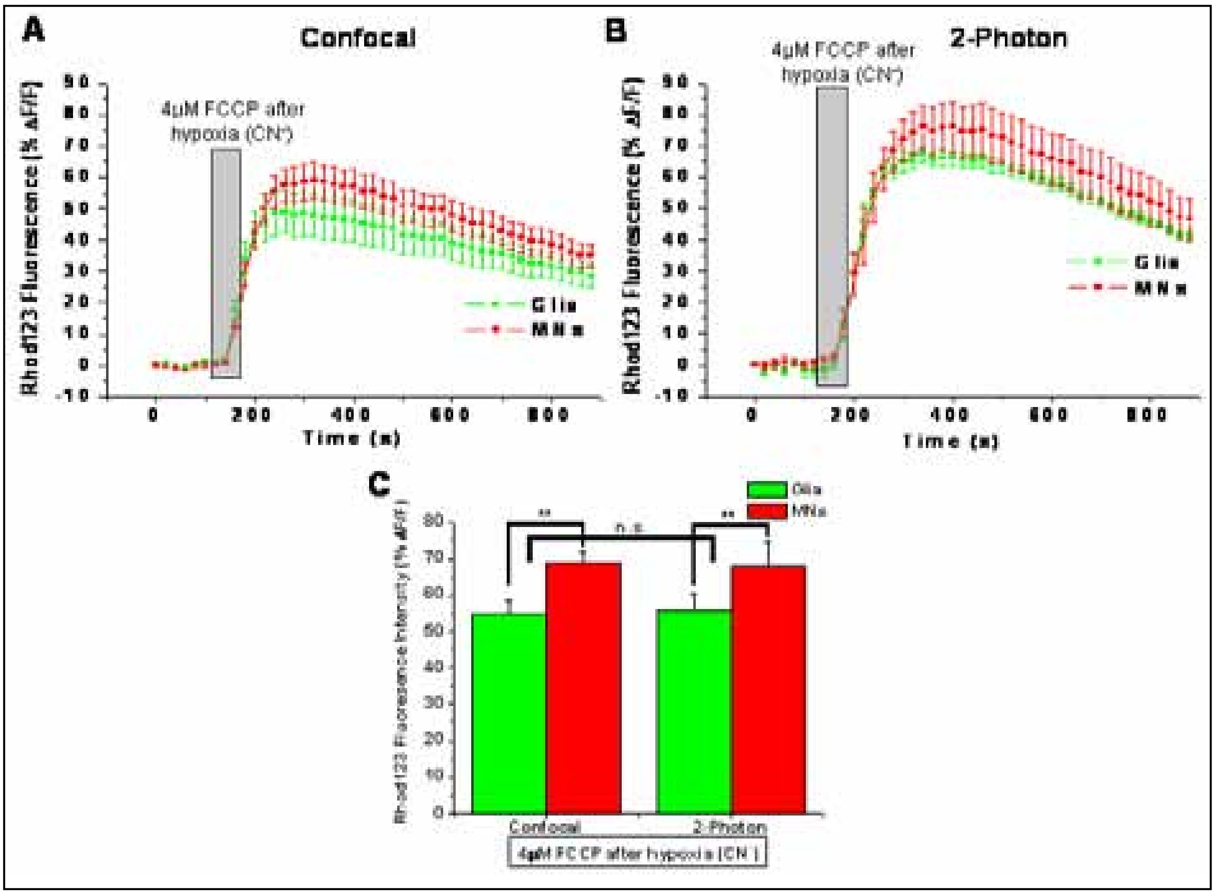

Fig. 3.6.10: Mitochondrial uncoupler FCCP–mediated ΔΨm changes measured after hypoxia in MNs and glial cells of rat brain stem slices using confocal and 2-photon microscopy. (A) Traces (confocal microscopy: 18 glial cells, 11 MNs) showing average mean Rhod 123 fluorescence signals normalized to base-line values, as a function of time in glial cells (green) and MNs (red) network in rat brain stem slice for a single representative experiment after 4µM FCCP application for 60s. (B) Traces (2-photon microscopy: 7 glial cells, 4 MNs) showing average mean Rhod 123 fluorescence signals normalized to base-line values, as a function of time in glial cells (green) and MNs (red) network in rat brain stem slice for a single representative experiment after 4µM FCCP application for 60s. Positions of FCCP (4µM, 60s) applications were indicated with the solid gray bars between the traces and the horizontal axis. (C) A bar diagram of the FCCP evoked (4µM, 60s) changes in peak mean fluorescence intensity of Rhod 123 fluorescence signals normalized to base-line using confocal and 2-photon microscopy. Graph showing FCCP evoked peak Rhod 123 fluorescence signal changes (% ΔF/F) measured with confocal microscopy (N=5) for glia (n=82) and MNs (n=70) were 54.98 ± 3.38 and 68.89 ± 3.20 (* $P<0.001$ compared to glia, significantly different) respectively whereas measurement with 2-photon microscopy (N=4), Rhod 123 fluorescence signal responses for glia (n=27) and MNs (n=16) were 55.97 ± 4.18 and 67.82 ± 6.99 respectively. Note that in both confocal and 2-photon measurement there is moderate but significant difference between glia and MNs. Data are expressed as means ± S.E.M. N= Number of experiments; n=Number of cells.

3.6.11 Assessment of long term ΔΨm recordings to check slice viability for glutamate, hypoxia and mitochondrial uncoupler induced neurotoxicity in motoneuron-glia network in rat brain stem slices

Previously, in acute slice preparations from most brain regions, neuronal and MNs-glia functions were recorded ranging from few seconds to min. Since the effects of neurotoxic agents are often manifested beyond this time scale, corresponding studies are typically performed on cultured cells. However, cell cultures are generated and maintained under vastly different conditions that can grossly alter neuronal properties (Metzger *et a*l., 2005). We propose that acute brain stem slices from neonatal rats (P1-P4) are a potent model which allows analysis of neuronal properties and cell viability within a time window of at least more than half an hour (Fig. 3.6.11).

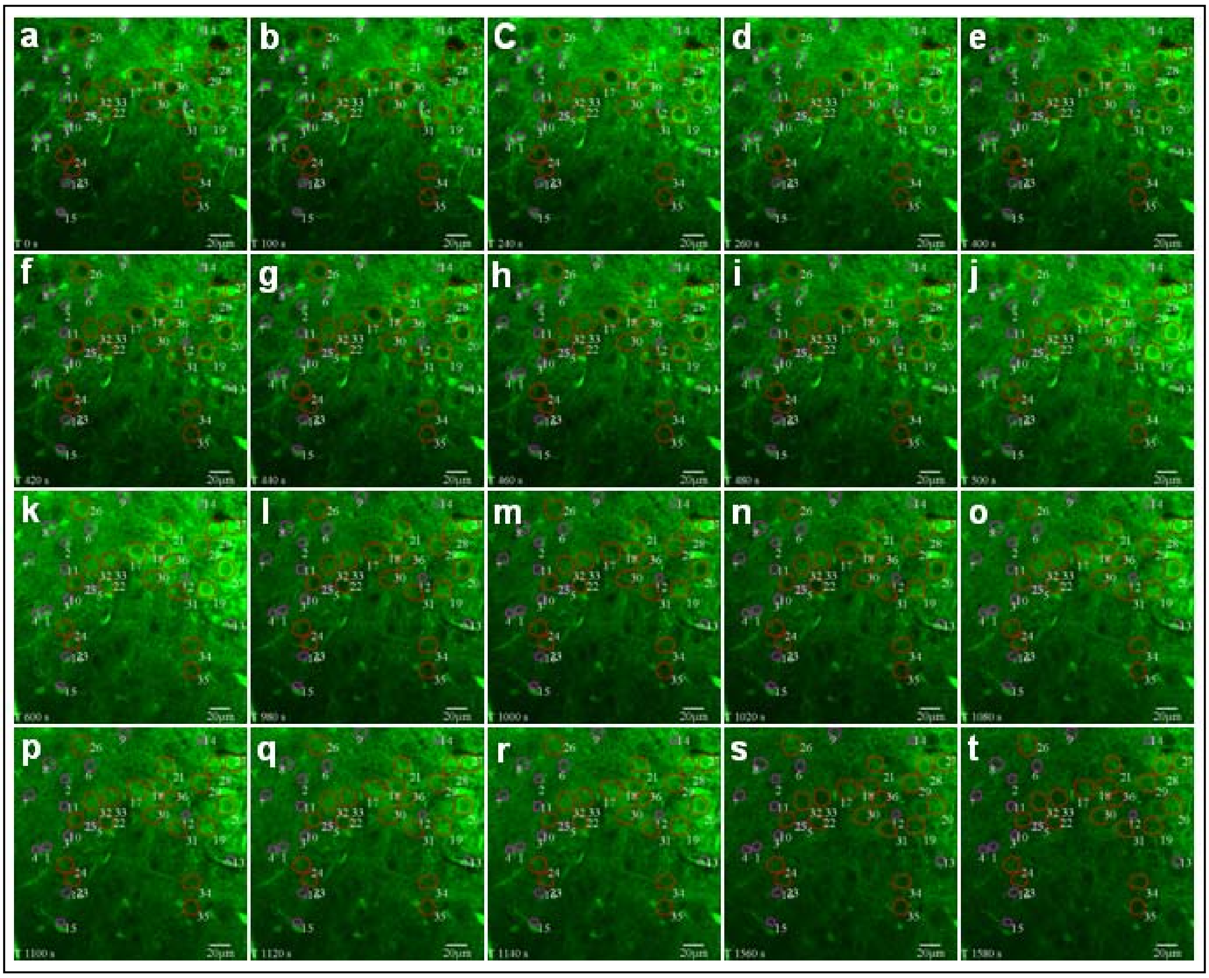

Fig. 3.6.11: Assessment of long term ΔΨm recordings to check slice viability in motoneuron-glia network in rat brain stem slices. A series of digital fluorescence photomicrographs just before application of neuromodulators (t=0s, control), glutamate induced initial response (t=100s, 1mM glutamate for 60s) and at defined times intervals (as indicated) after glutamate induced peak fluorescence intensity (240s-260s; c-d) and after baseline recovery following glutamate wash (400s, e) in glia (pink circle, 1-16) and MNs (red circle, 17-35) of rat brain stem slice network stained with Rhod

123 dye. Subsequently, hypoxia (5mM CN^-, at 420s for 60s) induced initial response (at t=440s for MNs, at t=480s for glia) and at defined time intervals (as indicated) after CN^- induced peak fluorescence intensity (500s, 600s; j-k) and after baseline recovery following CN^- wash (980s, l) in glia and MNs are illustrated. At last, massive mitochondrial uncoupler FCCP (4µM FCCP at 1000s for 60s, m) induced initial Rhod 123 response (at t=1020, n) and at defined time intervals (as indicated) after FCCP induced peak fluorescence intensity (1080-1140s; o-r) and after baseline recovery following FCCP wash (1560s, 1580s, s-t) in glia and MNs were recorded and digitized.

Accordingly, we have examined if acute slices from rat brain stem could be used within a time window of half an hour for assessment of long-term effects of neuromodulators. In Fig. 3.6.11a-t, we studied the action of glutamate, hypoxia and mitochondrial uncoupler FCCP on hypoglossal area of MNs-glia network loaded with Rhod 123 dye to monitor $\Delta\Psi m$ continuously in the same slice. The results indicated that indeed it is possible to record impact of several neuromodulators continuously for more than half an hour and rat MNs-glia brain stem slice network are a potent model which allows analysis of neuronal properties and cell viability within a time window of at least an hour (Fig. 3.6.11).

4. Discussion

The aim of the present study was to determine the role of mSOD1^{G93A} on cellular Ca^{2+} homeostasis and mitochondrial signaling pathways in selectively vulnerable MNs in ALS. In fact, recent evidences suggest that abnormalities in cellular Ca^{2+} signaling are common features in the pathogenesis of a range of neurodegenerative disorders, including ALS (Mattson *et al*., 2000). It is well known that Ca^{2+} is one of the most relevant intracellular messengers, being essential in neuronal development, synaptic transmission and plasticity, as well as in the regulation of various metabolic pathways in the brain level. In both subtypes of ALS associated with SOD1 mutation and in the sporadic disease, there have been several reports indicating that the involvement of mitochondria in the pathogenesis includes the generation of intracellular free radical species (Radi *et al*., 1997), ultrastructral changes in mitochondrial morphology (Sasaki & Iwata, 1996; Sasaki *et al*., 2004), swollen and vacuolar mitochondria (Wong *et al*., 1995), increased activity of complex I, III and IV in frontal cortex and spinal cord (Kong & Xu, 1998; Mattiazzi *et al*., 2002; Wiedemann *et al*., 2002). Impaired spinal cord (Fujita *et al*., 1996) and vulnerable individual spinal MNs (Borthwick *et al*., 1999) have also been reported. It has been proposed that this damage triggers the functional decline of MNs and the onset of pathology in ALS. The loss of $\Delta\Psi m$ (Carri *et al*., 1997), excitotoxic stimulation of AMPA/kainite receptors (Carriedo *et al*., 2000) and age related MN injury (Beal, 2002; Menzies *et al*., 2002) reported by many groups may contribute to ALS pathogenesis.

Further evidence for involvement of disruption of intracellular Ca^{2+} homeostasis arises from several studies of cellular and experimental animal models in which absence of Ca^{2+} binding proteins such as CB-D_{28K} and parvalbumin in MN populations lost early (hypoglossal, spinal, and lower cranial MNs) in ALS (Alexianu *et al*., 1994). These findings are in good agreement with a quantitative comparison of Ca^{2+} homeostasis where low cytosolic Ca^{2+} buffering capacity act as an important risk factor for degeneration and in contrast an increase in cytosolic Ca^{2+} buffering capacity could protect vulnerable MNs from degeneration both *in-vitro* and *in-vivo* (Beers *et al*., 2001; Van Den Bosch *et al*., 2002). Several lines of evidence explain altered Ca^{2+} homeostasis leading to MN degeneration in ALS, notably disturbance of glutamate neurotransmission and subsequent glutamate triggered Ca^{2+} entry (Heath & Shaw, 2002; Rao & Weiss, 2004), increased extracellular glutamate levels probably due to reduced glial glutamate uptake caused by oxidative damage to EAAT2 (Maragakis & Rothstein, 2001), study of fALS in cell lines and animal mouse models where potential mechanism for Ca^{2+} disruption is inhibition of glial glutamate transport by mSOD1 similar to those proposed for sALS (Trotti *et al*.,1999). In addition, in cell culture experiments, partial protection was also obtained by treatment with nifedipine, implicating Ca^{2+} entry through voltage-gated Ca^{2+} channels in mediating the toxicity of mSOD1^{G93A} in MNs (Tateno *et al*., 2004). Evidence also suggests that ROS generated in MNs can cross the plasma membrane and cause oxidative disruption of glutamate transporters in neighbouring astrocytes (Rao *et al*., 2003; Rao & Weiss, 2004). However, in ALS pathology, the nature of dysfunction is highly controversial after some recent findings where non-cell autonomous effect of glia on MNs in an embryonic stem cell-based ALS model and astrocytes expressing ALS-linked mSOD1 that release factors selectively toxic to MNs was shown (Di Giorgio *et al*., 2007; Holden, 2007; Julien, 2007; Nagai *et al*., 2007).

This study has been done in various cell culture as well as animal model systems to explore processes of mitochondrial disruption, disturb Ca^{2+} homeostasis and selective vulnerability of MNs in ALS. MNs stored a larger amount of calcium in the mitochondria and the disruption of mitochondrial Ca^{2+} uptake had a marked influence on both the peak amplitude of Ca^{2+} response as well as on the clearance of Ca^{2+} from the cytoplasm. The results described here provide definite confirmation of the distinct role of mitochondria in handling the Ca^{2+} metabolism in WT and mSOD1^{G93A} mice. Preparation of adult (8-9 weeks and 14-15 weeks) mice brain stem slices of WT and corresponding SOD1^{G93A} is particularly valuable because it preserves MNs in their physiological environment in a functionally intact state and provides a way to study disease progression in SOD1^{G93A} mice in a natural environment. This is highlighted by *in-vitro* slice preparation of the mouse brainstem, where the HMNs can be preserved within a neuronal network receiving rhythmic excitatory input from the 'Pre Botzinger complex' as part of the respiratory system. As demonstrated by several groups, Ca^{2+} oscillations in patch-clamp and Ca^{2+}-imaging experiments are closely related to the physiological regulation of MNs firing rates through Ca^{2+}-dependent channels after hyperpolarizations, primarily by coupling activity-evoked Ca^{2+} influx to activation of Ca^{2+}-dependent K^{+}-channels (Bayliss *et al*., 1997; Ladewig & Keller, 2000). In this report, we also studied the Ca^{2+} buffering capacity of primary neuronal culture from cortex of E_{18} mice transfected with low and high calcium binding proteins CB-D_{28K} where the observation categorizes the neurons very clearly into comparatively high-buffered and low-buffered neurons based on non transfected and low/high CB-D_{28K} transfected MNs. This is an essential attribute when we consider the survival chance of these MNs in ALS-related insults. Considering the prime participation of mitochondria not only in calcium homeostasis directly but also in the energy transduction (to operate other Ca^{2+} clearing mechanisms) and in enacting apoptosis, this manifestation is of immense importance.

Culture systems (i.e. slice culture or MNs primary culture) have proven valuable tools for physiological and biochemical characterization of ALS-related pathology over time and testing protective strategy for neuroprotection (Bar, 2000; Sachiko *et al*., 2005; Avossa *et al*., 2006). The data currently available so far leave several important questions unanswered; these include: 1) does the presence of mSOD1 cause morphological abnormalities of mitochondria when expressed at physiological levels? 2) Does the mitochondrial Ca^{2+} sequestration source specificity and spatiotemporal properties of $[Ca^{2+}]i$ signaling in WT and $SOD1^{G93A}$ transfected cells varies at physiological levels? 3) What are the functional consequences of any changes in mitochondrial function on Ca^{2+} homeostasis in the presence of $mSOD1^{G93A}$? This could potentially be addressed using a cellular model of SOD1-related MN injury (In our case SH-SY5Y neuroblastoma cells transfected with WT and SOD1G93A gene).

The present study endeavors to address all these questions using adult (8-9 weeks and 14-15 weeks) brain stem slices of WT and corresponding $SOD1^{G93A}$ mice, SH-SY5Y neuroblastoma cells transfected with WT-SOD1 and $SOD1^{G93A}$ gene, acute brain stem slices of P0-P4 wistar rats and primary culture of MNs transfected with CB-D_{28K} at levels approximating to those seen in the human ALS disease.

4.1 Monitoring ΔΨm in HMNs of WT and $mSOD1^{G93A}$ Mice Disrupting Mitochondrial Integrity by Mitochondrial Uncoupler FCCP

Monitoring mitochondrial metabolic function in brainstem slices was important choice to study the integrity of mitochondria. Measurement of ΔΨm is a good experimental measure to monitor the intactness and energy metabolism of the HMNs in WT and $mSOD1^{G93A}$ mice. To study the role of mitochondria in the selective vulnerability of HMNs of ALS, we employed protonophore FCCP as an effective drug alone or in combination with other drugs such as oligomycin. The action of FCCP could be very clearly studied from its effect on the $\Delta\Psi m$, ensuing $[Ca^{2+}]_i$ elevation and did not show any non-specific effect on cell membrane potential where as oligomycin act as an ATP synthase inhibitor, inhibits oxidative phosphorylation of ATP but not glycolytic production of ATP. The probability of the localization of FCCP on the plasma membrane and any resulting leak of Ca^{2+} ions was previously checked monitoring the current across the cell membrane in voltage-clamped HMNs, which did not reveal any change upon application of FCCP, whereas the application of 2mM Na^+-cyanide showed an immediate inward current (Bergmann & Keller, 2004). The measure of the spatial heterogeneity of the Rhod 123 signal is sensitive to the level of mitochondrial depolarization (Toescu & Verkhratsky, 2000). When Rhod 123 loaded HMNs were treated with 2µM FCCP, there was a sudden and reversible increase in fluorescence, indicating the transient loss of $\Delta\Psi m$ due to proton influx through Ca^{2+} uniporter (Fig. 3.1.1b). A number of conclusions have been drawn about the cellular energetics and state of mitochondria in MNs of WT and $SOD1^{G93A}$ mice under the influence of these drugs modulations.

4.2 Mitochondrial Status in Vulnerable HMNs of $SOD1^{G93A}$ Mice

The first part of this work has been to characterize the mitochondrial status and contribution of mitochondria in vulnerable HMNs of $SOD1^{G93A}$ mice. We have used the measure of mitochondrial depolarisation status to assess, in a qualitative way, the mitochondrial polarisation status in selectively vulnerable HMNs of ALS and drawn a number of conclusions about the cellular energetics and disease state of mitochondria. When Rhod 123 loaded HMNs were treated with 2µM FCCP for 20s to 4 min, there was a sudden and reversible increase in the fluorescence due to loss of $\Delta\Psi m$ (Fig. 3.1.1b). Changes in $\Delta\Psi m$ responses after FCCP application (normalised) were almost ~3 fold larger in WT compared to $SOD1^{G93A}$ mice at symptomatic stage of motor dysfunction, supporting the hypothesis that mitochondrial Ca^{2+} homeostasis is significantly disturbed in $SOD1^{G93A}$ mice and mitochondria play a crucial role in MN degeneration in $SOD1^{G93A}$ mice model of hALS. Furthermore, to check whether mitochondrial depolarization can affect the FCCP evoked $\Delta\Psi m$ response of these MNs; comparing efficiency of depolarisation induced mitochondria after 30mM K^+ depolarization stimulus showed that 30mM K^+ evoked responses in 8-9 weeks WT and corresponding $SOD1^{G93A}$ mice in pre symptomatic stage of motor dysfunction were comparable. In contrast, application of FCCP evoked responses were significantly smaller (~2.62 fold, n=24) in 14-15 weeks SOD1^{G93A} mice, suggesting impaired mitochondria (Fig. 3.1.3), as also described earlier (Ward *et al*., 2000).

The probability of reduction in cellular ATP due to inhibition of oxidative phosphorylation (dependent on $\Delta\Psi m$) and the reversal of ATP synthase in a futile cycle to regenerate $\Delta\Psi m$ was also checked, which results in hydrolysis of any cellular ATP stores and ATP produced by glycolysis. We would expect that ATP available for cellular processes such as membrane Ca^{2+} ATPases would be the lowest during bath application of FCCP. Bath application of oligomycin alone results in inhibition of ATP via oxidative phosphorylation, while $\Delta\Psi m$ remains intact due to the fact that cellular ATP is reduced but not depleted, as glycolysis provides some ATP production. In this condition, cellular ATP levels are reduced but to a lesser extent than in FCCP alone, as $\Delta\Psi m$ is intact and no reversal of ATP synthase occurs. Mitochondrial uptake of calcium may occur via the calcium uniporter supported by the intact electrochemical gradient. However, oligomycin alone did not cause any disruption of postdepolarisation and basal $[Ca^{2+}]_i$ regulation in HMNs of SOD1^{G93A} mice, even if at very low extent (Fig. 3.1.2). This probably indicates that ATP-dependent mechanism is only partially important in regulating $\Delta\Psi m$ in HMNs of 8-9 and 14-15 weeks WT and corresponding SOD1^{G93A} mice at pre symptomatic and symptomatic stage of motor dysfunction. These results also suggest that the oligomycin induced blockade of the mitochondrial F_1, F_0-ATP synthase have very minor contribution in the response of $\Delta\Psi m$ and possibility of reversal in a F_1, F_0-ATP synthase futile cycle or restoration of $\Delta\Psi m$ was more likely to occur in symptomatic stage of motor dysfunction as we saw a little bit higher Rhod 123 fluorescence in symptomatic SOD1^{G93A} mice compared to the corresponding SOD1^{G93A} mice at pre symptomatic stage of motor dysfunction (Fig. 3.1.2E). We assume that this could be due to several factors including aging, vulnerable MNs and the slow activity of the mitochondrial Na^+/Ca^{2+} exchanger. Furthermore, as the cellular buffering of $[Ca^{2+}]_i$ was not completely blocked in mSOD1 Tg mice, it indicates that some MNs are viable and as potent in WT as in SOD1^{G93A} mice at the symptomatic stage of ALS. In the confirmation experiment to determine whether $\Delta\Psi m$ restore when depolarised with FCCP, we used oligomycin together with FCCP to prevent any accelerated consumption of cellular ATP by reverse action of the ATP synthase and found that FCCP induced a prominent increase in Rhod 123 fluorescence signal of variable size and duration apparently reflecting collapse of mitochondria in greater extent compared to oligomycin where peak amplitude was negligible as seen in 8-9 and 14-15 weeks WT and corresponding pre symptomatic and symptomatic SOD1^{G93A} mice (Fig. 3.1.4).

4.3 The Effect of Mitochondrial Inhibition on [Ca^{2+}]i Release-Uptake Phenomenon and Ca^{2+} Transient in WT and SOD1^{G93A} Mice/Cell Culture Model of ALS

Our interest in studying the role of Ca^{2+} regulation and impact of mitochondrial inhibition on HMNs is based on several observations showing that mitochondria act as local calcium buffers, thus shaping spatiotemporal aspects of [Ca^{2+}]i signals. As previously described mitochondria in HMNs and FMNs had a major percentage of the Ca^{2+}, sequestered intracellularly after Ca^{2+} influx through the plasma membrane (Balakrishnan *et al.*, 2004). The main objective of the first part of this work was to characterize the contribution of mitochondrial buffering of voltage-activated Ca^{2+} loads in HMNs and evaluates the Ca^{2+} signaling in MNs that are particularly vulnerable in Tg mice models of hALS at pre symptomatic and symptomatic stage of motor dysfunction. Accordingly, we performed a semi quantitative analysis of Ca^{2+} homeostasis in HMNs of SOD1^{G93A} mice based on rapid CCD imaging approach.

The swiftness of mitochondrial Ca^{2+} uptake in HMNs of 8-9 weeks WT and corresponding SOD1^{G93A} mice was evident in the experiments where presence of FCCP caused a comparable increase in the amplitude of [Ca^{2+}]i transients (Fig. 3.1.6A & B), whereas in HMNs of 14-15 weeks WT mice increase in the amplitude of the [Ca^{2+}]i transients was ~2.18 fold greater than the corresponding symptomatic SOD1^{G93A} littermate (Fig. 3.1.6C & D). In HMNs of symptomatic SOD1^{G93A} mice (Fig. 3.1.6E), mitochondrial Ca^{2+}release was much less in amplitude after the preceding cytosolic Ca^{2+} increase. The higher load of calcium in HMNs of pre symptomatic WT/SOD1^{G93A} mice as well as symptomatic WT mice could be clearly attributed to the specialization of these cells to get hold of Ca^{2+}. This specialized property of mitochondria in HMNs could be vital during ALS pathology as the high glutamate concentration in synapses can lead to massive cellular entry and over-accumulation of Ca^{2+} in the mitochondria, which is a conventional trigger for mitochondrial swelling and permeability transition. Under such circumstances, HMNs of SOD1^{G93A} mice which employ mitochondria to buffer Ca^{2+} ions are at particular risk than MNs like TMNs and OMNs, which are supplied with abundance of Ca^{2+} chelating proteins. The vulnerability of the HMNs in ALS pretense many questions and the evident mitochondrial pathology observed in ALS patients and the animal models put forward a central role for the degradation of mitochondrial integrity and metabolism by uncontrolled mitochondrial Ca^{2+} accumulation which leads to a vicious circle of pathological mechanisms in ALS and is finally transformed into a fatal cycle. The 30mM K^+ induced Ca^{2+} transient in presence of intact mitochondria (14-15 weeks WT mice) was higher in amplitude than the $SOD1^{G93A}$ mice HMNs in presence of FCCP (Fig. 3.1.7). The excess Ca^{2+} which emerges in the second response (FCCP) seems to be hidden by the mitochondrial uptake during the first response (K^+). This also proposed a close positioning of mitochondria to the source of Ca^{2+} entry, i.e. to the voltage gated Ca^{2+} channels and disturbance of this mechanism in symptomatic $SOD1^{G93A}$ mice. Absence of such characteristics in symptomatic $SOD1^{G93A}$ mice (Fig. 3.1.6A-E) implies that mitochondria in HMNs serve a pivotal role in controlling the Ca^{2+} entering the cell and functional pathways induced by Ca^{2+}. The experiments also indicated that mitochondria contribute at great extent to the fast clearance of Ca^{2+} transients by taking up around 50 % of MNs Ca^{2+} loads even for small amplitude $[Ca^{2+}]i$ elevations (50-200 nM; physiological range; Balakrishnan and Keller observation), which is evident in our experiment where prevention of mitochondrial input in Ca^{2+} uptake, by using FCCP caused a severe delay in the recovery time of $[Ca^{2+}]i$ transients in symptomatic $SOD1^{G93A}$ mice. It seems to us that mitochondrial Ca^{2+} buffering of small peak amplitude elevations is much more prominent in MNs than other neuronal systems, such as sympathetic neurons (Friel & Tsien, 1994), dorsal root ganglion neurons (Werth *et al.*, 1996), hippocampal neurons (Mironov, 1995) and chromaffin cells (Herrington *et al.*, 1996).

Furthermore, we sought to know how this Ca^{2+} regulatory mechanism is governed in WT-SOD1 and $SOD1^{G93A}$ transfected SH-SY5Y cell culture model of ALS. At first, a comparative analysis of the Ca^{2+} influx was studied by following the dynamics of Ca^{2+} signal under depleted mitochondrial conditions in SH-SY5Y neuroblastoma cells transfected with WT-SOD1 and $SOD1^{G93A}$ gene by bath application of FCCP. Interestingly it was observed that in $SOD1^{G93A}$ transfected cells, Ca^{2+} influx was diminished (~1.86 fold) as compare to WT transfected cells where Ca^{2+} influx was more prominent and peak amplitude was achieved with in 2-3 min followed by baseline recovery in ~2 min contrast to $SOD1^{G93A}$ transfected cells which required almost 5-6 min for baseline recovery (Fig. 3.2.1A-D). After exposure to FCCP, the capacity of $mSOD1^{G93A}$ cells to transport $[Ca^{2+}]i$ to the extracellular space or to intracellular storage sites was much lower than the WT-SOD1 transfected cells. This accounted for the increased vulnerabitivity of cells possessing mSOD1^{G93A} gene. Interestingly, 30mM K^+ induced Ca^{2+} transient in presence of intact mitochondria (WT-SOD1 transfected SH-SY5Y cells) was smaller in amplitude than the SOD1^{G93A} transfected cells and excess Ca^{2+} which emerges in the second response hidden by the mitochondrial uptake during the first response was quite prominent in WT transfected SH-SY5Y cells as compared to SOD1^{G93A} transfected cells (Fig. 3.2.2A-D). This apparently reflects the variability in predominant Ca^{2+} clearing mechanisms of ALS-vulnerable and non vulnerable MNs. These results are in good agreement with the data obtained from motor nerve terminals (David & Barrett, 2003), cultured MNs (Carriedo *et al.*, 2000) and previous study on patch-clamped HMNs (Ladewig *et al.*, 2003), where significant mitochondrial Ca^{2+} uptake following voltage-activated Ca^{2+} influx were demonstrated.

4.4 Mechanism Underlying Mitochondria-ER Ca^{2+} Stores Coupling

Different intracellular pools participate in generating Ca^{2+} signals in neuronal cells and in shaping their spatio-temporal patterns as well as cell life-death cycle. Mitochondria (kinetic and hot spot hypothesis), and the ER (Different classes of channels with distinct properties and highly defined expression patterns) have been implicated in the regulation of $[Ca^{2+}]_i$ in many systems (Herrington *et al*.,1996; Schinder *et al*.,1996). In an attempt to understand more about the Ca^{2+} metabolism of HMNs, we studied the role of ER in Ca^{2+} handling in these MNs. ER in HMNs retained comparatively low quantity of calcium than mitochondria after $[Ca^{2+}]_i$ elevation, indicating its low efficiency to sequester Ca^{2+} in the HMNs of 14-15 weeks WT and SOD1^{G93A} mice which is slightly higher in 8-9 weeks mice (Fig. 3.1.8), indicating that the conventional Ca^{2+} storing function of mitochondria is dominating over ER Ca^{2+} accumulation in these MNs. The pre or post application of FCCP to CPA (SERCA pump inhibitor) on HMNs clearly caused a separate Ca^{2+} release response (Fig. 3.1.9). Presence of drug CPA which blocks the calcium uptake by ER have minimal effect on the propagation or peak amplitude of 30mM K^+ induced Ca^{2+} transients both in 8-9 and 14-15 weeks WT and SOD1^{G93A} mice HMNs. Besides, peak fluorescence amplitude in 14-15 weeks WT HMNs, ER Ca^{2+} release was quantitatively more than the MNs of SOD1^{G93A}. This indicates the explicit action of FCCP in our working model system and the existence of two separate intracellular Ca^{2+} stores where ER appears to play minimal role in buffering $[Ca^{2+}]$i after imposed Ca^{2+} loads in HMNs of SOD1^{G93A} mice and ER is most likely not impaired during ALS related

MN disease. Our hypothesis is strengthened by the fact that we got similar result in our cell culture model where WT-SOD1 and SOD1^{G93A} transfected SH-SY5Y cells shown that bath application of caffeine (not only selectively block Ca^{2+} uptake into ER and mitochondrial compartments but also trigger or prevent release from intracellular storage sites by ryanodine receptor (RyR)) led to relatively slow and weak increase of [Ca^{2+}]i and [Ca^{2+}]$_m$ which occurred with slightly higher kinetics in WT than the SOD1^{G93A} transfected SH-SY5Y cells (Fig. 3.3.2). This further explain that Caffeine-evoked ER-dependent Ca^{2+} release have minor contribution in mitochondrial mediated toxicity in SOD1^{G93A} transfected SH-SY5Y cells as reported earlier in other cell types and animal model (Murayama *et al*., 2000; Fill & Copello, 2002; Sher *et al*., 2007) .

Our results are in good agreement with the "hotspot hypothesis" that proposed that mitochondria preferentially accumulate Ca^{2+} at microdomains of elevated Ca^{2+}concentration ([Ca^{2+}]i) that exist near ER Ca^{2+} release sites and other Ca^{2+} channels. Accordingly, mitochondria may affect both Ca^{2+} release from the ER and capacitative Ca^{2+} entry across the plasma membrane, thereby shaping the size and duration of the intracellular Ca^{2+} signal in HMNs of WT and SOD1^{G93A} mice as well as WT-SOD1 and SOD1^{G93A} transfected SH-SY5Y cells and recruitment of these signals for selective MN degeneration. These events depend upon the Ca^{2+} sensitivity of the Ca^{2+} channels of the ER (allowing, for different Ca^{2+} concentrations and channel isoforms, positive or negative modulation of the Ca^{2+} release process) and the capacity of mitochondria to remove Ca^{2+} from the microdomain at the mouth of the channel. This effect has been confirmed in mammals, but the situation appears distinctly different in various cell models (Arnaudeau *et al*., 2001; Szabadkai *et al*., 2003). This indicates that various modulatory mechanisms exist, many of which still await molecular clarification at cellular and molecular level. As discussed above, overwhelming evidence confirms the idea that the measured high rate of Ca^{2+} accumulation of MNs mitochondria *in situ* largely depends on the proximity of mitochondria to the channels through which Ca^{2+} penetrates into the cytosol. A key, but still unanswered, question is whether this proximity is random and occurs only because some of these very abundant organelles, which are present throughout the cytosol, happen to be close to these channels, or whether there is a specific mechanism to ensure that mitochondria are located close to sites of Ca^{2+} influx and release(stochastic versus specific localization). The molecular mechanisms that define the organization of mitochondria in MNs of mice with regard to the ER and other Ca^{2+} sources, and the extent to which mitochondrial function varies among different cell types, are open questions whose answers remain to be determined.

4.5 Simultaneous Measurements of [Ca^{2+}]i and [Ca^{2+}]m Concentrations, Ca^{2+} Sequestration Source Specificity and Spatiotemporal Properties of WT-SOD1 and SOD1^{G93A} Transfected SH-SY5Y Cells

To reliably, separately and simultaneously detect relationships between cytosolic and mitochondrial Ca^{2+} signal ([Ca^{2+}]i release and $[Ca^{2+}]_m$ uptake) changes in the same cells, we developed a CCD camera imaging system that allowed us to simultaneously monitor cytosolic (Fura-2) and mitochondrial calcium concentrations (Rhod-2) with a temporal resolution in the millisecond time domain in WT and SOD1^{G93A} transfected SH-SY5Y neuroblastoma cells. This permitted us to clearly separate dynamic profiles of [Ca^{2+}]i and [Ca^{2+}]m. Using this method in Fig. 3.3.1, we demonstrated that in WT transfected cells FCCP evoked increase in [Ca^{2+}]i was mainly due to [Ca^{2+}]i and there is little impact of [Ca^{2+}]m on it. However, in SOD1^{G93A} transfected cells, FCCP evoked [Ca^{2+}]i was smaller and exhibited slower kinetics while emptying [Ca^{2+}]m. The lower and slower kinetics of [Ca^{2+}]m in SOD1^{G93A} transfected cells suggests that these cells have lower affinity for mitochondrial Ca^{2+} upload and these changes are likely represent severely disturbed and vulnerable mitochondria in SOD1^{G93A} transfected cells. The study made possible, for the first time, the simultaneous determination of [Ca^{2+}]i and [Ca^{2+}]m concentrations in SOD1^{G93A} transfected vulnerable MNs.

Furthermore, to know more about the relative impact of mitochondria and ER in differential [Ca^{2+}]i and [Ca^{2+}]m regulation, and its consequence on MN degeneration in SOD1^{G93A} transfected SH-SY5Y cells, we used caffeine a specific activator of Ca^{2+} influx from ryanodine receptor (RyR)-dependent Ca^{2+} stores to investigate ER-dependent Ca^{2+} release response (Solovyova *et al.*, 2002). Data in Fig. 3.3.2 shows that caffeine evoked a small and slow increase in [Ca^{2+}]i and $[Ca^{2+}]_m$ in WT transfected SH-SY5Y cells with slightly higher kinetics than the SOD1^{G93A} transfected cells, further affirm that caffeine-evoked ER-dependent Ca^{2+} release have minor contribution in mitochondrial mediated toxicity in SOD1^{G93A} transfected SH-SY5Y cells. In Fig. 3.3.2, rate of increase in Fura-2/Rhod-2 fluorescence following caffeine application was little bit slower and did not resume the baseline probably due to the slow activity of the mitochondrial Na^+/Ca^{2+} exchanger, the major pathway for mitochondrial Ca^{2+} efflux, as has previously been reported clearly in other articles (Leoty *et al*., 2001). Experimental observations during different pharmacological conditions support the concept that the presence of mSOD1^{G93A} severely disrupts mitochondrial Ca^{2+} regulation. Taken together, our fluorescence system promises to serve as a valuable tool to specify in detail mitochondrial and Ca^{2+}-related defects during mSOD1^{G93A}-mediated MN degeneration and closely parallels the incidence of neuronal death in mSOD1^{G93A} transfected SH-SY5Y cells.

4.6 Characteristic Low Ca^{2+} Buffering Capacity of Motoneuron and its Impact on Selective Motoneuron Vulnerability

The localization of calcium microdomains and the rapid Ca^{2+} uptake and release phenomenon are well known facts (Baron *et al*., 2003; Malli *et al*., 2003; Rizzuto *et al*., 2000, 2004). To what concentrations and how Ca^{2+} in the mitochondrial matrix of MNs rises is a matter of great debate because of the widely varying results obtained with different probes and calibration procedures used by different groups. However, several supporting evidences favor the hypothesis that resistant MNs have fairly high concentration of calcium binding proteins, which control calcium transients and plasma membrane extrusion in these neurons, where mitochondria has little role in terms of calcium buffering. On the other hand, in the vulnerable neurons (HMNs & FMNs), rapid Ca^{2+} uptake during neuronal activity was made by mitochondria to control the [Ca^{2+}]i, coexisting with the reduced calcium buffering proteins (Lips & Keller, 1999). This may offer a precise localization of the mitochondria into the hotspots of Ca^{2+} entry or a wide spread distribution of these organelles in the low buffer cytoplasm of susceptible MNs. Supporting evidences are also provided from the experimental results where Ca^{2+} involvement as a risk factor was indicated by the observation that Ca^{2+}-binding proteins such as CB-D$_{28k}$ and parvalbumin were absent in MN populations (HMN & SMN) lost early in ALS (Alexianu *et al.*, 1994). In contrast, results from dorsal vagal neurons containing plenty of Ca^{2+} sequestering proteins (De Leon *et al*., 1993), the delay in the τ of Ca^{2+} transients (FCCP influx) were not caused by mitochondrial permeability.

In order to check whether CB-D$_{28k}$ protect cells from dysfunction and degeneration via buffering of [Ca^{2+}]i, Ca^{2+} imaging studies following depolarization induced stimulus (60mM K^{+}) were done in primary neuronal cells obtained from mice cortex at E$_{18}$ expressing low and high CB-D$_{28k}$. Our results in Fig. 3.4.1 shows that indeed CB-D$_{28k}$ buffer [Ca^{2+}]i where low and high CB-D$_{28k}$ transfected cells display a significant (~2 times) reduction in the peak amplitude of the sustained $[Ca^{2+}]i$ increase. Decay time constant (τ) in CB-D_{28k} transfected cells was also relatively slower (~60s) contrast to non transfected cells where baseline recovery time is ~30-35s (Fig. 3.4.1(B)a-c; Fig. 3.4.2(A)) while showing little differences in the area under the time - concentration curve (AUC). The observation is in good agreement with the "Low buffering hypothesis" stating that low buffers provide MNs with rapid Ca^{2+} dynamics during physiological activity, but represent a significant risk factor during ALS-related MN disease (Vanselow and Keller, 2000). In conclusion, we believe that two most important features significant for MNs in ALS are: (i) Low buffers generate exceptionally large Ca^{2+} domains, but not in case of serious ALS like symptoms and (ii) In ALS vulnerable MNs buffering capacity is critically depends upon the domain size of mitochondria and ER. Therefore, we proposed a model where a portion of MN mitochondria interacts with areas of high $[Ca^{2+}]$ around influx sites due to low buffering induced excitotoxicity shown in Fig. 4.6.

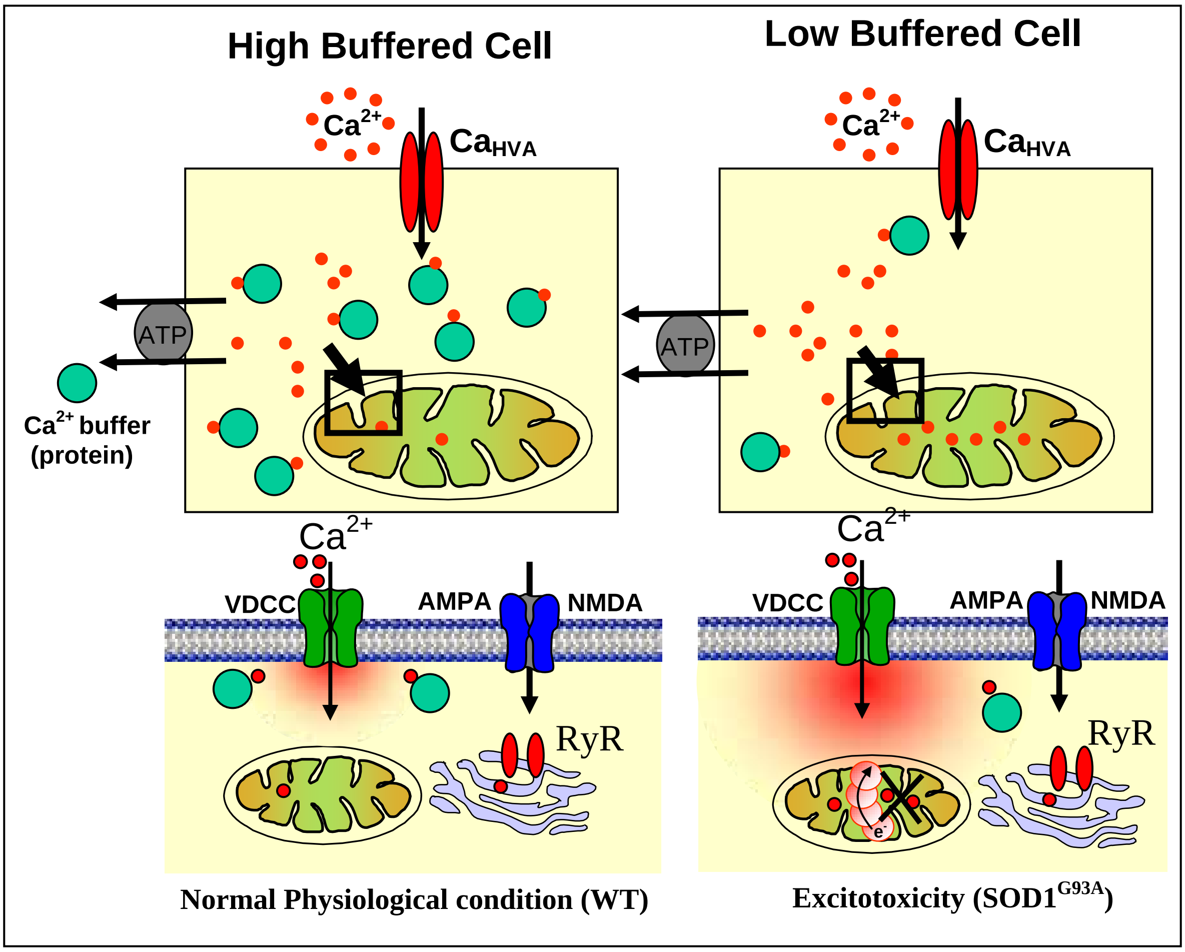
High Buffered Cell
Low Buffered Cell
Ca2+
CaHVA
Ca2+
CaHVA
ATP
ATP
Ca2+ buffer (protein)
Ca2+
Ca2+
VDCC
AMPA
NMDA
VDCC
AMPA
NMDA
RyR
RyR
e-
Normal Physiological condition (WT)
Excitotoxicity (SOD1G93A)

Fig. 4.6: Low Ca^{2+} buffering and excitotoxicity under physiological and pathophysiological conditions in MNs. Low Ca^{2+} buffering in ALS vulnerable HMNs exposes mitochondria to higher Ca^{2+} loads compared to high buffered cells. Under normal physiological conditions the neurotransmitter opens glutamate, NMDA and AMPA receptor channels alongwith voltage dependent Ca^{2+} channels (VDCC) with high glutamate release which is reuptake by EAAT1 and EAAT2, results in a small rise in intracellular calcium that can be buffered in the cell. In the ALS, disorder in the glutamate receptor

channels leads to high calcium conductivity and there by high Ca^{2+} loads, increase the risk for mitochondrial damage. This triggers mitochondrial production of reactive oxygen species (ROS), which then inhibit glial EAAT2 function. This leads to further increasing in glutamate concentrations in the synapse and further rises in postsynaptic calcium levelss contributes to the selective vulnerability of MNs in ALS.

4.7 Cross-Talk Between Motoneuron-Glia in ALS Vulnerability and Pathogenesis

The goal of these experiments was to develop a method of estimation for glia contribution to the pathophysiology of ALS, particularly through dysfunction of their glutamate transporters, which results in increased extracellular glutamate levels, reduced glutamate transport and excitotoxic damage to MNs earlier describe in great details by Rothstein and colleagues. Reduced clearance of extracellular glutamate was disease- and region- specific, particularly in brain stem and spinal cord (Rothstein *et al*., 1992, 1995). It is unclear whether dysfunction of glial glutamate transporter is causative of ALS or whether this dysfunction follows from oxidative damage that is initiated in MNs. One suggestion is that activation of AMPA receptors might lead to the release of ROS from spinal cord and brain stem MNs, which results in oxidation and local decrease of glutamate uptake in neighboring astrocytes. Accordingly, a pathological type of MNs-glia interaction that might contribute to the initiation of ALS is defined by a sequence of events- initiation of Ca^{2+} entry through glutamate receptors, followed by mitochondrial Ca^{2+} overload and subsequent production of ROS that impair glial glutamate uptake, which results in extracellular accumulation of glutamate and eventually exacerbation of Ca^{2+} entry into MNs (Rao *et al*., 2003; Seifert *et al*., 2006). Recent work suggests an alternative ALS pathogenic model suggesting that not only the proportion of mutant expressing cells but also the topographical relationship between affected MNs and healthy glial cells can influence the progression of the disease (Clement *et al*., 2003; Urushitani *et al*., 2006).

These new prospective have revived the question regarding the role of glia and its interaction with MNs in ALS. Considering that physiological implications of these findings are likely to be profound, we have shown that transient inhibition of mitochondrial function concurrent with glutamate exposure significantly reduces delayed neurotoxicity and very high $[Ca^{2+}]i$ alone are not toxic to MNs. However, the potential–driven uptake of Ca^{2+} into the mitochondria is essential to trigger excitotoxic neuronal death as described in Fig. 3.6.4 and 3.6.5 of results section portentous that typical hypoxia (5mM CN^{-}) response is not alter and relatively high after glutamate evoked [Ca^{2+}]i in MNs illustrating that MNs mitochondria indeed stores Ca^{2+} release from glia after glutamate application and not vulnerable to glutamate induced neurotoxicity at least for acute exposure. Though, weaker response and delayed recovery by 30-40s suggesting that glial cells might be partially vulnerable to glutamate induced Ca^{2+} neurotoxicity (Fig. 3.6.4). Further, experiments with mitochondrial uncoupler FCCP indicate that mitochondrial calcium uptake is necessary for expression of excitotoxicity in MNs but its implication is doubtful in glail cells as we have shown here a condition in which glutamate-stimulated increase in [Ca^{2+}]i are extremely high with mild toxicity in glia and little or no apparent toxicity in MNs and vice versa with FCCP (Fig. 3.6.6).

Consistent with our conclusion that blockade of Ca^{2+} uptake into the mitochondria is neuroprotective, as onset of MNs death is delayed by inclusion of acute hypoxia and FCCP, the changes in $\Delta\Psi m$ after hypoxia (Fig. 3.6.9) and FCCP (Fig. 3.6.10) induce mitochondrial depolarization have indeed profound impact. In contrast, glutamate induced depolarization (Fig. 3.6.8) have quite weaker response (Glutamate induce Rhod 123 release response was ~3 times weaker compare to CN^- and ~6 times weaker compare to FCCP) indicating that indeed mitochondria play greater role in MNs-glia mediated toxicity. The finding that mitochondrial Ca^{2+} uptake is essential for MNs injury but glia toxicity seems to be occurred via glutamate induced excitotoxicty, provide a new approach for protection against MNs and glia toxicity. Correct functioning of glia and their partnership with neighboring MNs seems to be essential for normal brain function and study of their interaction in physiology and pathophysiology of ALS is of great importance. An impressive example is recent findings where ALS pathology has been shown to depend on alterations in the local interactions between MNs, astrocytes and microglial cells. However, this explosion of findings raises further questions. First, what is the basis for cell-type specificity in ALS? Further investigation will probably provide a more fundamental understanding of ALS, because cell selectivity is a fundamental characteristic of this deadly yet obscure disease.

4.8 Drug Targets in ALS: Design and Implementation of Multidrug Therapies, Where Should We Aim?

A decade of experimentation using mice and rodents made Tg for human mSOD1 has yielded a mass of information about the mechanisms that underlie ALS, and suggestions for therapy.

However, the main rationale for the failure to translate experimentation in animals to patients might be that ALS is not only a multifactorial disease but also a multisystemic disease result of a complex neurotoxic cascade that involves molecular cross-talk between MNs, glia and astrocytes as well as muscle and affects several cell types (Bruijn *et al.*, 2004). Preclinical tests suffer from the fact that data are usually collected in animals of the same age and with the same mutation expressed in a homogeneous genetic background. By contrast, the age of onset, the progression and the severity of ALS in patients are heterogeneous, indicating that many (only partially known) potential genetic risk factors and modifying factors exist for sALS and some drugs are effective only if given before onset (Shaw, 2005). In the view of the fact mention above, we have tested several neuroprotective drugs *in-vitro* in brain stem slice preparation of WT and SOD1^{G93A} mice as well as in transfected SH-SY5Y cell culture to validate how drugs e.g. riluzole and melatonin rescue mitochondrial mediated oxidative stress and dysfunction in ALS. Our data suggest that riluzole moderately inhibits complex IV inhibitors induce [Ca^{2+}]$_i$ signaling via multiple mechanisms of ion channel modulation in 14-15 weeks symptomatic SOD1^{G93A} mice, however the effect of melatonin protection (see Fig. 3.5.1 & 3.5.2 in result section) in symptomatic SOD1^{G93A} mice was not significant. We think that the inhibition of [Ca^{2+}]i increase in SOD1^{G93A} mice might be attributed either to a strong blockade of Na^{+}-current by riluzole or direct reduction in the entry of Ca^{2+} through voltage-dependent Ca^{2+}-channels after first sodium azide application. This drug targeted stabilization of mitochondria-related signal cascades might represent a useful strategy for clinical neuroprotection in ALS.

In the view of recent findings of a non-cell-autonomous demise of MNs, design of multi drug combination therapies should be intended at the interception of multiple aspects of this cascade, rather than a single-drug treatment. Till now animal studies have shown that combination therapies and the method of delivery of a treatment is also often have synergistic effects in ALS, for example, riluzole administered with melatonin and vitamine E (inhibits Na^{+}-current activation and the apoptotic cascade), minocycline administered with creatine (inhibits microglia activation and the apoptotic cascade), or treatment with IGF-1 or VEGF retrogradely transported in MNs through viral vectors (Gurney *et al*., 1996; Kaspar *et al*., 2003; Zhang *et al*., 2003; Azzouz *et al*., 2004; Frieling *et al*., 2007). Alternative to pharmacological treatments, the recent developments in stem-cell research might provide possibilities for neural implantation therapy in patients with ALS (Garbuzova-Davis *et al*., 2003; Lepore & Maragakis, 2007; Lee *et al*., 2007). These lessons learned from a decade of work using the mSOD1 animal model, might help researchers trying to find cures for neurodegeneration where single-drug approaches have proven insufficient for effective treatment.

4.9 Consequence of Disturbed Mitochondrial Mechanism, Selective Vulnerability and its Implications for Pathogenesis - Proposed Mechanism and Interactive Model

Selective vulnerability of MNs in ALS-related disease and associated mouse models is closely linked to exceptional Ca^{2+} signaling mechanisms that are part of the physiological cell function, but seemingly also enhances the risk of disruption of Ca^{2+} homeostasis and mitochondrial dysfunction in vulnerable cells. Despite rigorous research, since description by Charcot more than 130 years ago, the molecular abnormalities which lead to damage of specific MNs in ALS are still dodging the scientific community. Earlier studies have suggested that uncontrolled Ca^{2+} entry and inefficacy to sequester this calcium causing selective damage leads to formation of vacuoles derived from the degenerating mitochondria in the MNs of the mouse model of ALS (Kong & Xu, 1998; Sasaki *et al*., 2004). In contrast to most other neurons, MNs have a low Ca^{2+}-buffering capacity due to the low expression of Ca^{2+}-buffering proteins and a high number of Ca^{2+}-permeable AMPA receptors resulting from a low expression of the GluR2 subunit. The combination of these two properties seems to be intrinsic to MNs and is most likely essential for their normal function. However, under pathological conditions, MNs could become over stimulated by glutamate and overwhelmed by Ca^{2+}, although whether downstream pathways activated by the intracellular Ca^{2+} increase are different in MNs compared to other neurons is not yet known.

Our experiments identify a specialized Ca^{2+} homeostasis characterized by low cytosolic Ca^{2+} buffering, where mitochondria play a major role for regulation of $[Ca^{2+}]_i$ transients in vulnerable MNs by taking up more than 50% of Ca^{2+} even at low cytosolic Ca^{2+} elevations. Low cytosolic Ca^{2+} buffering enhances the role of low affinity organelle buffers such as mitochondria in the cell. For example, large and long-lasting Ca^{2+} domains around influx sites enhance the risk of toxic Ca^{2+} accumulations and a subsequent activation of Ca^{2+} dependent neurodegenerative pathways under excitotoxic conditions. Indeed, a strong contribution of mitochondria and not ER Ca^{2+} uptake to buffering of Ca^{2+} profiles has been demonstrated recently (Bergmann & Keller, 2004; Ladewig *et al*., 2003). The prominent role of mitochondria in regulation of moderate Ca^{2+} loads in HMNs has important implications for pathological conditions such as in ALS for two reasons. First, the amount of Ca^{2+} taken up by the mitochondria is probably higher in MNs than in many other cell types (Carriedo *et al*., 2000; Sen *et al*., 2005). These high Ca^{2+} loads enhance the risk for generation of ROS, which are suggested to play a major role in initiating a death leading circle resulting in MN degeneration (Rao *et al*., 2003). Second, our experiments provide evidence that cytosolic Ca^{2+} critically depends on intact Ca^{2+} uptake into mitochondria. Thus, when mitochondrial Ca^{2+} uptake is disturbed and as seen by low Ca^{2+} uptake in $SOD1^{G93A}$ HMNs compare to WT (Late stage of motor dysfunction-symptomatic), MNs are directly put at risk to accumulate basal Ca^{2+} levels during repetitive oscillations. Additionally, the decreased ability to limit Ca^{2+} transients amplitudes in the cytosol and in particular in local domains when mitochondria are depolarised, enhances the risk of initiating Ca^{2+} dependent neurodegenerative pathways leading to cell death. A summary of the mechanisms identified is given in Fig. 4.9; where in the vulnerable MNs, the calcium buffering machinery is represented by the predominance of mitochondria, and by the calcium binding proteins in the non-vulnerable MNs.

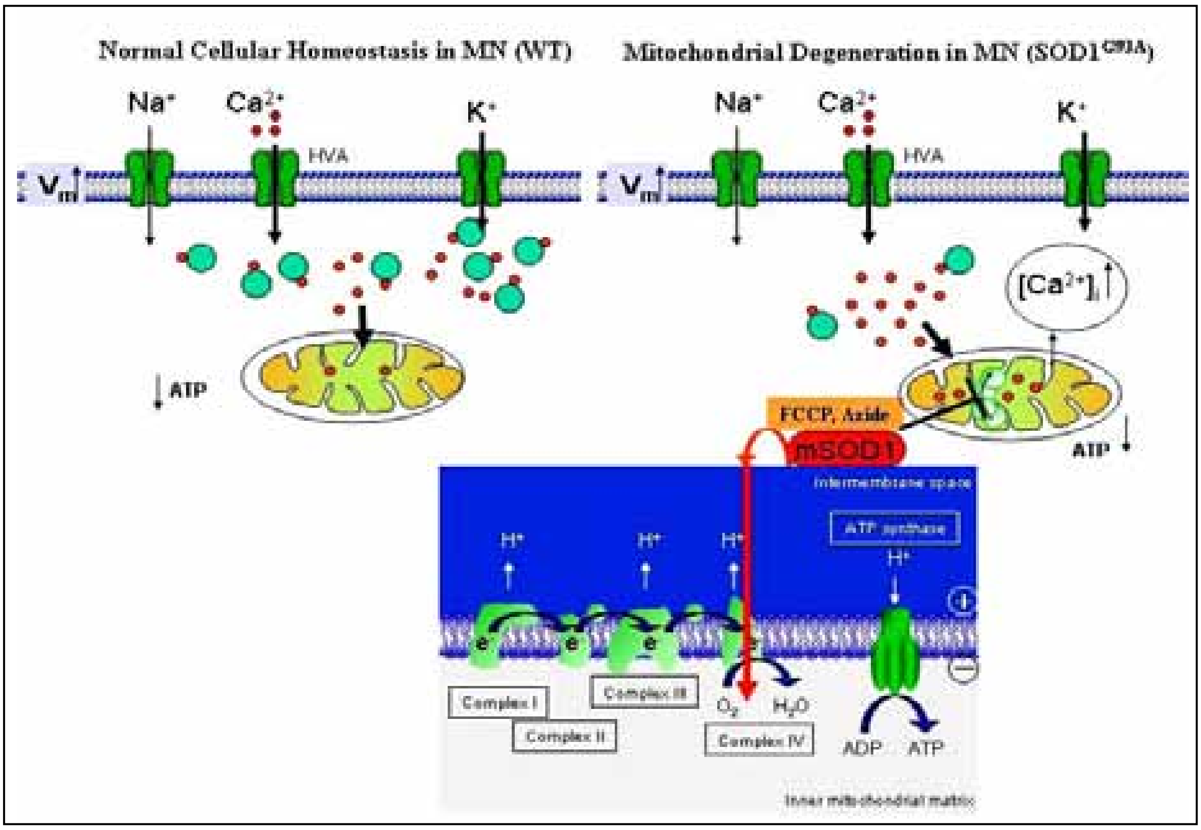
Normal Cellular Homeostasis in MN (WT)
Mitochondrial Degeneration in MN (SOD1G93A)
Na+
Ca2+
K+
HVA
Vm
ATP
[Ca2+]i
FCCP, Azide
mSOD1
ATP
Intermembrane space
ATP synthase
H+
e
Complex I
Complex II
Complex III
Complex IV
O2
H2O
ADP
ATP
Inner mitochondrial matrix

Fig. 4.9: Pathological mechanisms in the ALS, a differential functional model of interaction between mitochondria and high Ca^{2+}. FCCP and Azide/CN^- selectively depolarises hypoglossal motoneurons and increases their cytosolic Ca^{2+} load in vulnerable MNs. Furthermore, events following

mitochondrial inhibition in MNs inhibits complex IV of the electron transport chain leads to ROS generation. In addition, Inhibition of the respiratory chain furthermore decreases the $\Delta\Psi m$ leading to reduced Ca^{2+} uptake into the mitochondrial matrix and release of Ca^{2+} that was taken up during preceding activity. The risk becomes much higher when mitochondria are placed cardinally to buffer the calcium and to control the subsequent metabolic pathways, since an uncontrolled elevation in the cytosolic Ca^{2+} can lead to immediate cell death. Mitochondrial inhibition additionally decreases cellular ATP levels, and this further enhances accumulation of intracellular Ca^{2+}. The observed changes provide a potential mechanism of how mitochondrial inhibition can lead to selective motoneuron degeneration.

Conclusions

It is hypothesized that disrupted Ca^{2+} homeostasis and oxidative stress induced ROS have a vital role in propagating injury by targeting neighboring glia and by increasing the excitability of MNs. Perhaps as a consequence, excitotoxicty build up with increased activity-dependent Ca^{2+} influx and associated mitochondrial Ca^{2+} cycling. Given the mitochondrial disturbances, Ca^{2+} buffering becomes inefficient and cytosolic Ca^{2+} levels rise. Protective option is to increase the resistance of MNs to high intracellular Ca^{2+} concentrations by inducing defense mechanism and/or to inhibit the downstream pathways activated by increased intracellular Ca^{2+} concentrations. However, severely impaired HMNs are forbidden from taking functional advantage for neuronal protection in ALS. These include a more defined separation of spatial Ca^{2+} gradient signal cascades. Moreover, recent research data indicates that therapeutic options do not have to focus on MNs alone, as ALS seems to be a more intricate disease involving MNs, glia, astrocytes as well as muscle and in some cases inflammation and apoptosis. As a consequence, inhibiting microglial activation which prevents the release of toxic substances by these cells or stimulating astrocytes to increase glutamate uptake and/or secrete growth factors that modify the properties of the AMPA receptors present on the MNs could also be a valuable option. In conclusion, it seems that ALS is a multifactorial disease where under physiological conditions diffusion-restricted and tightly controlled domains might indeed have several functional advantages. Accordingly, therapeutic measures aimed at protecting mitochondrial function could be useful in various forms of ALS.

Finally, a combined pharmacological interference with many faces of excitotoxicity both at the MNs and at the surrounding glial cells will be most likely essential to extend survival of ALS patients. It is conceivable that a combination of therapies addressing the many intercellular targets in ALS could be successful at treating this once-obscure disease. Although at present, it is clear that more structural and functional studies are needed to identify potential cytosolic pathway and barriers that could lead to MN degeneration in ALS. Forthcoming studies could add to the understanding of why these processes preferentially damage MNs and the function of non-cell autonomous cell death (glia and astrocytes), if any.

Summary

Amyotrophic lateral sclerosis (ALS) is a fatal neurodegenerative disorder characterized by selective loss of a defined MN population in the brain stem and spinal cord of both human ALS and corresponding mouse models of this neurodegenerative disease. While disruptions of $[Ca^{2+}]i$ and a strong interaction between metabolic mechanisms and mitochondria have been associated with selective MNs degeneration, the underlying mechanisms are only little understood. Although the complex etiologies of ALS are not yet fully understood, a variety of studies indicate that mitochondrial dysfunction and disruption of the Ca^{2+} homeostasis represent critical neuropathological characteristics during the disease progression. On the basis of the studies done so far, little is known about the involvement of mitochondria in Ca^{2+} regulation of HMNs in 8-9 and 14-15 weeks adult WT and corresponding $SOD1^{G93A}$ mice. Therefore, the first aim of this dissertation was to define and evaluate the contribution of mitochondria in Ca^{2+} signaling and clearance of physiological Ca^{2+} loads in adult brain stem slice preparations from $SOD1^{G93A}$ mice containing selectively vulnerable HMNs and to compare the results to the corresponding wild-type (WT) littermates. Second, the work aimed at characterizing the cellular and morphological consequences of mitochondrial dysfunction in SH-SY5Y cells transfected with WT-SOD1 and $SOD1^{G93A}$ gene, with special attention to alteration in Ca^{2+} homeostasis. Furthermore, in order to check if calbindin-D_{28k} (CB-D_{28k}) protects cells from dysfunction and degeneration via buffering of $[Ca^{2+}]i$, Ca^{2+} involvement as a risk factor was studied in primary cultured neuronal cells at days E18 from cortex of mouse that expresses different levels of (low and high) CB-D_{28k} , as was previously shown that Ca^{2+}-binding proteins such as CB-D_{28k} and PV are absent in MN populations (HMNs/SMNs) lost early in ALS. Finally, we intend to study the mechanisms and possible role of glia in MNs-glia signaling, leading to MNs and glial cell death as a consequence of alterations in glutamate signaling, hypoxia induced cell death, mitochondrial depolarization and their clinical relevance in ALS.

To elucidate the underlying factors as well as consequences of mitochondrial dysfunction in ALS on MN membrane properties and intracellular Ca^{2+} homeostasis, we utilized rapid camera based CCD imaging techniques in 8-9 and 14-15 weeks adult brain stem slice preparations from mouse containing selectively vulnerable HMNs obtained from $mSOD1^{G93A}$ and corresponding healthy MNs in WT littermates. In the case of HMNs, which are

vulnerable to cell death in ALS, disruption of the ΔΨm by bath application of the mitochondrial "uncoupler" FCCP(2µM) provoked a substantial Ca^{2+} (Fura-2/AM) release from mitochondrial stores which was significantly diminished in HMNs of $SOD1^{G93A}$ mice at symptomatic stage (14-15 weeks adult mice) of motor dysfunction. Mitochondrial Ca^{2+} release responses after FCCP application were almost ~3 fold larger in WT as compared to $SOD1^{G93A}$ animals, supporting the hypothesis that mitochondrial Ca^{2+} homeostasis is significantly disturbed in the $SOD1^{G93A}$ mice. The application of the SERCA inhibitor Cyclopiazonic acid (CPA) to empty the ER Ca^{2+} store, in the presence of FCCP, resulted in a separate defined Ca^{2+} release, indicating that ER stores are able to operate independently of ΔΨm, but are significantly small and different from FCCP evoked Ca^{2+} release. Responses of ΔΨm (Rhod 123) were measured in HMNs after bath application of the mitochondrial uncoupler FCCP. Our results are in agreement with a model, where the presence of the mutated gene lead to a substantial disruption of the ΔΨm in symptomatic $SOD1^{G93A}$ animals (age of 14–15 weeks), whereas in corresponding WT and pre symptomatic (8-9 weeks) mice ΔΨm remains identical. To evaluate the contribution of mitochondria in buffering Ca^{2+} loads simultaneously in cytosol and mitochondria, we simultaneously monitor cytosolic ($[Ca^{2+}]i$) and mitochondrial calcium ($[Ca^{2+}]m$) concentrations in SH-SY5Y neuroblastoma cells transfected with either WT or mutant $SOD1^{G93A}$ gene, widely considered as a cellular model of fALS. At first, $[Ca^{2+}]i$ was monitored by loading SH-SY5Y cells with the fluorescent dye Fura-2 AM where bath application of 30mM KCl evoked reproducible, voltage dependent Ca^{2+} elevations, and responses were comparable in wtSOD1 and $mSOD1^{G93A}$ expressing cells. In contrast, bath application of FCCP (2µM) evoked significantly smaller (~1.86 fold, n = 23 cells) intracellular Ca^{2+} release responses in mSOD1 expressing cells, suggesting impaired mitochondrial calcium stores. To further test this idea, CCD camera imaging system that allows us to simultaneously monitor $[Ca^{2+}]i$ (Fura-2) and $[Ca^{2+}]m$ concentrations (Rhod-2) with a temporal resolution in millisecond time domain**,** utilizing a computer-controlled monochromator that rapidly switches between excitation wavelengths of 390nm (Fura-2) and 550nm (Rhod-2) and collects wavelengths above 565nm for both excitation conditions were developed. This permits us to clearly separate dynamic profiles of $[Ca^{2+}]i$ and $[Ca^{2+}]m$. An experimental observation during different pharmacological conditions (K+, FCCP and Caffeine) supports the concept that the presence of mSOD1 severely disrupts mitochondrial Ca^{2+} regulation.

To explain the consequences of buffering characteristics of MNs (The MNs which succumb to death in ALS showed a low Ca^{2+} buffering capacity), Ca^{2+} imaging studies following depolarization induced stimulus (60mM K^+) were done in primary neuronal cells expressing CB-D_{28k}. Our data shows that indeed CB-D_{28k} buffer $[Ca^{2+}]i$ where low and high CB-D_{28k} transfected cells display a significant (~2 times) reduction in the peak amplitude of the sustained $[Ca^{2+}]i$ increase. Decay time constant (τ) in CB-D_{28k} transfected cells was also relatively slower (~60s) in contrast to non-transfected cells, where baseline recovery time is ~30-35s while showing little differences in the area under the time - concentration curve (AUC). The observation is in good agreement with the “Low buffering hypothesis” stating that low buffers provide MNs with rapid Ca^{2+} dynamics during physiological activity, but represents a significant risk factor during ALS-related MN disease. Further, we made a comparative study of glia, MNs-glia signaling and relationship between $[Ca^{2+}]i$, $\Delta\Psi m$ and MNs-glia cross-talk. We develop a protocol which allows us a parallel observation of individually identified MNs and glial cells, and thus directly compare the physiological reactions in these two cell types in rat brain stem slice network. This procedure has a main advantage that even subtle differences in reactions can be outlined, because the MNs-glia networks are exposed to identical experimental conditions. We found significant differences between glial cell and MNs Ca^{2+} signaling. In glutamate treated MNs, the large rise in ROS generation is in parallel with large, sustained, glutamate-mediated Ca^{2+} influx from the extracellular space, which dominates over the Ca^{2+} release from the stores. In glial cells, the capacity to down regulate $[Ca^{2+}]i$ clearly provides protection against increased ROS generation. These results indicate that high levels of $[Ca^{2+}]i$ are not necessarily toxic to glia and MNs networks, and potential-driven uptake of Ca^{2+} into mitochondria is required to trigger NMDA receptor- stimulated neuronal death.

Taken together, the results presented here suggest that adult $SOD1^{G93A}$ animals are characterized by a substantial disruption of the $[Ca^{2+}]i$ / mitochondrial interplay and MN degeneration caused by mSOD1 may be attributed to long term exposures to altered Ca^{2+} homeostasis and mitochondrial dysfunction. These observations are in good agreement with the models suggesting that an impairment of the Ca^{2+}/ mitochondrial system is a critical element of ALS pathogenesis. A thorough understanding of these events will undoubtedly give clues to a better understanding of the processes involved in MN degeneration and thus help in designing better therapeutic strategies to treat selectively vulnerable MNs in ALS.

5. Bibliography

Aguado F, Espinosa-Parrilla JF, Carmona MA & Soriano E (2002). Neuronal activity regulates correlated network properties of spontaneous calcium transients in astrocytes in situ. *J Neurosci* 22: 9430–9444.

Alexianu ME, Ho, BK, Mohamed AH, La Bella V, Smith RG & Appel SH (1994). The role of calcium-binding proteins in selective motoneuron vulnerability in amyotrophic lateral sclerosis. *Ann Neurol* 36: 846-58.

Andersen PM, Sims KB, Xin WW, Kiely R, O'Neill G, Ravits J, Pioro E, Harati Y, Brower RD, Levine JS, Heinicke HU, Seltzer W, Boss M & Brown RH Jr. (2003). Sixteen novel mutations in the Cu/Zn superoxide dismutase gene in amyotrophic lateral sclerosis: a decade of discoveries defects and disputes. *Amyotroph Lateral Scler Other Motor Neuron Disord 4(2)*: 62-73.

Appel SH, Smith RG, Engelhardt JI & Stefani E (1994). Evidence for autoimmunity in amyotrophic lateral sclerosis. *J Neurol Sci* 124 Suppl: 14-9.

Appel SH, Smith RG, Alexianu M, Siklos L, Engelhardt J, Colom LV & Stefani E (1995). Increased intracellular calcium triggered by immune mechanisms in amyotrophic lateral sclerosis. *Clin Neurosci* (6): 368-74.

Appel SH & Simpson EP (2001). Activated microglia: the silent executioner in neurodegenerative disease? *Curr Neurol Neurosci Rep* 1(4):303-5.

Aquilano K, Vigilanza P, Rotilio G & Ciriolo MR (2006). Mitochondrial damage due to SOD1 deficiency in SH-SY5Y neuroblastoma cells: a rationale for the redundancy of SOD1. *FASEB J* 20: 1683-1685.

Araque A, Parpura V, Sanzgiri RP & Haydon PG (1998). Glutamate dependent astrocyte modulation of synaptic transmission between cultured hippocampal neurons. *Eur J Neurosci* 10: 2129–2142.

Arnaudeau S, Kelley WL, Walsh JV Jr. & Demaurex N (2001). Mitochondria Recycle Ca^{2+} to the Endoplasmic Reticulum and Prevent the Depletion of Neighboring Endoplasmic Reticulum Regions. *J Biol Chem* 276: 29430-29439.

Avossa D, Grandolfo M, Mazzarol F, Zatta M & Ballerini L (2006). Early signs of motoneuron vulnerability in a disease model system: Characterization of transverse slice cultures of spinal cord isolated from embryonic ALS mice. *Neuroscience* 138: 1179-1194.

Azbill RD, Mu X & Springer JE (2000). Riluzole increases high-affinity glutamate uptake in rat spinal cord synaptosomes. *Brain Res* 871: 175-180.

Azzouz M, Ralph GS, Storkebaum E, Walmsley LE, Mitrophanous KA, Kingsman SM, Carmellet P & Mazarakis ND (2004). VEGF delivery with retrogradely transported lentivector prolongs survival in a mouse ALS model. *Nature* 429: 413-417.

Babcock DF, Herrington J, Goodwin PC, Park YB & Hille B (1997). Mitochondrial participation in the intracellular Ca^{2+} network. *J Cell Biol* 136: 833-844.

Balakrishnan S, Bergmann F & Keller BU (2004) Mitochondria differentially regulate [Ca]i in brainstem motoneurons from mouse: implications for selective motoneuron vulnerability. Program No. 340.16 In 2004 Abstract Viewer and Itinerary Planner, Society for Neuroscience, online (http://sfn.scholarone.com/).

Bar PR (2000). Motor neuron disease in vitro: the use of cultured motor neurons to study amyotrophic lateral sclerosis. *Eur J Pharmacol* 405: 285-295.

Baron KT, Wang GJ, Padua RA, Campbell C & Thayer SA (2003). NMDA-evoked consumption and recovery of mitochondrially targeted aequorin suggests increased Ca^{2+} uptake by a subset of mitochondria in hippocampal neurons. *Brain Res* 993: 124-32.

Bausch AR & Roy G (1996). Volume-sensitive chloride channels blocked by neuroprotective drugs in human glial cells (U-138MG). *Glia* 18(1): 73-7.

Bayliss DA, Li YW & Talley EM (1997). Effects of Serotonin on Caudal Raphe Neurons: Inhibition of N- and P/Q-Type Calcium Channels and the After hyperpolarization. *J Neurophysiol* 77: 1362-1374.

Beal MF (2000). Mitochondria and the pathogenesis of ALS. *Brain* 123: 1291-1292.

Beal MF (2002). Oxidatively modified proteins in aging and disease. *In Free Radic Biol Med* pp. 797-803.

Beckman JS, Beckman TW, Chen J, Marshall PA & Freeman BA (1990). Apparent hydroxyl radical production by peroxynitrite: implications for endothelial injury from nitric oxide and superoxide. *Proc Natl Acad Sci USA* 87(4): 1620-4.

Beers DR, Ho, BK, Siklos L, Alexianu ME, Mosier DR, Habib Mohamed A, Otsuka Y, Kozovska ME, Smith RE, McAlhany RG & Appel SH (2001). Parvalbumin overexpression alters immune-mediated increases in intracellular calcium, and delays disease onset in a transgenic model of familial amyotrophic lateral sclerosis. *J Neurochem* 79: 499-509.

Beltran-Parrazal L & Charles A (2003). Riluzole inhibits spontaneous Ca2+ signaling in neuroendocrine cells by activation of K+ channels and inhibition of Na+ channels. *Br J Pharmacol* 140, 881-888.

Bensimon G, Lacomblez L, Meininger V & The ALS/Riluzole Study Group (1994). A Controlled Trial of Riluzole in Amyotrophic Lateral Sclerosis. *N Engl J Med* 330: 585-591.

Bendotti C, Calvaresi N, Chiveri L, Prelle A, Moggio M, Braga M, Silani V & De Biasi S (2001). Early vacuolization and mitochondrial damage in motor neurons of FALS mice are not associated with apoptosis or with changes in cytochrome oxidase histochemical reactivity. *J Neurol Sci* 191: 25-33.

Bennett MR, Farnell L & Gibson WG (2005). A Quantitative Model of Purinergic Junctional Transmission of Calcium Waves in Astrocyte Networks. *Biophys J* 89: 2235-2250.

Bergmann F & Keller BU (2004). Impact of mitochondrial inhibition on excitability and cytosolic Ca^{2+} levels in brainstem motoneurons from mouse. *J Physiol* 555: 45–59.

Berridge MJ (1993). A tale of two messengers. *Nature* 365: 388-389.

Berridge MJ (1997). Elementary and global aspects of calcium signalling. *J Physiol* 499: 291-306.

Billups B & Forsythe ID (2002). Presynaptic Mitochondrial Calcium Sequestration Influences Transmission at Mammalian Central Synapses. *J Neurosci* 22: 5840-5847.

Blumenfeld H, Zablow L & Sabatini B (1992). Evaluation of cellular mechanisms for modulation of calcium transients using a mathematical model of fura-2 Ca^{2+} imaging in Aplysia sensory neurons. *Biophys J* 63: 1146-1164.

Blankenfeld G, Verkhratsky AN & Kettenmann H (1992). Ca^{2+} Channel Expression in the Oligodendrocyte Lineage. *Eur J Neurosci* 4(11):1035-1048.

Borthwick GM, Johnson MA, Ince PG, Shaw PJ & Turnbull DM (1999). Mitochondrial enzyme activity in amyotrophic lateral sclerosis: implications for the role of mitochondria in neuronal cell death. *Ann Neurol* 46: 787-90.

Bowling AC, Schulz JB, Brown RH Jr & Beal MF (1993). Superoxide dismutase activity, oxidative damage, and mitochondrial energy metabolism in familial and sporadic amyotrophic lateral sclerosis. *J Neurochem* 61(6): 2322-5.

Brown RH Jr. & Robberecht W (2001). Amyotrophic lateral sclerosis: pathogenesis. *Semin Neurol* 21: 131-9.

Browne SE, Bowling AC, Baik MJ, Gurney M, Brown RH & Beal MF (1998). Metabolic Dysfunction in Familial, but Not Sporadic, Amyotrophic Lateral Sclerosis. *J Neurochem* 71: 281-287.

Bruijn LI, Houseweart MK, Kato S, Anderson KL, Anderson SD, Ohama E, Reaume AG, Scott RW & Cleveland DW (1998). Aggregation and motorneuron toxicity of an ALS-linked SOD1 mutant independent from wildtype SOD1. *Science* 281: 1851–1854.

Bruijn LI, Miller TM & Cleveland DW (2004). Unraveling the mechanisms involved in motor neuron degeneration in ALS. *Ann Rev Neurosci* 27: 723-749.

Bryson HM, Fulton B & Benfield P (1996). Riluzole: A review of its pharmacodynamic and pharmacokinetic properties and therapeutic potential in amyotrophic lateral sclerosis. *Drugs* 52(4): 549-63.

Budd SL & Nicholls DG (1996). A Reevaluation of the Role of Mitochondria in Neuronal Ca^{2+} Homeostasis. *J Neurochem* 66: 403-411.

Budd SL & Nicholls DG (1996). Mitochondria, Calcium Regulation, and Acute Glutamate Excitotoxicity in Cultured Cerebellar Granule Cells. *J Neurochem* 67: 2282-2291.

Budd SL (1998). Mechanisms of Neuronal Damage in Brain Hypoxia / Ischemia: Focus on the Role of Mitochondrial Calcium Accumulation. *Pharmacol Therap* 80: 203-229.
Budd SL, Tenneti L, Lishnak T & Lipton SA (2000). Mitochondrial and extramitochondrial apoptotic signalling pathways in cerebrocortical neurons. *Proc Natl Acad Sci USA* 97: 6161-6.

Carri MT, Ferri A, Battistoni A, Famhy L, Gabbianelli R, Poccia F & Rotilio G (1997). Expression of a Cu,Zn superoxide dismutase typical of familial amyotrophic lateral sclerosis induces mitochondrial alteration and increase of cytosolic Ca^{2+} concentration in transfected neuroblastoma SH-SY5Y cells. *FEBS Lett* 414: 365-8.

Carrì MT, Ceroni M, Ferri A, Gabbianelli R, Casciati A & Costa A (2001). Neurochemistry of SOD1 and familial amyotrophic lateral sclerosis. *Funct Neurol* 16(1): 73-82.

Carri MT, Ferri A, Cozzolino M, Calabrese L & Rotilio G (2003). Neurodegeneration in amyotrophic lateral sclerosis: the role of oxidative stress and altered homeostasis of metals. *Brain Res Bull* 61: 365–374.

Carriedo SG, Yin H Z & Weiss JH (1996). Motor Neurons Are Selectively Vulnerable to AMPA / Kainate Receptor-Mediated Injury In Vitro. *J Neurosci* 16: 4069-4079.

Carriedo SG, Sensi SL, Yin HZ & Weiss JH (2000). AMPA exposures induce mitochondrial Ca^{2+} overload and ROS generation in spinal motor neurons in vitro. *J Neurosci* 20: 240-50.

Cavagna M, O'Donnell JM, Sumbilla C, Inesi G & Klein MG (2000). Exogenous Ca^{2+}-ATPase isoform effects on Ca^{2+} transients of embryonic chicken and neonatal rat cardiac myocytes. *J Physiol* 528: 53-63.

Caviston JP & Holzbaur ELF (2006). Microtubule motors at the intersection of trafficking and transport. *Trends Cell Biol* 16: 530-537.

Charles AC, Merrill JE, Dirksen ER & Sanderson MJ (1991). Intercellular signaling in glial cells: calcium waves and oscillations in response to mechanical stimulation and glutamate. *Neuron* 6: 983–992.

Chen YC, Chen SJ, Chang HT, Huang JK, Wang JL, Tseng LL, Chang HJ, Su W, Law YP, Chen WC & Jan CR (2001). Mechanisms of diethylstilbestrol-induced calcium movement in MG63 human osteosarcoma cells. *Toxicol Lett* 122: 245-253.

Choi D, Koh J & Peters S (1988). Pharmacology of glutamate neurotoxicity in cortical cell culture: attenuation by NMDA antagonists. *J Neurosci* 8: 185-196.

Ching GY, Chien CL, Flores R & Liem RKH (1999). Overexpression of alpha-Internexin Causes Abnormal Neurofilamentous Accumulations and Motor Coordination Deficits in Transgenic Mice. *J Neurosci* 19: 2974-2986.

Ciriolo MR, De Martino A, Lafavia E, Rossi L, Carrì MT & Rotilio G (2000). Cu,Zn superoxide dismutase-dependent apoptosis induced by nitric oxide in neuronal cells. *J Biol Chem* 275: 5065-5072.

Clement AM, Nguyen MD, Roberts EA, Garcia ML, Boillee S, Rule M, McMahon AP, Doucette W, Siwek D, Ferrante RJ, Brown RH Jr, Julien JP, Goldstein LS & Cleveland DW (2003). Wild-type nonneuronal cells extend survival of SOD1 mutant motor neurons in ALS mice. *Science* 302(5642):113-7.

Cornell Bell AH, Finkbeiner SM, Cooper MS & Smith SJ (1990). Glutamte induces Calcium waves in cultured astrocytes: long range glial signaling. *Science* 247: 470-473.

Dal Canto MC & Gurney ME (1995). Neuropathological changes in two lines of mice carrying a transgene for mutant human Cu,Zn SOD, and in mice overexpressing wild type human SOD: a model of familial amyotrophic lateral sclerosis (fALS). *Brain Res* 676: 25-40.

Dani JW, Chemjavsky A & Smith SJ (1992). Neuronal activity triggers calcium waves in hippcampal astrocyte networks. *Neuron* 8:429-440.

David G, Barrett JN & Barrett EF (1998). Evidence that mitochondria buffer physiological Ca^{2+} loads in lizard motor nerve terminals. *J Physiol* 509: 59-65.

David G & Barrett EF (2000). Stimulation-Evoked Increases in Cytosolic [Ca^{2+}] in Mouse Motor Nerve Terminals Are Limited by Mitochondrial Uptake and Are Temperature-Dependent. *J Neurosci* 20: 7290-7296.

David G, Talbot J & Barrett EF (2003). Quantitative estimate of mitochondrial [Ca^{2+}] in stimulated motor nerve terminals. *Cell Calcium* 33: 197-206.

David JC, Yamada KA, Bagwe MR & Goldberg MP (1996). AMPA receptor activation is rapidly toxic to cortical astrocytes when desensitization is blocked. *J Neurosci* 16:200–209.

Di Giorgio FP, Carrasco MA, Siao MC, Maniatis T & Eggan K (2007). Non-cell autonomous effect of glia on motor neurons in an embryonic stem cell-based ALS model. *Nat Neurosci* 10(5): 608-614.

De Leon M, Covenas R, Narvaez JA, Aguirre JA & Gonzalez-Baron S (1993). Distribution of parvalbumin immunoreactivity in the cat brain stem. *Brain Res Bull* 32: 639-46.

De Sarro G, Siniscalchi A, Ferreri G, Gallelli L, & De Sarro A (2000). NMDA and AMPA/kainate receptors are involved in the anticonvulsant activity of riluzole in DBA/2 mice. *Eur J Pharmacol* 408: 25-34.

Dimroth P, von Ballmoos C & Meier T (2006). "Catalytic and mechanical cycles in F-ATP synthases. Fourth in the Cycles Review Series". EMBO Rep 7 (3):276-82.

Doble A (1996). The pharmacology and mechanism of action of riluzole. *Neurology* 47(6 Suppl 4): S233-41.

Duchen MR (2000). Mitochondria and Ca^{2+} in cell physiology and pathophysiology. *Cell Calcium* 28: 339-348.

Duchen MR (2000). Mitochondria and calcium: from cell signalling to cell death. *J Physiol* 15: 57-68.

Duchen MR, Surin A & Jacobson J (2003). Imaging mitochondrial function in intact cells. *Methods Enzymol* 361: 353-89.

Duffy S & MacVicar BA (1996). In vitro ischemia promotes calcium influx and intracellular calcium release in hippocampal astrocytes. *J Neurosci* 16(1):71-81.

Duprat F, Lesage F, Patel AJ, Fink M, Romey G & Lazdunski M (2000). The Neuroprotective Agent Riluzole Activates the Two P Domain K^+ Channels TREK-1 and TRAAK. *Mol Pharmacol 57*: 906-912.

Dykens JA, Stern A & Trenkner E (1987). Mechanism of kainate toxicity to cerebellar neurons in vitro is analogous to reperfusion tissue injury. *J Neurochem* 49(4):1222-8.

Eisen A, Stewart H, Schulzer M & Cameron D (1993). Anti-glutamate therapy in amyotrophic lateral sclerosis: a trial using lamotrigine. *Can J Neurol Sci* 20(4): 297-301.

Elliott JL & Snider WD (1995). Parvalbumin is a marker of ALS-resistant motor neurons. *Neuroreport* 6(3): 449-52.

Estevez AG, Crow J P, Sampson JB, Reiter C, Zhuang Y, Richardson GJ, Tarpey MM, Barbeito L & Beckman JS (1999). Induction of Nitric Oxide - Dependent Apoptosis in Motor Neurons by Zinc-Deficient Superoxide Dismutase. *Science* 286: 2498-2500.

Favaron M, Manev H, Alho H, Bertolino M, Ferret B, Guidotti A & Costa E (1988). Gangliosides prevent glutamate and kainate neurotoxicity in primary neuronal cultures of neonatal rat cerebellum and cortex. *Proc Natl Acad Sci USA* 85(19):7351-5.

Feeney CJ, Pennefather PS & Gyulkhandanyan AV (2003). A cuvette-based fluorometric analysis of mitochondrial membrane potential measured in cultured astrocyte monolayers. *J Neurosci Methods* 30: 13-25.

Ferrari D, Pinton P, Szabadkai G, Chami M, Campanella M, Pozzan T & Rizzuto R (2002). Endoplasmic reticulum, Bcl-2 and Ca^{2+} handling in apoptosis. *Cell Calcium* 32: 413-420.

Fields RD & Stevens-Graham B (2002). NEUROSCIENCE: New Insights into Neuron-Glia Communication. *Science* 298: 556-562.

Figlewicz DA, Krizus A, Martinoli MG, Meiniger V, Dib M, Rouleau GA & Julien JP (1994). Variants of the heavy neurofilament subunit are associated with the development of amyotrophic lateral sclerosis. *Hum Mol Genet* 3: 1757–1761.

Fill M & Copello JA (2002). Ryanodine Receptor Calcium Release Channels. *Physiol Rev* 82: 893-922.

Friel D & Tsien R (1994). An FCCP-sensitive Ca^{2+} store in bullfrog sympathetic neurons and its participation in stimulus-evoked changes in $[Ca^{2+}]i$. *J Neurosci* 14: 4007-4024.

Frieling H, Hillemacher T, Demling JH, Kornhuber J & Bleich S (2007). New options in the treatment of depression. *Psychiatrie.* Epub ahead of print.

Fujita K, Yamauchi M, Shibayama K, Ando M, Honda M & Nagata Y (1996). Decreased cytochrome c oxidase activity but unchanged superoxide dismutase and glutathione peroxidase activities in the spinal cords of patients with amyotrophic lateral sclerosis. *J Neurosci Res* 45: 276-81.

Garbuzova-Davis S, Willing A E, Zigova T, Saporta S, Justen EB, Lane JC, Hudson JE, Chen N, Davis CD & Sanberg PR (2003). Intravenous Administration of Human Umbilical Cord Blood Cells in a Mouse Model of Amyotrophic Lateral Sclerosis: Distribution, Migration, and Differentiation. *J Hematotherapy Stem Cell Res* 12: 255-270.

Gledhill JR & Walker JE (2005). Inhibition sites in F1-ATPase from bovine heart mitochondria. *Biochem J* 386(Pt 3):591-8.

Gledhill JR & Walker JE (2006). Inhibitors of the catalytic domain of mitochondrial ATP synthase. *Biochem Soc Trans* 34 (5):989-92.

Goodall EF & Morrison KE (2006).Amyotrophic lateral sclerosis (motor neuron disease): proposed mechanisms and pathways to treatment. *Expert Rev Mol Med* Vol. 8, Issue 11, 24 May, DOI: 10.1017/S1462399406010854.

Grillner S & Dickinson M (2002). Motor Systems. *Curr Opin Neurobiol* 12: 629-632.

Grosche J, Matyash V, Moller T, Verkhratsky A, Reichenbach A & Kettenmann H(1999). Microdomains for neuron–glia interaction: parallel fiber signaling to Bergmann glial cells, *Nat Neurosci* 2 : 139–143.

Grunnet M, Jespersen T, Angelo K, Frokjaer-Jensen C, Klaerke DA, Olesen SP & Jensen BS (2001). Pharmacological modulation of SK3 channels. *Neuropharmacology* 40: 879-887.

Grynkiewicz G, Poenie M & Tsien R (1985). A new generation of Ca^{2+} indicators with greatly improved fluorescence properties. *J Biol Chem* 260: 3440-3450.

Guo H, Lai L, Butchbach ME, Stockinger MP, Shan X, Bishop GA & Lin CL (2003). Increased expression of the glial glutamate transporter EAAT2 modulates excitotoxicity and delays the onset but not the outcome of ALS in mice. *Hum Mol Genet* 12(19): 2519-32.

Gunter TE, Yule DI, Gunter KK, Eliseev RA & Salter JD (2004). Calcium and mitochondria. *FEBS Lett* 567: 6-102.

Gurney ME, Pu H, Chiu AY, Dal Canto MC, Polchow CY, Alexander DD, Caliendo J, Hentati A, Kwon YW, Deng H-X, Chen W, Zhai P, Sufit RL & Siddique T (1994). Motor neuron degeneration in mice that express a human Cu, Zn superoxide dismutase. *Science* 264: 1772-1775.

Gurney ME, Cutting FB, Zhai P, Doble A, Taylor CP, Andrus PK & Hall ED (1996). Benefit of vitamin E, riluzole, and gabapentin in a transgenic model of familial amyotrophic lateral sclerosis. *Ann Neurol* 39(2): 147-57.

Hafezparast M, Klocke R, Ruhrberg C, Marquardt A, Ahmad-Annuar A, Bowen S, Lalli G, Witherden AS, Hummerich H, Nicholson S, *et al.* (2003). Mutations in Dynein Link Motor Neuron Degeneration to Defects in Retrograde Transport. *Science* 300: 808-812.

Hall ED, Jo AO & Gurney ME (1998). Relationship of microglial and astrocytic activation to disease onset and progression in a transgenic model of familial ALS. *Glia* 23: 249-256.

Haas J & Erdö SL (1991). Quisqualate-induced excitotoxic death of glial cells: transient vulnerability of cultured astrocytes. *Glia* 4(1):111-4.

Harris-White ME, Zanotti SA, Frautschy SA & Charles AC (1998). Spiral intercellular calcium waves in hippocampal slice cultures. *J Neurophysiol* 79: 1045–1052.

Heath PR & Shaw PJ (2002). Update on the glutamatergic neurotransmitter system and the role of excitotoxicity in amyotrophic lateral sclerosis. *Muscle Nerve* 26(4):438-58.

Henkel JS, Engelhardt JI, Siklós L, Simpson EP, Kim SH, Pan T, Goodman JC, Siddique T, Beers DR & Appel SH (2004). Presence of dendritic cells, MCP-1, and activated microglia/macrophages in amyotrophic lateral sclerosis spinal cord tissue. *Annals Neurol* 55: 221-235.

Herrington J, Park YB, Babcock DF & Hille B (1996). Dominant Role of Mitochondria in Clearance of Large Ca^{2+} Loads from Rat Adrenal Chromaffin Cells. *Neuron* 16: 219-228.

Hernandez-Guijo JM, Maneu-Flores VE, Ruiz-Nuno A, Villarroya M, Garcia AG & Gandia L (2001). Calcium-dependent inhibition of L, N, and P/Q Ca^{2+} channels in chromaffin cells: role of mitochondria. *J Neurosci* 15; 21(8):2553-60.

Higgins CMJ, Jung C, Ding H, & Xu Z (2002). Mutant Cu, Zn Superoxide Dismutase that Causes Motoneuron Degeneration Is Present in Mitochondria in the CNS. *J Neurosci* 22: 1-6.

Higgins CMJ, Jung C & Xu Z (2003). ALS-associated mutant $SOD1^{G93A}$ causes mitochondrial vacuolation by expansion of the intermembrane space and by involvement of SOD1 aggregation and peroxisomes. *BMC Neurosci* 4:16.

Higuchi M, Maas S, Single FN, Hartner J, Rozov A, Burnashev N, Feldmeyer D, Sprengel R & Seeburg PH (2000). Point mutation in an AMPA receptor gene rescues lethality in mice deficient in the RNA-editing enzyme ADAR2. *Nature* 406: 78-81.

Hirano A, Nakano I, Kurland LT, Mulder DW, Holley PW & Saccomanno G (1984). Fine structural study of neurofibrillary changes in a family with amyotrophic lateral sclerosis. *J Neuropathol Exp Neurol* 43: 471–80.

Hirano A (1991). Cytopathology of amyotrophic lateral sclerosis. *Adv Neurol* 56: 91-101.

Hirase H, Qian L, Barthó P & Buzsáki G (2004) Calcium Dynamics of Cortical Astrocytic Networks In Vivo. *PLoS Biol* 2(4): e96 doi:10.1371/journal.pbio.0020096.

Hoffman EK, Wilcox HM, Scott RW & Siman R (1996). Proteasome inhibition enhances the stability of mouse Cu/Zn superoxide dismutase with mutations linked to familial amyotrophic lateral sclerosis. *J Neurol Sci* 139(1): 15-20.

Holden C (2007). NEUROSCIENCE: Astrocytes Secrete Substance That Kills Motor Neurons in ALS. *Science* 316: 353a.

Holzbaur ELF (2004). Motor neurons rely on motor proteins. *Trends Cell Biol* 14: 233-240.

Hori O, Matsumoto M, Maeda Y, Ueda H, Ohtsuki T, Stern DM, Kinoshita T, Ogawa S & Kamada T (1994). Metabolic and biosynthetic alterations in cultured astrocytes exposed to hypoxia/reoxygenation. *J Neurochem* 62(4):1489-95.

Hoyaux D, Alao J, Fuchs J, Kiss R, Keller B, Heizmann CW, Pochet R & Frermann D (2000). S100A6, a calcium- and zinc-binding protein, is overexpressed in SOD1 mutant mice, a model for amyotrophic lateral sclerosis. *Biochimica Biophysica Acta* 1498: 264-272.

Hubert JP, Delumeau JC, Glowinski J, Prémont J & Doble A (1994). Antagonism by riluzole of entry of calcium evoked by NMDA and veratridine in rat cultured granule cells: evidence for a dual mechanism of action. *Br J Pharmacol* 113(1): 261-7.

Hubert JP, Burgevin MC, Terro F, Hugon J & Doble A (1998). Effects of depolarizing stimuli on calcium homeostasis in cultured rat motoneurones. *Br J Pharmacol* 125: 1421-1428.

Ince PG, Tomkins J, Slade JY, Thatcher NM & Shaw PJ (1998). Amyotrophic lateral sclerosis associated with genetic abnormalities in the gene encoding Cu/Zn superoxide dismutase: molecular pathology of five new cases, and comparison with previous reports and 73 sporadic cases of ALS. *J Neuropathol Exp Neurol* 57(10): 895-904.

Jaarsma D, Rognoni F, Duijn WV, Verspaget HW, Haasdijk ED & Holstege JC (2001). Cu-Zn superoxide dismutase (SOD1) accumulates in vacuolated mitochondria in transgenic mice expressing amyotrophic lateral sclerosis-linked SOD1 mutations. *Acta Neuropath* 102: 293-305.

Jacob S, Poeggeler B, Weishaupt JH, Siren AL, Hardeland R, Bahr M & Ehrenreich H (2002). Melatonin as a candidate compound for neuroprotection in amyotrophic lateral sclerosis (ALS): high tolerability of daily oral melatonin administration in ALS patients. *J Pineal Res* 33: 186-187.

Jaiswal MK, Balakrishnan S & Keller BU (2005). Rapid CCD fluorescence imaging reveals functional impairment of mitochondria in the adult SOD^{G93A} mouse model of human amyotrophic lateral sclerosis (ALS). *Pflugers Arch* 449(Supp01): P 23 -11.

Jaiswal MK, Stefan H, Balakrishnan S, Schomburg E & Keller BU (2006). Disruptions of [Ca]i and mitochondria in the adult SOD1^{G93A} mouse model of ALS: evidence from recordings *in vitro* and *in vivo*. Program No. 508.8 In 2006 Neuroscience Meeting Planner. Atlanta, GA: Society for Neuroscience, Online (http://www.sfn.org/am2006/).

Jehle T, Bauer J, Blauth E, Hummel A, Darstein M, Freiman TM & Feuerstein TJ (2000). Effects of riluzole on electrically evoked neurotransmitter release. *Br J Pharmacol* 130: 1227-1234.

Jou MJ, Jou SB, Chen HM, Lin CH & Peng TI (2002). Critical role of mitochondrial reactive oxygen species formation in visible laser irradiation-induced apoptosis in rat brain astrocytes (RBA-1). *J Biomed Sci* 9(6 Pt 1):507-16.

Jou MJ, Peng TI, Reiter RJ, Jou SB, Wu HY & Wen ST (2004). Visualization of the antioxidative effects of melatonin at the mitochondrial level during oxidative stress-induced apoptosis of rat brain astrocytes. *J Pineal Res* 37: 55-70.

Julien JP (2007). ALS: astrocytes move in as deadly neighbors. *Nat Neurosci* 10(5):535-537.

Julien JP & Beaulieu JM (2000). Cytoskeletal abnormalities in amyotrophic lateral sclerosis: beneficial or detrimental effects? *J Neurol Sci* 180: 7-14.

Jia Z, Agopyan N, Miu P, Xiong Z, Henderson J, Gerlai R, Taverna FA, Velumian A, MacDonald J & Carlen P (1996). Enhanced LTP in Mice Deficient in the AMPA Receptor GluR2. *Neuron* 17: 945-956.

Kaal EC, Vlug AS, Versleijen MW, Kuilman M, Joosten EA & Bar PR (2000). Chronic mitochondrial inhibition induces selective motoneuron death in vitro: a new model for amyotrophic lateral sclerosis. *J Neurochem* 74: 1158-65.

Kanno T, Fujita H, Muranaka S, Yano H, Utsumi T, Yoshioka T, Inoue M & Utsumi K (2002). Mitochondrial swelling and cytochrome c release: sensitivity to cyclosporin A and calcium. *Physiol Chem Phys Med NMR* 34: 91-102.

Kaspar BK, Llado J, Sherkat N, Rothstein JD & Gage FH (2003). Retrograde Viral Delivery of IGF-1 Prolongs Survival in a Mouse ALS Model. *Science* 301: 839-842.

Kieran D, Hafezparast M, Bohnert S, Dick JRT, Martin J, Schiavo G, Fisher EMC & Greensmith L (2005). A mutation in dynein rescues axonal transport defects and extends the life span of ALS mice. *J Cell Biol* 169: 561-567.

Kirischuk S, Scherer J, Moller T, Verkhratsky A & Kettenmann H(1995). Subcellular heterogeneity of voltage-gated Ca^{2+} channels in cells of the oligodendrocyte lineage. *Glia* 13(1):1-12.

Kirichok Y, Krapivinsky G & Clapham DE (2004). The mitochondrial calcium uniporter is a highly selective ion channel. *Nature* 22: 360-4.

Kirkinezos IG, Bacman SR, Hernandez D, Oca-Cossio J, Arias LJ, Perez-Pinzon MA, Bradley WG & Moraes CT (2005). Cytochrome c association with the inner mitochondrial membrane is impaired in the CNS of G93A-SOD1 mice. *J Neurosci* 5(25): 164-72.

Klingauf J & Neher E (1997). Modeling Buffered Ca^{2+} Diffusion Near the Membrane: Implications for Secretion in Neuroendocrine Cells. *Biophys J* 72: 674-690.

Kong J & Xu Z (1998). Massive mitochondrial degeneration in motor neurons triggers the onset of amyotrophic lateral sclerosis in mice expressing a mutant SOD1. *J Neurosci* 18: 3241-50.

Kovacs R, Kardos J, Heinemann U & Kann O (2005). Mitochondrial Calcium Ion and Membrane Potential Transients Follow the Pattern of Epileptiform Discharges in Hippocampal Slice Cultures. *J Neurosci* 25(17):4260–4269.

Kretschmer BD, Kratzer U & Schmidt WJ (1998). Riluzole, a glutamate release inhibitor, and motor behavior. *Arch Pharmacol* 358: 181-190.

Krieger C & Duchen M (2002). Mitochondria, Ca^{2+} and neurodegenerative disease. *Eur J Pharmacol* 5; 447(2-3):177-88.

Kriz J, Nguyen MD & Julien JP (2002). Minocycline Slows Disease Progression in a Mouse Model of Amyotrophic Lateral Sclerosis. *Neurobiol Dis* 10: 268-278.

Kruman II, Pedersen WA, Springer JE, & Mattson MP (1999). ALS-Linked Cu/Zn-SOD Mutation Increases Vulnerability of Motor Neurons to Excitotoxicity by a Mechanism Involving Increased Oxidative Stress and Perturbed Calcium Homeostasis. *Exp Neurol* 160: 28-39.

Kuner R, Groom AJ, Bresink I, Kornau HC, Stefovska V, Muller G, Hartmann B, Tschauner K, Waibel S & Ludolph AC (2005). Late-onset motoneuron disease caused by a functionally modified AMPA receptor subunit. *Proc Natl Acad Sci USA* 102: 5826-5831.

Kunst CB (2004). Complex Genetics of Amyotrophic Lateral Sclerosis. *Am J Hum Genet* 75(6): 933-47.

Ladewig T & Keller BU (2000). Simultaneous patch-clamp recording and calcium imaging in a rhythmically active neuronal network in the brainstem slice preparation from mouse. *Pflugers Arch* 440: 322–332.

Ladewig T, Kloppenburg P, Lalley PM, Zipfel WR, Webb WW & Keller BU (2003). Spatial profiles of store-dependent calcium release in motoneurones of the nucleus hypoglossus from newborn mouse. *J Physiol* 547: 775–787.

Lambrechts D, Storkebaum E, Morimoto M, Del-Favero J, Desmet F, Marklund SL, Wyns S, Thijs V, Andersson J & Van Marion I (2003). VEGF is a modifier of amyotrophic lateral sclerosis in mice and humans and protects motoneurons against ischemic death. *Nat Genet* 34: 383-394.

LaMonte BH, Wallace KE, Holloway BA, Shelly SS, Ascano J, Tokito M, Van Winkle T, Howland DS & Holzbaur ELF (2002). Disruption of Dynein/Dynactin Inhibits Axonal Transport in Motor Neurons Causing Late-Onset Progressive Degeneration. *Neuron* 34: 715-727.

Lang-Lazdunski L, Heurteaux C, Vaillant N, Widmann C & Lazdunski M(1999*)*. Riluzole prevents ischemic spinal cord injury caused by aortic crossclamping. *J Thorac Cardiovasc Surg* 117(5): 881-9.

Lee H, Al Shamy G, Elkabetz Y, Schoefield CM, Harrsion NL, Panagiotakos G, Socci ND, Tabar V & Studer L (2007). Directed Differentiation And Transplantation of Human Embryonic Stem Cell Derived Motoneurons. *Stem Cells*, May 3 [Epub ahead of print].

Leon J, Acuna-Castroviejo D, Escames G, Tan DX & Reiter RJ (2005). Melatonin mitigates mitochondrial malfunction. *J Pineal Res* 38: 1-9.

Leoty C, Huchet-Cadiou C, Talon S, Choisy S & Hleihel W(2001). Caffeine stimulates the reverse mode of Na^+/Ca^{2+} exchanger in ferret ventricular muscled. *Acta Physiologica Scandinavica* 172: 27-37.

Lepore AC & Maragakis NJ (2007). Targeted stem cell transplantation strategies in ALS. *Neurochem Internat,* In Press.

Lesage F (2003). Pharmacology of neuronal background potassium channels. *Neuropharmacology* 44: 1-7.

Lips MB & Keller BU (1998). Endogenous calcium buffering in motoneurones of the nucleus hypoglossus from mouse. *J Physiol* 511: 105–117.

Lips MB & Keller BU (1999). Activity-related calcium dynamics in motoneurons of the nucleus hypoglossus from mouse. *J Neurophysiol* 82: 2936–2946.

Lipton SA & Rosenberg PA (1994). Excitatory amino acids as a final common pathway for neurologic disorders. *N Engl J Med* 3; 330(9):613-22.

Liu J, Lillo C, Jonsson PA, Velde CV, Ward CM, Miller TM, Subramaniam JR, Rothstein JD, Marklund S, Andersen PM, Brannstrom T, Gredal O, Wong PC, Williams DS & Cleveland DW (2004). Toxicity of familial ALS-linked SOD1 mutants from selective recruitment to spinal mitochondria. *Neuron* 43: 5–17.

Llinas R, Sugimori M, Cherksey BD, Smith RG, Delbono O, Stefani E & Appel SH (1993). IgG from amyotrophic lateral sclerosis patients increases current through P-type calcium channels in mammalian cerebellar Purkinje cells and in isolated channel protein in lipid bilayer. *Proc Natl Acad Sci USA* 90(24): 11743-7.

Malgouris C, Daniel M & Doble A (1994). Neuroprotective effects of riluzole on or veratridine-induced neurotoxicity in rat hippocampal slices. *Neurosci Lett* 177: 95-99.

Malli R, Frieden M, Osibow K, Zoratti C, Mayer M, Demaurex N & Graier WF (2003). Sustained Ca^{2+} transfer across mitochondria is Essential for mitochondrial Ca^{2+} buffering, store-operated Ca^{2+}entry, and Ca^{2+} store refilling. *J Biol Chem* 45: 44769-79.

Mantz J, Chéramy A, Thierry AM, Glowinski J & Desmonts JM *(*1992*)*. Anesthetic properties of riluzole (54274 RP), a new inhibitor of glutamate neurotransmission**.** *Anesthesiology* 76(5): 844-8.

Maragakis NJ & Rothstein JD (2001). Glutamate transporters in neurologic disease. *Arch neurol* 58(3): 365-70.

Marin-Teva JL, Dusart I, Colin C, Gervais A, van Rooijen N & Mallat M (2004). Microglia Promote the Death of Developing Purkinje Cells. *Neuron* 41: 535-547.

Martin M, Macias M, Escames G, Reiter RJ, Agapito MT, Ortiz GG & Acuna-Castroviejo D (2000). Melatonin-induced increased activity of the respiratory chain complexes I and IV can prevent mitochondrial damage induced by ruthenium red in vivo. *J Pineal Res* 28(4): 242-8.

Martin M, Macias M, Leon J, Escames G, Khaldy H & Acuna-Castroviejo D (2002). Melatonin increases the activity of the oxidative phosphorylation enzymes and the production of ATP in rat brain and liver mitochondria. *The Int J Biochem Cell Biol* 34: 348-357.

Matlib MA, Zhou Z, Knight S, Ahmed S, Choi KM, Krause-Bauer J, Phillips R, Altschuld R, Katsube Y, Sperelakis N & Bers DM (1998). Oxygen-bridged Dinuclear Ruthenium Amine Complex Specifically Inhibits Ca^{2+} Uptake into Mitochondria in Vitro and in Situ in Single Cardiac Myocytes. *J Biol Chem* 273: 10223-10231.

Mattiazzi M, D'Aurelio M, Gajewski CD, Martushova K, Kiaei M, Beal MF & Manfredi G (2002). Mutated human SOD1 causes dysfunction of oxidative phosphorylation in mitochondria of transgenic mice. *J Biol Chem* 277: 29626-33.

Mattson MP, LaFerla FM, Chan SL, Leissring MA, Shepel PN & Geiger JD (2000). Calcium signaling in the ER: its role in neuronal plasticity and neurodegenerative disorders. *Trends Neurosci* 23: 222-229.

Matute C, Sanchez-Gomez MV, Martinez-Millan L & Miledi R (1997). Glutamate receptor-mediated toxicity in optic nerve oligodendrocytes. *Proc Natl Acad Sci USA* 5; 94(16):8830-5.

Matute C, Domercq M & Sanchez-Gomez MV (2006). Glutamate-mediated glial injury: mechanisms and clinical importance. *Glia* 15; 53(2):212-24.

McDonald JW, Althomsons SP, Hyrc KL, Choi DW & Goldberg MP (1998). Oligodendrocytes from forebrain are highly vulnerable to AMPA / kainate receptor-mediated excitotoxicity. *Nat Med* 4(3):291-7.

McMahon A, Wong BS, Iacopino AM, Ng MC, Chi S & German DC (1998). Calbindin-D_{28k} buffers intracellular calcium and promotes resistance to degeneration in PC12 cells. *Mol Brain Res* 54: 56-63.

Menzies FM, Cookson MR, Taylor RW, Turnbull DM, Chrzanowska-Lightowlers ZM, Dong L, Figlewicz DA & Shaw PJ (2002). Mitochondrial dysfunction in a cell culture model of familial amyotrophic lateral sclerosis. *Brain* 125: 1522–1533.

Menzies FM, Ince PG & Shaw PJ (2002). Mitochondrial involvement in amyotrophic lateral sclerosis. *Neurochem Inter* 40: 543-551.

Mironov SL (1995). Plasmalemmal and intracellular Ca^{2+} pumps as main determinants of slow Ca^{2+} buffering in rat hippocampal neurones. *Neuropharmacology* 34: 1123-1132.

Metzger F, Klapproth N, Kulik A, Sendtner M & Ballanyi K(2005). Optical assessment of motoneuron function in a "twenty-four-hour" acute spinal cord slice model from fetal rats. *J Neurosci Methods* 141(2):309-20.

Mostafapour SP, Lachica EA & Rubel EW (1997). Mitochondrial regulation of calcium in the avian cochlear nucleus. *J Neurophysiol* 78: 1928-34.

Muller M, Brockhaus J & Ballanyi K (2002). ATP-independent anoxic activation of ATP-sensitive K^+ channels in dorsal vagal neurons of juvenile mice in situ. *Neuroscience* 109: 313-328.

Murayama T, Kurebayashi N & Ogawa Y (2000). Role of Mg^{2+} in Ca^{2+}-Induced Ca^{2+} Release through Ryanodine Receptors of Frog Skeletal Muscle: Modulations by Adenine Nucleotides and Caffeine. *Biophys J* 78: 1810-1824.

Nagai M, Re DB, Nagata T, Chalazonitis A, Jessell TM, Wichterle H & Przedborski S (2007). Astrocytes expressing ALS-linked mutated SOD1 release factors selectively toxic to motor neurons. *Nat Neurosci* 10: 615-622.

Neher E (1995). The use of fura-2 for estimating Ca^{2+} buffers and Ca^{2+} fluxes. *Neuropharmacology* 34: 1423-1442.

Nett WJ, Oloff SH & McCarthy KD (2002). Hippocampal astrocytes in situ exhibit calcium oscillations that occur independent of neuronal activity. *J Neurophysiol* 87: 528–537.
Nicholls DG & Akerman KEO (1982). Mitochondrial calcium transport. *Biochim Biophys Acta* 683: 57–88.

Nicholls DG & Budd SL (2000). Mitochondria and Neuronal Survival. *Physiol Rev* 80: 315-360.

Nikolenko V, Nemet B & Yuste R (2003). A two-photon and second-harmonic microscope. *Methods* 30: 3-15.

Nowicky AV & Duchen MR (1998). Changes in $[Ca^{2+}]i$ and membrane currents during impaired mitochondrial metabolism in dissociated rat hippocampal neurons. *J Physiol* 507: 131-145.

Obinu MC, Reibaud M, Blanchard V, Moussaoui S & Imperato A (2002). Neuroprotective effect of riluzole in a primate model of Parkinson's disease: Behavioral and histological evidence. *Movement Disorders* 17: 13-19.

Oeda T, Shimohama S, Kitagawa N, Kohno R, Imura T, Shibasaki H & Ishii N (2001). Oxidative stress causes abnormal accumulation of familial amyotrophic lateral sclerosis-related mutant SOD1 in transgenic *Caenorhabditis elegans*. *Hum Mol Genet* 10: 2013-23.

Oka A, Belliveau MJ, Rosenberg PA & Volpe JJ (1993). Vulnerability of oligodendroglia to glutamate: pharmacology, mechanisms, and prevention. *J Neurosci* 13(4):1441-53.

Okatani Y, Wakatsuki A, Reiter RJ, Enzan H & Miyahara Y (2003). Protective effect of melatonin against mitochondrial injury induced by ischemia and reperfusion of rat liver. *Eur J Pharmacol* 469: 145-152.

Olney JW (1969). Brain lesions, obesity, and other disturbances in mice treated with monosodium glutamate. *Science* 9; 164 (880):719-21.

Olney JW & Sharpe LG (1969). Brain lesions in an infant rhesus monkey treated with monsodium glutamate. *Science* 17; 166(903):386-8.

Oosthuyse B, Moons L, Storkebaum E, Beck H, Nuyens D, Brusselmans K, Van Dorpe J, Hellings P, Gorselink M & Heymans S (2001). Deletion of the hypoxia-response element in the vascular endothelial growth factor promoter causes motor neuron degeneration. *Nat Genet* 28: 131-138.

Palecek J, Lips MB & Keller BU (1999). Calcium dynamics and buffering in motoneurones of the mouse spinal cord. *J Physiol* 520: 485–502.

Pappolla MA, Sos M, Omar RA, Bick RJ, Hickson-Bick DLM, Reiter RJ, Efthimiopoulos S & Robakis NK (1997). Melatonin Prevents Death of Neuroblastoma Cells Exposed to the Alzheimer Amyloid Peptide. *J Neurosci* 17: 1683-1690.

Parri HR, Gould TM & Crunelli V (2001). Spontaneous astrocytic Ca^{2+} oscillations in situ drive NMDAR-mediated neuronal excitation. *Nat Neurosci* 4: 803–812.

Paschen W (2000). Role of calcium in neuronal cell injury: which subcellular compartment is involved? *Brain Res Bull* 53: 409-413.

Paschen W & Frandsen A (2001). Endoplasmic reticulum dysfunction - a common denominator for cell injury in acute and degenerative diseases of the brain. *J Neurochem* 79: 719-725.

Paschen W & Mengesdorf T (2005). Endoplasmic reticulum stress response and neurodegeneration. *Cell Calcium* 38: 409-415.

Patel M, Day BJ, Crapo JD, Fridovich I & McNamara JO (1996). Requirement for superoxide in excitotoxic cell death. *Neuron* 16: 345–355.

Paxinos *et al.*, Chemoarchitectonic atlas of the rat brainstem, Academic Press, 1999.

Peters O, Schipke CG, Hashimoto Y & Kettenmann H (2003). Different mechanisms promote astrocyte Ca^{2+} waves and spreading depression in the mouse neocortex. *J Neurosci* 23: 9888–9896.

Pinton P, Ferrari D, Magalhaes P, Schulze-Osthoff K, Di Virgilio F, Pozzan T & Rizzuto R (2000). Reduced Loading of Intracellular Ca^{2+} Stores and Downregulation of Capacitative Ca^{2+} Influx In Bcl-2-Overexpressing Cells. *J Cell Biol* 148: 857-862.

Pinton P, Ferrari D, Rapizzi E, Di Virgilio F, Pozzan T & Rizzuto R (2002). A role for calcium in Bcl-2 action? *Biochimie* 84: 195-201.

Pivovarova NB, Hongpaisan J, Andrews SB & Friel DD (1999). Depolarization-induced mitochondrial Ca^{2+} accumulation in sympathetic neurons: spatial and temporal characteristics. *J Neurosci* 19: 6372-84.

Pivovarova NB, Nguyen HV, Winters CA, Brantner CA, Smith CL & Andrews SB (2004). Excitotoxic calcium overload in a subpopulation of mitochondria triggers delayed death in hippocampal neurons. *J Neurosci* 24: 5611-22.

Porter JT & McCarthy KD (1995). GFAP-positive hippocampal astrocytes in situ respond to glutamatergic neuroligands with increases in $[Ca^{2+}]i$. *Glia* 13(2):101-12.

Prieto M & Alonso F (1999). Differential sensitivity of cultured tanycytes and astrocytes to hydrogen peroxide toxicity. *Exp Neurol* 155:118–127.

Puls I, Jonnakuty C, LaMonte BH, Holzbaur ELF, Tokito M, Mann E, Floeter MK, Bidus K, Drayna D, Oh SJ, Brown RH, Ludlow CL & Fischbeck KH (2003). Mutant dynactin in motor neuron disease. *Nat Genet* 33: 455-456.

Radi R, Rubbo H, Bush K & Freeman BA (1997). Xanthine Oxidase Binding to Glycosaminoglycans: Kinetics and Superoxide Dismutase Interactions of Immobilized Xanthine Oxidase-Heparin Complexes. *Arch Biochem Biophys* 339: 125-135.

Ramirez JM, Quellmalz UJA & Wilken B (1997). Developmental Changes in the Hypoxic Response of the Hypoglossus Respiratory Motor Output In Vitro. *J Neurophysiol* 78: 383-392.

Rao SD, Yin HZ & Weiss JH (2003). Disruption of glial glutamate transport by reactive oxygen species produced in motor neurons. *J Neurosci* 23: 2627-2633.

Rao SD & Weiss JH (2004). Excitotoxic and oxidative cross-talk between motor neurons and glia in ALS pathogenesis. *Trends Neurosci* 27: 17-23.

Reaume AG, Elliott JL, Hoffman EK, Kowall NW, Ferrante RJ, Siwek DR, Wilcox HM, Flood DG, Beal MF, Brown RH, *et al.* (1996). Motor neurons in Cu/Zn superoxide dismutase-deficient mice develop normally but exhibit enhanced cell death after axonal injury. *Nat Genet* 13: 43-47.

Reiter RJ, Calvo JR, Karbownik M, QI W & Tan DX (2000). Melatonin and Its Relation to the Immune System and Inflammation. *Ann NY Acad Sci* 917: 376-386.

Rizzuto R, Brini M & Pozzan T (1993). Intracellular targeting of the photoprotein aequorin: a new approach for measuring, in living cells, Ca^{2+} concentrations in defined cellular compartments. *Cytotechnology* 11: 44-6.

Rizzuto R, Bastianutto C, Brini M, Murgia M & Pozzan T (1994). Mitochondrial Ca^{2+} homeostasis in intact cells. *J Cell Biol* 126: 1183-94.

Rizzuto R, Bernardi P & Pozzan T (2000). Mitochondria as all-round players of the calcium game. *J Physiol* 529: 37-47.

Rizzuto R (2003). Calcium mobilization from mitochondria in synaptic transmitter release. *J Cell Biol* 163: 441-443.

Rizzuto R, Duchen MR & Pozzan T (2004). Flirting in little space: the ER/mitochondria Ca^{2+} liaison. *Sci STKE* 13; 2004(215):re1.

Robertson J, Doroudchi MM, Nguyen MD, Durham HD, Strong MJ, Shaw G, Julien JP & Mushynski WE (2003). A neurotoxic peripherin splice variant in a mouse model of ALS. *J Cell Biol* 160: 939-949.

Rosenstock TR, Carvalho AC, Jurkiewicz A, Frussa-Filho R & Smaili SS (2004). Mitochondrial calcium, oxidative stress and apoptosis in a neurodegenerative disease model induced by 3-nitropropionic acid. *J Neurochem* 88(5): 1220-8.

Rothstein JD, Martin LJ & Kuncl RW (1992). Decreased glutamate transport by the brain and spinal cord in amyotrophic lateral sclerosis. *N Engl J Med* 326(22): 1464-8.

Rothstein JD, Van Kammen M, Levey AI, Martin LJ & Kuncl RW(1995). Selective loss of glial glutamate transporter GLT-1 in amyotrophic lateral sclerosis. *Ann Neurol* 38(1): 73-84.

Rothstein JD, Dykes-Hoberg M, Pardo CA, Bristol LA, Jin L, Kuncl RW, Kanai Y, Hediger MA, Wang Y, Schielke JP & Welty DF (1996). Knockout of Glutamate Transporters Reveals a Major Role for Astroglial Transport in Excitotoxicity and Clearance of Glutamate. *Neuron* 16: 675-686.

Rosen DR, Siddique T, Patterson D, Figlewicz DA, Sapp P, Hentati A, Donaldson D, Goto J, O'Regan JP, Deng HX, *et al.* (1993). Mutations in Cu/Zn superoxide dismutase gene are associated with familial amyotrophic lateral sclerosis. *Nature,* 362(6415): 59-62.

Rosen DR, Bowling AC, Patterson D, Usdin TB, Sapp P, Mezey E, McKenna-Yasek D, O'Regan J, Rahmani Z & Ferrante RJ, *et al.* (1994). A frequent ala 4 to val superoxide dismutase-1 mutation is associated with a rapidly progressive familial amyotrophic lateral sclerosis. *Hum Mol Genet* 3(6): 981-7.

Rowland LP (1998). Assisted Suicide and Alternatives in Amyotrophic Lateral Sclerosis. *N Engl J Med* 339: 987-989.

Rowland LP & Shneider NA (2001). Amyotrophic Lateral Sclerosis. *N Engl J Med* 344: 1688-1700.

Roy J, Minotti S, Dong L, Figlewicz DA & Durham HD (1998). Glutamate potentiates the toxicity of mutant Cu/Zn-superoxide dismutase in motor neurons by postsynaptic calcium-dependent mechanisms. *J Neurosci* 18: 9673-9684.

Ruangkittisakul A, Schwarzacher SW, Secchia L, Poon BY, Ma Y, Funk GD & Ballanyi K (2006). High Sensitivity to Neuromodulator-Activated Signaling Pathways at Physiological [K^+] of Confocally Imaged Respiratory Center Neurons in On-Line-Calibrated Newborn Rat Brainstem Slices. *J Neurosci* 26: 11870-11880.

Rutter GA, Burnett P, Rizzuto R, Brini M, Murgia M, Pozzan T, Tavare JM & Denton RM (1996). Subcellular imaging of intramitochondrial Ca^{2+} with recombinant targeted aequorin: Significance for the regulation of pyruvate dehydrogenase activity. *Proc Natl Acad Sci USA* 93: 5489-5494.

Sachiko T, Seiji K, Kazuyoshi S, Jun T, Riichiro K, Ichiro Y, Shoichi Y, Masayoshi T & Hidenao S (2005). Proteasome inhibition induces selective motor neuron death in organotypic slice cultures. *J Neurosci Res* 82: 443-451.

Sasaki S & Iwata M (1996). Ultrastructural study of synapses in the anterior horn neurons of patients with amyotrophic lateral sclerosis. *Neurosci Lett* 204(1-2): 53-6.

Sasaki S & Iwata M (1996). Impairment of fast axonal transport in the proximal axons of anterior horn neurons in amyotrophic lateral sclerosis. *Neurology* 47(2): 535-540.

Sasaki S, Warita H, Murakami T, Abe K & Iwata M (2004). Ultrastructural study of mitochondria in the spinal cord of transgenic mice with a G93A mutant SOD1 gene. *Acta Neuropathol* 107: 461-74.

Sasaki S, Warita H, Abe K & Iwata M (2005). Impairment of axonal transport in the axon hillock and the initial segment of anterior horn neurons in transgenic mice with a G93A mutant SOD1 gene. *Acta Neuropathol* (Berl) 110: 48-56.

Schinder AF, Olson EC, Spitzer NC & Montal M (1996). Mitochondrial dysfunction is a primary event in glutamate neurotoxicity. *J Neurosci* 16: 6125-33.

Schipke CG, Boucsein C, Ohlemeyer C, Kirchhoff F & Kettenmann H(2002). Astrocyte Ca^{2+} waves trigger responses in microglial cells in brain slices. *FASEB J* 16: 255–257.

Schuchmann S, Luckermann M, Kulik A, Heinemann U & Ballanyi K (2000). Ca (2+) - and metabolism-related changes of mitochondrial potential in voltage-clamped CA1 pyramidal neurons in situ. *J Neurophysiol* 83(3):1710-21.

Schwarzacher SW, Pestean A, Gunther S & Ballanyi K (2002). Serotonergic modulation of respiratory motoneurons and interneurons in brainstem slices of perinatal rats. *Neuroscience* 115: 1247-1259.

Seifert G, Schilling K & Steinhauser C (2006). Astrocyte dysfunction in neurological disorders: a molecular perspective. *Nat Rev Neurosci* 7(3):194-206.

Sen I, Nalini A, Joshi NB & Joshi PG (2005). Cerebrospinal fluid from amyotrophic lateral sclerosis patients preferentially elevates intracellular calcium and toxicity in motor neurons via AMPA / kainate receptor. *J Neurol Sci* 235: 45-54.

Shaw PJ, Forest V, Ince PG, Richardson JP & Wastell HJ (1995). CSF and plasma amino acid levels in motor neuron disease: elevation of CSF glutamate in a subset of patients. *Neurodegeneration* 4(2): 209-216.

Shaw PJ & Ince PG (1997). Glutamate, excitotoxicity and amyotrophic lateral sclerosis. *J Neurol* 244 (Suppl 2): S3-14.

Shaw PJ (2005). Molecular and cellular pathways of neurodegeneration in motor neurone disease. *J Neurol Neurosurg Psychiatry* 76: 1046-1057.

Sher AA, Hinch R, Noble PJ, Gavaghan DJ & Noble D (2007). Functional Significance of Na^+/Ca^{2+} Exchangers Co-localization with Ryanodine Receptors. *Ann NY Acad Sci* 1099: 215-220.

Sherman MY & Goldberg AL (2001). Cellular Defenses against Unfolded Proteins: A Cell Biologist Thinks about Neurodegenerative Diseases. *Neuron* 29: 15-32.

Siddique T, Figlewicz DA, Pericak-Vance MA, Haines JL, Rouleau G, Jeffers AJ, Sapp P, Hung WY, Bebout J & McKenna-Yasek D (1991). Linkage of a gene causing familial amyotrophic lateral sclerosis to chromosome 21 and evidence of genetic-locus heterogeneity. *N Engl J Med* 16: 1381-1384.

Siklos L, Engelhardt J, Harati Y, Smith RG, Joo F & Appel SH (1996). Ultrastructural evidence for altered calcium in motor nerve terminals in amyotrophic lateral sclerosis. *Ann Neurol* 39: 203-16.

Simpson PB & Russell JT (1997). Role of sarcoplasmic/endoplasmic-reticulum Ca^{2+}-ATPases in mediating Ca^{2+} waves and local Ca^{2+}-release microdomains in cultured glia. *Biochem J* 325(Pt 1): 239–247.

Simpson EP, Yen AA & Appel SH (2003). Oxidative Stress: a common denominator in the pathogenesis of amyotrophic lateral sclerosis. *Curr Opin Rheumatol* 15(6): 730-736.

Siniscalchi A, Bonci A, Mercuri NB & Bernardi G (1997). Effects of riluzole on rat cortical neurones: an in vitro electrophysiological study. *Br J Pharmacol* 120: 225-230.

Smith IF, Plant LD, Boyle JP, Skinner RA, Pearson HA & Peers C (2003). Chronic hypoxia potentiates capacitative Ca^{2+} entry in type-I cortical astrocytes. *J Neurochem* 85(5):1109-16.

Solovyova N, Veselovsky N, Toescu EC & Verkhratsky A (2002). Ca (2+) dynamics in the lumen of the endoplasmic reticulum in sensory neurons: direct visualization of Ca (2+)-induced Ca (2+) release triggered by physiological Ca (2+) entry. *EMBO J* 21(4): 622-30.

Soto C (2003). Unfolding the Role of Protein Misfolding in Neurodegenerative Diseases. *Nat Rev Neurosci* 4: 49-60.

Stefani A, Spadoni F & Bernardi G (1997). Differential Inhibition by Riluzole, Lamotrigine, and Phenytoin of Sodium and Calcium Currents in Cortical Neurons: Implications for Neuroprotective Strategies. *Exp Neurol* 147: 115-122.

Stock D, Leslie AG & Walker JE (1999). Molecular architecture of the rotary motor in ATP synthase. *Science* 26; 286(5445):1700-5.

Storch A, Burkhardt K, Ludolph AC & Schwarz J (2000). Protective Effects of Riluzole on Dopamine Neurons: Involvement of Oxidative Stress and Cellular Energy Metabolism. *J Neurochem* 75: 2259-2269.

Stosiek C, Garaschuk O, Holthoff K & Konnerth A (2003). In vivo two-photon calcium imaging of neuronal networks. *Proc Natl Acad Sci USA* 100: 7319-7324.

Stout AK, Raphael HM, Kanterewicz BI, Klann E & Reynolds IJ (1998). Glutamate-induced neuron death requires mitochondrial calcium uptake. *Nat Neurosci* 1(5): 366-73.

Strong MJ (2003). The basic aspects of therapeutics in amyotrophic lateral sclerosis. *Pharmacol Ther 98*: 379-414.

Strong MJ, Sashi K & Pant HC (2005). The Pathobiology of Amyotrophic Lateral Sclerosis: A Proteinopathy. *J Neuropath Exp Neurol* 64(8): 649-664.

Sul JY, Orosz G, Givens RS & Haydon PG 2004). Astrocytic Connectivity in the Hippocampus. *Neuron Glia Biology* 1: 3-11.

Svichar N, Shmigol A, Verkhratsky A & Kostyuk P (1997). ATP induces Ca2+ release from IP3-sensitive Ca2+ stores exclusively in large DRG neurones. *Neuroreport* 8(7): 1555-1559.

Swerdlow RH, Parks JK, Cassarino DS, Trimmer PA, Miller SW, Maguire DJ, Sheehan JP, Maguire RS, Pattee G & Juel VC (1998). Mitochondria in Sporadic Amyotrophic Lateral Sclerosis. *Exp Neurol* 153: 135-142.

Szabadkai G, Simoni AM & Rizzuto R (2003). Mitochondrial Ca^{2+} Uptake Requires Sustained Ca^{2+} Release from the Endoplasmic Reticulum. *J Biol Chem* 278: 15153-15161.

Tang Y & Zucker RS (1997). Mitochondrial involvement in post-tetanic potentiation of synaptic transmission. *Neuron* 18(3): 483-91.

Tateno M, Sadakata H, Tanaka M, Itohara S, Shin RM, Miura M, Masuda M, Aosaki T, Urushitani M, Misawa H & Takahashi R (2004). Calcium-permeable AMPA receptors promote misfolding of mutant SOD1 protein and development of amyotrophic lateral sclerosis in a transgenic mouse model. *Hum Mol Genet* 13: 2183-2196.

Toescu EC & Verkhratsky A (2000). Assessment of mitochondrial polarization status in living cells based on analysis of the spatial heterogeneity of rhodamine 123 fluorescence staining. *Eur J Physiol* 440: 941-947.

Trotti D, Rolfs A, Danbolt NC, Brown RH & Hediger MA (1999). SOD1 mutants linked to amyotrophic lateral sclerosis selectively inactivate a glial glutamate transporter. *Nat Neurosci* 2: 427-433.

Trump B & Berezesky I (1995). Calcium-mediated cell injury and cell death. *FASEB J* 9: 219-228.

Turner MR, Cagnin A, Turkheimer FE, Miller CCJ, Shaw CE, Brooks DJ, Leigh PN & Banati RB (2004). Evidence of widespread cerebral microglial activation in amyotrophic lateral sclerosis: an [11C](R)-PK11195 positron emission tomography study. *Neurobiol Dis* 15: 601-609.

Urushitani M, Sik A, Sakurai T, Nukina N, Takahashi R & Julien JP (2006). Chromogranin-mediated secretion of mutant superoxide dismutase proteins linked to amyotrophic lateral sclerosis. *Nat Neurosci* 9: 108-118.

Valentine JS & Hart PJ (2003). Bioinorganic Chemistry Special Feature: Misfolded Cu,Zn, SOD and amyotrophic lateral sclerosis. *Proc Natl Acad Sci USA* 100: 3617-3622.

Van Den Bosch L, Schwaller B, Vleminckx V, Meijers B, Stork S, Ruehlicke T, Van Houtte E, Klaassen H, Celio MR & Missiaen L (2002). Protective Effect of Parvalbumin on Excitotoxic Motor Neuron Death. *Exp Neurol* 174: 150-161.

Vanselow BK & Keller BU (2000). Calcium dynamics and buffering in oculomotor neurones from mouse those are particularly resistant during amyotrophic lateral sclerosis (ALS)-related motoneuron disease. *J Physiol* 525: 433-445.

Vergun O, Tatyana V. Votyakova & Reynolds IJ (2003). Spontaneous Changes in Mitochondrial Membrane Potential in Single Isolated Brain Mitochondria. *Biophys J* 85(5): 3358–3366.

Verkharatsky A, Orkand RK & Kettermann H (1998). Glial calcium: homeostasis and signaling function. *Phsiol Rev* 78: 99-141.

Verkhratsky A (2006). Glial calcium signaling in physiology and pathophysiology. *Acta Pharmacologica Sinica* 27: 773-780.

Vielhaber S, Kunz D, Winkler K, Wiedemann FR, Kirches E, Feistner H, Heinze HJ, Elger CE, Schubert W & Kunz WS (2000). Mitochondrial DNA abnormalities in skeletal muscle of patients with sporadic amyotrophic lateral sclerosis. *Brain* 123 (Pt 7): 1339-48.

Volterra A & Meldolesi J (2005). Astrocytes, from brain glue to communication elements: the revolution continues. *Nat Rev Neurosci* 6(8): 626-640.

Von Lewinski F & Keller BU (2005). Ca^{2+}, mitochondria and selective motoneuron vulnerability: implications for ALS. *Trends Neurosci 28*: 494-500.

Wagner ML & Landis BE (1997). Riluzole: a new agent for amyotrophic lateral sclerosis. *Ann Pharmacother* 31(6): 738-44.

Wang JL, Lee KC, Tang KY, Lu T, Chang CH, Chow CK, Chen WC, Su W, Law YP & Jan CR (2001). Effect of the neuroprotective agent riluzole on intracellular Ca^{2+} levels in IMR32 neuroblastoma cells. *Arch Toxicol* 75(4): 214-20.

Wang Y, Ou Mao X, Xie L, Banwait S, Marti HH, Greenberg DA & Jin K (2007). Vascular Endothelial Growth Factor Overexpression Delays Neurodegeneration and Prolongs Survival in Amyotrophic Lateral Sclerosis Mice. *J Neurosci 27*: 304-307.

Ward MW, Rego AC, Frenguelli BG & Nicholls DG (2000). Mitochondrial membrane potential and glutamate excitotoxicity in cultured cerebellar granule cells. *J Neurosci* 20:7208-19.

Warita H, Hayashi T, Murakami T, Manabe Y & Abe K (2001). Oxidative damage to mitochondrial DNA in spinal motoneurons of transgenic ALS mice. *Brain Res Mol Brain Res* 89: 147-52.

Wei H & Perry DC (1996). Dantrolene Is Cytoprotective in Two Models of Neuronal Cell Death. *J Neurochem* 67: 2390-2398.

Werth J, Usachev Y & Thayer S (1996). Modulation of calcium efflux from cultured rat dorsal root ganglion neurons. *J Neurosci* 16: 1008-1015.

Wetzel R (1994). Mutations and off-pathway aggregation of proteins. *Trends Biotech* 12: 193-198.

Wiedemann FR, Winkler K, Kuznetsov AV, Bartels C, Vielhaber S, Feistner H & Kunz WS (1998). Impairment of mitochondrial function in skeletal muscle of patients with amyotrophic lateral sclerosis. *J Neurol Sci* 156(1): 65-72.

Wiedemann FR, Manfredi G, Mawrin C, Beal MF & Schon EA (2002). Mitochondrial DNA and respiratory chain function in spinal cords of ALS patients. *J Neurochem* 80: 616-625.

Williamson TL, Bruijn LI, Zhu Q, Anderson KL, Anderson SD, Julien JP & Cleveland DW (1998). Absence of neurofilaments reduces the selective vulnerability of motor neurons and slows disease caused by a familial amyotrophic lateral sclerosis-linked superoxide dismutase 1 mutant. *Proc Natl Acad Sci USA 95*: 9631-9636.

Wokke J (1996). Riluzole. *The Lancet* 348: 795-799.

Wong PC, Pardo CA, Borchelt DR, Lee MK, Copeland NG, Jenkins NA, Sisodia SS, Cleveland DW & Price DL (1995). An adverse property of a familial ALS-linked SOD1 mutation causes motor neuron disease characterized by vacuolar degeneration of mitochondria. *Neuron* 14: 1105-16.

Wyatt CN & Buckler KJ (2004). The effect of mitochondrial inhibitors on membrane currents in isolated neonatal rat carotid body type I cells. *J Physiol* 556: 175-91.

Xu Z, Cork LC, Griffin JW & Cleveland DW (1993). Increased expression of neurofilament subunit NF-L produces morphological alterations that resemble the pathology of human motor neuron disease. *Cell* 73: 23-33.

Xu Z, Jung C, Higgins C, Levine J & Kong J (2004). Mitochondrial Degeneration in Amyotrophic Lateral Sclerosis. *J Bioenerg Biomembr* 36: 395-399.

Yamamoto HA & Tang HW (1996). Preventive effect of melatonin against cyanide-induced seizures and lipid peroxidation in mice. *Neurosci Lett* 207: 89-92.

Yokoo H, Shiraishi S, Kobayashi H, Yanagita T, Yamamoto R & Wada A (1998). Selective inhibition by riluzole of voltage-dependent sodium channels and catecholamine secretion in adrenal chromaffin cells. *Arch Pharmacol* 357: 526-531.

Yuste R, Lanni F & Konnerth A (2000). Imaging Neurons. Eds Cold Spring Harbour Laboratory Press, Cold Spring Harbour, New York.

Zhang W, Narayanan M & Friedlander RM (2003). Additive neuroprotective effects of minocycline with creatine in a mouse model of ALS. *Ann Neurol* 53: 267-270.

Zheng C, Nennesmo I, Fadeel B & Henter JI (2004). Vascular endothelial growth factor prolongs survival in a transgenic mouse model of ALS. *Ann Neurol* 56: 564-567.

Zhou Z & Neher E (1993). Mobile and immobile calcium buffers in bovine adrenal chromaffin cells. *J Physiol* 469: 245-273.

Zhu S, Stavrovskaya IG, Drozda M, Kim BYS, Ona V, Li M, Sarang S, Liu AS, Hartley DM, Wu DC, *et al.* (2002). Minocycline inhibits cytochrome c release and delays progression of amyotrophic lateral sclerosis in mice. *Nature* 417: 74-78.

Zoratti M & Szabo I (1995). The mitochondrial permeability transition. *Biochim Biophys Acta* 17; 1241(2):139-76.

Acknowledgments

This is an attempt to acknowledge all those who gave me help and support in the time that I spent at this fantastic place that is the University of Goettingen and who have been instrumental in making this project a success.

First of all I would like to extend my sincere and unplumbed gratitude to **Prof. Dr. Bernhard U. Keller** for giving me the unique possibility to work in his group and the insightful guidance during the development of the ideas in this thesis. His critical and experimental approach together with his acute insights has been an invaluable guide for my development as a graduate student. I would also like to thank him for the technical support, lab facilities and for the excellent financial support throughout the project periods.

I express my sincere thanks to **Prof. Dr. Reinhold Hustert** for agreeing to be the 1st Referent and Main examiner of my thesis. I am very grateful to **Prof. Dr. Friedrich-Wilhelm Schürmann** for granting permission to be the Co-referent of my thesis. I express my deep gratitude to **Prof. Dr. Ralf Ficner** and **Prof. Dr. Michael Hoppert** for being my examiners, **Prof. Dr. Hans-Joachim Fritz** and **Prof. Dr. Christiane Gatz** for agreeing to be the reviewers for my thesis. I express my extreme thanks to **Prof. Dr. Diethelm W. Richter**, Director of the institute for all the supports to fulfil my research and **Prof. Dr. Roland Nau**, **Dr. Sebastian Kugler** (Department of Neurology, University of Goettingen) and **Prof. Dr. Klaus Ballanyi** (Center for Neuroscience, University of Alberta, Canada) for the collaboration and cooperation to make this work successful. My sincere gratitude to Prof. Dr. Eike D. Schomburg, Prof. Dr. Michael Müller, Prof. Dr. Erwin Neher and Dr. Stefen for valuable discussions.

I am very grateful to Dr. Saju Balakrishnan for being a nice colleague and instructor for fluorescence imaging and Dr. Friedrike von Lewinski, MD, Ph.D for suggestion and scientific discussions which nourished the successful completion of this research. I would also like to thank to Dr. Bettina speilbaur for teaching me microarray work and basic molecular biology techniques.

Acknowledgments

I am very grateful for the support and discussions I had from my colleagues and members of the Klaus lab for sharing their experiences and expertise with slice preparation as well as confocal and two-photon calcium imaging work and beers with me in all circumstances. A special thanks goes to Dr. Counsello Margvadgo from Jack Feldman laboratory (University of California, Los Angeles) who share with me her technical experiences with rhythmic brain slice preparation and calcium imaging work. Thanks a lot to Prof. Fred S. Wouters who allow me to share Cell culture facility in his laboratory and members of his group for nice support and generous help.

I could not have completed this work without the influence and generous assistance of many individuals including Susan, Uwe and Axel for their tremendous support through timely supply of the experimental animals. The technical support from Ms. Cornelia Hühne is greatly acknowledged. Lots of thanks to Ms. Regina Sommer-Kluβ and Mr. Andreas Bock, our departmental secretary for unlimited support with official matters. Workshop members of the physiology institute for the excellent technical support and help with the instruments and Wayne Sidio, Peter Funk and Howard Schultens for timely help with the computer and technical support was greatly acknowledged. Thanks to Anamika, Anjana, Ankur, Bhavna and Nitin for reading and correcting my thesis at short notice. Thanks to Wolf Zech for the help with cell culture and German translation of part of my thesis.

I would also like to acknowledge the financial support of the SFB 406, Synaptic Interaction in Neuronal Networks (German Research Foundation) and Bernstein center fro computational neuroscience (German Ministry for science and education, BMBF) for salary support.

Last but not the least; I would like to accredit this achievement to my parents (**Mr. Ram Nath Jaiswal & Mrs. Sushila Jaiswal**), my uncle Shyam Bihari Jaiswal and Pashupati Nath Jaiswal, my brother Vinod Jaiswal and Dharmendra Jaiswal and my elder sister Mrs. Manju Jaiswal, who despite their physical absence had been of constant mental strength and inspiration during the entire course of this endeavour.

Above all thanks to God almighty for everything.

Manuscripts Published & In Preparation

1, **Manoj Kumar Jaiswal** & Bernhard U. Keller (2007). Impaired mitochondrial metabolism in hypoglossal motoneurons of adult SOD1^{G93A} mice: implications for [Ca^{2+}]i and selective vulnerability in ALS. *In preparation*.

2, **Manoj Kumar Jaiswal** & Bernhard U. Keller (2007). Riluzole but not Melatonin inhibits spontaneous Ca^{2+} signaling in hypoglossal motoneurons of adult SOD1^{G93A} mouse: neuroprotection for selective vulnerability in ALS. *In preparation*.

3, **Manoj Kumar Jaiswal,** Araya Ruangkittisakul, Nikoletta Bobecea, Lucia Secchia, Klaus Ballanyi & Bernhard U. Keller (2007). Confocal and 2-poton imaging of [Ca^{2+}]i and mitochondrial membrane potential in respiratory motoneuron and glial cells of Brain stem slices. *In preparation*.

4, **Manoj Kumar Jaiswal**, Christine Leutbecher, Wolf-Dieter Zech, Miriam Goos, Alberto Ferri, Maria Teresa Carrì, Roland Nau & Bernhard U. Keller (2007). Simultaneous measurement of cytosolic and mitochondrial calcium concentrations in a mtSOD1 cell culture model of motoneuron disease. *Submitted.*

5, Miriam Lotz, Wolf-Dieter Zech, **Manoj Kumar Jaiswal**, Saju Balakrishnan, Sandra Ebert, Maria Teresa Carri, Bernhard U. Keller and Roland Nau (2007). Expression of a Cu, Zn superoxide dismutase typical for familial amyotrophic lateral sclerosis increases the vulnerability of neuroblastoma cells to infectious injury. *BMC Infectious Diseases* 2007, 7:131.

6, **Manoj kumar Jaiswal** (2006)**.** DipteraWG: A relational database of Dipteran biodiversity of Western Ghat hot spots. *Bioinformatics Trends*, Vol 1, Issue 2 (http://www.celnet.in/BIIJOURNAL/Scope.aspx).

7, Aditya Saxena, Pritish Varadwaj, S Singh, **Manoj Jaiswal** , K Misra & T Lahiri (2006). Phylogentetic analysis of *Mycobacterium leprae* genome for identification of novel drug targets. *Indian Journal of Biotechnology* 5:58-61.

Meeting-Conference Abstracts & Talks

M. K. Jaiswal, C. Leutbecher, W. D. Zech, M. Goos, A. Ferri, M. T. Carri, R. Nau & B. U. Keller (2007). Simultaneous measurement of cytosolic and mitochondrial calcium concentrations in a mtSOD1 cell culture model of motoneuron disease. Program No. 489.23/Z20 In 2007 Neuroscience Meeting Planner. San Diego, CA: Society for Neuroscience, 2007. Online.(http://www.sfn.org/am2007/). Poster .

Jaiswal MK, Stefan H, Balakrishnan S, Schomburg E & Keller BU (2006). Disruptions of [Ca]i and mitochondria in the adult SOD1^{G93A} mouse model of ALS: evidence from recordings *in vitro* and *in vivo*. Program No. 508.8 In 2006 Neuroscience Meeting Planner. Atlanta, GA: Society for Neuroscience, Online (http://www.sfn.org/am2006/). Talk.

Manoj Kumar Jaiswal, Saju Balakrishnan & Bernhard U. Keller (2005). Impairment of mitochondrial mechanism in the adult SOD1 G93A mouse model of human amyotrophic lateral sclerosis (ALS) - An implication for neuroprotection. 30th Göttingen Neurobiology Conference 2005 and 6th Meeting of the German Neuroscience Society (http://www.neuro.uni-goettingen.de/NBCsearch/NBC05/index.php). Poster.

Jaiswal MK, Balakrishnan S & Keller BU (2005). Rapid CCD fluorescence imaging reveals functional impairment of mitochondria in the adult SOD^{G93A} mouse model of human amyotrophic lateral sclerosis (ALS). *Pflugers Arch* 449: Supp01) P 23 -11. 84th annual meeting of German physiological society (http://www.physiologische-gesellschaft.de/). Poster.

EURON Advanced Training in Immunohistochemistry “The use of double, triple and quadruple staining methods in neurobiology” at University of Maastricht, The Netherlands held between September 27–29, 2005, (http://www.euronschool.eu/)- EURON is an international Research School in Neuroscience.

Bettina Speilbauer, Jobst Landgrebe, **M. K. Jaiswal** & B. U. Keller (2004). High-density microarry technology: efficient synergy of experimental design, array production and data analysis. DeChema Frankfurt (http://events.dechema.de/Programm-page-526.html#poster). Poster.

Curriculum Vitae

Name: Manoj Kumar Jaiswal.

Date of Birth: 02.11.1976.

Father's Name: Ram Nath Jaiswal.

Mother's Name: Sushila Jaiswal.

Place of Birth: Bharkhar (Kaemur), India.

1992 - 1994: Pre-University, Queens College, Varanasi, India.

1995 - 1999: **Bachelor of Science** in **Chemistry** (Hons.), Banaras Hindu University, Varanasi, India.

1999 - 2001: **Master of Science** in **Biotechnology**, School of Biotechnology, Devi Ahilya University, Indore, India.

M.Sc. Dissertation: Extraction, Purification & Characterization of Pectin Methylesterase from potato ("*Solanum Tuberosum*").
(Supervisor: Prof. Anil Kumar)

2001 - 2002: **Advanced Diploma** in **Bioinformatic**s, Bioinformatics Center, University of Pune, India.

Advanced Diploma Dissertation: DipteraWG: A Relational database of Dipteran Biodiversity of Western Ghats.

01/2007-03/2007: **Scientific fellow** at the Center of Neuroscience, University of Alberta, Edmonton, Canada (Lab. Head: Prof. Klaus Ballanyi)

Project: Confocal / 2-Photon imaging of Ca^{2+} and $\Delta\Psi m$ in respiratory motoneuron and glial cells of rat brain stem slices.

2004 – 2007: **Doctorate (Ph.D) Student** with Prof. Dr. Bernhard U. Keller, Georg-August University, University of Goettingen, Germany.

Ph.D Dissertation: Optical analysis of $[Ca^{2+}]$i and mitochondrial signaling pathways: implications for the selective vulnerability of motoneurons in amyotrophic lateral sclerosis (ALS).